

FABRICATION AND OPTICAL PROPERTIES OF ERBIUM-  
DOPED GROUP IV NANOWIRES AND THEIR  
CORRESPONDING OXIDES

by

JI WU

Master of Science, July 2000  
Anhui University  
Hefei, Anhui, China

Submitted to the Graduate Faculty of the  
College of Science and Engineering  
Texas Christian University  
in partial fulfillment of the requirements  
for the degree of

Doctor of Philosophy

May, 2007



## ACKNOWLEDGEMENTS

First, I would like to thank my most respected graduate advisor, Dr. Jeffery L. Coffey for his constructive suggestions and beneficial supervision during my pursuit of the Ph.D. degree in the Department of Chemistry at Texas Christian University. I have learned a lot from these scientific discussions owing to his broad knowledge in the field of inorganic and material chemistry. I truly believe that his critical scientific thinking and the way to do research will definitely guide me to the success of my future career.

Secondly, I want to sincerely thank Prof. Yitai Qian at the University of Science and Technology of China, from whom I learned solid state chemistry and materials chemistry. Under his influence, my research interest has been shifted to inorganic material chemistry.

Thirdly, I really appreciate other people who ever assisted me in doing research in the past five years. Dr. Albright, Dr. Neilson, and Dr. Richards helped me a lot in revising my degree proposal. Dr. Zerda and his group members, Yuejian Wang, Monika Wieligor, and Stephen Nauyoks helped me with Raman spectroscopy and X-ray diffraction experiments. I also appreciate David Yale, Jerry Katchinska and Jaime Cuanzon for their professional assistance. Dr. Couch at the Department of Biology at TCU trained me how to use electron microscopes. The expertise of Dr. Alan Nichols at the University of Illinois-Chicago is also greatly appreciated. Finally, I would like to thank Dr. Coffey's group members and Xiaodi Kou in Dr. Hanna's group for help and scientific discussions.

Financial support from Robert A. Welch Foundation and National Science Foundation is also much appreciated by the author.

# TABLE OF CONTENTS

<b>Acknowledgements</b> .....	ii
<b>List of Figures</b> .....	viii
<b>List of Tables</b> .....	xvi
<b>List of Abbreviations</b> .....	xvii
<b>CHAPTER I.</b>	
<b>Literature Review</b> .....	1
1.0 Introduction.....	2
1.0.1 Moore’s Law .....	2
1.0.2 Top-Down vs. Bottom-Up Approach .....	3
1.0.3 Nanowires as Building Blocks in Nanotechnology .....	8
1.1 Group IV Photonics .....	16
1.1.1 Introduction.....	16
1.1.2 Luminescence of Group IV Semiconductors.....	19
1.1.2.1 Porous Group IV Semiconductors .....	26
1.1.2.2 Group IV Nanocrystals .....	27
1.1.2.3 Er-doped Group IV Semiconductors .....	30
1.2 Crystalline Nanowire Synthesis.....	37
1.2.1 Natural Growth of 1-D Structures.....	37
1.2.2 Use of 1-D Templates to Direct the Growth of 1-D Nanostructures .....	39
1.2.3 Growth of Nanowires via Vapor-Liquid-Solid (VLS) Mechanism.....	41
1.3 Electrospun Nanofiber Synthesis.....	47
1.3.1 Introduction.....	47
1.3.2 The Basics of Electrospinning .....	48
1.3.3 Mechanism of Electrospinning .....	49
1.3.4 Control of the Diameter and Morphology of Electrospun Fibers .....	51
1.3.5 Fabrication of Inorganic Electrospun Nanofibers.....	53
1.3.6 Alignment of Electrospun Fibers.....	54

1.4 Photophysics of Erbium Luminescence.....	56
1.4.1 Introduction.....	56
1.4.2 Excitation of Erbium Ions.....	58
1.4.3 Major Gain-Limiting Factors.....	60
1.4.4 Sensitizers for Erbium.....	63
1.4.5 Ge, SiGe and Group IV oxides as Host Materials for Erbium Ions.....	67
1.5 EXAFS Measurements.....	70
<b>CHAPTER II.</b>	
<b>Research Synopsis.....</b>	<b>73</b>
<b>CHAPTER III.</b>	
<b>Fabrication, Characterization and Optical Properties of Er-Doped Ge Nanowires .....</b>	<b>80</b>
3.0 Overview.....	81
3.1 Experimental.....	83
3.1.1 Er-Doped Ge Nanowire Synthesis.....	83
3.1.2 Instrumentation .....	85
3.2 Results and Discussion .....	87
3.2.1 The role of carbon in the preparation of Ge NWs .....	87
3.2.2 Characterization of Ge and Er-Doped Ge NWs.....	88
3.2.3 Control of Average Diameters of Ge NWs.....	95
3.2.4 Raman Spectroscopy of Ge NWs .....	97
3.2.5 High Resolution TEM.....	98
3.2.6 XPS Spectroscopy of Er-Doped Ge NWs.....	100
3.2.7 UV-visible Spectroscopy of Er-Doped Ge NWs .....	103
3.2.8 Near-Infrared Photoluminescence .....	104
3.3 Summary.....	108
<b>CHAPTER IV.</b>	
<b>The Impact of Erbium Incorporation on the Structure and Photophysics of Silicon-Germanium Nanowires.....</b>	<b>109</b>
4.0 Overview.....	110
4.1 Experimental.....	112
4.1.1 Er <sup>3+</sup> -Doped SiGe NWs Synthesis .....	112

4.1.2 Instrumentation .....	114
4.2 Results.....	116
4.2.1 Structural Characterization of the 3 Different NW Permutations .....	116
4.2.1.1 ‘Sandwich’ Structure .....	116
4.2.1.2 ‘Er-Surface Enriched’ SiGe Structure .....	121
4.2.1.3 ‘Co-deposited Si&Er’ Ge Core Structure .....	125
4.2.2 Micro-Raman Spectroscopy.....	130
4.2.2.1 ‘Sandwich’ Structure .....	130
4.2.2.2 ‘Er-Surface Enriched’ SiGe Structure .....	131
4.2.2.3 ‘Co-deposited Si&Er’ Ge Core Structure .....	133
4.2.3 UV-visible Absorption Spectroscopy .....	134
4.2.4 EXAFS Measurements.....	136
4.2.5 The Impact of NW Structure and Post-Fabrication Annealing on the Near IR Light Emission.....	141
4.2.5.1 Erbium & Silicon Co-Deposited Sample.....	142
4.2.5.2 Sandwich Structure.....	146
4.2.5.3 ‘Erbium Surface-Enriched’ SiGe Nanowires.....	148
4.3 Discussion.....	151
4.3.1 ‘Sandwich’ Structure .....	151
4.3.2 Erbium-Surface Rich Structure.....	152
4.3.3 Erbium-Silicon Co-Deposited Structure .....	153
4.4 Summary.....	155

## **CHAPTER V.**

### **Emissive Erbium-Doped Group IV Oxide Nanofibers Derived from an Electrospinning Process.....**

5.0 Introduction.....	158
5.1 Experimental.....	161
5.1.1 Fabrication of Er-doped Group IV Oxide Nanofibers .....	161
5.1.2 Preparation of Nanofiber Arrays.....	164
5.1.3 Fabrication of Crystalline Er-doped GeO <sub>2</sub> NWs .....	165
5.1.4 Instrumentation .....	167
5.2 Results and discussion .....	169
5.2.1 Er <sub>2</sub> O <sub>3</sub> Nanofibers .....	169
5.2.2 Er-doped SiO <sub>2</sub> Nanofibers .....	171
5.2.3 Er-doped GeO <sub>2</sub> Nanofibers.....	174
5.2.3.1 Characterization .....	174
5.2.3.2 Effect of Annealing Temperatures.....	176

5.2.3.3 FT-infrared (IR) Vibrational Spectroscopy .....	178
5.2.4 Er-doped SnO <sub>2</sub> Nanofibers .....	179
5.2.4.1 Characterization .....	179
5.2.4.2 SAED, HRTEM and XEDS Linescan Analysis .....	181
5.2.4.3 X-ray Diffraction .....	183
5.2.4.4 Effect of Annealing Temperatures on the Size of SnO <sub>2</sub> Nanocrystals.....	184
5.2.4.5 Effect of the Presence of Er <sup>3+</sup> Ions on the Size of SnO <sub>2</sub> Nanocrystals.....	187
5.2.5 Effect of PVP Concentration on the Diameter of Er-doped SnO <sub>2</sub> Nanofibers .....	190
5.2.6 Nanofiber Arrays .....	191
5.2.7 Er-doped Crystalline GeO <sub>2</sub> NWs.....	193
5.2.7.1 Characterization .....	193
5.2.7.2 XRD .....	195
5.2.7.3 Effect of Si Wafer Position on the Morphology of GeO <sub>2</sub> NWs.....	196
5.2.8 Near-IR Photoluminescence .....	198
5.2.8.1 Near-IR PL of Er <sub>2</sub> O <sub>3</sub> , Er-doped SiO <sub>2</sub> , GeO <sub>2</sub> , and SnO <sub>2</sub> nanofibers .....	198
5.2.8.2 PL Excitation Spectra of Er-doped Ge NWs, GeO <sub>2</sub> NWs, and GeO <sub>2</sub> Nanofibers.....	206
5.3 Summary.....	208

## CHAPTER VI.

<b>GeO<sub>x</sub> as a Broad Band Sensitizer for Er-doped SnO<sub>2</sub> Nanofibers .....</b>	<b>209</b>
6.0 Introduction.....	210
6.1 Experimental.....	212
6.1.1 Deposition of Ge on Er-doped SnO <sub>2</sub> Nanofibers.....	212
6.1.2 Growth of Ge Nanorods on SnO <sub>2</sub> and Er-doped SnO <sub>2</sub> Nanofibers .....	213
6.1.3 Instrumentation .....	213
6.2 Results and Discussion .....	215
6.2.1 Characterization.....	215
6.2.2 Growth of Ge Nanorods on SnO <sub>2</sub> and Er-doped SnO <sub>2</sub> Nanofibers .....	218
6.2.3 Micro-Raman Spectroscopy.....	221
6.2.4 Room and Low Temperature Photoluminescence .....	224
6.3 Summary.....	230

<b>CHAPTER VII.</b>	
<b>Gold-Induced Self-Assembly of Germanium Micropatterns and Their Use as Nanowire Templates</b> .....	232
7.0 Introduction.....	233
7.1 Experimental.....	236
7.1.1 Fabrication of Germanium Micropatterns .....	236
7.1.2 Preparation of CaCO <sub>3</sub> Nanowires Using Ge Micropatterns as Templates .....	237
7.1.3 Preparation of Si Nanowires Using Ge Micropatterns as Templates .....	238
7.1.4 Instrumentation .....	239
7.2. Results and Discussion .....	240
7.2.1 Characterization of Ge Micropatterns.....	240
7.2.2 Factors Affecting the Morphology of Ge Micropatterns .....	242
7.2.3 Possible Mechanism Underlying the Formation of Ge Micropatterns .....	246
7.2.4 Growth Directions of the Sidewalls of Ge Micropatterns .....	248
7.2.5 Growth of CaCO <sub>3</sub> Nanowires Using Ge Micropatterns as Templates .....	251
7.2.5.1 Overview.....	251
7.2.5.2 Characterization .....	252
7.2.5.3 Effects of Electrolyte and Precipitation Position .....	253
7.2.5.4 Effects of Substrates .....	254
7.2.5.5 Micro-Raman Spectroscopy.....	255
7.2.5.6 Mechanism Underlying the Formation of CaCO <sub>3</sub> Nanowires.....	257
7.2.6 Growth of Si Nanowires Using Ge Micropatterns as Templates .....	259
7.2.6.1 Overview.....	259
7.2.6.2 Results and Discussion .....	259
7.3 Summary.....	262
<b>CHAPTER VIII.</b>	
<b>Concluding Remarks</b> .....	263
<b>Appendix</b> .....	268
<b>References</b> .....	276
<b>Vita and Abstract</b>	

## LIST OF FIGURES

<b>1.</b> Projection of integrated circuit complexity by Moore's law matches well the technology roadmap of Intel .....	2
<b>2.</b> Diagram of conventional photolithography technology – a top-down approach .....	4
<b>3.</b> Diagram of a nanosensor based on a Si NW field effect transistor .....	9
<b>4.</b> Schematic illustration of a CdS nanowire laser and its emission spectra .....	10
<b>5.</b> Schematic illustrations of a boron-doped Ge NW FET, Ge/Si core/shell NW FET, and band structure of Si/Ge core/shell heterogeneous structure .....	12
<b>6.</b> Schematic illustration of fluidic-directed assembly of parallel and crossed-nanowire structures .....	13
<b>7.</b> Schematic illustration of a Langmuir-Blodgett approach to prepare nanowire arrays .....	14
<b>8.</b> Process diagram to create metallic nanowire arrays .....	15
<b>9.</b> Schematic illustration of antiphase boundary structures in GaAs epitaxially grown on Si .....	19
<b>10.</b> Theoretical band structures of cubic Si, Ge and GaAs .....	23
<b>11.</b> The reactor design for preparing randomly dispersed Er-doped Si NCs .....	33
<b>12.</b> Reactor design for preparing surface enriched Er-doped Si NCs .....	35
<b>13.</b> Reactor design for preparing both Si NWs and Er <sup>3+</sup> -surface enriched Si NWs .....	36
<b>14.</b> Schematic illustration of the mechanism for the formation of Se nanowires, as well as the SEM and HRTEM images of Se nanowires .....	39
<b>15.</b> TEM images of plan-view and cross-section of the porous alumina templates, and SEM image of Au nanotubes .....	41
<b>16.</b> Schematic illustration of the growth of a silicon crystal by VLS .....	42
<b>17.</b> A conventional Au-Ge binary phase diagram employed to illustrate nanowires growth .....	44
<b>18.</b> Real time TEM images of Ge NW growth in different stages .....	44

<b>19.</b> Schematic illustration of the basic setup for electrospinning .....	49
<b>20.</b> Photographs of poly(ethylene oxide) electrospun fibers taken using different capture times .....	50
<b>21.</b> Plots showing the dependence of the average diameter of PVP/TiO <sub>2</sub> nanofibers on various processing parameters .....	52
<b>22.</b> Schematic illustration of the grounding collector to obtain arrayed fibers and SEM image of the arrayed PVP fibers.....	55
<b>23.</b> Schematic representation of Er <sup>3+</sup> ion energy levels in solid host materials and room temperature PL spectrum for an Er-doped SiO <sub>2</sub> sample.....	58
<b>24.</b> The schematic illustration of a carrier-mediated excitation of Er <sup>3+</sup> ions that is assisted by Si NC.....	60
<b>25.</b> Schematic illustrations of co-operative upconversion and excited state absorption processes .....	62
<b>26.</b> Schematic representation of the Er <sup>3+</sup> ion sensitization process by Yb <sup>3+</sup> ion in Er-doped Yb <sub>2</sub> O <sub>3</sub> amplifier sample.....	64
<b>27.</b> UV-visible absorption spectrum of Er-doped SiO <sub>2</sub> glass implanted with silver ions.....	65
<b>28.</b> Schematic representation of the sensitization process of Er <sup>3+</sup> ion by Si NCs embedded in the Er-doped SiO <sub>2</sub> matrix.....	66
<b>29.</b> Original and Fourier transformed EXAFS spectra of Er-doped Si sample .....	72
<b>30.</b> Reactor design for preparing Ge nanowires.....	84
<b>31.</b> Reactor design for doping Ge nanowires with erbium ions.....	84
<b>32.</b> Optical image of the germanium powder and the mixture of germanium and carbon after heated at 1000 °C for 1.5 h (X10).....	88
<b>33.</b> Scanning electron microscopy image of Ge nanowires.....	89
<b>34.</b> X-ray energy dispersive spectrum of the Ge NWs shown in Figure 33... ..	90
<b>35.</b> Selected area electron diffraction pattern of single Ge NW.....	91
<b>36.</b> Transmission electron microscopy image of Ge NWs showing a gold catalyst sitting on the end of the nanowires.....	92

<b>37.</b> SEM image and XEDS spectrum of Er-doped Ge nanowires .....	93
<b>38.</b> TEM image and SAED pattern from a single Ge NW .....	94
<b>39.</b> Diameter distributions of Ge NWs grown using various He flow rates and reaction times .....	96
<b>40.</b> Micro-Raman spectrum of Ge NWs .....	97
<b>41.</b> HRTEM images of a typical Ge NW .....	98
<b>42.</b> HRTEM image of an Er-doped Ge NW .....	99
<b>43.</b> XPS spectra confirming the presence of erbium centers in these doped NWs .....	102
<b>44.</b> UV-visible absorption spectra of Er-doped Ge NWs annealed in air .....	104
<b>45.</b> Room temperature photoluminescence spectra of Er-doped Ge NWs .....	105
<b>46.</b> Normalized PL intensity for Er-doped Ge NWs annealed at 600 °C in air using various excitation wavelengths .....	106
<b>47.</b> General synthetic routes to Er-doped SiGe NWs .....	113
<b>48.</b> Reactor design for fabricating Er-doped SiGe NWs .....	114
<b>49.</b> SEM, TEM images, and XEDS linescans of the “Sandwich” structure Er <sup>3+</sup> -doped SiGe NWs .....	118
<b>50.</b> High-angle annular dark field (HAADF) TEM image of an individual “Sandwich” structure Er <sup>3+</sup> -doped SiGe NWs .....	119
<b>51.</b> HRTEM image of “Sandwich” structure Er <sup>3+</sup> -doped SiGe NWs .....	121
<b>52.</b> SEM, TEM images, and XEDS linescans of “Er-surface Enriched” SiGe NWs .....	123
<b>53.</b> HAADF TEM images “Er-surface Enriched” SiGe NWs .....	124
<b>54.</b> HRTEM image of a “Er-surface enriched” SiGe NW .....	125
<b>55.</b> SEM, TEM images, and XEDS linescans of the “Co-deposited Er&Si” Ge core NWs .....	127
<b>56.</b> Elemental mapping of a single “Co-deposited Er&Si” Ge core NW .....	128
<b>57.</b> HRTEM images of “Co-deposited Er&Si” Ge core NWs .....	129

<b>58.</b> Raman spectra of the ‘Sandwich’ Structure Er-doped SiGe NWs .....	131
<b>59.</b> Raman spectra of ‘Er-Surface Enriched’ SiGe NWs.....	132
<b>60.</b> Raman spectra of of the “Co-deposited Si&Er” Ge core NWs .....	134
<b>61.</b> UV-visible absorption spectrum of Er-doped SiGe NWs.....	135
<b>62.</b> Pseudo-RDF of Er-doped Ge NWs, two types of Er-doped SiGe NWs, and Er <sub>2</sub> O <sub>3</sub> .....	137
<b>63.</b> Room temperature photoluminescence (PL) spectra of all types of NWs.....	142
<b>64.</b> PL spectra of “Co-deposited Si&Er” Ge core NWs .....	144
<b>65.</b> Excitation wavelength dependence of three types of Er-doped SiGe NWs.....	146
<b>66.</b> PL spectra of “Sandwich” structure Er-doped SiGe NW. ....	147
<b>67.</b> PL spectra of “Er-surface enriched” SiGe NW.....	149
<b>68.</b> General procedures for fabricating Er <sub>2</sub> O <sub>3</sub> , Er-doped SiO <sub>2</sub> , GeO <sub>2</sub> , and SnO <sub>2</sub> nanofibers and schematic diagram of an electrospinning setup.....	163
<b>69.</b> Schematic illustrations of the electrospinning setups for (a) Strategy 1 and (b) Strategy 2.....	165
<b>70.</b> Reactor design for the fabrication of GeO <sub>2</sub> nanowires and its optical image.....	166
<b>71.</b> SEM images and XEDS spectrum of Er <sub>2</sub> O <sub>3</sub> nanofibers.....	170
<b>72.</b> Diameter distributions of Er <sub>2</sub> O <sub>3</sub> nanofibers annealed at 500 °C in air for 3 h and as-formed Er <sub>2</sub> O <sub>3</sub> /PVP nanofibers.....	171
<b>73.</b> SEM and TEM images, as well as XEDS spectrum of Er-doped SiO <sub>2</sub> nanofibers. ....	172
<b>74.</b> Diameter distributions of Er-doped SiO <sub>2</sub> nanofiber sample annealed at 500 °C and as-formed Er-doped SiO <sub>2</sub> /PVP nanofibers.....	173
<b>75.</b> SEM images and XEDS spectrum of Er-doped GeO <sub>2</sub> nanofibers .....	175
<b>76.</b> Diameter distributions of Er-doped GeO <sub>2</sub> nanofiber sample annealed at 500 °C and as-formed Er-doped GeO <sub>2</sub> /PVP nanofibers .....	176

<b>77.</b> SEM images of Er-doped GeO <sub>2</sub> nanofibers annealed at 500 °C; 700 °C; and 900 °C in air for 3 h. ....	177
<b>78.</b> FT-IR spectra of Er-doped GeO <sub>2</sub> nanofibers .....	179
<b>79.</b> SEM and TEM images, as well as XEDS spectrum of Er-doped SnO <sub>2</sub> nanofibers.....	180
<b>80.</b> Diameter distributions of Er-doped SnO <sub>2</sub> nanofiber sample annealed at 500 °C and as-formed Er-doped SnO <sub>2</sub> /PVP nanofibers.....	181
<b>81.</b> SAED pattern and HRTEM images of SnO <sub>2</sub> nanocrystals in an Er-doped SnO <sub>2</sub> nanofiber .....	182
<b>82.</b> HAADF image and XEDS linescans of an Er-doped SnO <sub>2</sub> nanofiber .....	183
<b>83.</b> XRD patterns of 4% Er-doped SnO <sub>2</sub> nanofibers annealed in air for 3 h at 900 °C and 1000 °C .....	184
<b>84.</b> XRD patterns of a 4% (atomic percentage) Er-doped SnO <sub>2</sub> nanofiber sample annealed at temperatures ranging from 500 to 1000 °C .....	185
<b>85.</b> TEM images of a 4% (atomic percentage) Er-doped SnO <sub>2</sub> nanofiber sample annealed at temperatures ranging from 500 to 1000 °C .....	187
<b>86.</b> XRD patterns of pure SnO <sub>2</sub> nanofibers and 4% Er-doped SnO <sub>2</sub> nanofibers .....	188
<b>87.</b> TEM images of 4% Er-doped SnO <sub>2</sub> nanofibers and pure SnO <sub>2</sub> nanofibers.....	189
<b>88.</b> SEM images and diameter distribution of thinner Er-doped SnO <sub>2</sub> nanofibers.....	191
<b>89.</b> SEM and optical images of nanofiber arrays (PVP, Er <sub>2</sub> O <sub>3</sub> , Er-doped SiO <sub>2</sub> ) .....	192
<b>90.</b> SEM and TEM images of crystalline GeO <sub>2</sub> NWs.....	194
<b>91.</b> SEM images and XEDS spectrum of Er-doped GeO <sub>2</sub> NWs.....	195
<b>92.</b> X-ray diffraction (XRD) pattern of as-formed GeO <sub>2</sub> NWs. ....	196
<b>93.</b> SEM images of GeO <sub>2</sub> NWs prepared under different conditions .....	197
<b>94.</b> PL comparison of all four types of nanofibers.....	199
<b>95.</b> PL spectra of Er-doped SnO <sub>2</sub> nanofiber samples with different erbium concentrations and annealed at various temperatures. ....	201

<b>96.</b> PL spectra of Er-doped SiO <sub>2</sub> nanofibers with various erbium concentrations . . . . .	202
<b>97.</b> PL spectra of Er-doped GeO <sub>2</sub> nanofibers with various erbium concentrations. . . . .	203
<b>98.</b> PL excitation spectra of Er <sub>2</sub> O <sub>3</sub> , Er-doped SnO <sub>2</sub> , SiO <sub>2</sub> , and GeO <sub>2</sub> nanofibers. . . . .	205
<b>99.</b> A typical near-IR photoluminescence of Er-doped GeO <sub>2</sub> nanowires . . . . .	206
<b>100.</b> PL excitation spectra of Er-doped Ge NWs, GeO <sub>2</sub> NWs, and Er-doped GeO <sub>2</sub> nanofibers. . . . .	207
<b>101.</b> Reactor design for depositing Ge on Er-doped SnO <sub>2</sub> nanofibers . . . . .	213
<b>102.</b> Illustration of the front, middle, and back parts of an Er-doped SnO <sub>2</sub> sample deposited with Ge . . . . .	215
<b>103.</b> SEM images and XEDS spectra of the front part and the middle part of the nanofiber sample . . . . .	216
<b>104.</b> TEM images of the front part and the back part of the nanofiber sample . . . . .	218
<b>105.</b> SEM images and XEDS spectrum of Ge nanorods grown on the sample . . . . .	219
<b>106.</b> SEM images and XEDS spectrum of Ge nanorods grown on pure SnO <sub>2</sub> nanofibers . . . . .	221
<b>107.</b> Raman spectra of pure SnO <sub>2</sub> nanofibers and Er-doped SnO <sub>2</sub> nanofibers deposited with Ge. . . . .	223
<b>108.</b> PL spectra of Er-doped SnO <sub>2</sub> nanofibers deposited with Ge . . . . .	225
<b>109.</b> PL spectra of Er-doped SnO <sub>2</sub> nanofibers deposited with Ge excited using a 532 nm green laser of 5 mW . . . . .	226
<b>110.</b> PL excitation spectra of the front part and the back part of an Er-doped SnO <sub>2</sub> nanofiber sample deposited with Ge . . . . .	227
<b>111.</b> Low temperature PL spectra of the front part and the back part of an Er-doped SnO <sub>2</sub> nanofiber sample deposited with Ge. . . . .	229
<b>112.</b> SEM image of a germanium inverse opal. . . . .	234
<b>113.</b> SEM image of 43 nm Co/Pd nano-island array fabricated using the IBPL method. . . . .	235
<b>114.</b> Reactor design for fabricating Ge micropatterns . . . . .	236

<b>115.</b> Diagram of the device for fabricating calcium carbonate nanowires using Ge micropatterns as templates .....	238
<b>116.</b> Diagram of the reactor design for fabricating Si nanowires using Ge micropatterns as templates.....	239
<b>117.</b> SEM image of germanium micropatterns fabricated through annealing a 3 nm Au-coated n-type Ge (100) wafer at 830 °C for 4 h in helium gas .....	240
<b>118.</b> SEM images and XEDS spectra of Ge micropatterns with/without a multifaceted island in the center .....	241
<b>119.</b> SEM images of as-cleaned Ge (100) wafer, Ge (100) wafer and 3 nm thick Au-coated Ge (100) wafer after being annealed at 830 °C for 4 h .....	242
<b>120.</b> SEM images of 8 nm thick Au-coated Ge (100) wafer annealed for 4 h at 400 °C, 600 °C and 830 °C .....	243
<b>121.</b> SEM images of Ge micropatterns obtained through annealing (100) Ge wafer coated with 3 nm Au, 8 nm Au, and 20 nm Au. ....	244
<b>122.</b> SEM images of Au-coated Ge wafer obtained using different He flow rates and annealing times.....	245
<b>123.</b> AFM image of Si <sub>0.7</sub> Ge <sub>0.3</sub> islands, TEM image of Co <sub>5</sub> Ge <sub>7</sub> islands and SEM image of Ge pores .....	247
<b>124.</b> SEM images and simulated projections of plane-view and vertical-view of Ge micropatterns. ....	250
<b>125.</b> XEDS spectrum, SEM and TEM images of CaCO <sub>3</sub> nanowires precipitated on the Ge micropatterns.....	253
<b>126.</b> XEDS spectrum and SEM images of CaCO <sub>3</sub> nanowires and microcubes deposited on the Ge micropatterns across and below the meniscus line.....	254
<b>127.</b> SEM images of CaCO <sub>3</sub> cubes precipitated on a Ge (100) n-type wafer, a freestanding sputtered Au film, and a 15 nm Au-coated p-type Si (100) wafer .....	255
<b>128.</b> Raman spectra of CaCO <sub>3</sub> nanowires and CaCO <sub>3</sub> microcubes .....	257
<b>129.</b> SEM of a typical CaCO <sub>3</sub> nanorod growing from one micropattern to another .....	259
<b>130.</b> XEDS spectrum and SEM images of Si NWs grown on Ge micropatterns.....	261

<b>131.</b> Reactor design for preparing ZnO microrods and microbelts .....	269
<b>132.</b> SEM images of as-prepared ZnO microrods, ZnO microbelts, and ZnO dendrites.....	270
<b>133.</b> SEM images and XEDS spectra of ZnO microbelts and microrods immersed in SBF at 37 °C for 3 weeks, 4 weeks, and 5 weeks .....	272
<b>134.</b> SEM images and XEDS spectra of Zn metal and ZnO powder that have been immersed in a SBF solution for 3 weeks. ....	274

## LIST OF TABLES

<b>Table 1.</b> Quantitative analysis of the first coordination shell of Er-doped Si.....	72
<b>Table 2.</b> Control of Ge NWs mean diameters by varying the helium flow rate and reaction time.....	95
<b>Table 3.</b> Atomic concentrations of Ge and Er on the edge and center of a Ge NW.....	100
<b>Table 4.</b> Quantitative XEDS analyses of 3 points shown in Figure 50.....	120
<b>Table 5.</b> Quantitative XEDS analyses of 2 points shown in Figure 53.....	124
<b>Table 6.</b> Erbium coordination parameters for all the samples studied.....	140
<b>Table 7.</b> Average diameters of SnO <sub>2</sub> nanocrystals in Er-doped SnO <sub>2</sub> fibers that were annealed at temperatures ranging from 500 to 1000 °C.....	186
<b>Table 8.</b> Average diameters of SnO <sub>2</sub> nanocrystals in pure and Er-doped SnO <sub>2</sub> nanofibers annealed at 1000 °C.....	189
<b>Table 9.</b> Transistor performance summary at 300, 77, and 4.5 K for a 0.12 × 10 μm <sup>2</sup> SiGe emitter.....	233

## LIST OF ABBREVIATIONS

AFM	atomic force microscopy
ALD	atomic layer deposition
APBs	antiphase boundaries
BZ	Brillouin zone
CaP	$\text{Ca}_{10}(\text{PO}_4)_6(\text{OH})_2$
CMOS	complementary metal oxide semiconductor
CVD	chemical vapor deposition
DI	de-ionized
DOF	depth of focus
ESA	excited state absorption
EXAFS	extended X-ray absorption fine structure
FET	field effect transistor
FWHM	full widths at half maximum
HAADF	high-angle annular dark field
ICDD	International Center for Diffraction Data
ID	inner diameter
IR	infrared
JCPDS	Joint Committee for Powder Diffraction Studies
MBE	molecular beam epitaxy
MFC	mass flow controller
NC	nanocrystal
NT	nanotube

NW	nanowire
1-D	one-dimensional
PDF	powder diffraction file
PDMS	poly(dimethylsiloxane)
PEO	poly(ethylene oxide)
PL	photoluminescence
PVA	poly(vinyl alcohol)
PVP	poly(vinyl pyrrolidone)
RF	radiofrequency
SAED	selected area electron diffraction
SBF	simulated body fluid
SEM	scanning electron microscopy
SNAP	superlattice nanowire pattern transfer
SPE	solid phase epitaxy
TEM	transmission electron microscopy
TEOS	tetraethyl orthosilicate
THF	tetrahydrofuran
tmhd	2,2,6,6-tetramethyl-3,5-heptanedionato
UV	ultraviolet
VLS	vapor-liquid-solid
XEDS	X-ray energy dispersive spectroscopy
XPS	X-ray photoelectron spectroscopy
XRD	X-ray diffraction

*CHAPTER I.*

Literature Review

## 1.0 Introduction

### 1.0.1 Moore's Law

Moore's Law is an empirical observation made in 1965 by Gordon E. Moore, a co-founder of Intel, which states that the number of transistors on an integrated circuit for minimum component cost doubles every 24 months.<sup>1</sup> Although Moore's Law was initially a future projection based on past observations, it has been widely accepted both as a goal and as guidance for the entire microelectronics industry. It is amazing that the roadmap of integrated circuit complexity matches so well the prediction in the past 40 years, as shown in Figure 1.<sup>2</sup>

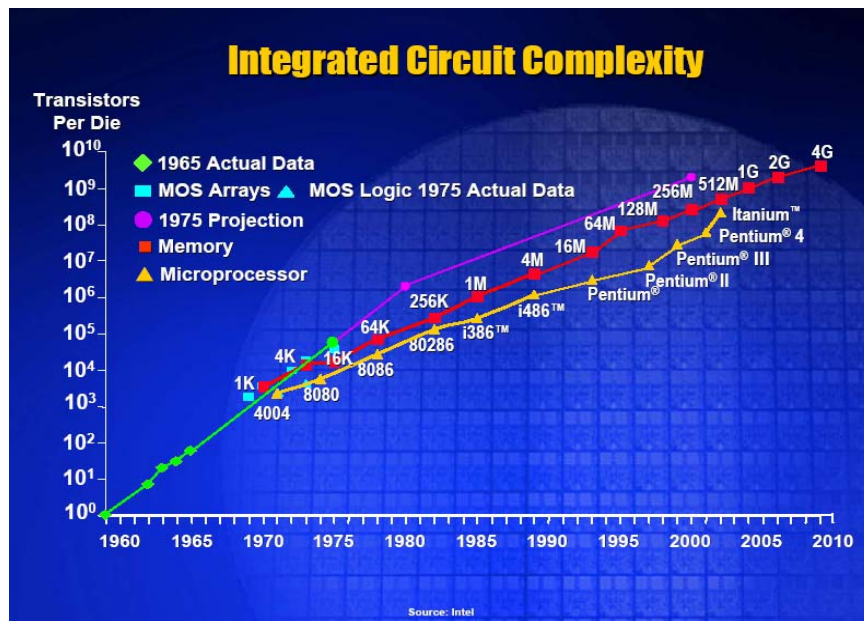


**Figure 1.** Projection of integrated circuit complexity by Moore's law matches well the technology roadmap of Intel (adapted from ref. 2).

However, in 2005, Moore predicted that the law will not continue forever, because the fundamental limits will be reached in the next 10 to 20 years when the channel width and gate thickness of transistor becomes close to that of atomic dimensions.<sup>3</sup> Those limitations involve manufacturing, materials, and economics. For example, since the current electronics industry is based on lithographic patterning of circuit element, very expensive short wavelength light sources have to be used to fabricate nano-scale transistors, which also challenges the fabrication techniques involving mask, lens, and photoresist.<sup>4</sup> Furthermore, when the thickness of a traditional SiO<sub>2</sub> gate is reduced to just a few atomic layers, electrons could tunnel through thin films so that it stops acting like a switch.<sup>5</sup> To surpass those limits, revolutionary breakthroughs, rather than evolutionary advancement, are required by modern microelectronic industry.<sup>6</sup>

### **1.0.2 Top-Down vs. Bottom-Up Approach**

To integrate more functional units such as transistors on a single chip, small transistors must be made. In general terms, there are two strategies to fabricate small structures:<sup>6</sup> one is a top-down approach that is mainly based on using photolithography; another one is the so-called bottom-up approach that relies on the assembly of basic building blocks, e.g. nanowires (NWs) and quantum dots.

Top-down approaches that are mainly based on photolithography begin with a piece of wafer such as Si and then reduce its lateral dimensions via patterning to obtain nanostructures.<sup>7</sup> This conventional technology has been well developed and widely used by the modern electronic industry to make microchips. Figure 2 shows the basic steps of photolithography.<sup>7</sup> First, a mask (negative) containing the required patterns is fabricated

using laser beam. In the next step, a beam of light shines through the mask, and then passes through a lens that focuses the image onto a photosensitive coating of organic polymer (called the photoresist) on the surface of a silicon wafer. Finally, the photoresist struck by the light can be selectively removed so that the pattern is replicated onto the wafer.

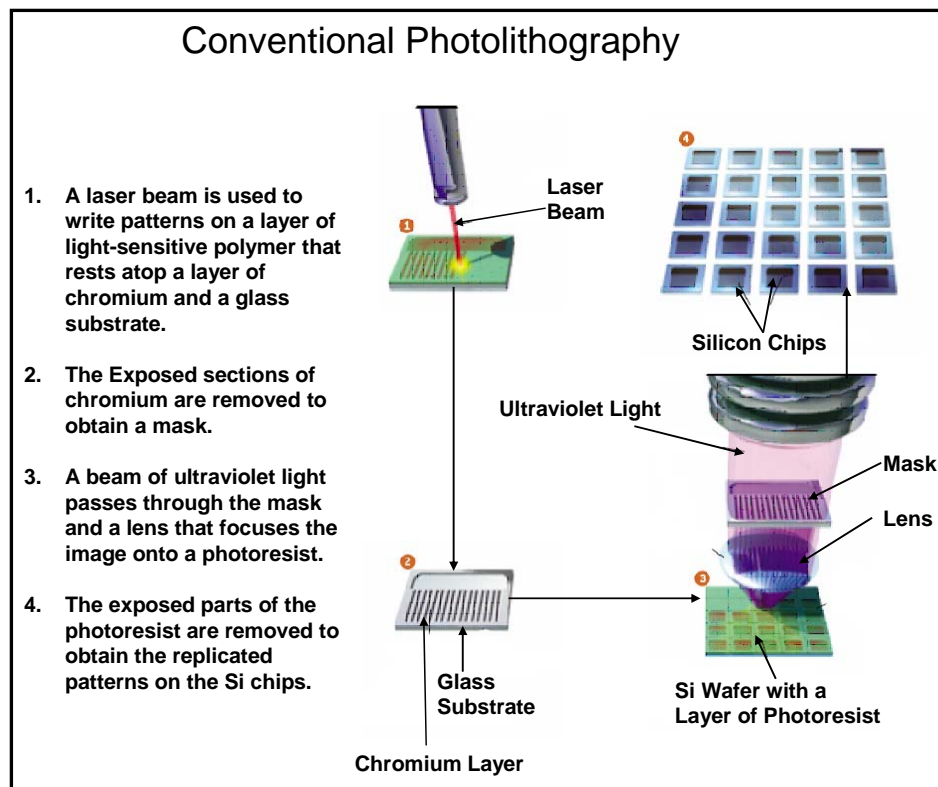


**Figure 2.** Diagram of conventional photolithography technology – a top-down approach (adapted from ref. 7).

Although refined photolithography can be used to make structures smaller than 100 nm, doing so is extremely difficult, expensive, and inconvenient owing to their intrinsic limitations.<sup>8</sup> First, the minimum resolution  $R$  achievable with projection lithography is determined by equation (1),<sup>4</sup> where  $\lambda$  is the light wavelength,  $k_1$  is a process-dependent

parameter in the range of 0.4 to 1, and NA stands for numerical aperture whose value is less than 1 if the surrounding medium is air.

$$R = k_1\lambda/NA \quad (1)$$

According to this equation, a light source with a wavelength at least shorter than 250 nm, e.g. X-ray, electron beam, or ultra-deep ultraviolet (UV), has to be used to obtain a resolution smaller than 100 nm. These light sources are expensive and less available.

Secondly, the depth of focus (DOF) is governed by equation (2),<sup>4</sup> where  $k_2$  is a process-dependent parameter in the range from 0.4 to 1, and  $\lambda$  and NA are defined as before.

$$DOF = k_2\lambda/(NA)^2 \quad (2)$$

Improved resolution by an increase of the value of NA and a decrease of the value of  $\lambda$  can lead to the reduction of DOF. In the microelectronic industry, a DOF of 500 nm or deeper is preferred for a comfort process control, and otherwise the final patterns obtained will be blur and less distinct.<sup>9</sup>

Thirdly, the stability of the photoresist has to be improved so that it will not be decomposed under the strong irradiation of those light sources with short wavelengths. Finally, new photolithographic equipment using shorter wavelength light will cost tens to hundreds of millions of dollars, which will prohibit or at least limit their accessibility for laboratory scientists.<sup>4</sup>

A bottom-up approach is a way to fabricate complex functional structures via an assembly of synthesized nanoscale building blocks, e.g. atoms, molecules, nanoparticles and nanowires. This approach can easily make ultra-small nanostructures inexpensively and has the potential to go far beyond the limits of top-down technology. However, the as-prepared nanoparticles tend to agglomerate in a random manner due to their huge surface area, and how to further arrange those random structures into designed and interconnected patterns cheaply still remains a big challenge.<sup>8</sup>

Two of the most representative bottom-up methods are those used to fabricate quantum dots and nanowires (NWs).<sup>8,10</sup> Quantum dots are crystals that contain only several hundreds of atoms, whose sizes are close to the diameter of the bulk exciton of a given material.<sup>11</sup> One of the most common examples of quantum dots are those of the II-VI variety, of which there are multiple ways to fabricate. One approach is based on traditional colloidal chemistry, which was pioneered in the early 1980s by Fendler.<sup>12</sup> In this approach, metallic cations were first reacted with a surfactant, such as inverse micelles, which were then exposed to the corresponding anions resulting in the formation of II-VI group nanocrystals. Steigerwald et al. found that these nanocrystals are metastable and can be stabilized by capping reagents such as organic ligands.<sup>13</sup> In their approach, CdSe nanocrystals were first synthesized in inverse micelles. Next, the surface of these nanocrystals was coated with extra Cd<sup>2+</sup> ions by the addition of Cd(ClO<sub>4</sub>)<sub>2</sub> solution. PhSeTMS (phenyl(trimethylsilyl)selenium), was then added to cap the surface of CdSe nanocrystals with phenyl groups. These phenyl-capped CdSe nanocrystals are hydrophobic and stable in air for 8-10 months.<sup>13</sup> However, since it is very difficult to control the size and shape of these inverse micelles, the quality of these nanocrystals is also difficult to be controlled. Another approach is to control the size of

nanocrystals by kinetically hindering the nucleation and growth process of nanocrystals through varying the precursor concentrations, reaction temperatures, and ligand concentrations. This approach was pioneered in the early 1990s by Steigerwald et al. and then further refined by Murray et al.<sup>14,15</sup> Steigerwald et al. decomposed the organometallic precursor of CdSe,  $\text{Cd}(\text{SePh})_2$ , in the solution of 4-ethylpyridine to obtain uniform CdSe nanocrystals with a typical diameter of  $\sim 3.0$  nm.<sup>14</sup> In 1993, Murray et al. prepared monodispersed CdE (E = S, Se, Te) quantum dots via the pyrolysis of organometallic reagents in a hot coordination solvent.<sup>15</sup> In their approach,  $(\text{CH}_3)_2\text{Cd}$  was first added to tri-n-octylphosphine (TOP) in a glove box, which was then mixed with appropriate amount of tri-n-octylphosphine selenide (TOPSe) in TOP. The mixture was heated at  $\sim 230$  °C for several hours to obtain high quality CdSe quantum dot samples. The air-sensitive and toxic organometallic cadmium precursors can be further substituted using nontoxic and stable reagents such as Cd metal, CdO, and  $\text{Cd}(\text{CH}_3\text{COO})_2$ .<sup>16,17</sup> These quantum dots can emit light with tunable wavelengths due to the variable band gaps associated with their sizes.<sup>18</sup> This useful property makes them a suitable candidate as biological markers.<sup>18,19</sup>

Another class of nanomaterial is called nanowire. Lieber et al. fabricated semiconductor nanowires via a vapor-liquid-solid (VLS) synthetic route, which was originated by Wagner and Ellis at the Bell Telephone Laboratories, Inc.<sup>10,20</sup> Those nanowires are single crystals and can be used as building blocks for more complex nanoscale devices, such as nanotransistors, nanolasers, etc, which will be described later in this chapter.

### 1.0.3 Nanowires as Building Blocks in Nanotechnology

The central issue of current nanotechnology is to develop efficient bottom-up methods to fabricate complex devices and functional systems using nanoscale materials as building blocks. One-dimensional nanowires themselves can function both as active devices and interconnects, which makes them good candidates as building blocks in an integrated nanostructure.<sup>10</sup> Nanowires with precisely controlled sizes, composition, and doping can be prepared via a number of techniques. These include the vapor-liquid-solid (VLS) synthetic route, electrospinning processes, 1-dimensional templating methods, and the natural growth of 1-D structures, all of which will be described in the following sections of this chapter.

These nanowires have been employed as building blocks to successfully generate nanosensors, nanophotonic and nanoelectronic devices, etc.<sup>21,22,23</sup> For one example, boron-doped Si NWs were used to build highly sensitive, real-time field effect transistor (FET)-based sensors for biological and chemical species as shown in Figure 3.<sup>21</sup> The mechanism underlying those sensors is that carriers within the nanowires will be depleted or accumulated in response to the binding of chemical and biological species at the nanowire surface, which results in changes in nanowire conductance. The amine and oxide-functionalized Si NWs can be used to detect the pH changes in the range of 2-9. In biological systems, the vitamin biotin (molecular weight = 244) can recognize and bind the protein streptavidin (molecular weight = 53K) via non-covalent bonds to form a complex with an association constant of  $\sim 10^{15}$ . Biotin-modified Si NWs nanosensors can detect streptavidin binding down to a concentration as low as 10 pM.

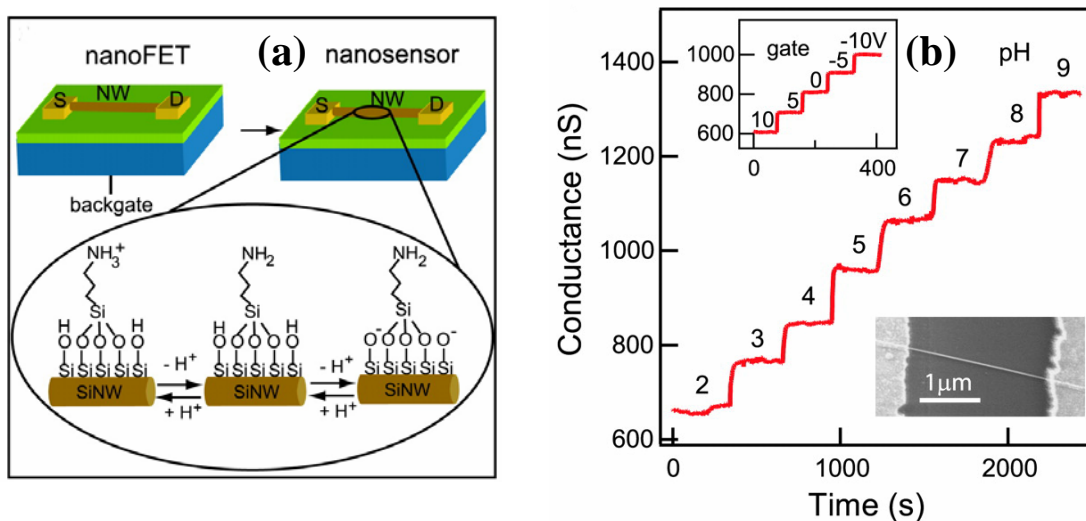


**Figure 3.** (a) Diagram of a nanosensor based on a Si NW field effect transistor (the Si NWs are functionalized with amine groups). (b) The conductance of the transistor is decreasing linearly when the pH values are increasing from 2-9 (adapted from ref. 21).

Nanowires can also be used as photonic building blocks to fabricate an electrically pumped nanolaser, as shown in Figure 4.<sup>23</sup> CdS nanowires on the order of 50-100 nm in width can serve as Fabry-Pérot cavities, that is, optical-resonator cavities. When electrons are injected from the top metal layer into a n-type CdS semiconductor nanowire, and holes are injected from the p-type Si substrate, electroluminescence will emit via electron-hole recombination within the CdS nanowire, as shown in Figure 4b. Figure 4c shows that a very sharp peak of luminescence is obtained using a 280 μA injection current, which is characteristic of lasing.

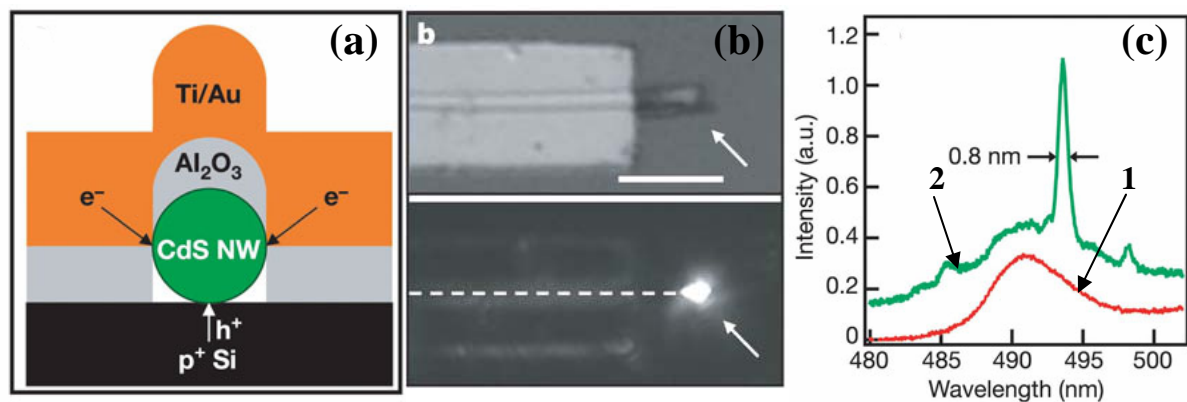


**Figure 4.** (a) Schematic illustration of the cross-section of the CdS nanowire laser ( $\text{Al}_2\text{O}_3$  is dielectric gate, Ti/Au is metal contact and  $\text{p}^+$  Si is used as substrate). (b) Top panel shows an optical image of the CdS nanowire laser, and the bottom panel shows the electroluminescence image at room temperature using an injection current of  $\sim 80 \mu\text{A}$  (arrows show the end of the CdS nanowire, and the scale bar is  $5 \mu\text{m}$ ). (c) Emission spectra recorded from a CdS nanowire laser using injection current of  $200 \mu\text{A}$  (1) and  $280 \mu\text{A}$  (2) (adapted from ref. 23).

Ge, Ge/Si core/shell and SiGe NWs are good candidates as building blocks for the fabrication of nanoscale field effect transistors (FETs) due to their high carrier mobilities relative to Si.<sup>10,24,25</sup> Dai et al. fabricated boron-doped p-type Ge NW FETs as shown in Figure 5a. The boron-doped Ge NWs were prepared using a vapor-liquid-solid (VLS) synthetic route.<sup>24</sup> A layer of 12 nm thick  $\text{HfO}_2$  gate dielectric was grown on the Ge NW via an atomic layer deposition (ALD) technique. It was found that the hole mobility of the p-type Ge NWs is as high as  $600 \text{ cm}^2 \text{ V}^{-1} \text{ s}^{-1}$ , which is much higher than that of Si NWs ( $120\text{-}180 \text{ cm}^2 \text{ V}^{-1} \text{ s}^{-1}$ ).<sup>24</sup> Until now, there are very few reports on the hole mobility of transistors built

with chemically synthesized Ge NWs. The highest hole mobility reported for a Ge metal oxide semiconductor FET (MOSFET) is  $700 \text{ cm}^2 \text{ V}^{-1} \text{ s}^{-1}$ .<sup>26</sup> In bulk single crystal Ge, the hole mobility is  $1800 \text{ cm}^2 \text{ V}^{-1} \text{ s}^{-1}$ .<sup>24</sup> Xiang et al. used Ge/Si core/shell nanowires as building blocks to fabricate nanoscale FETs with high hole mobilities as shown in Figure 5b.<sup>25</sup> First, Ge NWs with an average diameter of 17.6 nm were prepared via a VLS synthetic route, and then a layer of 1.7 nm Si was deposited via a chemical vapor deposition (CVD) technique using silane as source on the surface of Ge NW to form Ge/Si core/shell nanowires. Next, a layer of 4 nm  $\text{HfO}_2$  gate dielectric was deposited on the nanowire via an ALD method and Al/Au was used as contacts. The as-fabricated Ge/Si core/shell NW FET has a hole mobility of  $730 \text{ cm}^2 \text{ V}^{-1} \text{ s}^{-1}$  for a 190 nm long NW, which is higher than those of pure Ge NW FETs and Ge MOSFETs. This relatively higher hole mobility is due to the quantum confinement of the hole gas in the Ge valence band, which can be explained using Figure 5c.<sup>25</sup> Because there is a  $\sim 0.5 \text{ eV}$  valence band offset between the Ge and Si in this heterogeneous structure, holes will be accumulated (confined) in the Ge channel when the Fermi level ( $E_F$ ) lies below the valence band edge of the Ge, resulting in the enhancement of carrier mobilities.

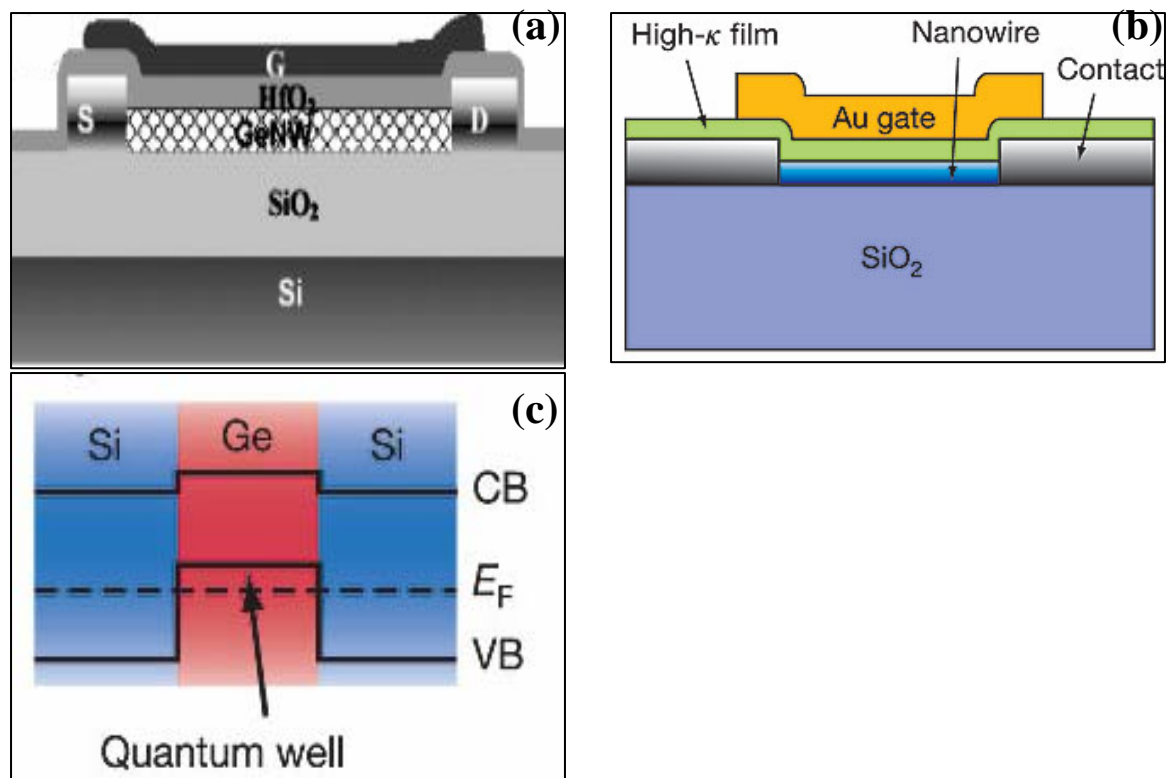


**Figure 5.** Schematic illustrations of (a) boron-doped Ge NW FET (G is gate, S is source, D is drain, HfO<sub>2</sub> is gate dielectric and contact used is Ti/W.), adapted from ref. 24. (b) Ge/Si core/shell NW FET. (c) Band structure of Si/Ge core/shell heterogeneous structure. Note: (b) and (c) are adapted from ref. 25.

Those nanowires can be further organized into larger scale arrays through fluidic-directed assembly and Langmuir-Blodgett technique that were developed by the Lieber group.<sup>27,28</sup> In the fluidic-directed assembly method, parallel NWs arrays are prepared by passing suspensions of the NWs through a microfluidic channel formed between a poly(dimethylsiloxane) (PDMS) mold and a flat substrate as shown in Figure 6.<sup>27</sup> Furthermore, crossed arrays can be readily achieved with another repeating flow that is

perpendicular to the first flow. The spacing and spatial position can be controlled by the density of the solution and the surface patterning of the substrate, respectively.

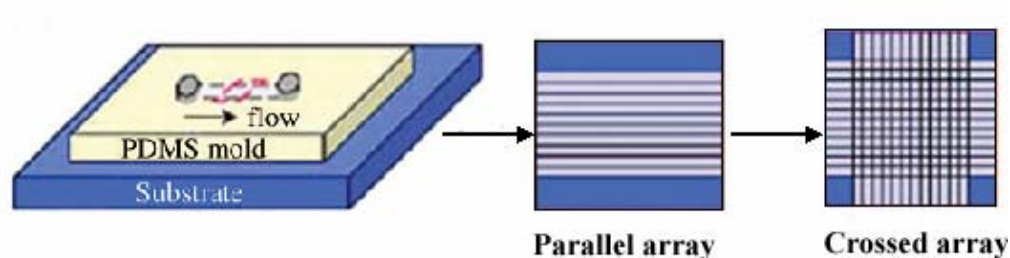


**Figure 6.** Schematic illustration of fluidic-directed assembly of parallel and crossed-nanowire structures, adapted from ref. 27.

The Langmuir-Blodgett approach is illustrated in Figure 7.<sup>28</sup> First, nanowires are suspended in nonpolar solvents containing surfactant 1-octadecylamine, and spread on the surface of an aqueous phase in a Langmuir-Blodgett trough. After compression, NWs can be aligned along their axes with the average spacing controlled by the compression process. The aligned NWs were then transferred to a substrate to make a parallel array, and crossed arrays can be achieved by transferring another layer of parallel NWs perpendicular to the first layer. This “log-on-a-river” approach offers a relatively straightforward pathway for the step-by-step assembly into hierarchically-organized nanodevices with ultra-high density, which has tremendous impact on the nanoscale electronics and optoelectronics.<sup>29</sup>

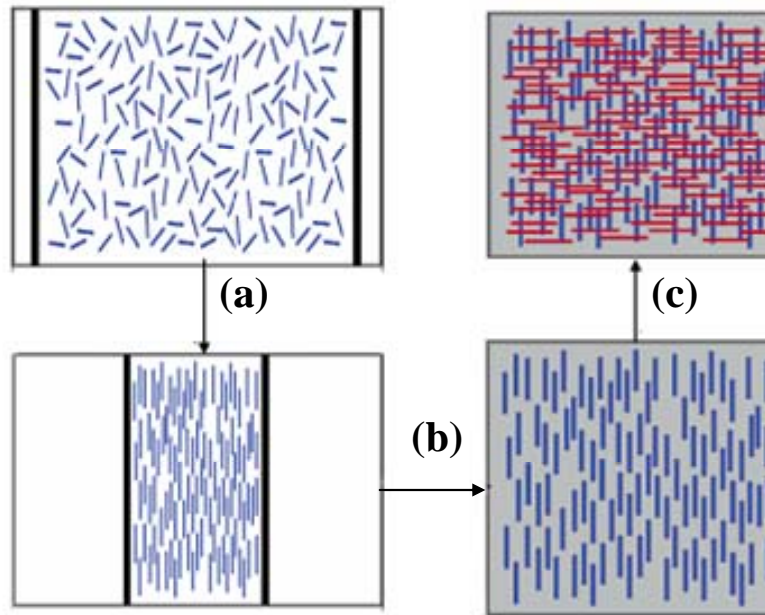


**Figure 7.** Schematic illustration of a Langmuir-Blodgett approach to prepare nanowire arrays. (a) Random nanowires dispersed on the Langmuir film is arrayed by compression. (b) Parallel nanowires arrays are transferred to a substrate such as Si wafer. (c) Crossed arrays can be achieved by transferring another layer of parallel NWs perpendicular to the first layer (adapted from ref. 28).

Recently, Heath's group has reported the fabrication of arrays of metallic nanowires via a superlattice nanowire pattern transfer (SNAP) method, as shown in Figure 8.<sup>30</sup> In their approach, a superlattice of GaAs/Al<sub>0.8</sub>Ga<sub>0.2</sub>As was first created using a molecular beam epitaxy (MBE) technique. The AlGaAs layers were then selectively removed using a buffered oxide etchant to create gaps between the GaAs layers. Next, metals such as Pt and Au were deposited on the top of the GaAs layers through an electron beam evaporation method to form metallic wires. During the metal deposition, the superlattice was tilted by 36°

with respect to the evaporation flux to make the metal deposited only on the GaAs layers. The wire widths are defined by the thickness of the GaAs layer, and the separation between the wires is controlled by the thickness of the AlGaAs layers. The metallic wires on the GaAs layers were then transferred to a silicon wafer coated with a thin epoxy (glue) film by contacting. The GaAs oxide layer at the nanowire-GaAs interface was etched away using a KI/I<sub>2</sub> aqueous solution. Finally, a brief oxygen plasma etch was employed to remove the residual epoxy layer. These metallic nanowires array can also be used as a mask to fabricate semiconductor nanowire arrays.

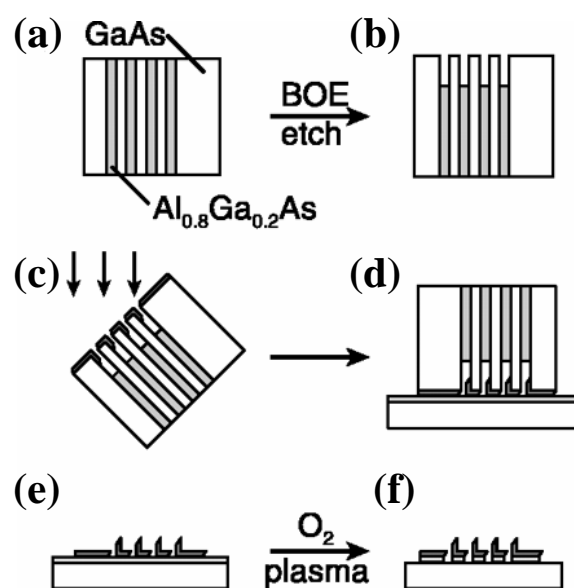


**Figure 8.** Process diagram to create metallic nanowire arrays. (a) The GaAs/AlGaAs superlattice; (b) AlGaAs layers were selectively etched; (c) metal deposition while the superlattice is tilted at 36°; (d) contact of the superlattice onto a silicon wafer coated with a thin layer of epoxy film; (e) release of metal wires by etching away the GaAs oxide; and (f) an O<sub>2</sub> plasma etching to remove the epoxy layer. Adapted from ref. 30.

## 1.1 Group IV Photonics

### 1.1.1 Introduction

Although the rapid development of the microelectronics technology has contributed enormously to the information revolution since the 1960s, nevertheless the ever-increasing demand for data to be transported at ever higher rates is driving the silicon microelectronics to its fundamental limits (Moore's Law). Therefore, scientists are searching for new technologies to extend or replace microelectronics. Among these technologies, photonics, especially Group IV photonics, has attracted enormous interest recently.<sup>31</sup> This technology relies on the fact that extremely higher data transport rates are achievable using photons instead of electrons because photons transport about 10 times faster than an electric current does, and light can offer a terahertz (THz) bandwidth to be modulated for computing.<sup>31</sup> Furthermore, this technology is absent of the current tunneling effect and short channel effects. The current tunneling effect is a serious problem in microelectronics when the thickness of the transistor gate dielectric is shrinking down to several nanometers.<sup>5</sup> In metal oxide FETs, when the length and width of a transistor channel is so short that it is comparable to the lengths and widths of the source and drain, short channel effects such as mobility degradation (current loss) and velocity saturation (switching delay) will appear.<sup>32</sup>

A number of applications for Group IV semiconductor photonics have been envisioned, such as optical computing, optical links between electronic processors, and interconnects between optical fibers and electronic processors.<sup>31</sup> Each of these applications requires the development of a number of separate devices, e.g. waveguides, amplifiers, photodetectors, modulators (both amplitude and frequency), wavelength division

multiplexers (WDM), signal splitters and optical sources, etc. Furthermore, current photonic devices are much larger than electronic transistors.<sup>31,33</sup> So the fabrication of nanoscale photonic building blocks, e.g. NWs and nanofibers is in much demand in order to integrate high density photonic units on a single chip to outperform the electronic counterpart.

Most of the above required devices have been realized to date except for the optical sources.<sup>34</sup> Until now, Group IV semiconductors have proven to be poor materials for optical sources due to the presence of strong non-radiative recombination pathways caused by their intrinsic indirect band gap structure (explained below). Currently, dominant optoelectronic sources are made of III-V semiconductors that can emit luminescence efficiently due to their direct band gap. For example, since the room temperature direct band gap of aluminum gallium indium nitride ( $\text{Al}_x\text{Ga}_y\text{In}_{1-x-y}\text{N}$ ) varies from 2.0 to 6.2 eV, depending on its composition, it has been widely used to fabricate light emitting devices ranging from the UV to the red.<sup>35</sup>

It has been a long-standing wish to integrate these III-V materials onto a Si chip to make it compatible with the current microelectronics industry. However, the integration has been shown to be problematic and costly due to the lattice and thermal expansion coefficient mismatches between the silicon and III-V group crystals.<sup>36</sup> The lattice mismatch can cause the formation of strains and high density interfacial defects such as edge dislocations. Dislocations are linear defects around which some atoms of the crystal lattice are misaligned. Edge dislocations are caused by the termination of a crystal plane in the middle of a crystal. In such a case, the adjacent crystal planes are bending around the edge of the terminating crystal plane.<sup>37</sup> For a representative example, when GaAs is heteroepitaxially grown on Si substrate, a high defect density is produced due to the 4.1% lattice mismatch between GaAs

and Si resulting in the device degradation.<sup>38</sup> The lattice constants for Si and GaAs are 5.431 Å and 5.653 Å, respectively. To reduce the defect density, compositionally graded buffer layers (a so-called virtual substrate) have been used.<sup>39</sup> Motorola Labs recently used a layer of single crystal strontium titanate (STO) as a virtual substrate to connect GaAs to Si, which was used to fabricate high performance metal semiconductor FETs (MESFETs).<sup>40</sup> MESFETs possess a relatively high transit frequency so that they can be used to fabricate microwave amplifiers and circuits.<sup>40</sup> Although the problem of strain between Si and STO is resolved using this method, the conformity of GaAs coating on STO still remains a problem.<sup>40</sup>

The thermal expansion coefficient mismatch between Si and III-V group materials causes stress when the integrated system is operated at high or fluctuating temperatures resulting in wafer bowing and micro-cracks.<sup>41</sup> In addition, it is also found to be the cause of dislocations.<sup>41</sup>

Finally, the formation of antiphase boundaries (APBs) is another serious problem in the epitaxial growth of polar III-V semiconductors, such as GaAs on Si.<sup>42</sup> The cubic GaAs lattice consists of alternating layers of Ga and As atoms spaced a quarter of the lattice constant apart along the [100] direction. Once there is a monoatomic step on the surface of Si substrate, the lattice rotates 90° at the step boundary resulting in the formation of APBs as shown in Figure 9.<sup>42</sup> On the other hand, a double atomic surface step causes a 180° rotation of the lattice resulting in the annihilation of APBs. Since the APBs are crystal planes composed of As-As and Ga-Ga bonds, they are highly charged leading to the reduction of carrier mobility, which is deleterious to device performance.<sup>43</sup>

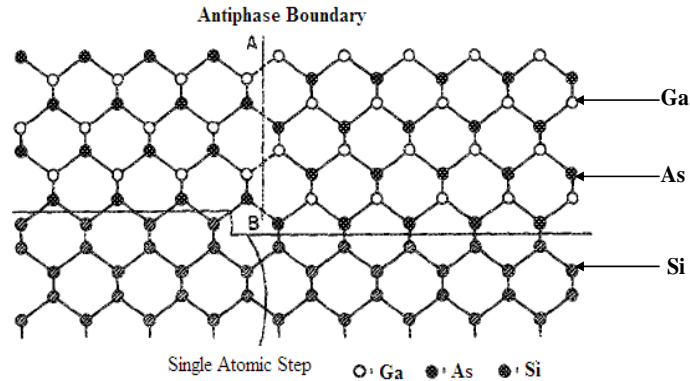


**Figure 9.** Schematic illustration of antiphase boundary structures in GaAs epitaxially grown on Si. Adapted from ref. 42.

### 1.1.2 Luminescence of Group IV Semiconductors

Luminescence is the light emitted by sources other than a hot, incandescent body, including electroluminescence, photoluminescence, etc.<sup>44</sup> Luminescence is caused by the transition of electrons within a substance from higher energy levels to lower energy levels. For example, in the case of photoluminescence (PL), a substance absorbs photons resulting in the excitation of its electrons into a permissible higher energy level that is regulated by quantum mechanics, and then these electrons return back to a lower energy level accompanied by the emission of light, or luminescence.<sup>44</sup> The wavelength of photoluminescence is determined by the energy difference between the initial and final states of the transition.

In terms of band theory, semiconductors are considered to have a filled valence band and an empty conduction band at zero Kelvin.<sup>45</sup> The luminescence of semiconductors is closely related to their band gap, that is, the energy difference between the top of the valence band and the bottom of the conduction band. When a semiconductor absorbs energy above its

band gap, an electron will be excited from the valence band to the conduction band leaving behind a positive charge, called a hole, in the valence band. The negative electron and the positive hole are attracted each other by a Coulomb force to form a bound electron-hole pair that moves in hydrogen-like orbits to form an exciton.<sup>45</sup> When these excitons recombine radiatively, luminescence is emitted.<sup>46</sup>

The efficiency of this electron-hole recombination process is closely related to the nature of the electronic band structure of a solid, usually plotted as the energy (E) vs. the momentum (or wave vector, k) of the carriers (electrons and holes) in the first Brillouin zone (BZ).<sup>46</sup> So what is the first Brillouin zone? The construction and illustration of Brillouin zone for a 3-dimensional lattice is quite difficult to follow. However, the construction of Brillouin zone for a one-dimensional lattice serves as an effective illustration. In a one-dimensional periodic potential, the wave function of a particle (usually, an electron) can be expressed using Bloch's theorem as follows:<sup>47</sup>

$$\Psi_k = \sum e^{ikna} x_n \quad (3)$$

where  $\Psi$  is the Bloch wavefunction, k is the wave vector, n is the label of each particle in the one-dimensional lattice (n = 0, 1, 2, etc), a is the lattice spacing, and x is a basis function for each particle ( $x_0, x_1, x_2$ , etc). When  $k = 0$ ,  $\Psi_0 = x_0 + x_1 + x_2 + \dots$ , which is corresponding to the most bonding Bloch wavefunction. When  $k = \pi/a$ ,  $\Psi_0 = x_0 - x_1 + x_2 - x_3 \dots$ , which corresponds to the most antibonding Bloch wavefunction. However, there is a finite range of k values before they repeat themselves, that is,  $|k| \leq \pi/a$ . This range is the so-called first

Brillouin zone. The number of  $k$  values is equal to the number of microscopic unit cells in a macroscopic crystal. The wave vector,  $k$  can be calculated using the equation (4):<sup>47</sup>

$$p = \hbar k \quad (4)$$

where  $p$  is the electron momentum,  $\hbar$  is the reduced Planck's constant ( $h/2\pi$ ), and  $k$  is the wave vector as defined above. The energy ( $E$ ) can be calculated from Schrodinger's equation using a pseudopotential Hamiltonian that consists of a kinetic energy term and a weak pseudopotential term as expressed by the following equation:<sup>48</sup>

$$H = 1(\hbar^2/2m)\nabla^2 + V_p(r) \quad (5)$$

where  $H$  is the pseudopotential Hamiltonian,  $\hbar$  is the reduced Planck's constant ( $h/2\pi$ ),  $m$  is the mass of a particle,  $\nabla$  is nabla operator,  $V_p$  is the pseudopotential, and  $r$  is the distance of a particle from the atomic nucleus. An empirical pseudopotential is used to replace the complicate real potential experienced by an electron in the bulk lattice in order to greatly reduce the computing time and effort involved to solve Schrodinger's equation.<sup>48</sup> The lengthy and complex procedures for pseudopotential generation has been discussed in the literature.<sup>48</sup>

The x-axis labels denoted by Roman letters in the band structure refer to the high symmetry points in the first Brillouin zone.  $\Gamma$  is the center of the first Brillouin zone.  $L$ ,  $X$  and  $K$  are the intersection points between the  $[111]$ ,  $[100]$  and  $[110]$  directions and the boundary of first Brillouin zone, respectively. It is notable that the valence band structure for

most semiconductors is quite similar, that is, the maximum energy is located at the  $\Gamma$  point, the center of first Brillouin zone (Figure 10).<sup>46,49</sup> However, the conduction band structures for different substances are quite dissimilar due to the difference in their crystal structures, bond lengths, electronegativities, etc. Figure 10 shows the theoretical electronic band structures of cubic Si, Ge, and GaAs.<sup>49</sup>

The band gap is defined as the energy difference between the maximum in valence band at  $k = 0$  and the minimum in the conduction band. When this minimum occurs at  $k = 0$ , the semiconductor is called a direct band gap semiconductor because the initial and final states of a transition have the same momentum ( $k = 0$ ). For example, GaAs belongs to this kind of semiconductor (Figure 10c). In a direct band gap semiconductor, an electron is excited into the conduction band minimum at  $k = 0$  and then decays in a straightforward manner to the valence band state also at  $k = 0$  by emitting a photon of energy equal to the band gap.

However, in the cases of Group IV semiconductors such as Ge and Si, the minima in the conduction band and the maxima in the valence band do not occur at the same momentum (Figure 10a and 10b). These semiconductors are called indirect band gap semiconductors. In these semiconductors, a change of electron momentum ( $k$ ) is required before electron-hole recombination.<sup>46</sup> This change is achieved by transferring the momentum to the lattice via a phonon of appropriate momentum and energy.<sup>46</sup> Since the electron-hole recombination of indirect band gap semiconductors involves a simultaneous three-body event (electron, hole and phonon), the efficiency of light emission is much lower than that of direct band gap semiconductors. Furthermore, the presence of non-radiative pathways such as the Auger relaxation process combined with the extreme long radiative recombination lifetimes

(of the order of microseconds for silicon) also make indirect band gap semiconductors poor candidates for light emitting sources.<sup>46</sup> In the Auger process, the excited electrons transfer their energy to other electrons before returning back to their ground state without emitting photons.

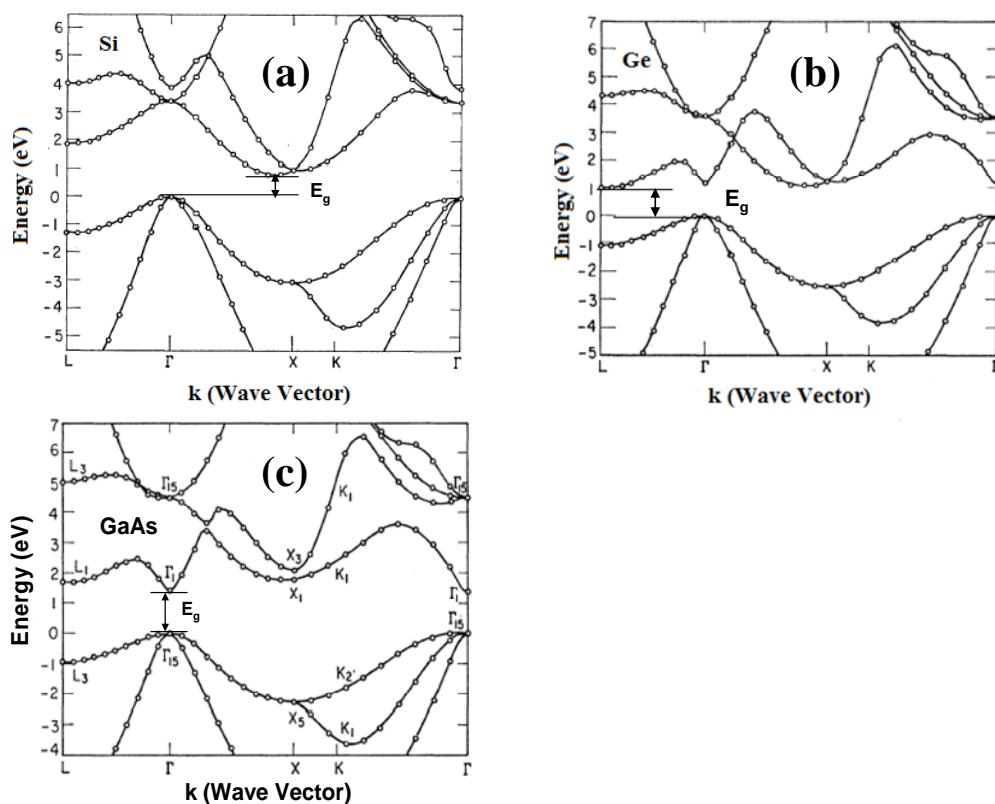


**Figure 10.** Theoretical band structures of cubic (a) Si, (b) Ge and (c) GaAs. Adapted from ref. 49.

Fortunately, there are several approaches available to make these indirect band gap semiconductors luminescent: 1) band structure engineering such as in the case of  $\text{Ge}_x\text{Sn}_{1-x}$  alloys;<sup>46</sup> 2) quantum confinement, such as in the cases of porous Si and Group IV

semiconductor nanocrystals;<sup>46</sup> 3) impurity-mediated luminescence such as in the case of Er-doped Group IV semiconductors.<sup>46</sup>

One strategy to generate a luminescent direct gap of Group IV semiconductors has been attempted through alloying. For example, it was calculated that addition of 23 to 65% (atomic percentage) Sn to Ge can help make direct band gap SnGe alloys.<sup>50</sup> However, the huge lattice mismatch between Ge and Sn creates high density of dislocations that are very efficient nonradiative pathways. As a consequence, the efficiency of light emission from this semiconductor alloy is very low.<sup>46</sup>

There are two approaches based on quantum size effects which make indirect gap materials emissive, including zone folding and quantum confinement effects.<sup>51,52</sup> The zone folding approach is one of the most effective means to convert an indirect band gap transition into a quasi-direct one, which was first proposed by Gnutzman et al.<sup>51</sup> In this approach, a superlattice structure of Si and Si-Ge with certain periodicity ( $d$ ) is used to reduce the size of the first Brillouin zone from  $\pi/a$  ( $a$  is the lattice constant) to  $\pi/d$  in the [100] direction, ideally folding the conduction band bottom to the  $\Gamma$  point and resulting in the formation of a quasi-direct band gap material. However, in practice, an intense light emission from such a superlattice structure has not yet been realized, mainly due to two problems.<sup>46</sup> One is the interfacial strains caused by the lattice mismatch between these two superlattices. Another one is that although the transition is direct in reciprocal space, they are indirect in real space because that the electrons and holes are located separately in Si and Ge.

Quantum confinement in films (1-D), wires (2-D), and dots (3-D), whose sizes are close to their bulk exciton Bohr radius, provides another alternative to make indirect band gap semiconductors emissive.<sup>52</sup> For nanocrystals in the quantum-confined size regime, the

relationship between the band gap and the size of the nanocrystals can be expressed using equation (6) that was proposed by Brus in 1986.<sup>53</sup>

$$E(R) = E_g + 2\pi^4 (1/m_e^* + 1/m_h^*)/(h^2R^2) - 1.8e^2/(\epsilon_2R) + \text{small terms} \quad (6)$$

where  $R$  is the radius of the nanocrystallite,  $E(R)$  is the enlarged band gap,  $E_g$  is bulk band gap,  $m_e^*$  and  $m_h^*$  stand for the effective masses of electron and hole, respectively,  $\epsilon_2$  is the dielectric constant of the nanocrystallite, and “small terms” are related to the polarization of the surface molecules. When the size is close to the exciton Bohr radius, the second term that is related to the quantum confinement is much bigger than the third term that is related to Coulomb interactions. From this equation, it can be easily seen that band gap will be enlarged when the size decreases. It was calculated that the band gap of a CdS nanocrystal (NC) with a  $R = 2.5$  nm can be enlarged by 0.24 eV compared with the bulk band gap of CdS.<sup>53</sup> Along with an enlarged band gap, quantum confinement effects can also cause the wave functions (solutions to Schrödinger’s equation) of carriers to spread out in terms of momentum, which means that the locations of carriers are spreading out all over the volume of the wave function. According to quantum mechanics, the location and momentum cannot be determined with arbitrary accuracy in favor of a blurred picture of probabilities.<sup>54</sup> As a consequence, the chance for excited electrons to appear at the center of the BZ will be increased resulting in the increase of the likelihood of radiative transitions. Furthermore, since the excitons are confined in these nanocrystals, the non-radiative Auger recombination process that is related to the exciton-phonon interaction could be much suppressed, and the

surface defects and impurities in these nanocrystals will greatly affect the exciton relaxation process.<sup>55</sup>

Lastly, doping Group IV semiconductors with erbium ions is another very promising method to make these indirect band gap materials luminescent due to the intra-4f  $^4I_{13/2} \rightarrow ^4I_{15/2}$  transition at 1540 nm associated with this rare earth center.<sup>46</sup> This approach will be described in detail in the section regarding the photophysics of erbium luminescence.

### 1.1.2.1 Porous Group IV Semiconductors

Porous Si was first obtained 50 years ago by Uhlir at Bell Labs during the studies of the electropolishing of Si in HF-based aqueous solutions.<sup>56</sup> He observed that the surfaces of these etched Si wafers possessed a red or brown color. However, research concerning porous silicon was largely neglected until Canham demonstrated that it can emit tunable room temperature luminescence efficiently in 1990.<sup>57</sup> Based on optical absorption measurements, Lehman et al. reported in 1991 that porous Si possesses an enlarged band gap relative to bulk Si, and this phenomenon was attributed to quantum size effects.<sup>58</sup> The formation of porous Si involves a continuous process of electrochemical oxidation and subsequent acid dissolution of the oxides.<sup>55</sup>

Porous Si based structures have been reported to emit luminescence whose wavelengths range from infrared to the near ultraviolet.<sup>55</sup> Several mechanisms have been proposed trying to explain the origin of its luminescence, some of which are still controversial. Canham viewed the structure of porous Si as a network of interconnecting quantum Si wires.<sup>55</sup> He attributed the origin of the luminescence to the quantum confinement of carriers in these crystalline Si wires.<sup>57</sup> The peak of the luminescence can be shifted to

shorter wavelengths by changing the anodization conditions to obtain a finer wire network, which is consistent with this quantum confinement mechanism.<sup>55</sup> The broadening of the peak is attributed to the size distribution of the wires in the porous Si.<sup>55</sup> However, the exciton decay time (PL observed lifetime) for porous Si is about tens of microseconds, which is much longer than that of the direct band gap materials (on the order of nanoseconds). This fact raises the possibility that the luminescence is still from an indirect band gap transition.<sup>46</sup> Furthermore, this mechanism cannot explain why the photoluminescence goes to a maximum at ~200 K and is completely quenched at temperature below a few Kelvin.<sup>46</sup> This phenomenon implies that the radiative process might still be assisted by phonons, which is characteristic of indirect band gap semiconductors. Other proposed mechanisms suggest that the luminescence of porous Si might be also related to the surface states, defects and hydride-termination of porous Si.<sup>46</sup>

Besides porous Si, crystalline porous SiGe obtained by anodic etching in a HF / C<sub>2</sub>H<sub>5</sub>OH/H<sub>2</sub>O electrolyte demonstrated a photoluminescence (650-750 nm) spectrum very similar to that of porous Si.<sup>59</sup> Miyazawa et al. anodized bulk Ge in an aqueous HF electrolyte to achieve porous germanium, from which a weak band gap luminescence was observed.<sup>60</sup> Recently, it was reported that porous Ge can also be prepared by a bipolar etch in a HCl-based aqueous solution.<sup>61</sup> The mechanism underlying the luminescence is not clearly understood yet.<sup>62</sup>

#### **1.1.2.2 Group IV Nanocrystals**

Very small Group IV nanocrystals (NCs) can also emit efficient luminescence due presumably to quantum confinement effects similar to porous silicon structures.<sup>63</sup> These

nanocrystals can be prepared in large quantities through two general synthetic methods. One type is solution-based methods, while the other one is based on vapor phase technique.

In 1992, Heath synthesized single crystalline Si NCs whose sizes range from 5-3000 nanometers.<sup>64</sup> The synthesis was based on the reduction of SiCl<sub>4</sub> or SiCl<sub>3</sub>R (R= H, octyl) by elemental Na in pentane or hexane. The reaction was conducted in autoclave at high pressure (>100 atm) and high temperature (385°) for several days. In 1992, Wilcoxon et al. prepared highly crystalline, size-selected Si NCs in reverse micelles under relatively more mild conditions.<sup>65,66</sup> Their approach relies on the controlled nucleation and growth of Si nanocrystals in the interior of inverse micelles.<sup>66</sup> SiX<sub>4</sub> (X = Cl, Br, or I) was first dissolved in the interior of these inverse micelles, whose size ranges from 1-10 nm. Next, Si(IV) was reduced to elemental Si using an anhydrous metal hydride such as LiAlH<sub>4</sub>. Control over the Si nanocrystal sizes was realized by varying the micelle size, intermicellar interaction, etc.<sup>66</sup> All solvents and surfactants used must be anhydrous and very pure (high pressure liquid chromatography grade) to prevent the oxidation of Si NCs and inhomogeneous nucleations.<sup>66</sup> In 1996, Kauzlarich et al. used Zintl salts such as KSi or NaSi as a starting reagent to synthesize Si NCs with an average diameter of 2.3 nm.<sup>67</sup> In their fabrication method, KSi was first mixed with SiCl<sub>4</sub>, and then refluxed in tetrahydrofuran (THF) for several days to obtain Si NCs. The reaction can be expressed using the following equation:<sup>67</sup>



Recently, Baldwin et al. used sodium naphthalide and SiCl<sub>4</sub> as starting materials to prepare Si NCs in large quantities.<sup>68</sup> In their method, sodium naphthalide was added to SiCl<sub>4</sub> in 1,2-

dimethoxyethane to form a dark brown suspension. Then 1-octanol is added to the suspension resulting in the formation of a yellow solution with a white precipitate. The solvent and naphthalene were removed under a reduced pressure. The resulting orange solid was extracted with hexane to obtain Si nanoparticles whose sizes range from 2 to 12 nm. The resulting particles are crystalline cubic Si with a (111) orientation. It is noteworthy that as-fabricated Si NCs are air sensitive and have to be treated with alcohol to terminate the surface with OR groups ( $R = CH_3$ ) to stabilize them.

Wilcoxon et al. also fabricated Ge nanocrystals in inverse micelles.<sup>69</sup> In the approach, the surfactants such as nonionic aliphatic polyethers or quaternary ammonium cationic surfactants were dissolved in anhydrous THF to obtain micelles. An anhydrous ionic salt ( $GeCl_4$ ) was then dissolved in the hydrophilic interior of micelles. The total absence of water prevented the oxidation of Ge into  $GeO_2$ .  $Ge(IV)$  was then reduced to  $Ge(0)$  by  $LiAlH_4$  in THF solution. The sizes of the Ge clusters range from 2 to 10 nm. Upon excitation by a 400 nm light, strong photoluminescence at 420 nm was observed for Ge NCs with an average diameter of 2 nm, assumed to occur due to the direct transition from  $\Gamma_{25} - \Gamma_{15}$  in the first Brillouin zone of Ge.<sup>69</sup>

A three step procedure involving a vapor phase technique was used to prepare visibly luminescent Si nanocrystals.<sup>70</sup> First, a mixture of disilane-helium was flowed into a pyrolysis chamber of 1000 °C, followed by immediate dilution into a  $O_2$ -He mixture and decrease of temperature to 200-300 °C to stop the nanoparticles growth. The particles were then collected in a solution of ethylene glycol to yield a colloid. The resulting surface-oxidized nanoparticles are crystalline and can emit weak luminescence ranging from 500 to 900 nm at room temperature. The low quantum efficiency is due to the presence of nonradiative

pathways that shorten the lifetime of Si excitons. The sizes of Si NCs can be controlled by varying the He flow rate and the concentration of disilane.<sup>70</sup>

### 1.1.2.3 Er-doped Group IV Semiconductors

Currently, there are a number of techniques to dope erbium ions into Group IV semiconductors, including molecular beam epitaxy (MBE), ion implantation, sputtering, liquid phase epitaxy and chemical vapor deposition (CVD).<sup>34</sup> Among these techniques, the majority of work has been focused on ion implantation that uses high energy erbium ions to bombard the host materials.<sup>71</sup> This method provides a high degree of control over the position and concentration of implanted ions by tuning the applied electrical potentials and the fluences of erbium ions. However, the crystallinity of the host materials is usually damaged by this high energy bombardment process. Therefore, high temperature post-annealing is required to recover the crystallinity. When the substrate is an insulator, a layer of conductive metal coating is required in order to reduce any electrical charging effects. The coating can be etched off using a NaOH solution after implantation.<sup>72</sup>

Solid phase epitaxy (SPE) is a technique that can load high concentrations of erbium ions into host materials.<sup>73</sup> This technique relies on the fact that phase transitions can cause the concentration redistribution of impurity ions (Er in this case) at a moving phase boundary. In this method, Er ions are first implanted into amorphous host materials, and then the materials are annealed at relatively low temperature (e.g. 500 °C) for long time to regain their crystallinity. As the amorphous / crystalline interface moves toward the outer surface, a high concentration of Er is built up in the upper layer resulting in the trapping and

segregation of Er in crystalline silicon. Using this method, an Er concentration as high as  $2 \times 10^{20}$  atoms/cm<sup>3</sup> in silicon has been achieved.<sup>73</sup>

Molecular beam epitaxy (MBE) provides an efficient method to dope erbium into thin film Group IV semiconductors without the problem of crystallinity damage associated with the bombardment process in the ion implantation method.<sup>74</sup> In this method, an electron beam is used to evaporate Si, and Er is evaporated thermally using a Knudsen cell. They are then grown atom by atom on the substrate in the high vacuum MBE chamber. The temperature of the substrate is tuned to obtain highly crystalline material. A major problem of this method is that it is difficult to incorporate high concentrations of erbium into Group IV semiconductors such as Si without destroying the epitaxial growth.<sup>74</sup> This problem is due to the low solubility of erbium in crystalline silicon. The use of amorphous silicon and co-dopants such as oxygen can alleviate this problem significantly.<sup>34</sup>

Sputtering methods are another choice for introducing erbium into Group IV semiconductors.<sup>75</sup> In this technique, solid Er and the desired semiconductor targets are first bombarded by a plasma beam (e.g. Ar<sup>+</sup>) that is generated by a radiofrequency (RF) magnetron and then deposited on a substrate. Although this method is relatively cost-efficient, it is very difficult to prepare highly crystalline Er-doped materials.<sup>76</sup>

Chemical vapor deposition (CVD) is also an alternative technique to prepare Group IV semiconductors doped with erbium ions in thin film form.<sup>77</sup> In this technique, the mixture of semiconductor precursor (SiH<sub>4</sub> or Si<sub>2</sub>H<sub>6</sub>) and erbium organometallic precursor are decomposed at elevated temperatures to prepare thin film structure materials. There are two commonly used CVD techniques: plasma enhanced CVD (PECVD), and low pressure CVD (LPCVD). PECVD can help lower the growth temperature, and LPCVD can improve the

conformity and purity of the films as compared to atmospheric pressure CVD (APCVD). Commonly used erbium organometallic CVD precursors are  $\text{Er}(\text{tmhd})_3$  (tmhd = 2,2,6,6-tetramethyl-3,5-heptanedionato) and  $\text{Er}(\text{fod})_3$  (fod = 6,6,7,7,8,8,8-heptafluoro-2,2-dimethyloctane-3,5-dione). Both precursors are bulky molecules with the center  $\text{Er}^{3+}$  ion coordinated by three negatively charged diketonate ligands.

Our laboratories have developed approaches to prepare  $\text{Er}^{3+}$ -doped Si nanocrystals (NCs) (both randomly dispersed and surface enriched) and  $\text{Er}^{3+}$ -surface enriched Si NWs.<sup>78,79,80</sup> To investigate the effects of the erbium doping on quantum confined Si NCs, Coffey, et al. first synthesized randomly dispersed Er-doped Si NCs in 1999.<sup>78</sup> These emissive Er-doped Si NCs could be employed as building blocks in the fabrication of Si-based nanophotonic devices. Figure 11 shows the reactor design for preparing randomly dispersed Er-doped Si NCs. A He gas stream is directed through a warmed bubbler filled with erbium CVD precursor ( $\text{Er}(\text{tmhd})_3$ ) and then mixed with a gas stream of helium-diluted disilane (0.48%  $\text{Si}_2\text{H}_6$  in He). The typical flow rates for disilane and He gas stream are 4.0 and 3000 sccm, respectively, which are controlled by two mass flow controllers (MFC). The mixture is transported downstream to a heating region (a ceramic oven, varying from 1.5 to 6.0 cm) and pyrolyzed at 1000 °C resulting in the formation of Si NCs. Although the exact steps to form Si NCs are not clear, it is generally believed that disilane loses hydrogen to form silylenes ( $\text{Si}_n\text{H}_{2n}$ ) during this pyrolysis process resulting in the formation of non-crystalline oligomers, which can serve as embryos for the later growth of solid crystalline Si NCs.<sup>78</sup> Erbium ions are assumed to be kinetically trapped in the lattice via a non-equilibrium process.<sup>78</sup> The resulting Si nanocrystal-containing aerosol then flows through a bubbler filled with ethylene glycol where the particles are collected. The sizes of these nanocrystals range

from 1 to 5 nm depending on the oven length and disilane concentration. As-prepared randomly dispersed Er-doped Si NCs are strongly emissive at 1540 nm. Photoluminescence (PL) excitation spectra show that the PL intensities at different excitation wavelengths are correlated to the absorption spectra of Si NCs, which means that Si NC acts as a sensitizer for erbium ions (to be discussed in detail later in this chapter).

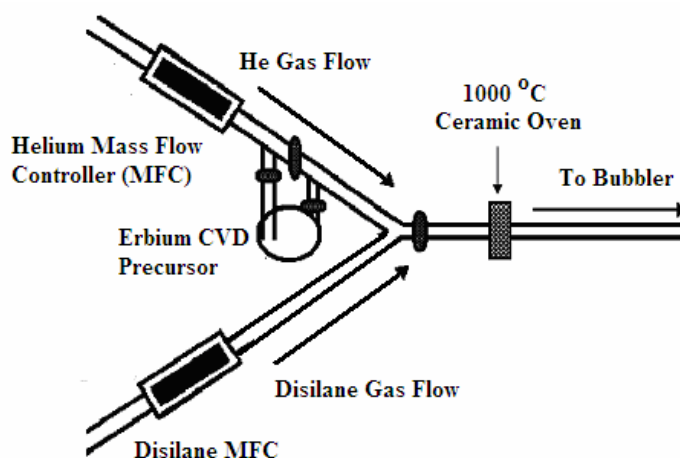


**Figure 11.** The reactor design for preparing randomly dispersed Er-doped Si NCs showing erbium CVD precursor and disilane are co-pyrolyzed by a 1000 °C ceramic oven. Adapted from ref. 78.

In the case of randomly dispersed Er-doped Si NCs, it was difficult to exclude the possibility that the majority of  $\text{Er}^{3+}$  ions had actually diffused to the surface given the high reaction temperature (1000 °C) and the low solubility of Er in crystalline Si.<sup>79</sup> Thus Coffey, et al. developed a new synthetic route that deliberately confines erbium to the surface of a Si nanocrystal in order to explore this possibility. Any differences in optical properties should thus be associated with the average locations of  $\text{Er}^{3+}$  ions.<sup>79</sup> The reactor design for

synthesizing surface enriched Er-doped Si NCs is similar to that for randomly dispersed Er-doped Si NCs except that two ceramic ovens are used to pyrolyze disilane and  $\text{Er}(\text{tmhd})_3$  separately (Figure 12). First disilane undergoes pyrolysis to form silicon nanocrystals followed by a separate step where they are combined with the vapor of the  $\text{Er}^{3+}$  source that is generated by pyrolyzing erbium CVD precursor in another heating section. Typically, the temperatures for decomposing disilane and CVD precursor are 1000 and 750 °C, respectively. The sizes of the surface enriched nanocrystals range from 20.7 to 26.7 depending on the temperatures and lengths of the ovens used.<sup>79</sup> Due to the parameters of this experiment erbium is expected to be located on the shell of these Si nanocrystals.<sup>79</sup> As-prepared samples do not emit luminescence at 1540 nm; however, a strong luminescence is achieved after a 1 h annealing at 800 °C in either vacuum or  $\text{N}_2$ . Near-IR photoluminescence (PL) excitation spectra of surface enriched Er-doped Si NCs show that  $\text{Er}^{3+}$  ions can only be excited efficiently using 488 nm and 514 nm lasers, which is characteristic of direct excitation of Er ions (to be discussed in detail later in this chapter). This difference confirms to some degree that erbium is located in the interior of Si clusters in the case of randomly dispersed Er-doped Si NCs.

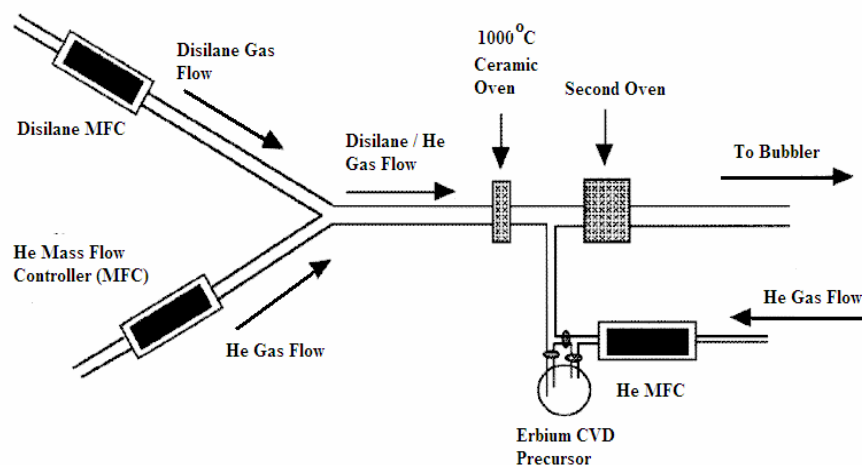


**Figure 12.** Reactor design for preparing surface enriched Er-doped Si NCs showing that the erbium CVD precursor and disilane are pyrolyzed separately by two ceramic ovens (the first one is  $\sim 1000$  °C and the second one has a temperature ranging from 750-900 °C.) Adapted from ref. 79.

In addition to the above Er-doped zero-dimensional Si NCs, it is also important to fabricate Er-doped one-dimensional (1-D) nanowires that have potential applications as building blocks to fabricate nanoscale optoelectronic devices.<sup>80</sup> As mentioned above, nanowires can be assembled into patterned structures via several approaches, and have been successfully employed as building blocks to fabricate nanophotonic and nanoelectronic devices. Therefore, Coffey, et al. fabricated  $\text{Er}^{3+}$ -surface enriched Si NWs, whose reactor design is shown in Figure 13.<sup>80</sup> To synthesize  $\text{Er}^{3+}$ -surface enriched Si NWs, Si NWs are first prepared via a vapor-liquid-solid (VLS) synthetic route. A  $5 \times 15$  mm piece of p-type Si containing thermally evaporated Au islands is placed in an alumina boat, which is placed in a quartz tube reactor and annealed at 600 °C for 2 h in a 3000 sccm He gas stream. Silane (0.1

% in UHP grade He) is then introduced into the system at a flow rate of 40 sccm. Typically, the growth of Si NWs lasts for 2 min. In the next step, a 3000 sccm He gas stream is directed to a warm bubbler containing erbium CVD precursor ( $\text{Er}(\text{tmhd})_3$ ). The vapor of the CVD precursor is carried downstream to a heat section (a 15 cm ceramic oven) of 600 °C, where it is pyrolyzed, resulting in the formation of  $\text{Er}^{3+}$ -surface enriched Si NWs. Transmission Electron Microscope (TEM) imaging combined with a quantitative elemental analysis confirms that Er is concentrated on the shell of these NWs. The resultant NWs can emit weak luminescence at 1540 nm after annealing in a vacuum at 900 °C. PL excitation spectra show that the PL intensities are quite insensitive to the excitation wavelengths, which suggests that the luminescence of these NWs is from both the direct excitation of  $\text{Er}^{3+}$  ions on the shell and the carrier-mediated excitation of  $\text{Er}^{3+}$  ions in the core.<sup>80</sup>

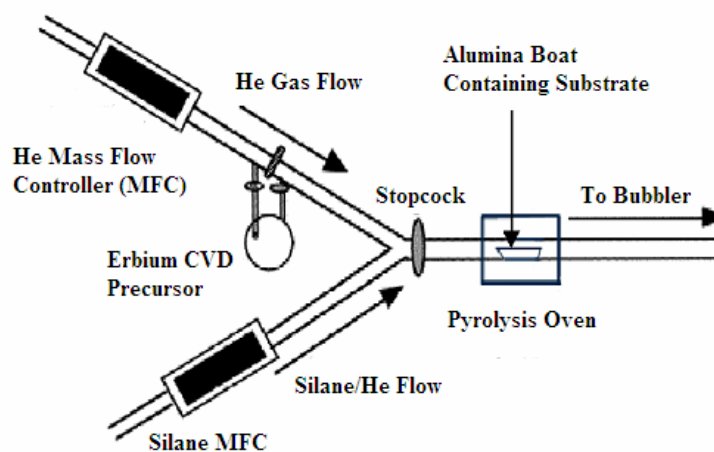


**Figure 13.** Reactor design for preparing both Si NWs and  $\text{Er}^{3+}$ -surface enriched Si NWs.

Adapted from ref. 80.

## 1.2 Crystalline Nanowire Synthesis

Recently, one-dimensional nanostructures, such as nanowires (NWs) and nanotubes (NTs) have been investigated extensively due to their unique optical, electrical and electromechanical properties as the consequence of their wire-like structure.<sup>81</sup> As mentioned above, these NWs and NTs can be used as building blocks to construct more complex nanoscale devices through a bottom-up assembly method.<sup>27,28,30</sup> How can one obtain nanowires? In general, there are three most important and well-investigated growth methods to fabricate one-dimensional (1-D) crystalline nanomaterials,<sup>82</sup> which includes (a) the natural growth of 1-D structures, (b) the use of 1-D templates to direct the growth of 1-D nanostructures, and (c) the introduction of a liquid/solid interface to control the 1-D nanocrystal growth, such as vapor-liquid-solid (VLS) synthetic routes. Our attention will be mainly focused on the VLS synthetic route since it has been demonstrated to be capable of producing various kinds of highly crystalline semiconductor NWs with a controllable size range and a good reproducibility.<sup>83</sup> It becomes our emphasis also because that this approach was used to fabricate single crystalline Ge NWs, the starting materials in this dissertation.

### 1.2.1 Natural Growth of 1-D Structures

There are many solid state materials that can naturally grow into 1-D nanostructures due to the presence of an anisotropic bonding in their crystallographic structures.<sup>82</sup> Chalcogens, e.g. Se, represent an ideal example for generating 1-D nanostructures naturally. Xia and co-workers have recently demonstrated a solution-phase approach to synthesize trigonal phase Se nanowires without exotic seeding materials and templates.<sup>84</sup> In the first step

of their approach, selenious acid was reduced by excess hydrazine to form solid selenium at an elevated temperature as given by equation (8):<sup>84</sup>



The initial product is composed of spherical amorphous selenium colloids with diameters of ~300 nm. When the hot solution was cooling down to room temperature, some tiny Se nanocrystallites would precipitate. Meanwhile the amorphous Se slowly dissolved into the solution and subsequently grew on the Se nanocrystalline seeds. A possible mechanism of the formation of Se nanowires has been proposed as shown in Figure 14a.<sup>85</sup> In the trigonal phase, Se atoms tend to form polymeric helical chains via covalent bonding along *c*-axis. These helical chains can be readily packed into a hexagonal lattice through van der Waals interactions. Since covalent bonding is much stronger than van der Waals interactions, crystallization tends to occur along the *c*-axis resulting in the formation of 1-D nanostructures. Figure 14b shows the scanning electron microscope (SEM) image of these NWs that have an average diameter of ~30 nm, and lengths up to hundreds of microns. HRTEM images of a Se nanowire (Figure 14c) confirm that the nanowire is a single crystal with a d-spacing value of 0.16 nm corresponding to a (001) growth direction.

There are also other examples for the natural growth of 1-D nanostructures, such as Te,<sup>86</sup> a SeTe alloy,<sup>87</sup> (SN)<sub>x</sub> inorganic polymer nanowires,<sup>88</sup> etc.

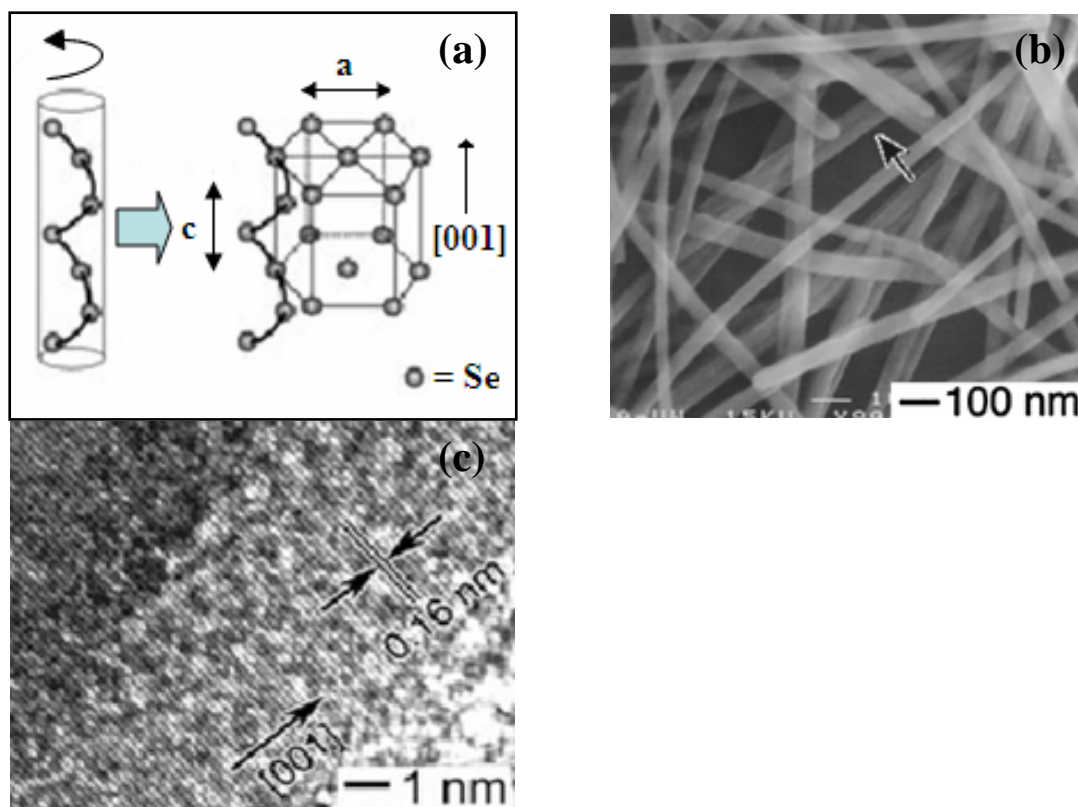


**Figure 14.** (a) Schematic illustration of the mechanism for the formation of Se nanowires (adapted from ref. 85). (b) SEM image of Se nanowires with an average diameter of  $\sim 30$  nm (adapted from ref. 84). (c) HRTEM image of a single Se nanowire with a 0.16 nm d-spacing value corresponding to a [001] growth direction (adapted from ref. 85).

### 1.2.2 Use of 1-D Templates to Direct the Growth of 1-D Nanostructures

Various kinds of 1-D templates can serve as scaffolds within (or around) which different materials can be shaped into 1-D nanostructures with a morphology complementary to that of the templates. For one example, channels in porous  $\text{Al}_2\text{O}_3$  have been used as templates to fabricate various kinds of nanowires successfully.<sup>89</sup> In this method, porous templates are first prepared by anodizing Al foil in acid solution or purchased from

commercial sources. These materials are then loaded into the pores via sputtering, injection, chemical or electrochemical deposition. After solidification and appropriate anneal, highly crystalline nanowires can be produced. This method can be used to prepare various kinds of 1-D nanomaterials such as metals, semiconductors, and ceramics. For example, Martin et al. used porous alumina as a template to fabricate gold nanofibers.<sup>89</sup> In the first step, porous alumina membranes were prepared via an anodic etching of Al metal in acidic medium. Pore densities as high as  $10^{11}$  pores per square centimeter were achieved. Figures 15a and 15b show the TEM images of plan-view and cross-section of these porous alumina templates. Next, the membrane was used as a cathode for electroplating. This method has been used to prepare copper, platinum and gold nanotubes successfully (Figure 15c).<sup>89</sup> To prepare metal nanowires, an elongated electroplating deposition time is employed.<sup>89</sup> It is notable that porous alumina can also serve as a template to grow other materials, e.g. enzyme and polymer. However, this method has one fundamental limit, that is, the template has to be removed after the fabrication is finished.

Besides these porous  $\text{Al}_2\text{O}_3$  films, there are plenty of other templates that have been employed to generate 1-D crystalline nanomaterials, such as existing nanowires<sup>90</sup> and nanotubes (DNA and CNTs),<sup>91</sup> and 1-D organic surfactant micelles.<sup>92</sup>

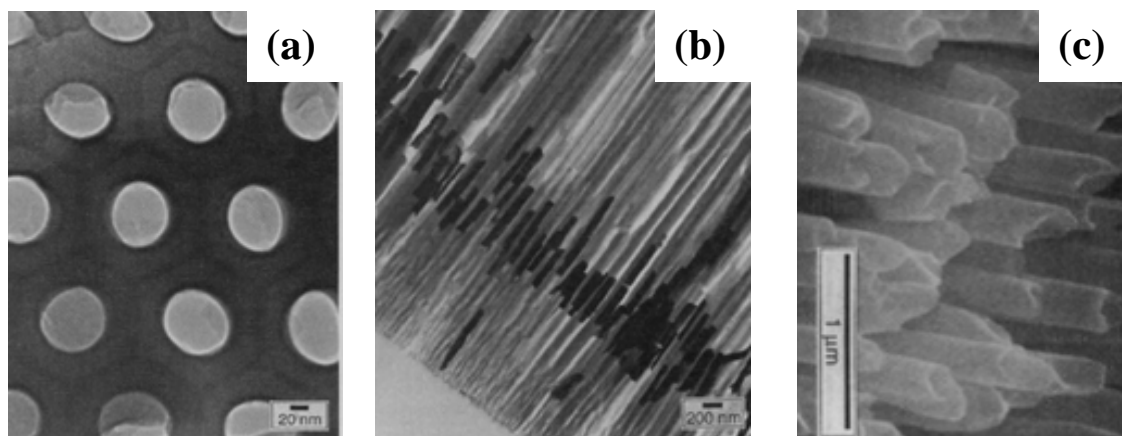


**Figure 15.** TEM images of (a) plan-view and (b) cross-section of the porous alumina templates. (c) SEM image of Au nanotubes. Adapted from ref. 89.

### 1.2.3 Growth of Nanowires via Vapor-Liquid-Solid (VLS) Mechanism

Among all synthetic routes to grow nanowires, the VLS synthetic approach seems to be the most successful one in producing single crystalline nanowires with a relatively high yield. This approach was first created by Wagner & Ellis at Bell Telephone Laboratories to produce Si microwhiskers in the 1960s.<sup>20</sup> In the first step of their approach, a small particle of Au was placed on the surface of a (111) Si wafer that was then heated to 950 °C to form a small droplet of Au-Si alloy as shown in Figure 16a. Next, silicon tetrachloride was introduced as the source of Si, with H<sub>2</sub> as a reducing agent. The Si was dissolved in the liquid droplet and then precipitated at the interface between solid Si wafer substrate and the liquid alloy. By a continuation of this process the alloy droplet was lifted from the Si substrate and sat atop the growing whisker as shown in Figure 16b. The growth direction was found to be [111] and the side faces of the whisker were [211] and [110] as shown in Figure 16c. Provided that there is enough supply of Si source, the growth of Si whisker in length will not

stop until the Au is consumed completely. Other metals, e.g. Pt, Ag, Pd, Cu, or Ni can also be used to grow Si whiskers.<sup>20</sup> It is notable that the growth temperature of the VLS synthetic approach must be higher than the eutectic temperature point of these alloys according to this mechanism. This approach can also be used to generate compound whiskers, such as  $\text{Al}_2\text{O}_3$  and GaAs,<sup>20</sup> in which an excess amount of the one of the component materials can act as a liquid-forming impurity like gold.

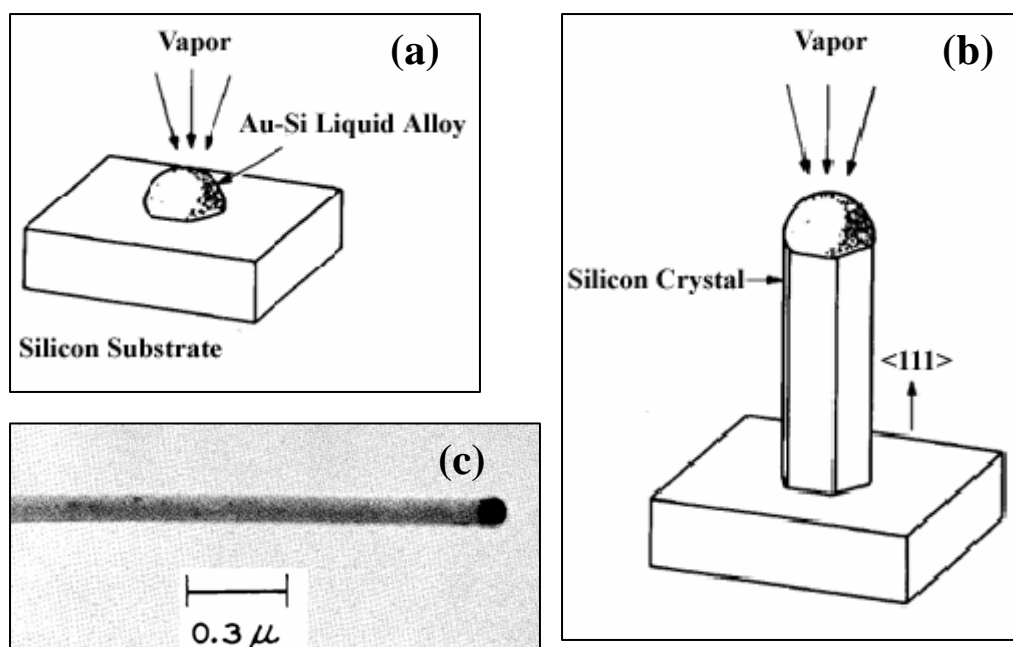


**Figure 16.** Schematic illustration of the growth of a silicon crystal by VLS. (a) Initial condition with a liquid droplet on Si substrate. (b) Growing crystal with a liquid droplet at the tip. (c) TEM image of a ~100 nm Si whisker with a (111) orientation. Adapted from ref. 20.

Recently, the VLS synthetic route has been further explored independently by Lieber & Yang to prepare various kinds of inorganic semiconductor nanowires and nanorods.<sup>83,93</sup>

Yang et al. used in situ TEM imaging techniques and equilibrium phase diagram to explain the VLS growth of Ge NWs.<sup>93</sup> Figure 17 illustrates the conventional Au-Ge binary phase diagram employed to explain the compositional and phase evolution during the three major stages in Ge NWs growth, that is, alloying process, nucleation and axial growth. Figure 18 shows real time TEM images of Ge NWs in different growth stages. In the alloying process, Ge vapor and solid Au nanoparticles (Figure 18a) will form liquid alloys at a deposition temperature above the Ge-Au eutectic point (361 °C) (Figure 18b). With an increasing amount of Ge vapor dissolution, Ge is supersaturated in the liquid droplet resulting in the nucleation of a single crystalline nanowire (Figure 18c). It was estimated that the nucleation generally occurs at Ge weight percentages of 50-60% at 800 °C, which is slightly different from the calculated value of 40% (weight).<sup>93</sup> This difference indicates that the nucleation indeed occurs in a supersaturated alloy liquid. It is notable that two Ge nanocrystals can occasionally precipitate from a single alloy droplet.<sup>93</sup> Once the Ge nanocrystal nucleates at the liquid/solid interface, further condensation and dissolution of Ge vapor into the nanocrystal seed will lead to the axial growth of Ge nanowire (Figure 18d).

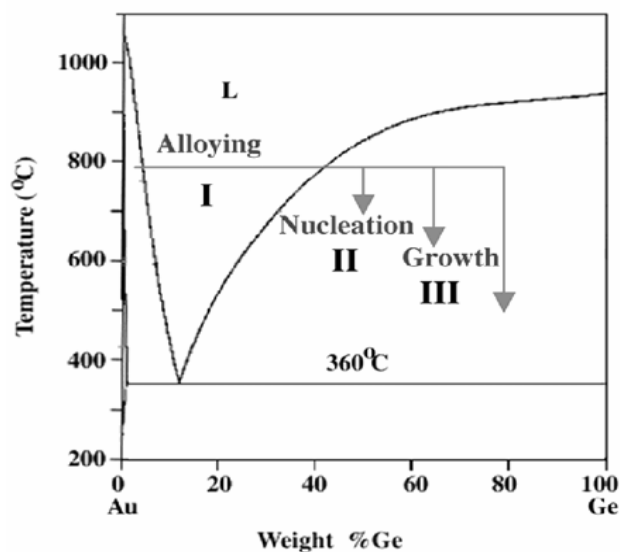


**Figure 17.** A conventional Au-Ge binary phase diagram employed to illustrate the compositional and phase evolution during the three stages of nanowires growth (alloying, nucleation and growth). Adapted from ref. 93.

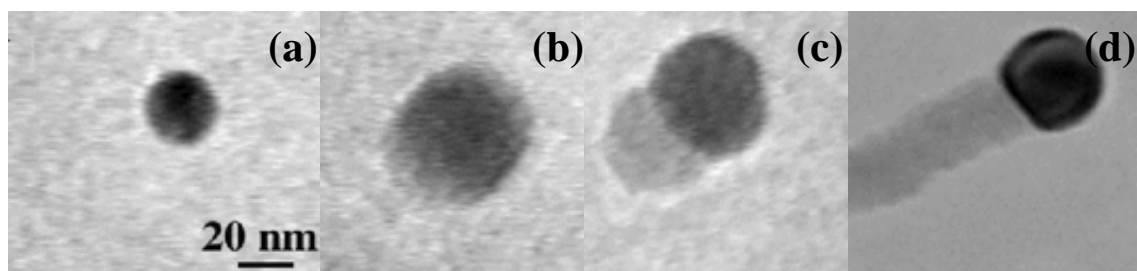


**Figure 18.** Real time TEM images of Ge NW growth in different stages. (a) A solid Au nanoparticle. (b) Au nanoparticle starts to alloy with Ge vapor. (c) Nucleation of Ge NW. (d) Growth of Ge NW with Au sitting on the tip of NW. Adapted from ref. 93.

Ge vapor prefers to diffuse to and condense at the existing solid/liquid interface rather than forming another nanocrystal on the liquid droplet, primarily due to the fact that less energy will be required compared with a secondary nucleation process.<sup>93</sup> After the reactor is

cooled down below the eutectic point, the alloy droplets solidify on the tips of Ge nanowires. The size of the liquid droplet remains almost unchanged during the entire process of nanowire growth, which suggests that the droplet serves as a virtual template to confine the lateral growth of an individual nanowire.<sup>93</sup> In general, an elongated deposition time leads to the formation of longer nanowires. It is notable that not all metal droplets can stay on the tips of these nanowires due to the presence of large interfacial thermal expansion differences that can dislocate the catalysts during the cooling process.<sup>93</sup>

Once a nanowire has begun growing, the surfaces of both the liquid droplet and the solid semiconductor are exposed to the vapor, which means that the vapor could be further absorbed radially on the liquid droplet and axially on the surface of the solid nanowire. In the case of growing Si nanowires using SiH<sub>4</sub>, for example, the dissociative chemisorption of silane on the surface of a silicon nanowire is blocked by the hydrogen termination at a lower temperature.<sup>94</sup> Si atoms will be preferentially incorporated into the liquid droplet rather than at the solid nanowire surface resulting in the formation of Si nanowire with a diameter matching that of the Au catalyst.<sup>94</sup> However, a radial growth on the nanowire surface could occur simultaneously along with a one-dimensional axial growth when such a site-blocking reagent is absent.<sup>95</sup> It is notable that the pressure, temperature, carrier gas flow rate and reactant species can be used to control the growth mode of the nanowires efficiently.<sup>94</sup>

Besides Si and Ge elemental semiconductor NWs, the VLS synthetic route has also been used to generate 1-D nanostructures of a large variety of compound semiconductors, e.g. III-V group semiconductors (GaN, GaAs, GaP, InP and InAs)<sup>83</sup> and II-VI semiconductors (ZnO, ZnS, ZnSe, CdO, CdS and CdSe).<sup>82,96,97</sup>

Although the VLS synthetic method has been proved to be a powerful method to generate single crystalline semiconductor nanowires, several major problems of this method still have to be overcome. For one example, the necessary use of a metal catalyst could pose a serious problem for Si complementary metal oxide semiconductor (CMOS) processing because metals can trap electrical carriers (electrons and holes) to reduce the carrier mobilities in the semiconductor nanowires.<sup>98</sup>

## 1.3 Electrospun Nanofiber Synthesis

### 1.3.1 Introduction

Among the large number of fabrication methods demonstrated to generate 1-D nanostructures, electrospinning seems to be a straightforward, cost-effective and versatile method for producing nanofibers with a high yield and controllable diameters.<sup>99</sup> The electrospinning method can trace its roots back to an electrostatic spray process that was developed about 100 years ago.<sup>99</sup> Later in 1934, Formalas first described the operation of electrospinning for producing polymer fibers in his patent.<sup>100</sup> In the 1990s, this method was revived by the Reneker group at the University of Akron<sup>101</sup> and the Xia group at the University of Washington,<sup>99</sup> which was used to generate a broad range of organic polymers and organic-inorganic composites nanofibers.

In electrospinning, a high voltage electrical potential is used to induce the formation of a viscous liquid polymer jet. The electrified jet is stretched and flies to the grounding electrode under the electrostatic interactions between the surface charges on the jet and the electrical field. Based on experimental conditions, a solid fiber with diameters ranging from microns to tens of nanometers is formed after the solvent is evaporated. Electrospun nanofibers are extremely long and have huge surface areas, and a wealth of materials can be fabricated into electrospun nanofibers.<sup>99</sup> Furthermore, these electrospun nanofibers can be aligned into ordered structures cost-effectively.<sup>102</sup> As a consequence, they have broad applications, such as nanofiber-reinforced composites, scaffolds for tissue engineering, nanofiber-based sensors, nanofiber-based electrical and optical devices, sacrificial templates for generating inorganic 1-D nanostructures, etc.<sup>99</sup> For example, MacDiarmid et al.

demonstrated that electrospun nanofibers of p-type polyaniline/poly(ethylene oxide) (PEO) blends can be used as building blocks to fabricate Si back-gated field emission transistors (FET).<sup>103</sup>

### 1.3.2 The Basics of Electrospinning

The basic setup for electrospinning fibers is shown in Figure 19.<sup>99</sup> In general, the setup consists of three components: a high voltage power supply, a spinneret (metallic needle), and a collector (grounding electrode). Usually a direct current power supply is used to carry out the electrospinning process. The metallic needle is connected to a syringe containing polymer solution or inorganic/organic composite polymer solution. A syringe pump may be used to obtain a controllable feed rate of polymer solution. As an electric potential is applied between the spinneret and the collector, the polymer droplet at the tip of the spinneret becomes electrified and the induced charges are evenly distributed on the surface of the droplet. The charged droplet will be exposed to two types of electrostatic interaction forces.<sup>99</sup> One is the repulsion force between the surface charges and another is the Coulomb force between the surface charges and the applied electrical field.<sup>99</sup> Consequently, the liquid droplet will be stretched and distorted into a conical structure known as the Taylor cone (inset in Figure 19). Once the surface tension of the polymer droplet is surpassed by the electrostatic forces, the electrified jet will undergo stretching and whipping process. After the evaporation of the solvent, solid nanofibers will form and be deposited on the grounding collector randomly as shown in the inset of Figure 19.<sup>99</sup>

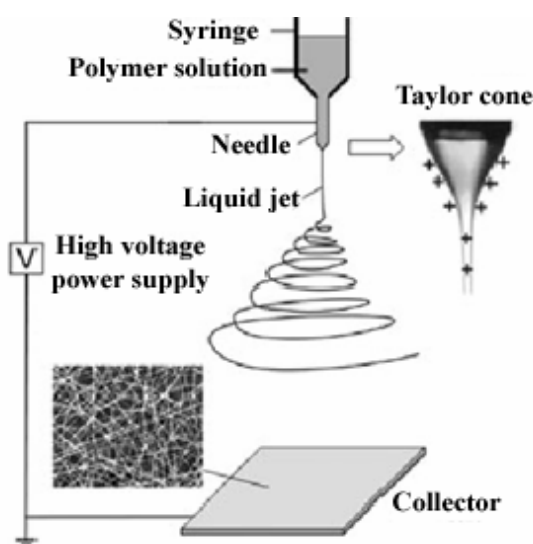


**Figure 19.** Schematic illustration of the basic setup for electrospinning. Insets are Taylor cone structure of the electrified droplet (left top) and a typical SEM image of the poly(vinyl pyrrolidone) (PVP) electrospun nanofibers deposited on the collector (right bottom). Adapted from ref. 99.

### 1.3.3 Mechanism of Electrospinning

Although the setup for electrospinning is very simple, the exact spinning mechanism is quite complex due to the complications of the electro-fluid interactions.<sup>99</sup> Before 1999, the formation of nanofibers was attributed to the splitting of the electrified jet as the consequence of the repulsion force between the surface charges on the liquid droplet.<sup>99</sup> However, the Reneker group observed that the formation of nanofibers was caused by the bending instability associated with the electrified jet.<sup>101</sup> Figure 20 shows photographs of a spinning jet taken by both slow and high speed cameras. It seems that the jet was starting to split at a

certain distance from the spinneret (Figure 20a); however, high speed photography confirms that the fiber is actually bending and stretching rather than splitting (Figure 20b).

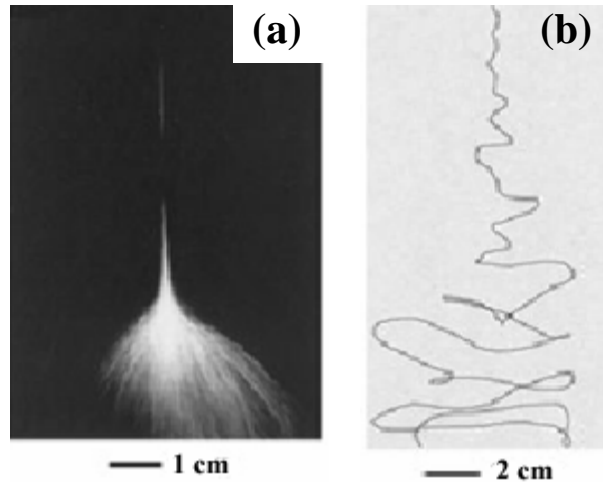


**Figure 20.** Photographs of poly(ethylene oxide) electrospun fibers taken using different capture times (a) 1/250 second and (b) 18 nanosecond, adapted from ref. 99.

Combining experimental observations and electrohydrodynamic theories, several research groups have set up mathematical models to investigate the electrospinning process. The Reneker group treated the charged liquid polymer jet as a system of connected viscoelastic dumbbells and used equation (9)<sup>101</sup> to calculate the perturbation force applied on the fiber during the bending process:

$$\delta = \delta_o \exp[(2e^2/m \ell_1^3)^{1/2} t] \quad (9)$$

where  $\delta$  is the growth of the initial bending perturbation,  $\delta_o$  is the initial bending perturbation ( $t = 0$ ),  $e$  is charge,  $m$  is mass,  $\ell$  is the length of the ideal rectilinear jet, and  $t$  stands for time.

The jet path predicted using the above perturbation force matches well their experimental observations. The Rutledge group modeled the jet as a long slim thread to interpret the bending phenomenon.<sup>104</sup> This group believes that bending instability is mainly caused by the interaction between the electric field and the surface charges on the jet. The formation of thin nanofibers is obtained by stretching in the instability region. All of these studies provide a better understanding of the mechanism involved in the electrospinning process and ideally assist experimental scientists in the quest for new designs to better control the diameter and structure of electrospun nanofibers.

#### **1.3.4 Control of the Diameter and Morphology of Electrospun Fibers**

The diameter and morphology of electrospun fibers are greatly affected by the intrinsic properties of the polymer (concentration, elasticity, electrical conductivity and type of polymer) and the solvent (the polarity, volatility and surface tension of the solvent), and the operation conditions (the applied voltage, the distance between the spinneret and the collector, and feeding rate of the polymer solution).<sup>99</sup>

The formation of beads along with fibers in electrospinning is a very common problem that was found to be associated with the viscosity, the surface tension and the density of surface charges on the electrified jet.<sup>99</sup> Xia's group demonstrated that the amount of round balls in poly(vinyl pyrrolidone) (PVP) electrospun fibers can be greatly reduced or eliminated by increasing the viscosity of polymer solution.<sup>99</sup> Addition of conductive salts such as tetramethylammonium chloride to the polymer solution can increase the density of charges on the surface of the jet resulting in lowering the surface tension, which leads to the effective elimination of round ball shapes in the fiber.<sup>99</sup> The use of solvents with lower

surface tension could also help reduce the number of beads (round balls) in the electrospun fibers. Besides the above factors, Tan and co-workers found that the formation of round balls is also correlated to the applied voltage.<sup>105</sup> When the applied voltage is so high that the conical structure of the droplet is deformed, the density of round balls will be greatly increased.

The diameters of electrospun fibers can be controlled varying the concentration and conductivity of the polymer solution, the electrical field strength, and the feed rate of the solution.<sup>106</sup> For one example, the average diameter of PVP/TiO<sub>2</sub> nanofibers prepared using a 0.02 g/ml PVP in ethanol solution is only ~50 nm, whereas the average diameter of nanofibers prepared using a 0.05 g/ml solution is ~250 nm, as shown in Figure 21a.<sup>106</sup> When the electric field strength is in the range from 0.6-1.4 kV/cm, a higher electric field can lead to the formation of thick nanofibers (Figure 21b). However, the relationship between the applied voltage and the diameters of electrospun fibers becomes unclear when the electric field is above that range.<sup>106</sup> A high feeding rate can cause the formation of thicker fibers as shown in Figure 21c.

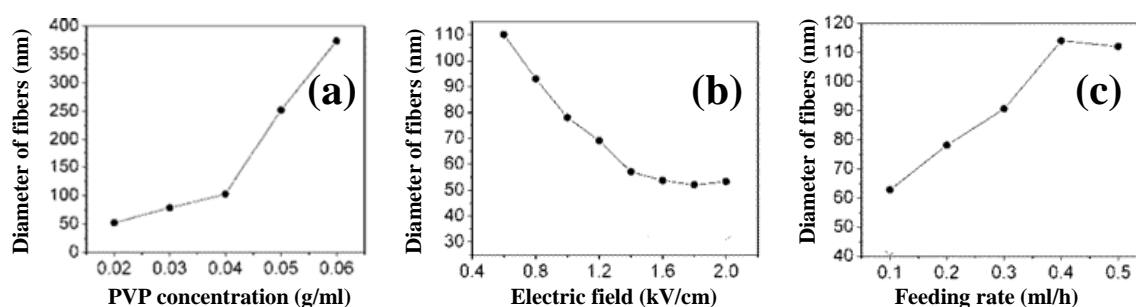


**Figure 21.** Plots showing the dependence of the average diameter of PVP/TiO<sub>2</sub> nanofibers on various processing parameters: (a) concentration of PVP; (b) electric field strength; (c) feeding rate of the solution. Adapted from ref. 106.

### 1.3.5 Fabrication of Inorganic Electrospun Nanofibers

Conventionally, electrospinning has been dominated by the fabrication of organic polymer nanofibers. Recently, this method has been modified to prepare composite nanofibers using a sol-gel precursor solution.<sup>107</sup> For one example, Larsen et al. have demonstrated the direct electrospinning of viscous inorganic sol-gel solutions to prepare  $\text{TiO}_2/\text{SiO}_2$  and  $\text{Al}_2\text{O}_3$  nanofibers.<sup>107</sup> The hydrolysis rate of the sol-gel precursors was controlled by adjusting the pH values and aging conditions so that the solution possesses a viscosity similar to that of conventional polymer solution for electrospinning. However, since it is very difficult to control the viscosity of the sol-gel solution precisely, the diameters of the fibers prepared using this direct electrospinning are also hard to control.<sup>99</sup>

Xia and Li recently developed a new approach to prepare inorganic nanofibers, in which the hydrolysis of the sol-gel precursor took place in the polymer jet rather than in the stock solution.<sup>106</sup> In this approach, metal alkoxide sol-gel precursors were mixed with a PVP polymer solution in alcohol. PVP was used to control the viscosity of the solution and served as a template to generate 1-D nanostructures. After electrospinning, the metal alkoxide was hydrolyzed by reacting with the moisture in air to form a continuous gel network within the PVP matrix resulting in the formation of inorganic/polymer composite nanofibers. After an appropriate anneal at an elevated temperature in air, the organic PVP was removed so that pure inorganic fibers were obtained. Figure 21 shows a TEM image of  $\text{TiO}_2$  nanofibers prepared using this method.<sup>106</sup> This approach has also been extended to fabricate  $\text{SiO}_2$ ,  $\text{SnO}_2$ ,  $\text{GeO}_2$  and  $\text{BaTiO}_3$  nanofibers successfully.<sup>99</sup> In addition to PVP, poly(vinyl alcohol) (PVA) and PEO have also been employed as a sacrificial template to generate inorganic nanofibers such as  $\text{Al}_2\text{O}_3$ ,  $\text{CuO}$ , and  $\text{NiO}$ .<sup>99,108</sup>

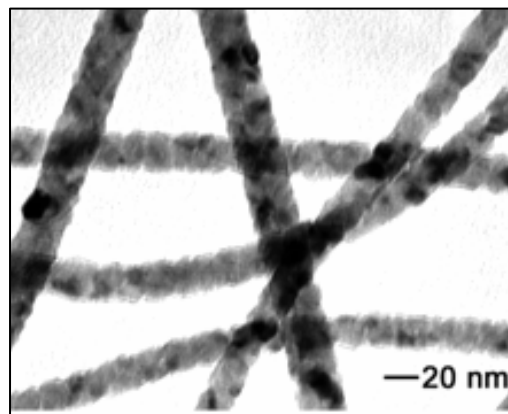


**Figure 21.** Typical TEM images of  $\text{TiO}_2$  polycrystalline electrospun nanofibers with an average diameter of  $\sim 20$  nm. Adapted from ref. 106.

### 1.3.6 Alignment of Electrospun Fibers

Aligned 1-D nanostructures have a number of potential applications in fabricating electronic and photonic devices.<sup>109</sup> However, as-formed nanofibers are randomly deposited on the grounding collector due to the presence of bending instability during electrospinning process.<sup>109</sup> In order to obtain well-aligned electrospun nanofibers, several creative approaches have been developed by modifying the designs of the grounding collector.<sup>109,110</sup> Zussman et al. used a tapering wheel-like disk as the grounding collector to generate aligned nanofibers.<sup>110</sup> Aligned fibers were found to be deposited on the sharpened edge of the wheel collector. These authors believe that the sharpened edge of the wheel could greatly increase the local electrical field strength so that the charged fibers were wound on the edge preferentially. It is also possible that the fibers were further arrayed by the repulsive interaction between these charged nanofibers.

Xia's group developed another grounding collector design to obtain an array of nanofibers as shown in Figure 22a.<sup>109</sup> The collector is composed of two pieces of conductive Si wafers separated by an insulating gap, and the well-aligned nanofibers can be obtained across the insulating gap (Figure 22b). This type of nanofiber array is believed to be caused by two types of electrostatic interactions.<sup>109</sup> One is the electrostatic attraction between the positively charged fibers and the negatively charged Si wafers that can stretch the fibers to align themselves along the direction perpendicular to the edges of the conductive Si wafers. Another one is the electrostatic repulsion between deposited fibers that can further enhance the degree of alignment.

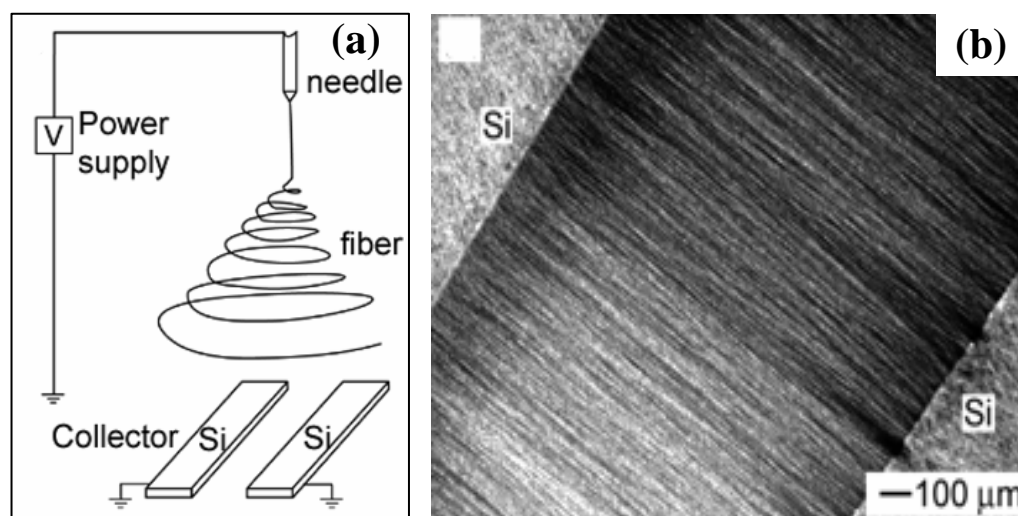


**Figure 22.** (a) Schematic illustration of the grounding collector to obtain arrayed fibers across the insulating gap. (b) SEM image of the arrayed PVP fibers. Adapted from ref. 109.

## 1.4 Photophysics of Erbium Luminescence

### 1.4.1 Introduction

Erbium ( $^{68}\text{Er}$ ) is one of the 15 lanthanide elements, which was discovered in 1842 at the Swedish town of Ytterby.<sup>111</sup> Pure erbium metal has an electronic configuration of  $[\text{Xe}] 4f^{12} 6s^2$ . As an ion, erbium usually loses one 4f electron and both of the 6s to form  $\text{Er}^{3+}$  whose electronic configuration is  $[\text{Xe}] 4f^{11}$ . The 11 4f electrons are shielded from the surrounding matrix by two closed 5s and 5p shells resulting in the little difference of 4f energy levels in different host materials.<sup>111</sup> Energy levels in  $\text{Er}^{3+}$  ions are conventionally labeled according to their orbital angular momentum ( $l$ ) and spin angular momentum ( $s$ ) using term symbols such as  $^4I_{13/2}$  or  $^2F_{7/2}$  (Russell-Saunders notation). The letter refers to the total orbital angular momentum ( $L$ ) of the ion that is equal to the sum of the orbital angular momentum of all individual electrons in the ion. According to the Clebsch-Gordan series scheme, S stands for an  $L$  of 0, P of 1, F of 3, I of 6, etc.<sup>34</sup> The left superscript is the number of possible orientations of the total spin of the ion, which is equal to  $2S + 1$ , where  $S$  is the total spin angular momentum of the ion. The right subscript is the total angular momentum of the ion ( $J = L + S$ ).

Figure 23a shows the schematic diagram of the 4f electronic energy levels for  $\text{Er}^{3+}$  ion in solid host materials.<sup>111</sup> For free  $\text{Er}^{3+}$  ion, the intra-4f electronic transitions are parity forbidden because all the energy states are odd (u) and the parity selection rule (also called the Laporte rule) requires that the parity of the initial and final states of an electronic transition must be different ( $g \leftrightarrow u$ ).<sup>34</sup> For the  $\text{Er}^{3+}$  ion in solid host materials, however, the crystal field produced by the surrounding atoms of the solid host causes the perturbation of

the 4f orbital of erbium ions resulting in the mixing of levels with different parities. As a consequence, these electronic transitions are partially allowed.<sup>34</sup> Erbium becomes technologically important because the intra-4f  $^4I_{13/2} \rightarrow ^4I_{15/2}$  transition (first excited state to the ground state) coincides with the wavelength of maximum transmission (1.54  $\mu\text{m}$ ) in silica-based optical telecommunication technology.<sup>112</sup> Figure 23b shows the room temperature photoluminescence (PL) spectrum of Er-doped silica film obtained using a 488 nm laser pump. The Stark splitting due to the crystal field of the host material reduces the degeneracy of the 4f energy levels giving rise to the shoulder peak at 1551 nm.<sup>113</sup> At room temperature, Stark splitting is also the major reason for luminescence broadening.<sup>113</sup>

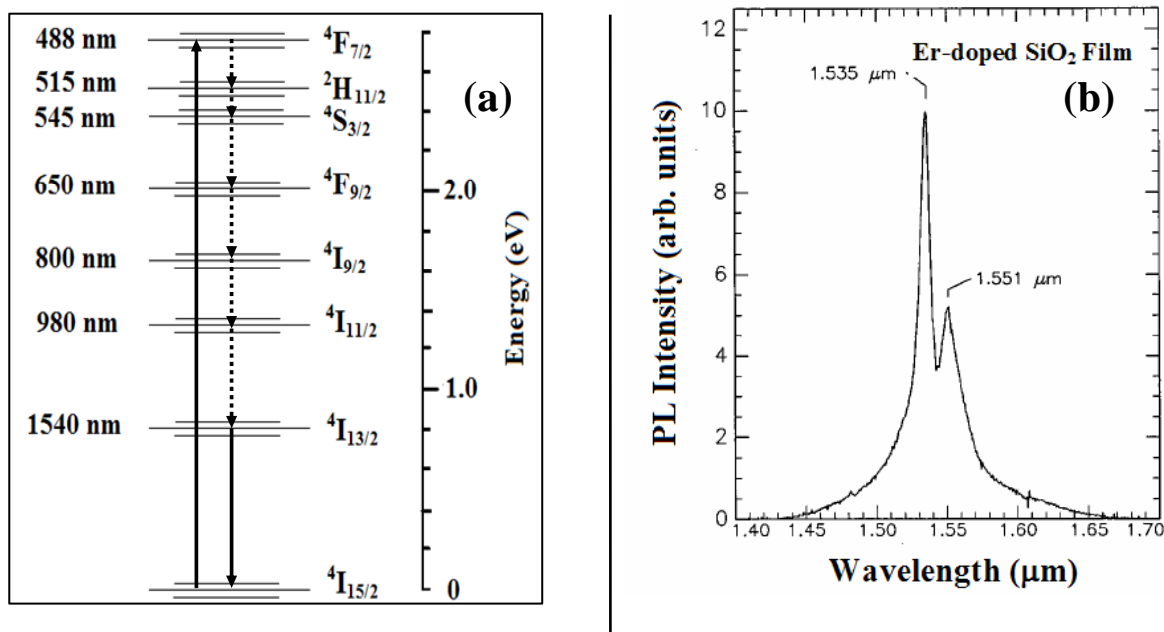


**Figure 23.** (a) Schematic representation of  $\text{Er}^{3+}$  ion energy levels in solid host materials showing an excitation at 488 nm followed by a series of rapid non-radiative relaxation and emission at 1540 nm (adapted from ref. 111). (b) Room temperature photoluminescence spectrum for an Er-doped  $\text{SiO}_2$  sample ( $\lambda_{\text{pump}} = 488$  nm, pump power = 250 mW, adapted from ref. 113).

#### 1.4.2 Excitation of Erbium Ions

In general, there are two ways to excite erbium ions: (a) direct excitation of erbium ions; and (b) carrier-mediated excitation of erbium ions that is assisted by a sensitizer.<sup>78,79,80,114</sup> Figure 23a shows the  $\text{Er}^{3+}$ -related transitions for direct excitation. In the direct excitation mode,  $\text{Er}^{3+}$  ions are first directly excited to the corresponding energy level depending on the wavelength of the optical pump used. For example, using a 488 nm optical pump, ground state  $\text{Er}^{3+}$  ions can be excited to the  $^4\text{F}_{7/2}$  energy level. Since the cross sections

of  $\text{Er}^{3+}$  ions for stimulated emission are very small (typically on the order of  $10^{-21} \text{ cm}^2$ ), large photon fluxes are needed to get high enough optical gain for population inversion.<sup>115</sup> Furthermore, the pump efficiency is closely related to the wavelengths of the optical excitations; that is, the energy of the incoming photons must match the energy difference between the initial and final states of the transition so that an optical resonance can be achieved.<sup>79</sup> In the next step, the excited  $\text{Er}^{3+}$  ions rapidly relax to the first excited energy level ( $^4\text{I}_{13/2}$ ) via a series of nonradiative multi-phonon emission (an Auger process). Finally,  $\text{Er}^{3+}$  ions at the first excited energy level are further de-excited to the ground state ( $^4\text{I}_{15/2}$ ) by emitting a photon with a wavelength of 1540 nm. Since the  $\text{Er}^{3+}$  ions at the first excited energy level have an extremely long lifetime (up to 20 ms, depending on the host materials), the interaction between the host material and  $\text{Er}^{3+}$  ions is critical to the efficiency of the 1.54  $\mu\text{m}$  light emission.<sup>115</sup>

Figure 24 shows the schematic illustration of a carrier-mediated excitation of Er ions that is assisted by sensitizers such as Si nanocrystals (NCs).<sup>34</sup> In this carrier-mediated excitation mode, Si NCs are first excited by absorbing incoming pumping photons to form free excitons that have the following relaxation pathways:<sup>34,114,116</sup> (a) dissociation into free carriers (electrons and holes), (b) radiative recombination to emit photons and (c) trapping at Er-related defects (through Auger process) to form bound excitons. Next, the bound excitons further lower their energy through an Auger relaxation process and then excite  $\text{Er}^{3+}$  ions from the ground state to the first excited state ( $^4\text{I}_{15/2}$  to  $^4\text{I}_{13/2}$ ) via energy resonance. It is also possible that the excited  $\text{Er}^{3+}$  ions transfer their energy back to Si NCs to be de-excited. However, this backtransfer process is much slower than the excitation transfer process in the case of Er-doped amplifier sensitized by Si NCs. Finally, the excited  $\text{Er}^{3+}$  ion relaxes to the

ground state by emitting a photon at 1540 nm. It is noteworthy that the excitation efficiency for the carrier-mediated excitation of  $\text{Er}^{3+}$  ion is closely related to the absorption spectrum of the sensitizer rather than that of  $\text{Er}^{3+}$  ion.<sup>114</sup>

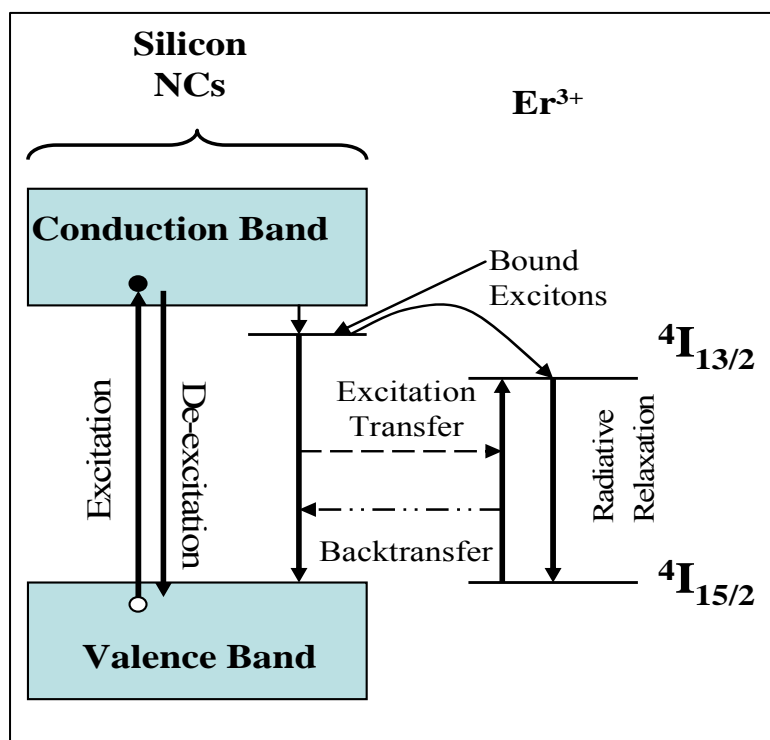


**Figure 24.** The schematic illustration of a carrier-mediated excitation of  $\text{Er}^{3+}$  ions that is assisted by Si NC, a sensitizer (adapted from ref. 34).

### 1.4.3 Major Gain-Limiting Factors

The most important gain-limiting factor is the concentration of optically active  $\text{Er}^{3+}$  ions in the host materials. The maximum gain per unit length is determined by the product of the cross-section for stimulated emission and the active erbium concentration.<sup>115</sup> Since the erbium has a very small absorption cross section for stimulated emission, relatively high Er

concentrations ( $10^{19}$ - $10^{20}$  Er atoms/cm<sup>3</sup>) are required to obtain a reasonable optical gain for its practical applications.<sup>115</sup> Therefore, the host materials must have a high solubility for erbium ions; otherwise Er ions will precipitate from the host matrix resulting in the decrease of the Er-related PL intensity.<sup>117</sup> This requirement is based on a direct excitation of erbium ions. In the case of carrier-mediated excitation of erbium ions, the concentration can be much lower while a reasonable PL intensity is achievable.<sup>114</sup>

Excitation wavelength is another important factor affecting the PL intensity of erbium ions.<sup>115</sup> As mentioned above, in the direct excitation mode, the excitation efficiency will be much higher when the wavelength matches the energy difference of the initial and final states of the optical transition. Recall that in the carrier-mediated excitation mode, however, the optical gain is more related to the absorption spectrum of the sensitizers rather than that of erbium ions.

At high erbium concentrations, an Er<sup>3+</sup> ion at the first excited state can de-excite by transferring its energy to a neighboring Er<sup>3+</sup> ion at the first excited state, resulting in the neighboring erbium ion to be excited to a higher energy level as shown in Figure 25a.<sup>115</sup> This process is called cooperative up-conversion, and can cause the decrease of the PL intensity at 1540 nm. The up-conversion coefficient is closely related to the dielectric constant and phonon energy of the host materials.<sup>115</sup>

At high erbium concentrations, another effect called excited state absorption (ESA) process can also greatly limit the optical gain of the Er-doped amplifiers (Figure 25b).<sup>115</sup> In this process, an excited erbium ion absorbs an incoming photon, and be further excited to higher energy level. Recall that Er<sup>3+</sup> ions have extremely long lifetime at the first excited state. Therefore, this de-excitation pathway is very serious when the population of the Er<sup>3+</sup>

ions at the first excited state is very high. As a consequence, the excitation efficiency and optical gain are greatly reduced.

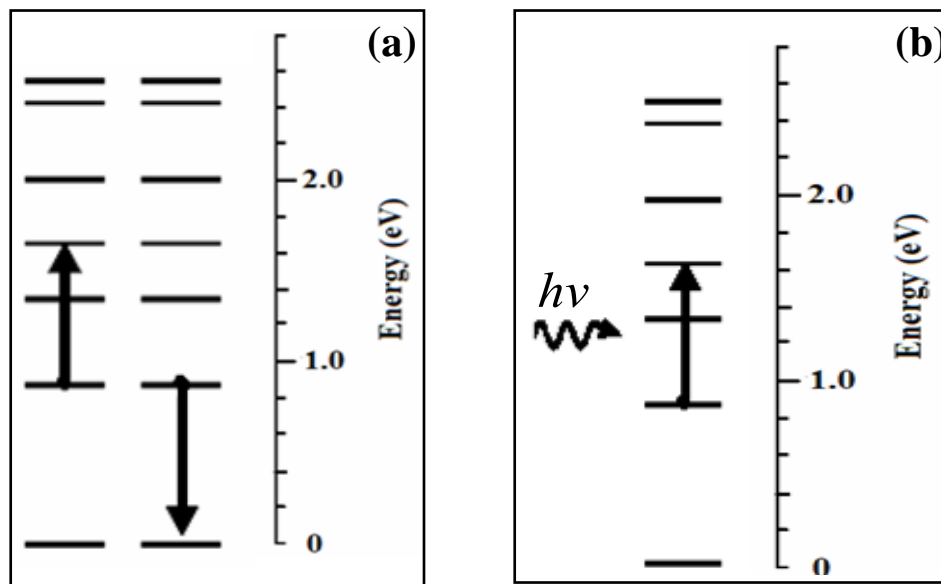


**Figure 25.** Schematic illustrations of (a) co-operative upconversion process showing one excited Er<sup>3+</sup> ion is de-excited and another one is excited to high energy state. (b) The process of excited state absorption showing that an Er<sup>3+</sup> ion at the first excited state is further excited to higher energy state. Adapted from ref. 115.

There are some other non-radiative quenching effects that can reduce the optical gain. For example, Er-doped amplifiers containing significant amounts of residual water emit weak luminescence at 1540 nm because the OH stretching vibration is resonant with the transition from the first excited state to the ground state of Er<sup>3+</sup> ion, resulting in the energy transfer of excited Er<sup>3+</sup> ion to OH vibration.<sup>118</sup> Another example is the room temperature quenching effect that is very prominent in Er-doped crystalline bulk silicon.<sup>119</sup> This gain limiting effect is mainly caused by the enhanced energy backtransfer rate from the excited erbium ions to

the bulk Si matrix and the increased disassociation rate of the bound Si excitons at higher temperatures. This quenching effect has recently been solved by co-doping with impurities, such as oxygen, carbon, nitrogen and fluorine.<sup>34</sup> It is notable that these impurities can also greatly increase the solubility of erbium in silicon, leading to the further enhancement of the PL intensity.<sup>34,116</sup>

#### 1.4.4 Sensitizers for Erbium

In general, there are three classes of sensitizers:<sup>114</sup> (1) metal ions (e.g.  $\text{Yb}^{3+}$ ), (2) semiconductor nanocrystals (e.g. Si NCs) and (3) organic complexes. The first reported sensitizer for erbium was  $\text{Yb}^{3+}$  ions.<sup>120</sup> The sensitization process relies on the fact that the  $^2\text{F}_{5/2}$  energy level of  $\text{Yb}^{3+}$  is nearly resonant in energy with the  $^4\text{I}_{11/2}$  energy level of  $\text{Er}^{3+}$  and the absorption cross section of a  $\text{Yb}^{3+}$  ion at 980 nm is almost one order of magnitude higher than that of an  $\text{Er}^{3+}$  ion.<sup>120</sup> Figure 26 presents the sensitization process of  $\text{Er}^{3+}$  ions in an Er-doped  $\text{Yb}_2\text{O}_3$  sample using a 980 nm optical pump.<sup>120</sup> First, 980 nm photons are efficiently absorbed by a  $\text{Yb}^{3+}$  ion and can then be transferred to excite an  $\text{Er}^{3+}$  ion either from  $^4\text{I}_{15/2}$  to  $^4\text{I}_{11/2}$  or from  $^4\text{I}_{11/2}$  to  $^4\text{I}_{7/2}$ . Next, these excited  $\text{Er}^{3+}$  ions at higher energy levels de-excite to the  $^4\text{I}_{13/2}$  level through an Auger relaxation process, and then emit a photon with a wavelength of 1540 nm to relax to the ground state. As a consequence, a significant increase of the PL intensity at 1540 nm is achieved. It should be noted that the reverse energy transfer process from excited  $\text{Er}^{3+}$  ion to  $\text{Yb}^{3+}$  ion is also possible, but this transfer rate is much less significant relative to the sensitization process.<sup>114</sup>

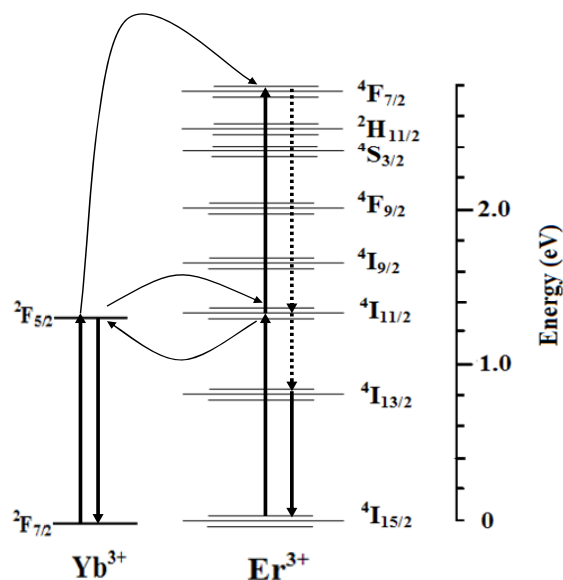


**Figure 26.** Schematic representation of the  $\text{Er}^{3+}$  ion sensitization process by  $\text{Yb}^{3+}$  ion in Er-doped  $\text{Yb}_2\text{O}_3$  amplifier sample. Adapted from ref. 120.

Silver ions ( $\text{Ag}^+$ ) were found to be another sensitizer for erbium ions. This sensitization process is closely related to the absorption spectrum of  $\text{Ag}^+$ -implanted Er-doped silica glass.<sup>121</sup> Figure 27 shows a representative spectrum. It is assumed that the absorbed energy by silver ions can be transferred to erbium ions through a carrier-mediated process. As a consequence, the 1540 nm PL intensity is enhanced by a factor of 70 using a 488 nm excitation wavelength.<sup>121</sup>

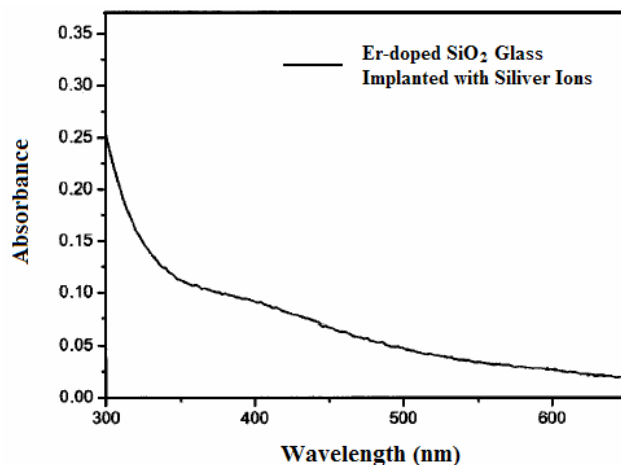


**Figure 27.** UV-visible absorption spectrum of Er-doped SiO<sub>2</sub> glass implanted with silver ions showing that it has broad absorption tail ranging from 300 to 500 nm. Adapted from ref. 121.

Recently, Fujii et al. reported that Si nanocrystals (NCs) can serve as a sensitizer for erbium in an Er-doped SiO<sub>2</sub> film embedded with Si NCs.<sup>122</sup> Figure 28 shows a schematic representation of this sensitization process.<sup>123</sup> First, a photon is absorbed by the Si nanocrystals (2-5 nm) to generate an exciton. This Si exciton will recombine radiatively to emit a photon or relaxes to form a bound exciton. The bound exciton will further lose energy through an Auger process and then transfer its energy to an Er<sup>3+</sup> ion provided that the erbium ion is physically close enough to the exciton.<sup>114</sup> The presence of Si NCs can increase the effective absorption cross section of Er at 458 nm by six orders of magnitude compared with that of Er-doped SiO<sub>2</sub> sample ( $10^{-15}$  cm<sup>2</sup> vs.  $10^{-21}$  cm<sup>2</sup>).<sup>114</sup> However, it was calculated that 1 Si NC can only sensitize about 1 Er<sup>3+</sup> ion, which means the Er concentration must be very low (~0.1%), otherwise Er<sup>3+</sup> ions cannot be sensitized efficiently.<sup>114</sup> Since Si NCs are

semiconducting, this type of amplifier can be electrically excited to emit electro-luminescence.

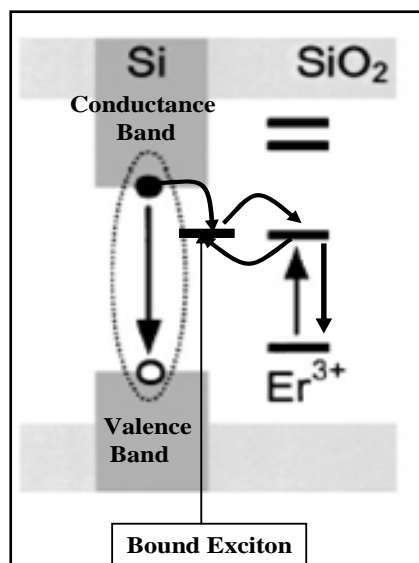


**Figure 28.** Schematic representation of the sensitization process of Er<sup>3+</sup> ion by Si NCs embedded in the Er-doped SiO<sub>2</sub> matrix. Adapted from ref. 123.

Some polydentate cyclic ligands such as C<sub>51</sub>H<sub>73</sub>NO<sub>11</sub> can coordinate with Er<sup>3+</sup> ions to form complexes that can emit strong 1540 nm luminescence, presumably due to the energy transfer from the ligands to the Er<sup>3+</sup> ions through energy resonance.<sup>124</sup> C<sub>51</sub>H<sub>73</sub>NO<sub>11</sub> has nine donor atoms: three carboxylic oxygens, five ethereal oxygens, and one nitrogen atom, forming a cage like structure.<sup>125</sup>

In general, these sensitizers have one common point that they have a broad light absorption spectrum and can then transfer the absorbed energy efficiently to Er ions, giving rise to an enhancement of Er-related light emission.

#### 1.4.5 Ge, SiGe and Group IV oxides as Host Materials for Erbium Ions

Our group has explored the possibility of making Si, an indirect band gap Group IV semiconductor, emissive via the introduction of impurity ions ( $\text{Er}^{3+}$ ) into Si nanocrystals (NCs) and nanowires (NWs).<sup>78-80,126-128</sup> One goal was that the physical confinement could suppress Auger quenching effects, or depopulation of shallow-trapped conduction band electrons. Therefore, Si NCs and NWs should be promising host materials for  $\text{Er}^{3+}$  ions. Er-doped Si NCs could be employed to fabricate semiconducting waveguides and amplifiers operating at 1.54  $\mu\text{m}$ . Emissive Er-doped Si NWs can be used as free-standing one-dimensional building blocks to fabricate semiconducting nanophotonic devices via a bottom-up approach.

In terms of other possible host materials, germanium (Ge) possesses several interesting attributes for this purpose. For example, it has been reported that the optical absorption edge of Ge nanocrystals can shift towards higher energy with decreased size.<sup>129,130</sup> As a consequence, this infers that the self-absorption of the Er-doped Ge at 1.54  $\mu\text{m}$  should be reduced in a nanoscale architecture and the laser-pumping efficiency of Ge nanowires will be increased due to phonon confinement effects,<sup>131</sup> i.e. the reduction of exciton-acoustic-phonon interactions as the result of host size reduction to the nanometer regime.<sup>132</sup> The energy of a Ge exciton is close to the 1.54  $\mu\text{m}$   $^4\text{I}_{13/2} \rightarrow ^4\text{I}_{15/2}$  transition, which is also beneficial to a perceived increase in pump efficiency.<sup>133</sup> In addition, the optical band gap of  $\text{GeO}_x$  can be easily tuned from 0.75-5 eV by varying the annealing time, a property that can assist in trapping energy and transferring it to  $\text{Er}^{3+}$  ions.<sup>134-136</sup>

It was found by our research that although  $\text{Er}^{3+}$ -doped Ge NWs show better performance in terms of light emission intensity at 1.54  $\mu\text{m}$  relative to  $\text{Er}^{3+}$ -doped Si NW

analogs,<sup>80,137</sup> Ge NWs are readily oxidized due to their large surface/volume ratio and thermodynamic instability, which can fundamentally limit their functionality.<sup>138</sup> In this regard, the incorporation of Si into Ge NWs should circumvent this problem by forming stable SiGe alloys that passivate the reactive surface. Furthermore, SiGe alloys have tunable band gaps,<sup>139</sup> which can be engineered to sensitize  $\text{Er}^{3+}$  ions via a carrier-mediated process. SiGe alloys have much higher optical absorption cross-section than erbium ions, which could be utilized to absorb light source more efficiently and the absorbed energy could probably be transferred to erbium ions to enhance Er-related PL intensity.<sup>115</sup> SiGe alloys also possess other useful properties as a host material for  $\text{Er}^{3+}$  ions. For example, these alloys have a variable refractive index that is determined by the ratio of germanium (Ge) to silicon (Si), which makes them suitable for optical waveguides.<sup>140</sup> Furthermore, SiGe materials that could be grown epitaxially on Si wafers can be integrated with the silicon microelectronics industry more readily.<sup>141</sup>

Group IV oxides have been demonstrated to be good candidates for optical devices.<sup>112</sup> Among these oxides, silica possesses multiple advantages including a broad spectral transmission range, easy to clad, a strong tolerance to harsh chemical environments, a high resistance to laser damage, etc.<sup>142</sup> Especially, this host material is fully compatible with the silica-based optical fiber industry and has been successfully employed to fabricate 2-dimensional Er-doped film waveguides and amplifiers.<sup>112</sup>  $\text{SnO}_2$  also possesses several appropriate properties for an optical waveguide. First, it is highly optically transparent (80-90% transparency in the visible light region).<sup>143</sup> Secondly,  $\text{Er}^{3+}$  ions could substitute interstitial  $\text{Sn}^{4+}$  ions in the rutile phase  $\text{SnO}_2$  lattice so that the direct Er-Er coupling interactions would be much suppressed.<sup>144</sup> Thirdly,  $\text{SnO}_2$  is a wide band gap n-type

semiconductor ( $E_g = 3.6$  eV) due to the presence of donor sites such as oxygen vacancies and interstitial  $\text{Sn}^{4+}$  ions,<sup>143</sup> which means that an electroluminescence could be obtained from an Er-doped  $\text{SnO}_2$  sample via an electrical excitation. Germanate based glasses also have potential applications in optical devices because of their low transmission loss in the infrared region.<sup>145</sup> These glasses also have good mechanical strength, high thermal stability, and high refractive index, which make them suitable candidates for optical fibers.<sup>146</sup> Recently, optical fibers based on undoped  $\text{GeO}_2$  glasses have been successfully used for high power laser delivery at  $2.94 \mu\text{m}$  (wavelength of the erbium substituted yttrium aluminium garnet laser).<sup>147</sup>

## 1.5 EXAFS Measurements

Extended X-ray Absorption Fine Structure (EXAFS) measurement is a powerful technique for probing the local coordination structure around a specific element giving information on the number and chemical identities of neighboring atoms, as well as the average bond lengths.<sup>79,148</sup> Since the X-ray source is an intense synchrotron radiation whose energy ranges from 200 to 35,000 eV, this technique can be used for atoms in any kind of environment, e.g. crystalline solids, amorphous phases, liquids, and etc.<sup>149</sup> EXAFS spectra are displayed as graphs of the X-ray absorption coefficient of a given material versus energy.<sup>150</sup> In an EXAFS measurement, an absorbed photon ejects a photoelectron from the atom, leaving behind a hole. The ejected photoelectron has an energy that is equal to that of the absorbed photon minus the binding energy of the initial core state.<sup>150</sup> These photoelectrons are backscattered by the surrounding non-excited atoms. The backscattered photoelectron waves interfere with the forwarding-propagating waves, resulting in the modulation of the measured X-ray absorption coefficient and thereby causing oscillations in the EXAFS spectrum.<sup>150</sup> The phase and amplitude of the backscattered waves are dependent on the type of atom doing the backscattering and on the distance between the backscattering atom and the central atom,<sup>150</sup> which makes it possible to obtain structural information on the central excited atom. Fourier transformation analysis of the absorption spectra gives a radial distribution function centered on the absorbing atoms, which helps filter out background absorption and visualize the various shells of neighboring atoms surrounding the central atom.<sup>148</sup> The theoretical equation of the EXAFS signal can be represented as equation (10):<sup>150</sup>

$$\chi(k) = (1/k)\Sigma(N_j/R_j^2)f_j(k, \pi)\sin\{2kR_j + \alpha(k)\}\exp(-2R_j/\lambda)\exp(-2\sigma_j^2k^2) \quad (10)$$

in which  $\chi$  is the oscillatory modulation of absorption cross section;  $N_j$  is the number of atoms in the  $j$ th shell at distance  $R_j$ ;  $\alpha(k)$  is the sum of the central atom and ligand phase shifts;  $\sigma_j^2$  is the mean square relative displacement from equilibrium (Debye-Waller factor);  $\lambda$  is the photoelectron mean free path. The  $k$  is the photoelectron wave vector that is defined by the equation (11):<sup>151</sup> where  $m_e$  is the electron mass,  $h$  is Planck's constant,  $E_o$  is the threshold energy of the absorption edge, and  $E$  is the absolute energy.

$$k^2 = 2m_e(E-E_o)/h \quad (11)$$

EXAFS spectroscopy has been extensively used to investigate the Er structural environment in different host materials, especially in Si.<sup>148</sup> Figure 29a shows EXAFS spectra of Er-doped (100) Si samples prepared using an ion-implantation technique, in which  $\text{Er}_2\text{O}_3$  and  $\text{ErSi}_2$  were used for comparisons.<sup>148</sup> Table 1 demonstrates the quantitative analysis of the Er-O bond lengths and coordination numbers in the above samples using the filtered data shown in Figure 29b.<sup>148</sup> It can be clearly seen that erbium ions have different structural environments in  $\text{Er}_2\text{O}_3$  and Si. For example, Er has a coordination number of 6 with oxygen in  $\text{Er}_2\text{O}_3$ , whereas the number is only 4.4 in an Er-doped Si sample that has been annealed at 620 °C for 3 h.

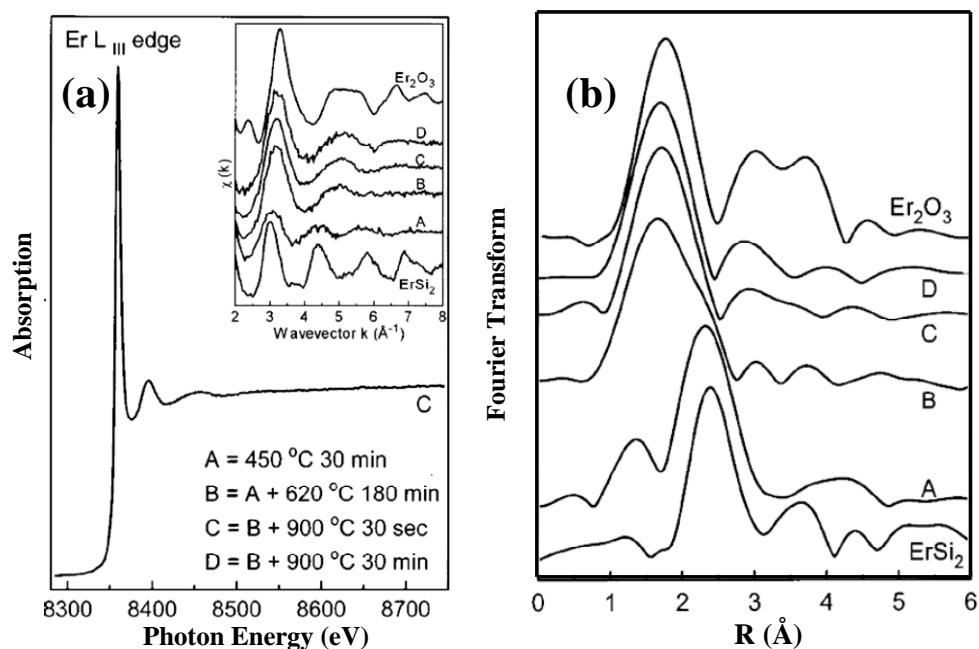


**Figure 29.** (a) An original EXAFS spectra of the Er L<sub>III</sub> absorption edge of Er-doped Si sample annealed under condition C, and the inset shows all EXAFS spectra for the sample annealed under conditions of A-D (note: Y-axis is EXAFS signal  $\chi(k)$ ). (b) Fourier transformed EXAFS spectra obtained from the data shown in (a). (Note: Y-axis is EXAFS signal multiplied by  $k^2$ , and X-axis is interatomic distance.). Adapted from ref. 148.

**Table 1.** Quantitative analysis of the first coordination shell on the filtered data. N is the average coordination number, R is the interatomic distance, and A-D stand for the sample annealed under various conditions. Adapted from ref. 148.

Sample	ErSi <sub>2</sub>	A	B	C	D	Er <sub>2</sub> O <sub>3</sub>
Atom	Si	Si	O	O	O	O
N	10	6 ± 2	4.4 ± 0.6	5.1 ± 0.5	5.0 ± 0.5	6
R ( $\text{\AA}$ )	2.994	3.01 ± 0.04	2.27 ± 0.02	2.27 ± 0.02	2.26 ± 0.02	2.26

*CHAPTER II.*

Research Synopsis

Since the transistor and gate materials in modern microelectronic industry are reaching their fundamental limits as the size of transistor is getting close to that of atoms and molecules, revolutionary new technologies must be developed to transcend this barrier. Optoelectronics and photonics are two of those new technologies that have attracted intensive attention recently. The advantage is that much higher data transfer rates are achievable using photons rather than electrons to switch on and off the logic devices. Despite their dominance in microelectronics, Group IV semiconductors, e.g. Si, Ge and SiGe have so far proved to be poor choices for optical sources owing to their intrinsic indirect bandgap properties. Although quantum dots of those semiconductors can emit efficient luminescence, the wavelength is different from the 1.50-1.60  $\mu\text{m}$  that is used in silica based optical fiber industry. Doping Group IV semiconductors with  $\text{Er}^{3+}$ , however, is a promising method to prepare electronic devices with efficient optical function, since the transition from  $^4\text{I}_{13/2}$  to  $^4\text{I}_{15/2}$  of erbium ions at 1.54  $\mu\text{m}$  lies at a transmission maximum for silica-based waveguides. Furthermore, semiconducting nanowires doped with erbium could serve as building blocks to assemble more optoelectronic units on a single chip via a bottom-up approach. It is also important to fabricate compositionally compatible sub-wavelength Er-doped Group IV oxide nanofibers, which could be used as freestanding nanowaveguides, nanoamplifiers, nanoconnectors, and building blocks for integrating high-density optical units.

First, Ge NWs with controllable diameters were prepared via a vapor-liquid-solid (VLS) synthetic route as described in Chapter 3. Carbon and germanium powder mixture was heated at high temperature to generate adequate amount of vapor, and the vapor was carried downstream by helium carrier gas and deposited on the silicon wafer coated with thin Au film to prepare Ge NWs. Diameters of the NWs can be controlled varying helium flow rates

and reaction times. Micro-Raman spectroscopy and X-ray energy dispersive spectroscopy (XEDS) confirms that the NWs are mainly composed of crystalline Ge and trace amount of oxygen due to the surface oxidation. Transmission electron microscopy (TEM) studies show that there is Au catalyst on the tip of Ge NW, which implies that NWs grow through a VLS synthetic route. High resolution TEM and selected area electron diffraction (SAED) pattern confirm that NWs are single crystal diamond cubic germanium with a d-spacing value of 3.25 Å, which corresponds to an (111) orientation. The as-prepared Ge NWs were then deposited with a layer of erbium using CVD method to prepare Er-doped Ge NWs. SAED pattern and high resolution TEM confirm that the core is crystalline diamond cubic germanium and the shell is amorphous. XEDS shows that erbium concentrations in the shell and core are 17%, and 5%, respectively, which suggests that this type of NWs possesses a distinct core-shell structure. X-ray photoelectron spectroscopy (XPS) suggests that the surface of these Ge NWs is partially oxidized, and erbium is in 3 plus charge state. The as prepared Er-doped Ge NWs and the NWs annealed in N<sub>2</sub> do not emit luminescence. After being annealed in air at 600 °C, however, the NWs become emissive and display an excitation pathway similar to carrier-mediated excitation of the erbium ions. EXAFS data show that the erbium coordination number is 8 in Er-doped Ge NWs, which is higher than that in Er<sub>2</sub>O<sub>3</sub>, and the Er-O bond length is longer than that for Er<sub>2</sub>O<sub>3</sub>.

Since Ge NWs are readily oxidized, Si was introduced to form stable SiGe alloys in order to circumvent this problem. Furthermore, SiGe alloys possess tunable band gaps that could be utilized to excited Er<sup>3+</sup> ions more efficiently through an energy resonance process. In Chapter 4, three sequences of depositing Si and Er on the core Ge NWs were employed to fabricate three structurally distinct NWs: “Sandwich”, “co-deposited”, and “Er Surface-

Enriched” Er-doped SiGe NWs. TEM images and XEDS linescans show that “Sandwich” NWs have no detectable erbium ions in the shell and most erbium ions are concentrated in the SiGe core. High resolution TEM imaging of annealed NWs shows that the core is crystalline SiGe alloy, and the shell is amorphous. Micro-Raman spectroscopy is consistent with this observation. In contrast, TEM images and XEDS linescans of “Er Surface-Enriched” NWs show that core is Ge rich and erbium ions are concentrated in the shell. High resolution TEM (HRTEM) imaging and micro-Raman spectroscopy confirm that the core is crystalline SiGe alloy, and there is a layer of epitaxial Si on the boundary with the crystalline core. Compared with other two types of NWs, “co-deposited” NWs possess more uniform diameters and smoother surfaces, which is confirmed by the TEM images. HRTEM, XEDS linescans, and 2-dimensional elemental mapping of these “co-deposited” NWs show that the core is Ge rich, and Si & Er in a polycrystalline fashion are concentrated in the shell.

As-formed three types of Er-doped SiGe NWs cannot emit luminescence at 1.54  $\mu\text{m}$ . However, they become emissive at 1540 nm after being annealed in  $\text{N}_2$  or air. Among those three types of Er-doped SiGe NWs, “co-deposited” NWs can emit the strongest Er-related luminescence. EXAFS structural data show that erbium is coordinated to 8 oxygen atoms in  $\text{Er}^{3+}$ -doped Ge NWs, “co-deposited” NWs, and “Sandwich” NWs. This number is higher than that of  $\text{Er}_2\text{O}_3$  standard, in which erbium is coordinated to 6 oxygen and weakly emissive. Furthermore, Er-O bond lengths in these Er-doped NWs are more relaxed relative to  $\text{Er}_2\text{O}_3$  standard. Photoluminescence (PL) excitation spectra suggest that light emission of “Er Surface-Enriched” and “co-deposited” NWs is from the carrier-mediated excitation of the erbium ions. In contrast, the Er-related luminescence of “Sandwich” NW is from the direct excitation of erbium ions in the host.

To further understand the mechanism underlying the light emission from Er-doped Ge and SiGe NWs, we prepared their corresponding oxides doped with erbium in the form of nanofibers. Furthermore, for practical long term significance, it is very important to fabricate freestanding one-dimensional waveguides and amplifiers in order to integrate more optical units on a single chip. In Chapter 5,  $\text{Er}_2\text{O}_3$ , Er-doped  $\text{SiO}_2$ ,  $\text{GeO}_2$ , and  $\text{SnO}_2$  nanofibers were fabricated using a new electrospinning approach combined with a sol-gel process. The as-formed nanofibers were then annealed in air at 500 °C or higher to remove templating polymers in order to prepare pure inorganic Er-doped Group IV oxide fibers. Scanning electron microscopy (SEM) images of Er-doped  $\text{GeO}_2$  nanofibers reveal that the morphology of the nanofibers is sensitive to temperature. FT-IR spectra of Er-doped  $\text{GeO}_2$  nanofibers annealed at various temperatures were also measured. TEM imaging of Er-doped  $\text{SnO}_2$  nanofibers indicates that the fibers are composed of small  $\text{SnO}_2$  nanoparticles. Electron Diffraction (ED) pattern confirms that the nanoparticles are polycrystalline tetragonal  $\text{SnO}_2$ . High resolution TEM image shows that the nanocrystals have a d-spacing value of 3.389 Å, which corresponds to an (110) orientation of tetragonal  $\text{SnO}_2$ . XEDS linescans suggest that there is no significant erbium precipitation in  $\text{SnO}_2$  matrix up to 4% level after the fibers were annealed at 900 °C for 3 h. Powder X-ray diffraction (XRD) measurements and TEM studies confirm that the presence of erbium ions and lower annealing temperatures will lead to the formation of  $\text{SnO}_2$  nanocrystals with smaller diameters. Furthermore, Er-doped  $\text{SnO}_2$  nanofibers can be aligned across an insulating gap between two conductive grounding electrodes. In terms of near-IR photoluminescence, Er-doped  $\text{GeO}_2$  nanofibers can emit much stronger luminescence than any other nanofiber. The PL excitation spectrum of Er-doped  $\text{GeO}_2$  annealed at lower temperature is characteristic of a carrier-mediated excitation

of the erbium ions, which further confirms the Er-related PL mechanism of Er-doped Ge NWs. However, the other three types of nanofibers display an excitation mode similar to direct excitation of erbium ions.

Since the above research demonstrated  $\text{GeO}_x$  to be an effective sensitizer for  $\text{Er}^{3+}$  ions, it was then introduced into Er-doped  $\text{SnO}_2$  purposely to further increase its PL intensity in Chapter 6. As prepared Er-doped  $\text{SnO}_2$  nanofibers placed on a regular Si wafer substrate were first annealed in air at 500 °C to remove organic composite, and then deposited with Ge via a vapor transport method. SEM and TEM images reveal that the “front part” of the sample (~10% of the sample that is closest to the oven) possesses a film-like structure, and other parts of the sample are composed of fibers with lots of nanoparticles on their surface. Micro-Raman measurements confirm that  $\text{SnO}_2$  was reduced by Ge vapor to produce elemental tin in the “front part” of the sample, and the “back part” of the sample (~70% of the sample that is far away from the oven) is still mainly composed of  $\text{SnO}_2$ . Compared with Er-doped  $\text{SnO}_2$  nanofibers annealed at 900 °C, the fibers deposited with Ge can emit almost two orders of magnitude stronger luminescence at 1.54  $\mu\text{m}$ . Furthermore, the erbium ions in Er-doped  $\text{SnO}_2$  nanofibers deposited with Ge can be excited using broadband light sources, e.g. 476 to 532 nm laser lines. Low temperature PL spectra show that PL intensity of the front part of the sample dropped by ~60% while the temperatures are increased from 100 to 300 K, whereas PL intensity of the back part of the sample was reduced only by ~35%.

Finally, in the last chapter of this dissertation, the gold-induced self-assembly of Ge micropatterns, an accidental discovery, is described. As a proof of their possible utility, the Ge micropatterns were then used as templates to grow  $\text{CaCO}_3$  and Si nanorods. Ge micropatterns were produced by heating the Ge (100) wafer coated with a thin Au film at 830

°C for 4h under the protection of helium gas. SEM images show that the patterns are square or rectangular with or without multifaceted island in the middle of the patterns. XEDS confirms that the islands are comprised of Au-rich AuGe alloys. The presence of ultra-thin Au films and longer annealing times are critical to form more regular Ge micropatterns, whereas helium flow rates do not significantly affect the morphology. No regular patterns are achievable if annealing temperature is reduced to 400 °C. The slopes of those micropatterns have  $\langle 111 \rangle$  orientations according to our SEM measurements and basic crystallography principles. Using an electrochemical deposition method  $\text{CaCO}_3$  nanorods were produced on the Ge micropatterns along the meniscus line. The solutions used are simulated body fluid (SBF) or aqueous  $\text{CaCl}_2 \cdot 2\text{H}_2\text{O}$  &  $\text{NaHCO}_3$  solution. XEDS confirms that the rods are mainly composed of calcium. Control experiments demonstrate that the Ge/Au patterns are necessary for the formation of  $\text{CaCO}_3$  rods. Micro-Raman spectroscopy measurements further confirm that the rods and cubes are calcite calcium carbonate. Ge micropatterns were also used as templates to grow Si nanorods via a VLS synthetic route. Using silane as Si precursor, Si nanorods were produced via a CVD method on the Ge/Au micropatterns. SEM studies indicate that the as-formed Si nanorods possess a tapering structure, and the most rods are growing perpendicular to the slopes, which is consistent with the  $\langle 111 \rangle$  orientations of those slopes.

*CHAPTER III.*

Fabrication, Characterization and Optical Properties of Er-  
Doped Ge Nanowires

### 3.0 Overview

As mentioned in Chapter 1, one-dimensional nanowires have potential applications as building blocks for generating nano-scale devices. The incorporation of erbium ions into Group IV indirect band gap semiconductors is a promising way to make them emissive at 1.54  $\mu\text{m}$ . Among these group IV semiconductors, germanium (Ge) possesses several interesting attributes that make it a good candidate as a host material for erbium. First, the optical absorption edge of Ge nanocrystals should shift towards higher energy with decreased size.<sup>129,130</sup> As a consequence, this infers that the absorbed energy by nano-scale germanium could be used to excite  $\text{Er}^{3+}$  ions through energy resonance transfer. Next, the laser-pumping efficiency of Ge nanowires will be increased due to phonon confinement effects,<sup>131</sup> i.e. the reduction of exciton-acoustic-phonon interactions as the result of host size reduction to the nanometer regime.<sup>132</sup> In addition, given the ease of germanium oxidation, the optical band gap of  $\text{GeO}_x$  can be easily tuned from 0.75-5 eV by varying the annealing time, a property that can assist in trapping energy and transferring it to  $\text{Er}^{3+}$  ions.<sup>134,135</sup> Therefore, doping Ge NWs with erbium ions is an efficient way to produce photonic building blocks at the nano scale, which has potential applications in the fabrication of more complex nanophotonic devices.

In this chapter, Ge NWs of different diameters were first prepared via a new straightforward vapor transport method. Erbium was then deposited on the Ge core NWs through the decomposition of an erbium precursor  $\text{Er}(\text{tmhd})_3$  (tmhd = 2,2,6,6-tetramethyl-3,5-heptanedionato) to form Er-doped Ge NWs. These NWs were structurally characterized using transmission electron microscopy (TEM), high-resolution electron microscopy (HREM), scanning electron microscopy (SEM), X-ray energy dispersive spectroscopy

(XEDS), and selected area electron diffraction (SAED). X-ray photoelectron spectroscopy (XPS) was used to characterize the surface composition of these wires. UV-visible electronic absorption spectra show a broad absorption tail due presumably to the presence of surface  $\text{GeO}_x$  and possible quantum confinement of Ge NWs. Micro-Raman spectroscopy data indicates that the NWs are composed of crystalline germanium. The photoluminescence (PL) properties of Er-doped Ge NWs and the conditions necessary for activation of this emission are also explored.

## 3.1 Experimental

### 3.1.1 Er-Doped Ge Nanowire Synthesis

A two-step process was used to synthesize Er-doped Ge NWs. First Ge NWs of various diameters were prepared by a vapor transport method. The reactor design for fabricating Ge NWs is shown in Figure 30. Quartz tubing of 20 mm inner diameter (ID) was used to construct the reactor, and mass flow controllers (MKS Inc.) were employed to control the gas flow rates of helium (UHP semiconductor grade (Praxair)). In a typical reaction, an alumina boat containing a mixture of 10 mg carbon (J.T. Baker) and 22 mg germanium powder (Strem) in a C:Ge molar ratio of  $\sim 3:1$  was placed in the reactor. A 5 x 15 mm p-type Si wafer piece possessing thermally deposited Au islands was placed into another alumina boat that was positioned in the quartz tube reactor approximately 3 cm from the edge of the oven. The boat containing a given C:Ge mixture was heated (by a 15 cm ceramic oven) at 850 °C for 2h, and then at 1000 °C for 1.5 h under the protection of helium at a flow rate of 3000 sccm. The temperature of the Ge NWs growth is  $\sim 560$  °C. At the end of the reaction period, a thick brown film can be easily seen on the wafer.

In the next step, the deposition of  $\text{Er}^{3+}$  ions on the surface of Ge nanowires is achieved via the pyrolysis of  $\text{Er}(\text{tmhd})_3$ , followed by a subsequent thermal annealing step. The reactor design for this step is shown in Figure 31. The ID of the quartz tubing is 20 mm, and mass flow controllers were used to control the flow rates of helium. In order to dope the as-prepared sample with erbium ions, 15 mg of  $\text{Er}(\text{tmhd})_3$  was heated to 145 °C in a bubbler, and  $\text{Er}(\text{tmhd})_3$  vapor was transported downstream by helium to a pyrolysis oven operating at 500 °C where the as-prepared sample is located. The oven was maintained at 500 °C for 1 h.

The resultant product, appearing as a dark brown film, was annealed in air at 600 °C in order to achieve a strongly luminescent sample.

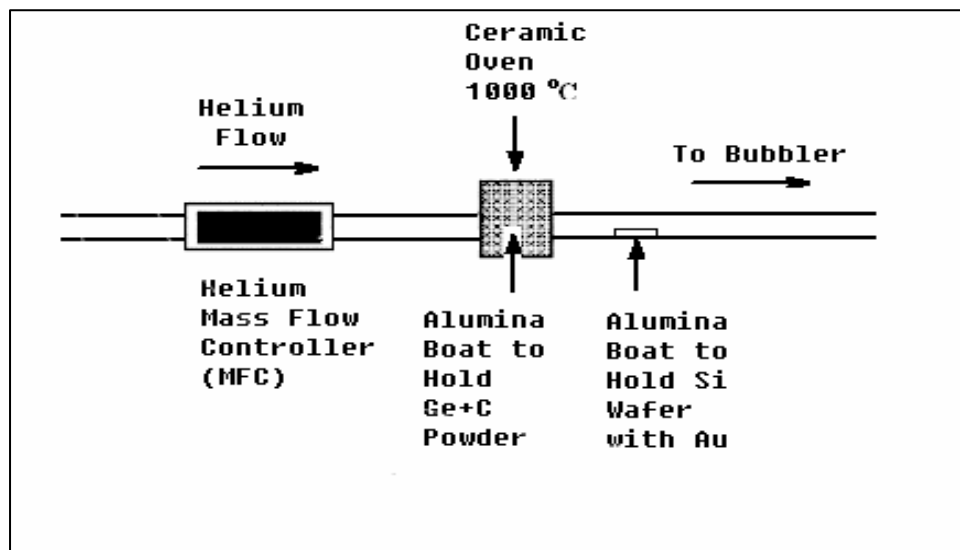


**Figure 30.** Reactor design for preparing Ge nanowires.

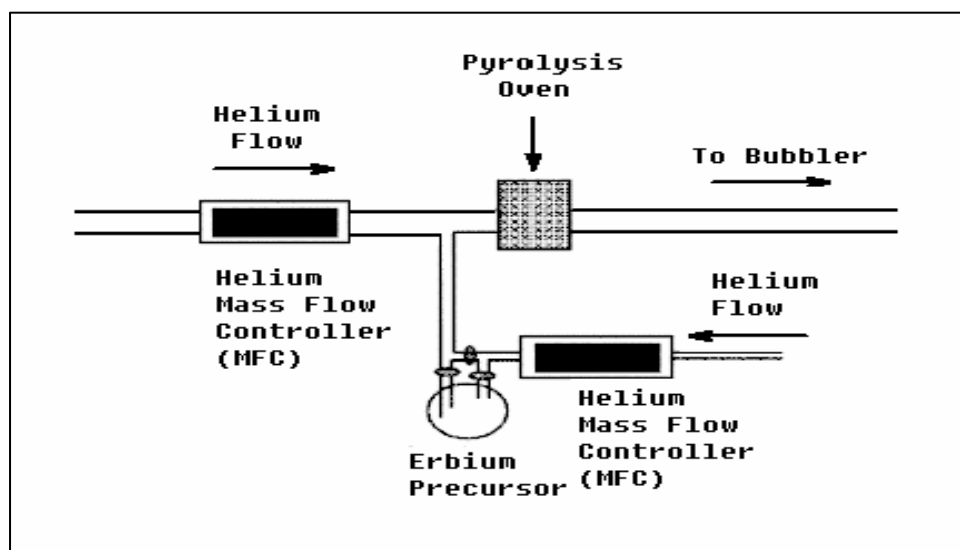


**Figure 31.** Reactor design for doping Ge nanowires with erbium ions.

### 3.1.2 Instrumentation

Structural characterization of both types of nanowire materials were performed using a JEOL JEM-3010 transmission electron microscope (TEM) equipped with a Thermo Noran Vantage XEDS system; a Hitachi S-3000N VP-SEM (scanning electron microscope) with an Oxford Instruments Inca XEDS system at the University of Illinois-Chicago (UIC). Specimens for TEM characterization were prepared by dispersing the sample with a 10  $\mu$ l drop of 2-propanol and then placing the drop onto a grid. Selected area electron diffraction patterns (SAED) and X-ray energy dispersive spectroscopy (XEDS) analyses of individual nanowires were obtained during TEM analyses. EDX analyses of macroscopic nanowires were performed using a JEOL JSM-6100 SEM at TCU and Hitachi S-3000N VP-SEM at UIC. Low-resolution ( $\pm 4$  nm) near-IR photoluminescence (PL) spectra were obtained using an Applied detector Corp. liquid N<sub>2</sub>-cooled Ge detector in conjunction with a Stanford Research Systems Chopper/Locked-in amplifier and an Acton Research Corp. 0.25 m monochromator. Excitation was provided by a Coherent Ar<sup>+</sup> laser. Emitted light was collected at a 40° angle relative to the excitation direction. A 1000 nm cutoff filter (Melles Griot) was positioned over the monochromator entrance slit to filter out second- and third-order light. A Hewlett-Packard 8452A diode array spectrometer was used for UV-visible absorption spectroscopy.

Raman spectra were recorded using a Raman micro-imaging system in the laboratory of Prof. Zerda at the Physics Department of TCU, which consists of a laser, optical microscope, spectrometer, and a CCD detector. The argon ion laser operating at 514 nm was used as exciting light. The sample was mounted onto a computer controlled X-Y-Z stage to be focused, and the scattered light was collected by the spectrometer and recorded by a CCD

detector with a resolution of about  $4.0 \text{ cm}^{-1}$ . An Olympus BH-2 microscope with a 100X objective allowed the collection of scattered light from spots as small as  $1 \text{ }\mu\text{m}$  in diameter. X-ray photo-electron spectroscopy (XPS) was performed *ex situ* with a standard Al anode source in a Vacuum Generators ESCALab Mark-II system at the University of Texas at Dallas.

## 3.2 Results and Discussion

### 3.2.1 The role of carbon in the preparation of Ge NWs

For the preparation of the core Ge NW structures necessary for these experiments, a simple vapor transport method that relies on a combination of Ge + C in the original reactant source has been developed. While Ge-C alloying is thermodynamically disfavored under these conditions,<sup>93,152</sup> the presence of carbon particles drastically reduces the ability of the (molten) Ge to agglomerate into larger droplets such that the maximum surface area of the molten Ge and subsequent optimal evaporation of Ge are retained as shown in Figure 32. Carbon also can reduce the amount of native germanium oxide on the germanium powder through carbothermal reduction, in which  $\text{GeO}_2$  (melting point = 1115 °C) is reduced by C to form volatile GeO (melting point = 710 °C) and C is oxidized into CO.<sup>153</sup> It is notable that this fabrication method avoids the use of expensive and flammable chemical vapor deposition (CVD) precursors such as germane and digermane, while achieving a decent yield of Ge NWs.

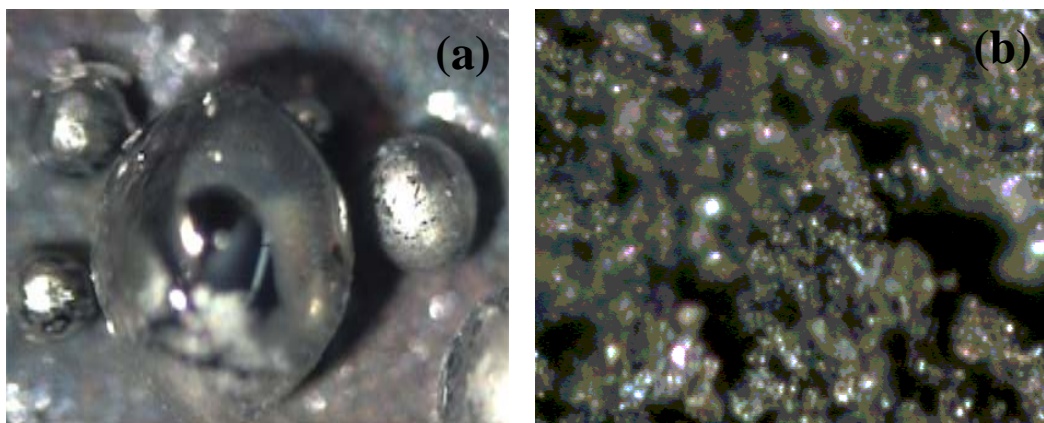


**Figure 32.** (a) Optical image of the germanium powder after heated at 1000 °C for 1.5 h (X10) showing the formation of large Ge droplets. (b) Optical image of the mixture of germanium and carbon after heated at 1000 °C for 1.5h (X10) showing that the agglomeration of small Ge droplets is greatly reduced.

### 3.2.2 Characterization of Ge and Er-Doped Ge NWs

Scanning electron microscopy (SEM) images of a typical undoped Ge NW sample obtained using a Hitachi S-3000N VP-SEM are shown in the figure below. The sample consists of densely interwoven nanowires with widths ranging mostly from 80-140 nm and length up to several tens of microns. The preparative conditions for this type of Ge NWs are those associated with the ~123 nm average diameter sample shown in Table 2.

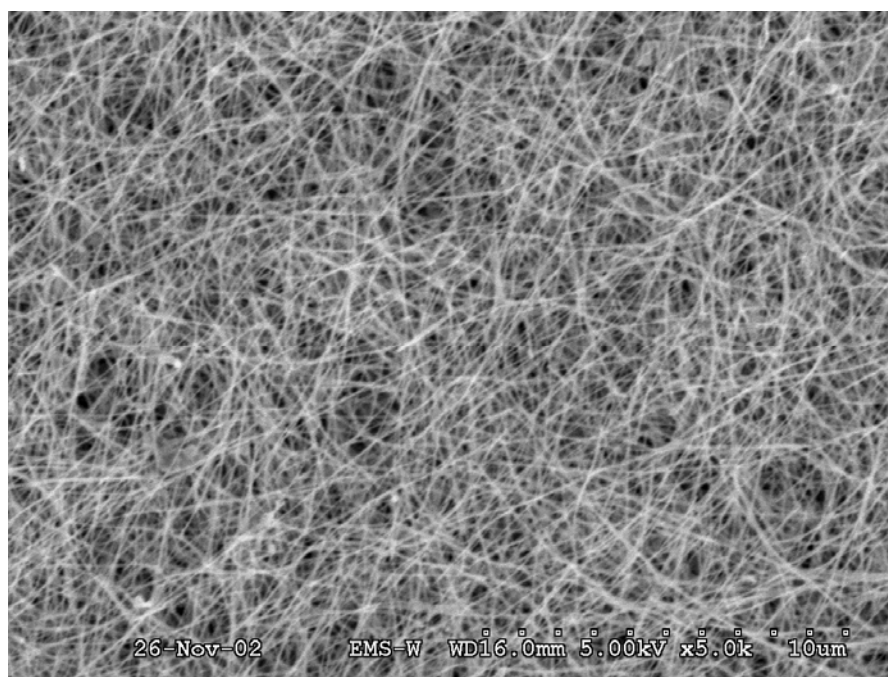


**Figure 33.** Scanning electron microscopy image of Ge nanowires with a  $\sim 123$  nm average diameter.

X-ray energy dispersive spectroscopy (XEDS) system on an SEM at the University of Illinois-Chicago was used to determine the composition of these NWs. High energy electron beam generated in the SEM chamber bombards the sample so that electrons in the inner shell could be removed to form vacancies. Electrons in the outer shell will fill those vacancies, and X-ray photons will be emitted with a wavelength corresponding to the energy difference between these two shells. Since different atoms have different shell energies, elements can be detected by measuring their emitted X-ray energies. As shown in Figure 34, the spectrum confirms that the nanowires are composed primarily of germanium with some residual

oxygen due to the surface oxidation of NWs.<sup>154</sup> The Ge-L shell and O-K shell peaks are located at 1.2 and 0.52 KeV, respectively.

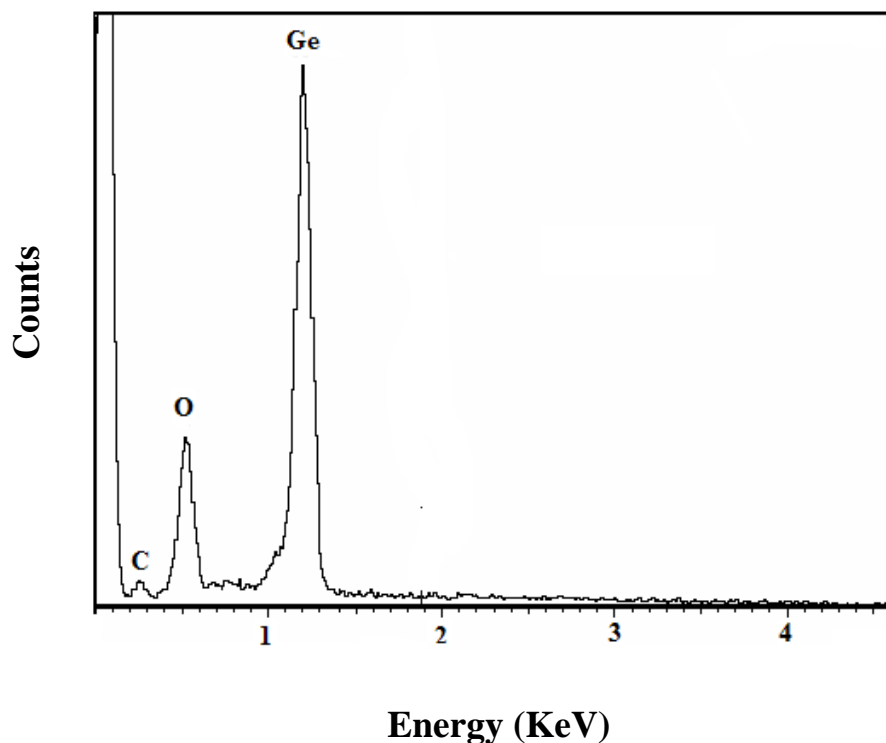


**Figure 34.** X-ray energy dispersive spectrum of the Ge NWs shown in Figure 33.

A selected area electron diffraction (SAED) pattern performed on a single Ge NW consists of discrete diffraction spots, which is characteristic of crystalline germanium. The distance from the spot to the central point of the beam is called spacing of spots  $r$  that can be used to calculate the diffraction angle  $\theta$  using equation (12), where the  $L$  stands for length of the camera that has a value of 25 cm in this case. If the wavelength of electron beam  $\lambda$  is known, the lattice spacing  $d$  can be solved using the Bragg equation (13). This wavelength of the electron beam is related to the accelerating voltage, and  $hkl$  stands for the Miller indices of crystal planes. The orientations of these diffraction planes are associated with their  $d$

spacing values, which are listed in the powder diffraction file database, e.g. PDF (powder diffraction file) of the ICDD (International Center for Diffraction Data).

$$\tan(2\theta) = r/L \quad (12)$$

$$2d_{hkl}\sin\theta = \lambda \quad (13)$$

The diffraction pattern of a single Ge NW is shown in the Figure 35. The three closest diffraction spots to the central point in different directions are from the (111), (331) and (422) crystal planes of the diamond cubic phase germanium, according to our calculated results using the above method.

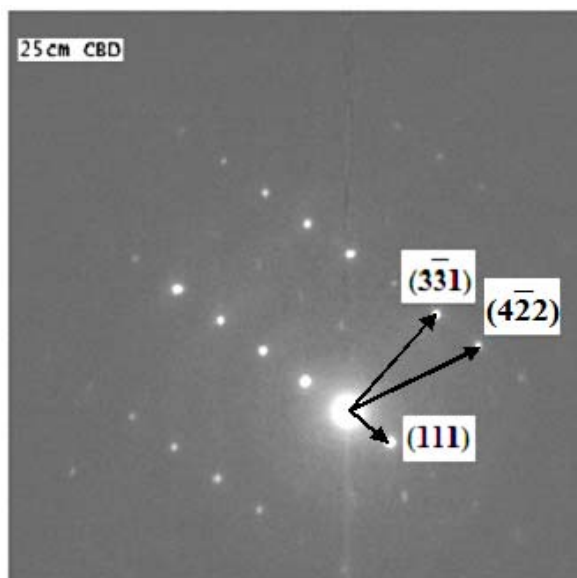


**Figure 35.** Selected area electron diffraction pattern of single Ge NW.

A selected TEM image of Ge NWs is shown in Figure 36, where the gold catalyst nanoparticle sits on the end of the Ge NW, confirming the expected vapor-liquid-solid (VLS) mechanism in this synthetic route; this image also suggests a layer of amorphous germanium oxide present with widths of 2~3 nm surrounding the Ge core. The stark contrast between

gold and germanium is caused by the big difference in X-ray atomic absorption cross section between these two elements.<sup>155</sup>

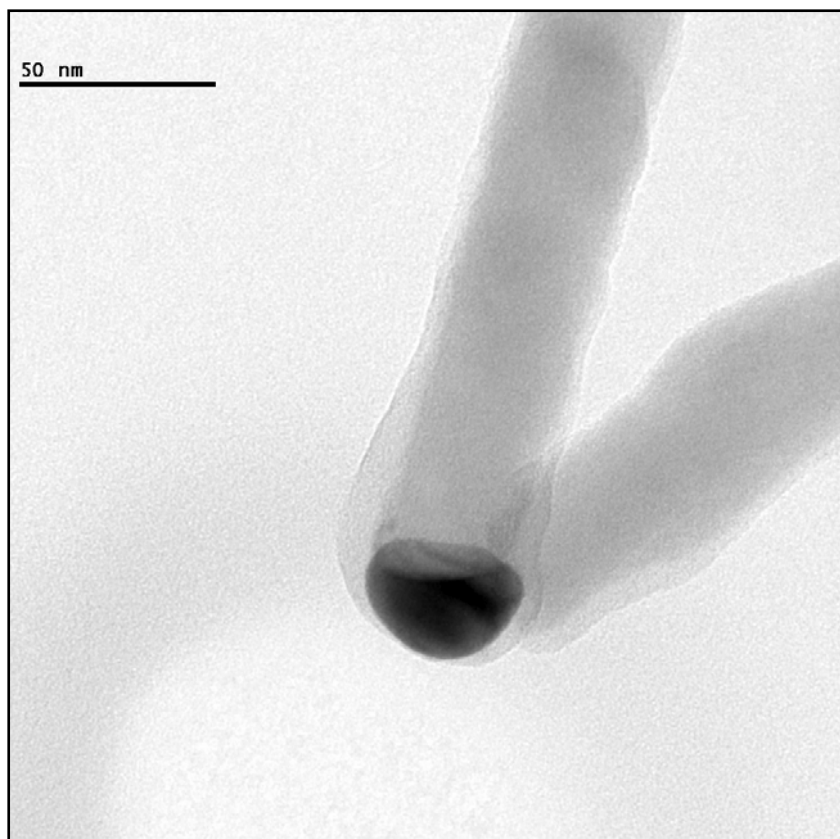


**Figure 36.** Transmission electron microscopy image of Ge NWs showing a gold catalyst sitting on the end of the nanowires.

A SEM image of Er-doped Ge NWs is shown in Figure 37. It was found that the mean diameter of these nanowires does not change significantly after erbium exposure when compared to their original value. The presence of the erbium in the nanowires is confirmed by XEDS analysis, where the Er- $L\alpha$  and  $M\alpha$  peaks are at 6.9 and 1.4 KeV, respectively. The Si-K peak at 1.7 KeV (Figure 37b) is from the silicon substrate.

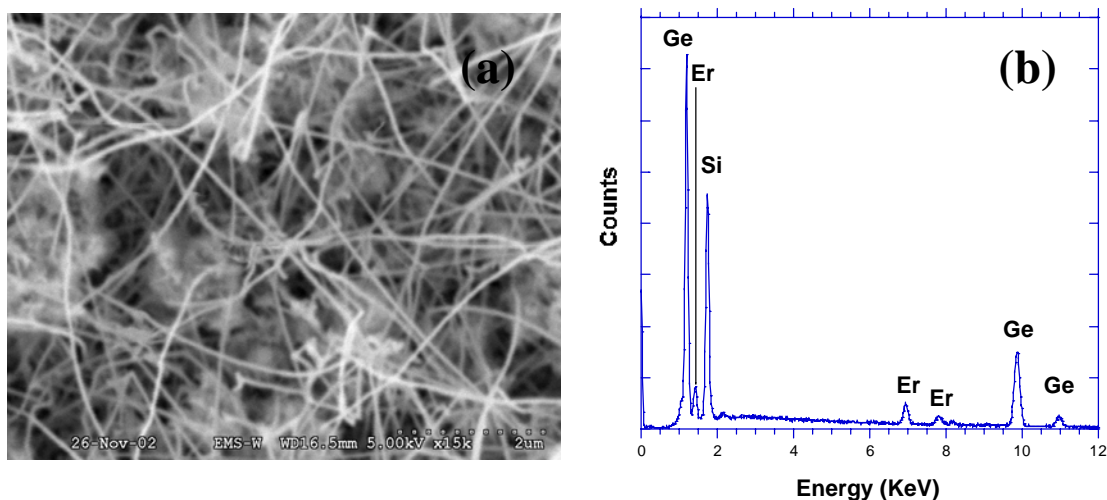


**Figure 37.** (a) A scanning electron microscopy image of Er-doped Ge nanowires and (b) XEDS spectrum of Er-doped Ge NWs confirming the presence of erbium in the nanowires.

A TEM image and SAED pattern of Er-doped Ge NWs are shown in Figure 38. The TEM image shows that the NW has a darker contrast relative to an as-formed Ge NW due to the presence of erbium that has a higher X-ray atomic absorption cross section than germanium. The SAED pattern performed on the single NW is composed of discrete spots indicating that the wire is crystalline. The first three diffraction spots closest to the central point of the beam are from the (111), (220), and (331) crystal planes of cubic phase germanium. Er-related diffraction patterns are not observed due to the small amount of Er or, alternatively, an amorphous structure.

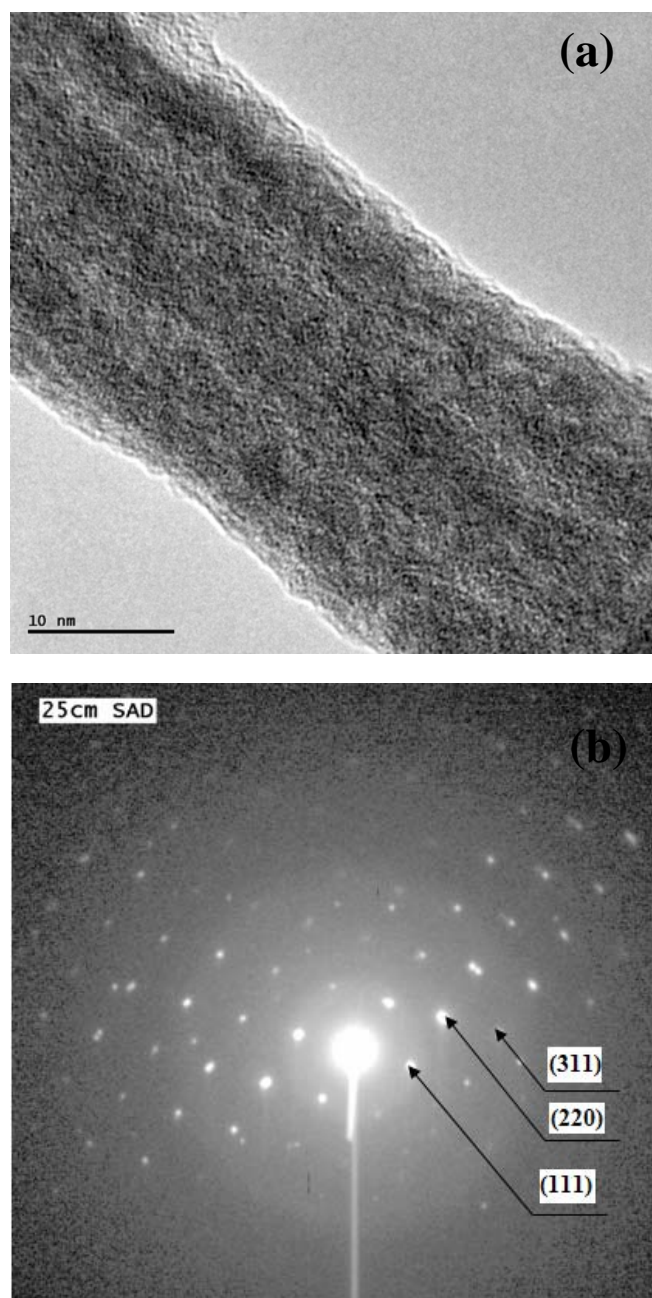


**Figure 38.** (a) TEM image of a single Er-doped Ge NW and (b) SAED pattern from the single NW showing that the first 3 diffraction spots are from (111), (220) and (311) crystal planes of diamond cubic Ge.

### 3.2.3 Control of Average Diameters of Ge NWs

The average diameter of Ge NWs prepared by this synthetic route has been determined by measuring 60-80 NWs for each preparative condition using their corresponding SEM images. The average diameters and associated fabrication conditions for various types of Ge NWs are listed in Table 2, and Ge NW diameter distributions for each type of nanowire are presented in Figure 39. In general, longer reaction times and higher helium flow rates lead to the formation of thicker Ge NWs. Increasing He flow rate likely impacts local Ge concentration present at a given Au catalyst island in terms of reactant supersaturation, which causes the mean NW width to increase; the narrower size distribution observed for the thinner nanowires relative to that of the thicker nanowires reflects this point. The presence of thicker wires as the result of longer reaction times presumably arises from increased catalyst size as a result of continued substrate annealing during the growth process. It is also possible that there is an increased radial growth of germanium on the nanowire along with elongated reaction times.<sup>156</sup>

**Table 2.** Control of Ge NWs mean diameters by varying the helium flow rate and reaction time

He flow rate (sccm)	Reaction duration (min)	Mean diameter (nm)
3000	90	123
3000	40	80
3000	20	74
1500	90	69
1500	20	45

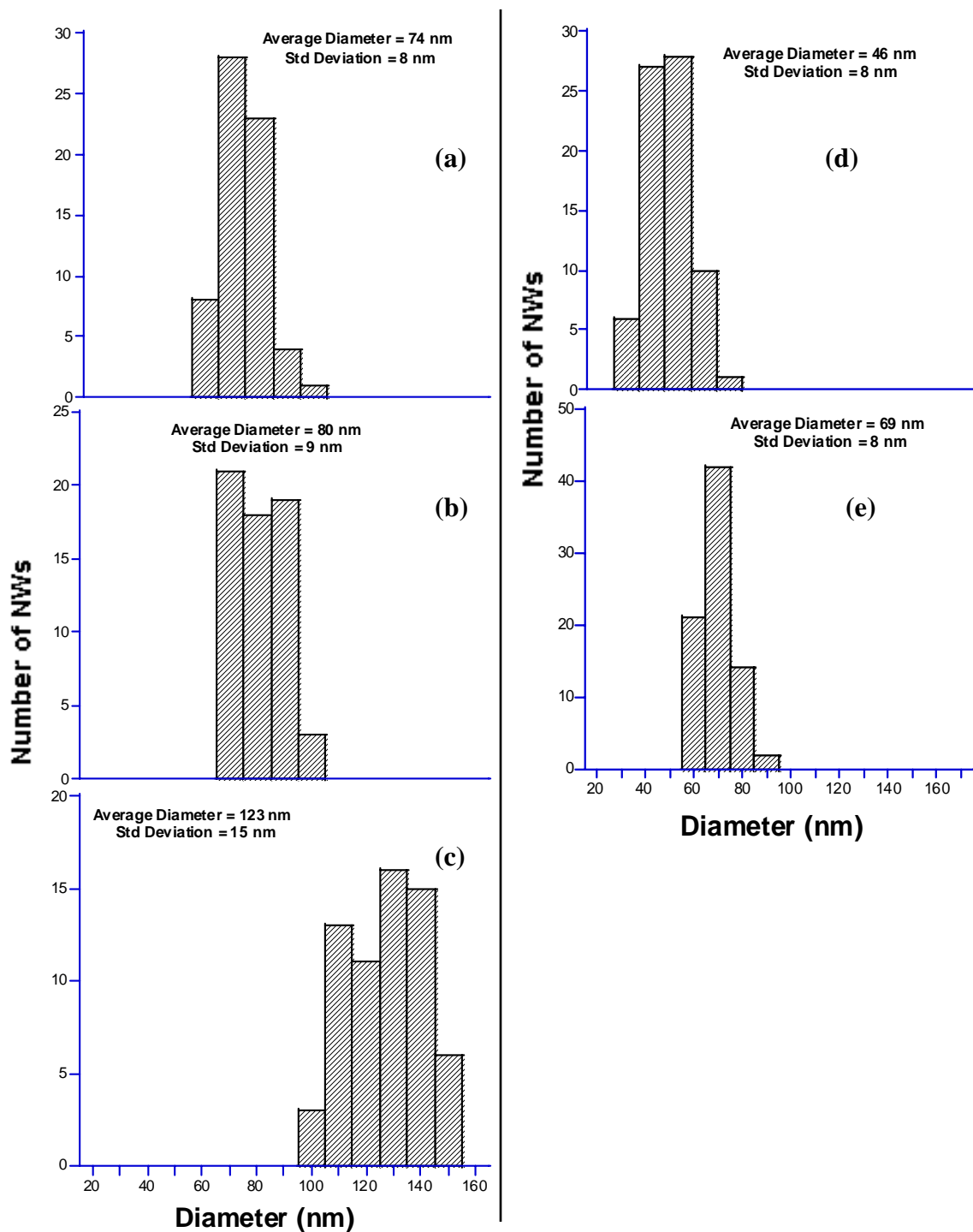


**Figure 39.** Diameter distributions of Ge NWs grown using a 3000 sccm helium flow rate for (a) 20 minutes, (b) 40 minutes, (c) 1.5 h; and using a 1500 sccm helium flow rate for (d) 20 minutes and (e) 1.5 h.

### 3.2.4 Raman Spectroscopy of Ge NWs

Raman spectroscopy is a spectroscopic technique used to investigate vibrational, rotational, and other low-frequency modes of condensed materials. This technique relies on the fact that the inelastic scattering (both Stokes and anti-Stokes scatterings) of photons by the molecules can cause a frequency change (Raman shift) of these photons. Since different molecules and solid phases have different Raman shift values, this technique can be used for composition and phase identifications. Figure 40 illustrates a typical Raman spectrum of Ge NWs with an average diameter of  $\sim 123$  nm. The Raman shift at  $307\text{ cm}^{-1}$  is associated with the optical phonon scattering of Ge NWs, which is close to that of bulk crystalline Ge.<sup>157</sup> The Raman peak at  $519\text{ cm}^{-1}$  originates from the crystalline Si substrate.<sup>158</sup>

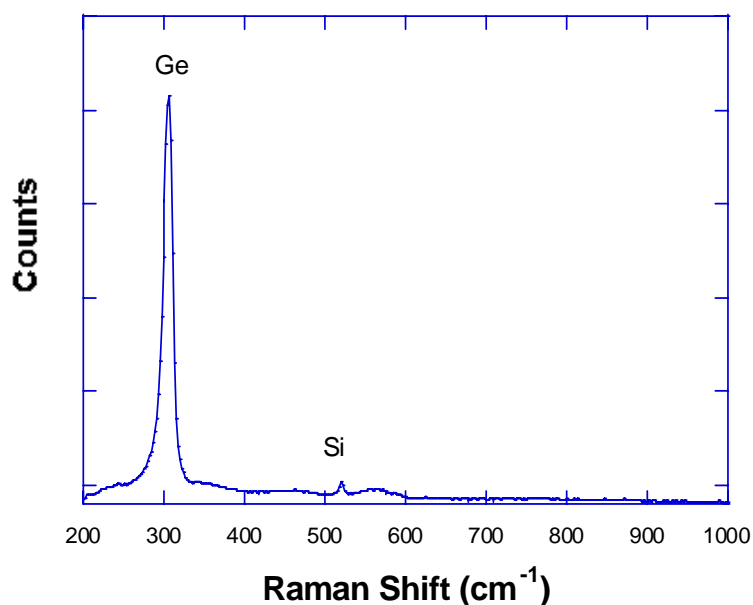


**Figure 40.** Micro-Raman spectrum of Ge NWs with an average diameter of  $\sim 123$  nm showing that there is a sharp Ge-Ge phonon scattering peak at  $307\text{ cm}^{-1}$ , which is consistent with the presence of highly crystallized Ge.

### 3.2.5 High Resolution TEM

High Resolution Transmission Electron Microscopy (HRTEM) is an extremely powerful method to investigate the atomic structure of crystalline materials. It has a very high resolution probe that can be used to obtain lattice images, which is very useful in identifying phases and compositions of these materials. A JEOL JEM-3010 transmission electron microscope (TEM) equipped with a Thermo Noran Vantage XEDS system that has a 15 nm probe at the University of Illinois at Chicago was used to explore the atomic structure and composition of both Ge and Er-doped Ge NWs. A HRTEM image of a Ge NW as shown in Figure 41 indicates that the nanowire is single crystal (for the measured length scale) with a  $d$  spacing of 0.325 nm. This corresponds to the [111] growth direction of the cubic phase of germanium (JCPDS-ICDD PDF # 04-0545). The deviation of  $d$  spacing value is -0.002 nm.

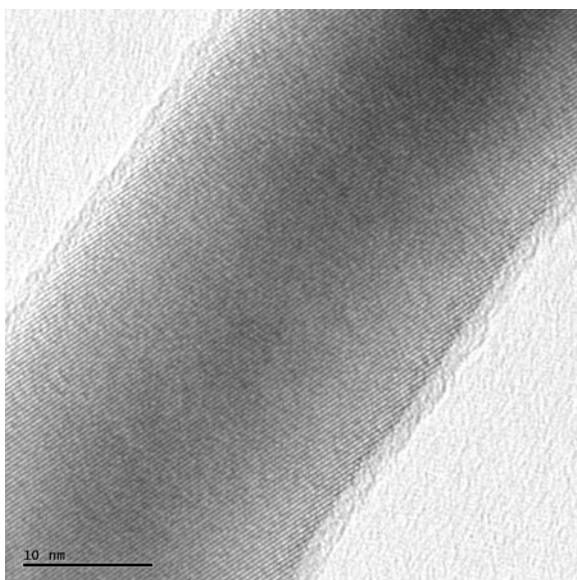


**Figure 41.** HRTEM images of a typical Ge NW showing that it has a  $d$ -spacing value of 0.325 nm corresponding to the [111] growth direction of cubic germanium.

A HRTEM image and compositional analysis (from XEDS) of Er-doped Ge NWs are shown in Figure 42 and Table 3, respectively. Lattice images at atomic resolution carried out on the single wire reveal that the core of the wires consists of crystalline Ge and an ultrathin shell. The measured  $d$ -spacing value 0.333 nm is slightly higher than that of (111) crystal plane of cubic germanium, that is, 0.327 nm. The calculated relative error of  $d$  spacing value is 1.2%. It is notable the relative error of  $d$  spacing value is closely related to the materials, magnifications, and crystal plane spacings.<sup>159</sup> In the case of defect-free crystal, the estimated relative error was reported to be  $\sim 0.5\%$ , and this value can be further reduced using Fourier transform patterns of HREM images.<sup>159</sup> Two distinct regions were found on the wires by quantitative elemental analyses. One is the central region that has a low Er concentration (5.4%), and the other region is at the edge where a higher Er concentration is found (17.9%).

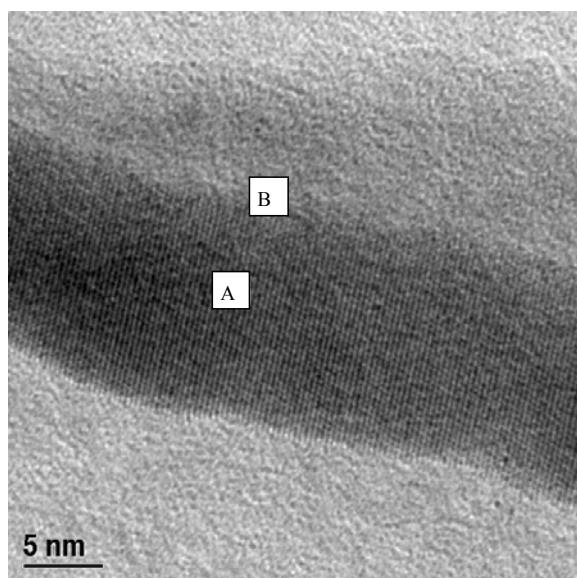


**Figure 42.** HRTEM image of an Er-doped Ge NW showing the core is crystalline with an amorphous shell.

**Table 3.** Atomic concentrations of Ge and Er on the edge and center of a Ge NW

Region	At% Ge	At% Er
A	94.6	5.4
B	82.1	17.9

### 3.2.6 XPS Spectroscopy of Er-Doped Ge NWs

X-ray photoelectron spectroscopy (XPS) is a powerful surface chemical analysis technique that can be used to analyze the chemical composition and electronic state of materials. It can collect spectral information from a depth of 1-10 nm with a maximum detection limit up to 0.1 atom% depending on the materials studied. In XPS, a photon is absorbed by an atom in a molecule or solid, leading to ionization and the emission of a core (inner shell) electron. The energy of a photon is given by the Einstein relation as shown in equation (14):<sup>160</sup>

$$E = h\nu \quad (14)$$

where  $h$  stands for Planck's constant, and  $\nu$  is the frequency of the X-ray radiation employed. Conservation of energy requires that the kinetic energy,  $E_k$  of those photoelectrons is determined by electron binding energy,  $E_b$  and energy of X-ray radiation,  $h\nu$  as given by equation (15):<sup>160</sup>

$$E_k = h\nu - E_b \quad (15)$$

The experimentally measured value of  $E_k$  is given by equation (16):<sup>160</sup>

$$E_k = h\nu - E_b - E_w \quad (16)$$

where  $E_w$  is the work function of the spectrometer. Different elements and an element in different oxidation states have a characteristic set of binding energy peaks in their corresponding photoelectron spectrum, which can be used in determining their electronic states and compositions.

The lack of a distinct visible Er-rich layer (in contrast to Er-doped Si NWs) led us to employ XPS to further probe the interfacial composition and electronic states of these Er-doped Ge NWs. X-ray photoelectron spectroscopy (XPS) was performed ex situ at the University of Texas at Dallas. XPS spectra of Er-doped Ge NWs prepared using a 600 °C doping temperature are shown in Figure 43, which confirms the presence of both Er as well as Ge in the shell of these wires, as evidenced by the characteristic Ge 3d band at 32.29 eV as well as the Er 4d peak observed at 170 eV. The binding energy for the Ge 3d (~32 eV) appears to be consistent with Ge-O bonding. The fact that the entire surface layer appears oxidized (i.e., no “metallic” Ge 3d feature detected at ~28 eV) suggests that the depth sampled by the XPS is fully oxidized. Presumably, the oxidation could occur from the processing and/or the fact that these samples are analyzed ex situ. The Er line shape makes definitive chemical bonding identification difficult: apparently, the spin-orbit splitting is too small to be resolved, but nevertheless consistent with Er-O bonding.<sup>161</sup>

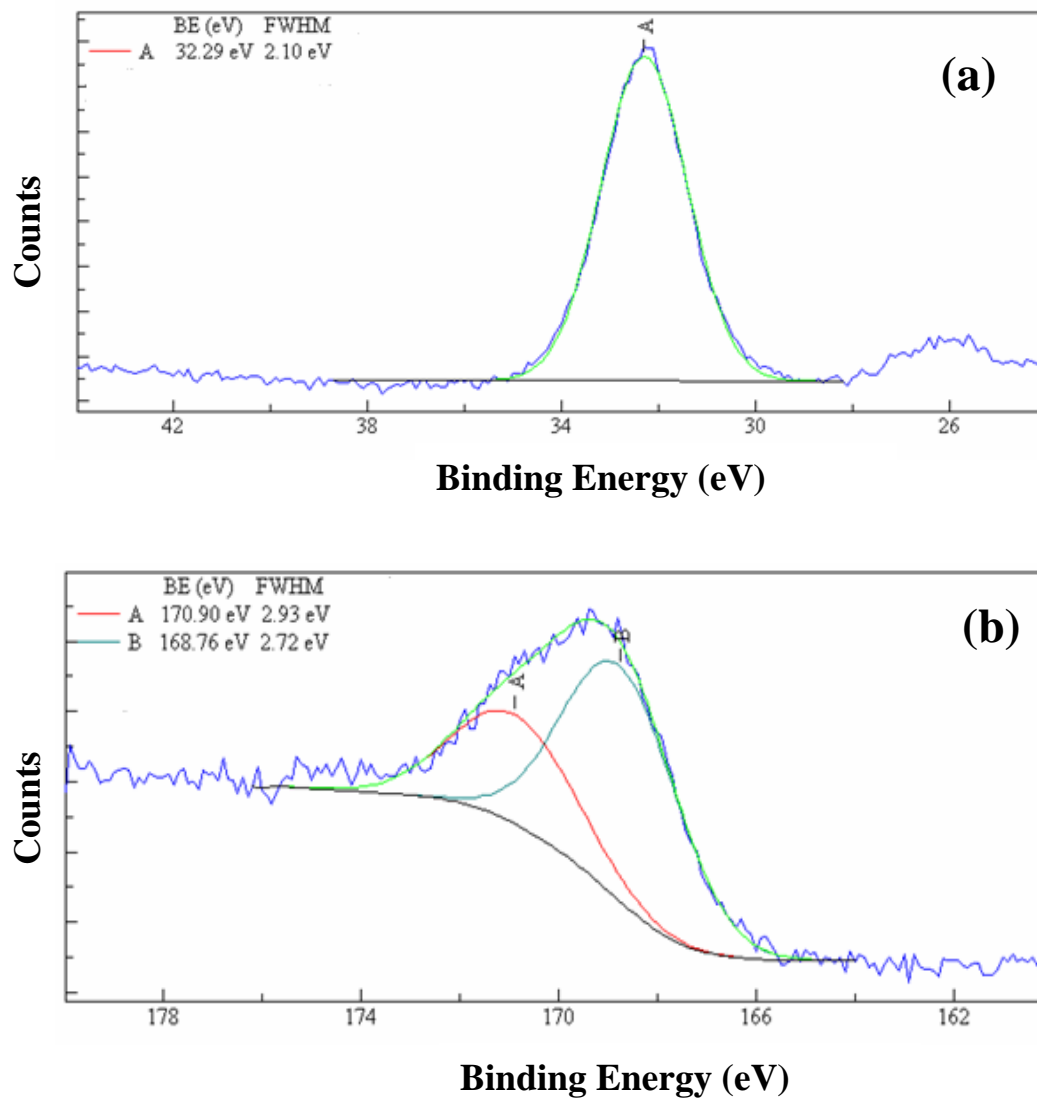


**Figure 43.** XPS spectra confirming the presence of erbium centers in these doped NWs prepared using a 600 °C doping temperature (a) spectral region associated with the Ge 3d; (b) spectral region corresponding to the Er 4d bands.

### 3.2.7 UV-visible Spectroscopy of Er-Doped Ge NWs

The UV-visible absorption spectrum for a typical Er-doped Ge NWs sample that was annealed at 600 °C in air and then suspended in ethylene glycol is shown in Figure 44. The spectrum reveals a broad absorption tail with an onset of absorption near 640 nm. There are two possibilities for the origin of this broad absorption tail. First, while the bandgap of bulk Ge ( $E_b \sim 0.66\text{eV}$  at 300 K) is too low to absorb photons in this wavelength range efficiently, a size reduction of the Ge core after being annealed in air could result in the bandgap widening to facilitate this absorption process. For example, it has been reported that the 1.2 nm thick Ge NW with a (111) orientation has a bandgap as big as 1.6 eV.<sup>162</sup> Secondly, any significant amount of  $\text{GeO}_x$  formed during anneal in air can further assist light absorption in this wavelength range. Depending on how much oxygen is supplied, it should be noted that the optical bandgap of  $\text{GeO}_x$  is tunable from 0.75 to 5 eV,<sup>134,135</sup> and so it is certainly possible that the presence of  $\text{GeO}_x$  leads to the appearance of this absorption tail.

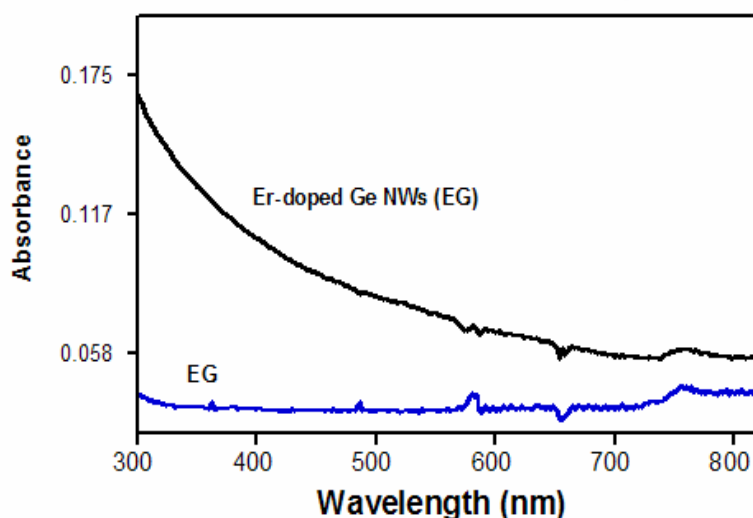


**Figure 44.** UV-visible absorption spectra of Er-doped Ge NWs in ethylene glycol (EG), and ethylene glycol. The sample was prepared using Ge NWs with a mean diameter of  $\sim 123$  nm and annealed at  $600$  °C in air.

### 3.2.8 Near-Infrared Photoluminescence

Figure 45 presents the room-temperature photoluminescence (PL) spectra of Er-doped Ge NWs prepared under different conditions. First, it must be stressed that the as-formed Er-doped Ge NWs do not demonstrate the  $1540$  nm luminescence associated with the ( ${}^4I_{13/2} \rightarrow {}^4I_{15/2}$ ) transition under excitation at  $488$  nm. However, annealing such a sample in air at  $600$  °C results in strong enhancement of PL at  $1540$  nm. Such a result is not surprising given the established need of  $\text{Er}^{3+}$  to possess a local non-centrosymmetric oxygen-rich coordination environment to accommodate optical activity,<sup>163</sup> and it is likely that this oxygen-rich anneal promotes this effect. It is also found that a shorter Er incorporation time (thereby lowering the effective  $\text{Er}^{3+}$  concentration) can help to increase the PL intensity. Shortening the doping time from  $1$  h to  $0.5$  h boosts the PL intensity by more than  $60$  %

(again, see the spectra of Figure 45). Correspondingly, if we attempt to increase the local Er concentration by shifting to a smaller diameter Ge core NW, (reduced from 123 nm to 80 nm on average), the PL intensity will be substantially reduced by more than 60%. These concentration-dependent observations are consistent with previous measurements regarding Er-doped Si nanowires,<sup>80</sup> where a diminished Er<sup>3+</sup> PL signature is noted as the NW core size is reduced. This is presumed to arise as a consequence of greater induced self-quenching by local erbium-erbium interactions in a confined surface shell.

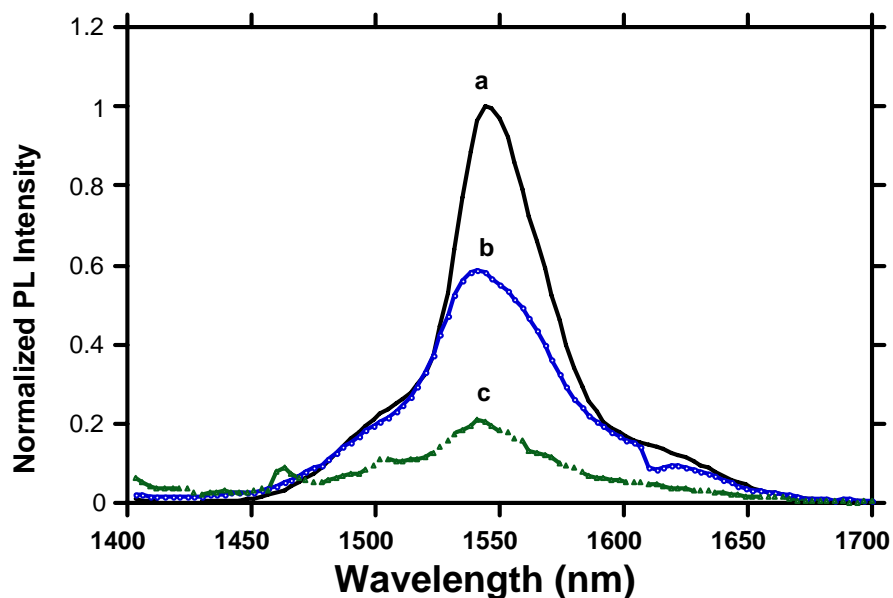


**Figure 45.** Room temperature photoluminescence spectra of Er-doped Ge NWs for samples which have been annealed in air. (a) 123 nm Ge NWs, 30 min Er<sup>3+</sup> exposure. (b) 123 nm Ge NWs, 1 h Er<sup>3+</sup> exposure. (c) 80 nm Ge NWs, 1 h Er<sup>3+</sup> exposure. All spectra were recorded at room temperature using a laser power of 400 mW.

To further understand the mechanism underlying the light emission, excitation wavelength dependence experiments were carried out on Er-doped Ge NWs annealed at 600 °C in air. Figure 46 shows the normalized PL intensity for Er-doped Ge NWs as a function of excitation wavelength. With the exception of 476 nm, a steady diminution of Er<sup>3+</sup> PL intensity is observed with increasing excitation wavelength (in the range of 476-514 nm), suggesting some type of carrier-mediated pathway. It is notable that erbium ions can be excited more efficiently using 488 and 514 nm laser pumps in a direct excitation pathway because erbium ions have maximum absorption at those two wavelengths. In the carrier-mediated pathway, however, the excitation is correlated to the absorption spectrum of sensitizer rather than that of erbium ions as mentioned in Chapter 1.

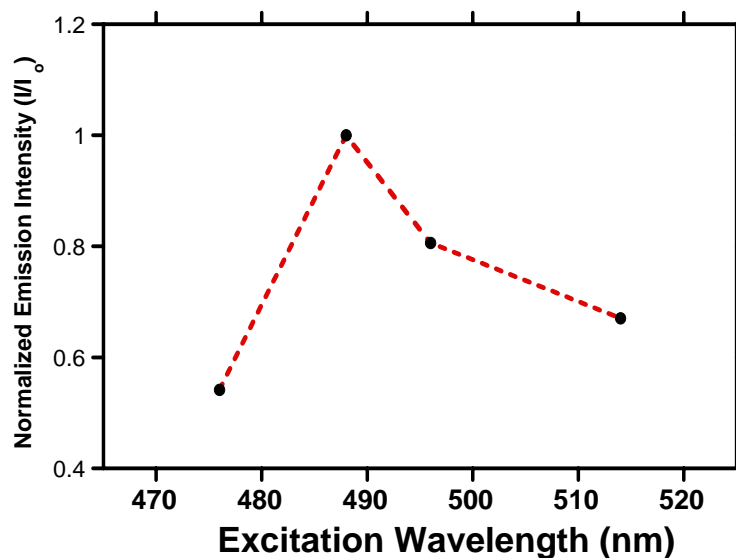


**Figure 46.** Normalized PL intensity for Er-doped Ge NWs annealed at 600 °C in air using various excitation wavelengths ranging from 476-514 nm.

UV/visible absorption spectra of Er-doped Ge NWs suggest that two scenarios are possible for the origin of the near IR light emission. First, while the bandgap of bulk Ge is too low to permit efficient energy transfer to the rare earth centers, some minor size-induced band gap widening could facilitate this effect. More likely, however, and consistent with the experimental conditions employed, is participation of germanium oxide in the process. Germanium oxide is a good host material for  $\text{Er}^{3+}$  because it has a sufficiently high refractive index to allow light propagation, a low phonon energy that is crucial to luminescence efficiency of an Er-doped amplifier,<sup>164</sup> and useful optical transmission in near and middle infrared region of spectrum up to 4.8  $\mu\text{m}$ .<sup>165</sup> Hence after a sufficient thickness of germanium oxide is formed after annealing in air, and a critical density of  $\text{Er}^{3+}$  centers are sufficiently diffused at this interfacial boundary, the PL intensity was significantly increased. Recall that the formation of germanium oxide on the surface of Ge NWs has already been confirmed by our XPS data. Depending on how much oxygen is supplied, the optical band gap of  $\text{GeO}_x$  is tunable from 0.75 to 5 eV,<sup>134,135</sup> and so it is certainly possible that the  $\text{GeO}_x$  carrier-mediated energy transfer excites the relevant  $\text{Er}^{3+}$  centers. The weak PL under vacuum annealing conditions may be caused by short of oxygen for  $\text{Er}^{3+}$  ions to diffuse. The lack of photoluminescence of the as-formed sample can be attributed to the Er-Er cross relaxation due to high concentration of  $\text{Er}^{3+}$  ions on the surface before annealing, or the presence of a non-optically active coordination environment.

### 3.3 Summary

In summary, Er/Ge core-shell nanowires were synthesized successfully via a simple vapor transport method. The basic building block, Ge NWs with different diameters, can be prepared by varying the helium flow rate and reaction time, and the addition of carbon can greatly increase the Ge vapor supply at a given temperature. TEM images show that gold catalyst islands can be found on the tip of Ge NW, which implies that the NWs grow through a VLS synthetic route. As-formed Ge NWs are single crystals possessing an (111) orientation, which is confirmed by both SAED and HREM characterization data. Analyses of the doped NWs via TEM, SEM, SAED, XEDS and XPS show that the core of the nanowires is composed of crystalline Ge with Er mostly distributed on the shell. After an initial high temperature anneal in air, thicker wires, lower pyrolysis temperatures and shorter Er<sup>3+</sup> incorporation times are beneficial to increasing the PL intensity at 1540 nm. UV-visible absorption spectroscopy shows that those annealed NWs can absorb light ranging from 300 to 600 nm due presumably to the presence of GeO<sub>x</sub>. Additional effort is likely required, however, to permit a detailed understanding of the luminescence mechanism of these structures and in the long term, fabricate more complex nanowire compositions.

*CHAPTER IV.*

The Impact of Erbium Incorporation on the Structure and  
Photophysics of Silicon-Germanium Nanowires

## 4.0 Overview

Silicon-Germanium (SiGe) alloys are currently of great interest due to their extensive applications in the fields of microelectronics and microoptoelectronics.<sup>36</sup> A number of applications are envisioned as a consequence of their useful properties as described in Chapter 1: microwave and millimeter-wave applications;<sup>141</sup> quantum cascade terahertz lasers;<sup>166,167</sup> and enhanced p-type field-effect transistors (FETs).<sup>168,169</sup> As a strategy toward the bottom-up fabrication of silicon-compatible 1.54  $\mu\text{m}$  light emitters, waveguides, and detector building blocks, our group has explored the preparation and optical properties of  $\text{Er}^{3+}$ -doped Si nanocrystals (NCs) as well as  $\text{Er}^{3+}$ -surface enriched Si and Ge NWs, which are described in the previous chapters. Compared with Ge NWs, SiGe alloy NWs possess two pointed advantages: (1) tunable band gaps and (2) stable surface structures. Tunable band gaps could be utilized to excite  $\text{Er}^{3+}$  ions more efficiently via an energy resonance, and stable surface structures will greatly enhance the performance reliability of any future devices. As a fundamental step to evaluate the merit of SiGe alloy as potential building blocks for nanoscale optoelectronic devices, one-dimensional (1-D) Er-doped SiGe nanowires (NWs) are fabricated herein.

In this chapter, we report multi-step processes for the fabrication of  $\text{Er}^{3+}$ -doped SiGe NWs and characterization of their optical properties. Three different alloyed architectures are obtained by altering the deposition sequence of Si and  $\text{Er}^{3+}$  on a Ge NW core; after each unique sequence, alloying is obtained by thermal annealing at elevated temperatures. These sequences include: (1) the co-deposition of Si and  $\text{Er}^{3+}$  on top of the Ge core; (2) the introduction of an  $\text{Er}^{3+}$  layer between the Ge and Si layers (a sandwich structure); (3) the

deposition of Si onto the Ge NW core, followed by an Er<sup>3+</sup>-rich layer on its outermost surface. The structure of products obtained from these reactions are interpreted considering the role of erbium altering the diffusion between the Ge and Si layers and the subsequent impact of thermal treatment on erbium light emission. A combination of electron microscopies – TEM, HRTEM, conventional SEM, field emission SEM (FE SEM), in concert with energy dispersive probe mapping and Raman microanalyses - are used for this purpose. The Er coordination environment, a crucial influence to luminescence intensity, was determined by EXAFS.

## 4.1 Experimental

### 4.1.1 Er<sup>3+</sup>-Doped SiGe NWs Synthesis

The overall synthetic strategy for Er<sup>3+</sup>-doped SiGe NWs is illustrated in Figure 47. Each type of doped NW structure is based on a Ge core NW fabricated by a simple vapor-transport method as described in Chapter 3.<sup>137</sup> To describe briefly, a mixture of carbon (J. T. Baker) and germanium powder (Strem) with a C/Ge molar ratio of 3:1 was loaded into an alumina boat and then placed in a quartz tube reactor. A 5 × 8 mm<sup>2</sup> piece of a Si wafer covered with a 12 nm thermally evaporated Au film was placed in another alumina boat that was positioned 3 cm from the edge of the oven. The ceramic oven (30 cm in length) was heated at 850 °C for 2h, and then at 1000 °C for 1.5 h under a 3000 sccm helium (Praxair, UHP grade) flow. Upon completion of the reaction, a thick brown fluffy film can be easily seen on the wafer. The average yield of the Ge NWs is about 0.3 mg. In all experiments involving Si and Er deposition the Ge nanowires must be used immediately in the next step of fabrication to avoid surface oxidation, which will result in rough and bumpy morphologies of the added Si/Er layers.

In the second step, three different permutations involving deposition of Er<sup>3+</sup> and Si on the Ge core NWs were employed to make three structurally unique nanostructures. Route 1 is the simultaneous co-deposition of Si and Er<sup>3+</sup> on top of the Ge core. Route 2 is the initial deposition of Er<sup>3+</sup> ions on top of Ge core, and then a layer of Si is deposited subsequently on the Er<sup>3+</sup> layer using SiH<sub>4</sub> as precursor. Route 3 is the deposition of Si on top of Ge core with a final exposure of Er<sup>3+</sup> ions deposited on the outermost NW surface coating. The Si atoms were obtained via the pyrolysis at 500 °C of 0.5% silane diluted in helium (Voltaix) flowing

at 4.0 sccm and further diluted by 3000 sccm helium (Praxair, UHP grade). The  $\text{Er}^{3+}$  atoms were obtained from  $\text{Er}(\text{tmhd})_3$  vapor (Strem).  $\text{Er}(\text{tmhd})_3$  was heated to 145 °C in a bubbler, and its vapor was carried downstream by 3000 sccm of helium (Praxair, UHP grade) to the pyrolysis oven operating at 500 °C.

### Synthetic Routes to Er-doped SiGe NWs

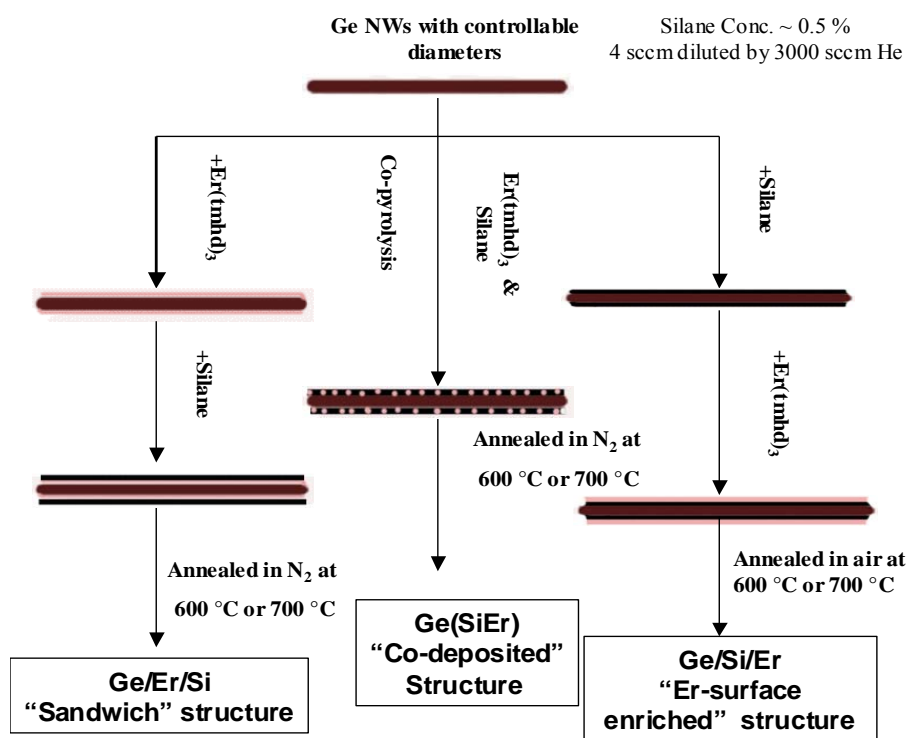


**Figure 47.** General synthetic routes to Er-doped SiGe NWs.

The resultant resulting Si/Er coated Ge NWs were annealed in a  $\text{N}_2$  atmosphere or in air. The reactor design for preparing Ge NWs is described in Chapter 3, and the one for fabricating Er-doped SiGe NWs is illustrated in Figure 48. Buffered-HF Improved (Transene, Inc., AR grade) was employed to etch away the oxide shell of the ‘co-deposited Si&Er’ NWs.

The etching time is 5 minutes, and the etched NWs were rinsed with 2-propanol for several times, and dried in air before measuring their photoluminescence.

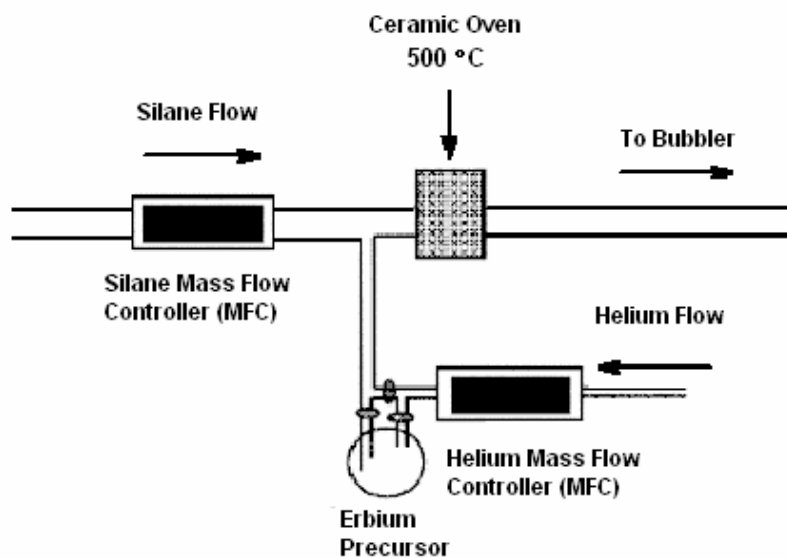


**Figure 48.** Reactor design for fabricating Er-doped SiGe NWs.

#### 4.1.2 Instrumentation

Structural characterization of all samples was performed using a JEOL JEM-2010F field emission transmission electron microscope (TEM) at the University of Illinois-Chicago, which can also be used to obtain high resolution TEM images. The TEM operates both in transmission and scanning transmission modes. A probe size of 1 nm was used for both point analysis and XEDS linescan across the nanowires. Specimens for TEM characterization were prepared by dispersing the sample with a 10  $\mu$ L drop of 2-propanol and then placing the drop onto a grid. XEDS analyses of macroscopic nanowire samples were performed using a JEOL JSM-6100 SEM at Texas Christian University. Low resolution ( $\pm 4$  nm) near-IR photoluminescence (PL) spectra were obtained using the system described in Chapter 3.

Raman spectra were recorded using a Raman micro-imaging system located in the laboratory of Prof. Zerda at the Physics Department of TCU (as described in Chapter 3). Extended X-ray absorption spectroscopy (EXAFS) at the Er L3 edge was performed at the XAS beamline of the Brazilian National Synchrotron Light Laboratory (LNLS) storage ring at Campinas, SP, Brazil. X-ray absorption was measured by fluorescence with a N<sub>2</sub> cooled Canberra SL 30165 Si(Li) detector and standard photon counting techniques with the samples kept at room temperature. Sample of bulk Er<sub>2</sub>O<sub>3</sub> was used as reference standard for determining coordination number and bond lengths of Er-O.

## 4.2 Results

### 4.2.1 Structural Characterization of the 3 Different NW Permutations

The 3 different types of Er-doped SiGe NWs were structurally characterized using SEM, TEM, HRTEM, and XEDS spectroscopy. Usually, the starting materials, Ge NWs have an average diameter of  $\sim 123$  nm. The structures of these NWs will be described separately in this section.

#### 4.2.1.1 'Sandwich' Structure

Figure 49 shows an SEM image, TEM image, XEDS spectra and XEDS linescans of 'sandwich' structure Er<sup>3+</sup>-doped SiGe NWs prepared by depositing 1 h erbium precursor and 1 h Si (silane) on Ge core NWs. A SEM image of as-prepared Er-doped SiGe NWs reveals a dense film of NWs with lengths of up to several tens of microns and an average diameter of  $\sim 196 \pm 28$  nm. XEDS analysis of a macroscopic (i.e. microns) area confirms that the NWs are composed primarily of Si and Ge with a relatively small percentage of Er, where the Ge-L, Er-M and Si-K peaks are located at 1.2, 1.4 and 1.7 KeV, respectively. The TEM image of NWs annealed for 1 h at 600 °C in N<sub>2</sub> shows a dark 30 nm heavier core and a lighter 15 nm shell. The difference in contrast originates from the changes in atomic numbers of the constituent elements.

XEDS linescanning analysis using a probe size of 1 nm was used to investigate the elemental distribution of Si, Ge, Er and O across a single NW. The XEDS linescans of an individual NW show that the dark core is Ge-rich, and the light-contrast shell is predominantly composed of Si and some O (not shown). Germanium can also be found in the

outer shell near the core/shell interface. According to literature reports, significant amounts of Ge can diffuse into polycrystalline Si at elevated temperatures ranging from 800 °C to 900 °C along the grain boundaries;<sup>170</sup> the diffusivity of Ge in polycrystalline silicon is also considerably higher than that for single-crystal silicon, which is a closer analogy to our samples. The Er concentration is almost constant throughout the SiGe core with only a slightly higher value at the interface between the core and the shell. There is no detectable Er in the outer silicon shell.

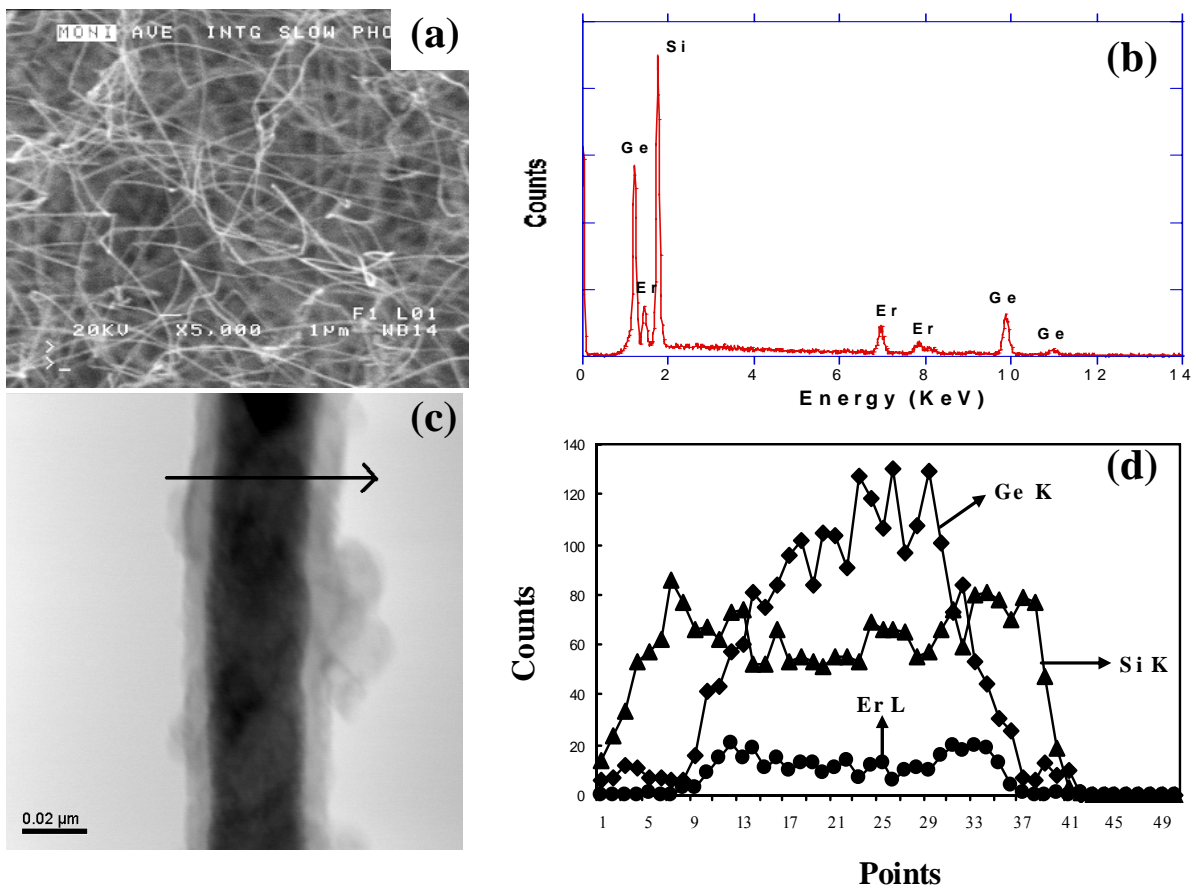


**Figure 49.** (a) SEM image of the “Sandwich” structure  $\text{Er}^{3+}$ -doped SiGe NWs. (b) Macroscopic XEDS spectrum of the NWs. (c) TEM image of a typical NW with a  $\sim 30$  nm SiGe core and a  $\sim 15$  nm amorphous  $\text{SiO}_2$  shell (XEDS confirms O-rich surface). (d) XEDS linescans of the NW shown in (b) suggest that an average loading of  $\sim 2\%$   $\text{Er}^{3+}$  is present in the center of the NWs.

Figure 50 presents the high-angle annular dark field (HAADF) TEM image of an individual “Sandwich” structure  $\text{Er}^{3+}$ -doped SiGe NWs annealed at  $600^\circ\text{C}$  for 1 h in  $\text{N}_2$ . The image contrast in HAADF TEM is much more sensitive to the atomic mass than that in conventional bright field TEM, where heavier elements contribute to brighter contrast. It is

noteworthy that most heavy elements are concentrated in the core. Table 4 shows the quantitative XEDS analyses of 3 points shown in Figure 50, which indicates that there are three distinct regions on the nanowires. One is the center of the NW that has a lower Er concentration (2.6 %); another region is located at the interface between the bright shell and the dark core, which has a higher Er concentration (6.7 %); the third one is the flaky shell, with negligible Er present. This result is interpreted in terms of a preferential diffusion of erbium into the crystalline SiGe core instead of the amorphous silica shell. Very similar results were derived from other linescans across the NWs.

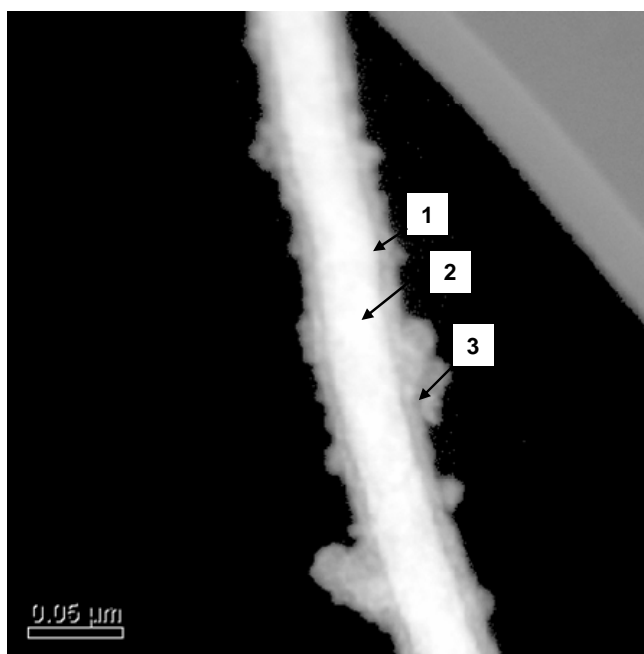


**Figure 50.** High-angle annular dark field (HAADF) TEM image of an individual “Sandwich” structure  $\text{Er}^{3+}$ -doped SiGe NWs annealed at 600 °C for 1 h in  $\text{N}_2$ .

**Table 4.** Quantitative XEDS analyses of 3 points shown in Figure 50 indicating that there are three distinct regions on the nanowire.

<b>Label</b>	<b>at% Si</b>	<b>at% Ge</b>	<b>at% Er</b>
Point 1	50.3	43.0	6.7
Point 2	21.0	76.4	2.6
Point 3	91.7	8.3	0

These compositional analyses have been complemented by high-resolution TEM (HRTEM) imaging. Figure 51 shows a typical HRTEM image confirming the presence of lattice fringes across the core and an amorphous shell. The determined interplanar spacing of 1.99 Å is consistent with a SiGe crystalline alloy rather than the original Ge core. A stoichiometry of  $\text{Si}_{0.13}\text{Ge}_{0.87}$  for the core was calculated using a linear interpolation method based on a d-spacing of 1.99 Å (1.92 Å of Si (220), JCPDS-ICDD PDF No. 27-1402; 2.00 Å of Ge (220), JCPDS-ICDD PDF No. 04-0545). Recall in Chapter 3 that the relative error of HRTEM measurements can be as high as  $\pm 0.02$  Å.

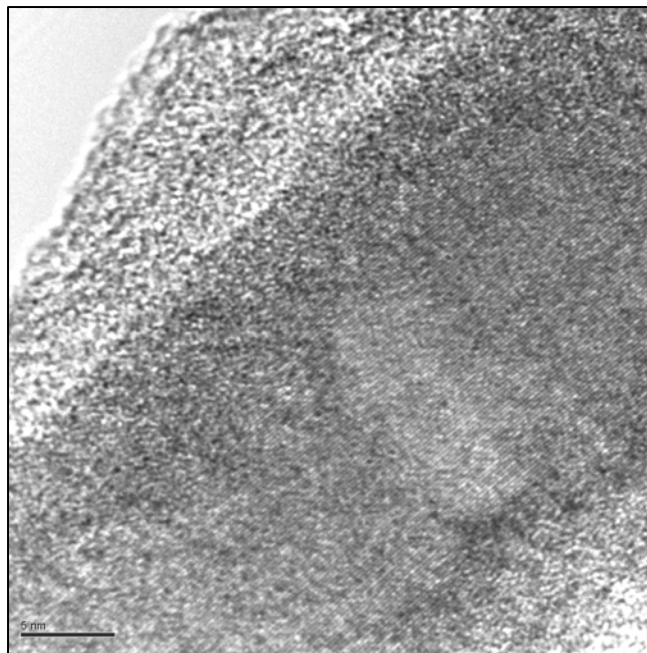


**Figure 51.** HRTEM image of “Sandwich” structure  $\text{Er}^{3+}$ -doped SiGe NWs annealed at 600 °C for 1 h shows the core is crystalline  $\text{Si}_{0.13}\text{Ge}_{0.87}$  with a d-spacing of 1.99 Å and the shell is amorphous (Scale bar = 5 nm).

#### 4.2.1.2 ‘Er-Surface Enriched’ SiGe Structure

Figure 52 shows the SEM, TEM images and XEDS spectra of ‘Er-surface enriched’ SiGe NWs that were prepared using a silane exposure time of 10 minutes and Er precursor deposition time of 1 h. It is noteworthy that very thick Si-rich SiGe wires (400 nm on average) were produced using the same fabrication conditions as that of ‘Sandwich’ NWs, which are not emissive at 1540 nm, as described later in this chapter. Therefore, the fabrication conditions were varied to reduce the relative concentration of Si in these wires. A SEM image of these nanowires demonstrates that ‘Er-surface enriched’ SiGe NWs with an average diameter of  $\sim 175 \pm 25$  nm can be fabricated successfully by this route with a relatively high

yield and long aspect ratio. A macroscopic XEDS analysis of the nanowires suggests that this sample has a higher concentration of Ge and lower ratio of Si and Er relative to those of the 'sandwich' NWs shown in Figure 49. A TEM image of a typical NW annealed at 600 °C in air shows that diameter of the NW is ~40 nm and the core is only ~15 nm due to the extent of oxidation of the sample. Similarly, the oxidized shell contributes to the difference in diameter measured by TEM and SEM. Combined with its concurrent TEM image, XEDS linescans of the NW (Figure 52d) indicate that Ge and Si can diffuse into each other, and the lighter shell is mainly composed of Er and Si. A considerable amount of oxygen is also present in this sample due to the oxidation that occurred during the annealing process.

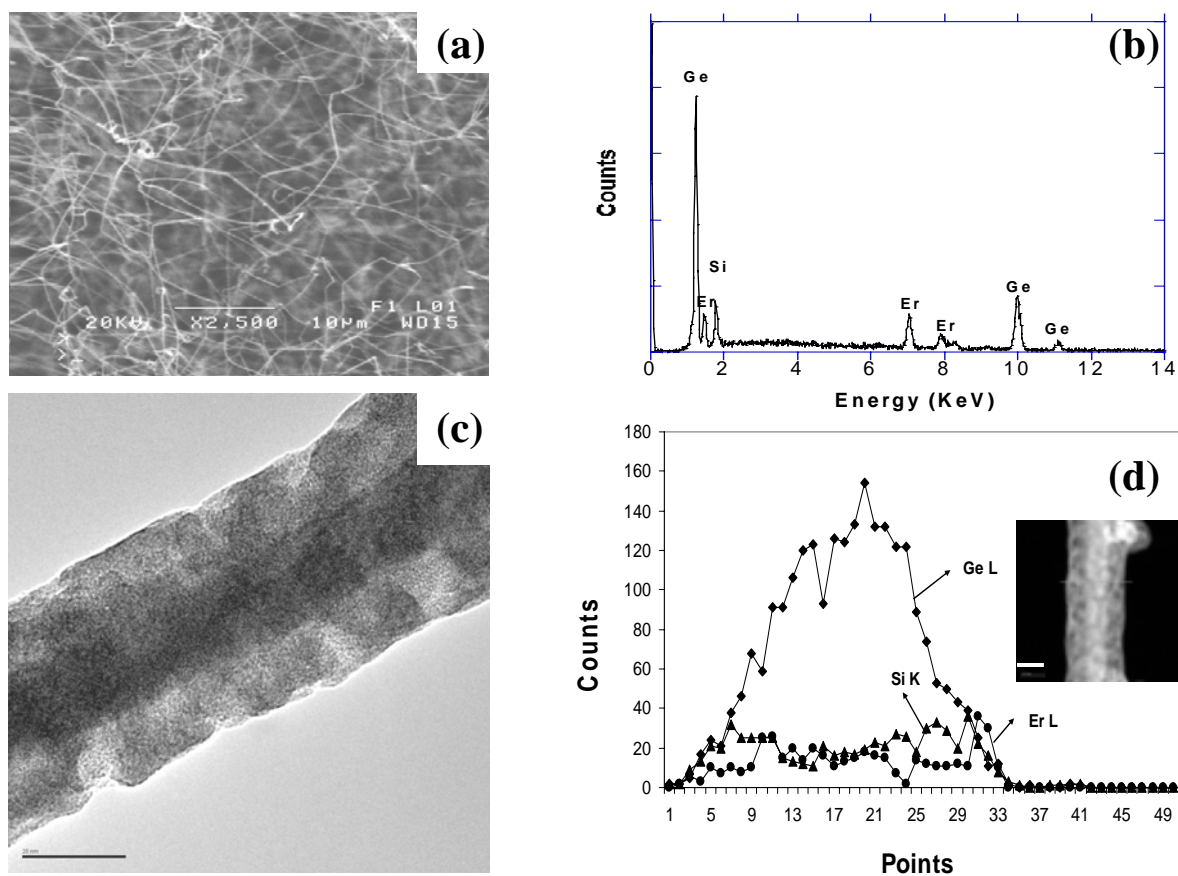


**Figure 52.** (a) SEM image of “Er-surface Enriched” SiGe NWs; (b) XEDS spectrum of the NWs; (c) TEM image of a typical NW shows that the diameter is  $\sim 40$  nm and the core is  $\sim 15$  nm (scale bar = 20 nm); (d) XEDS linescans of the NW shown in the inset suggest that an average loading of  $\sim 6\%$   $\text{Er}^{3+}$  is present in the center of the NWs (scale bar = 20 nm).

Figure 53 presents the HAADF TEM image of “Er-surface Enriched” SiGe NWs, and Table 5 shows the quantitative XEDS analysis of the two points shown in Figure 53. In terms of erbium concentration, two distinct regions were found on the wires: one is the central core region with a low Er concentration ( $\sim 6\%$ ), and the other region is at the edge with a much

higher Er concentration (21%). The surface layer seems to be unstable and can be easily damaged by the electron beam during scanning.

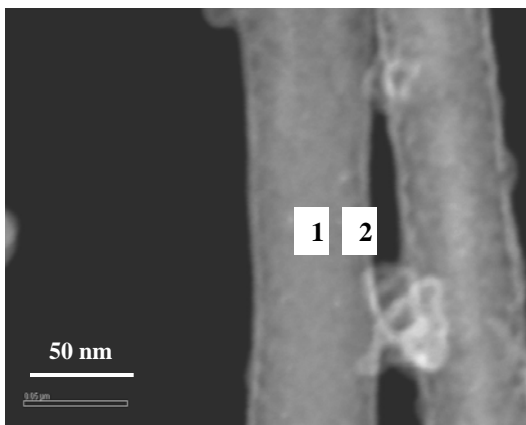


**Figure 53.** HAADF TEM images “Er-surface Enriched” SiGe NWs annealed at 600 °C for 1 h in air. XEDS analyses were performed on the two points as shown by the 2 arrows (scale bar = 50 nm).

**Table 5.** Quantitative XEDS analyses of 2 points shown in Figure 53 indicating that there are two distinct regions on the nanowire.

at %	Si	Ge	Er
Point 1	31.0	62.8	6.5
Point 2	33.0	46.0	21.0

A HRTEM image of a ‘Er-surface enriched’ SiGe NW shown in Figure 54a confirms this amorphous character of the shell, along with a crystalline core with a d-spacing of 3.19 Å

that corresponds to the (111) orientation of  $\text{Si}_{0.6}\text{Ge}_{0.4}$  (3.14 Å of Si (111), JCPDS-ICDD PDF No. 27-1402; 3.25 Å of Ge (111), JCPDS-ICDD PDF No. 04-0545). The HRTEM image of another nanowire shown in Figure 54b from this sample indicates that there is epitaxial growth of Si on the boundary of the crystalline core, since the lattice constant of that region, 3.15 Å, is very close to 3.14 Å of Si (111) (JCPDS-ICDD PDF No. 27-1402).

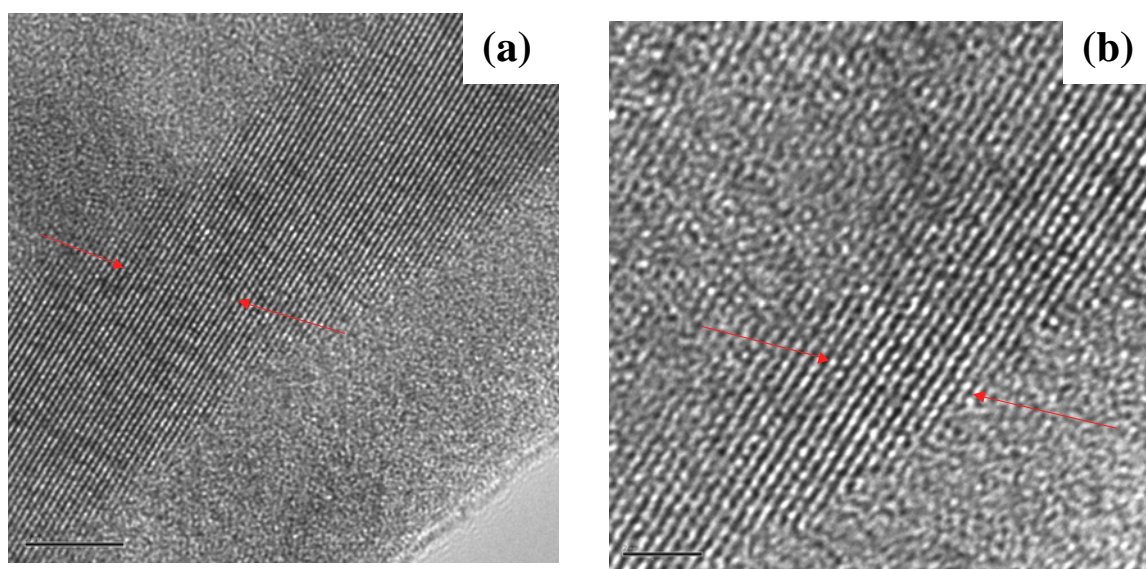


**Figure 54.** (a) HRTEM image of a “Er-surface enriched” SiGe NW annealed at 600 °C in air for 1 h shows that the crystalline core has a d-spacing of 3.19 Å. (b) HRTEM image of another NW indicates that there is epitaxial growth of Si on the boundary of the crystalline core, since the lattice constant is 3.15 Å that is very close to that of Si (111) (3.14 Å) (JCPDS-ICDD PDF No. 27-1402). Note: Scale bar = 5 nm in both images.

#### 4.2.1.3 ‘co-deposited Si&Er’ Ge Core Structure

A SEM image of the “co-deposited Si&Er” Ge nanowires (Figure 55a) presents structures with an average diameter of  $\sim 149 \pm 13$  nm that were fabricated by this process.

The associated XEDS spectrum (Figure 55b) indicates that this sample has a higher concentration of Er compared with the other two types of NWs due presumably to the enhanced solubility of Er initiated by this co-deposition method. TEM images (Figure 55c) show that this type of NW possesses a relatively smoother surface and a uniform diameter relative to those of the other two types of NWs. From the image contrast shown, it is difficult to distinguish the core from the shell. However, XEDS linescans (Figure 55d) of a given NW suggests that major components in the core are Ge and Si, with the shell possessing higher concentrations of Si and Er (~23 at. %). It would appear that Ge cannot diffuse into the shell easily under these conditions, which is reflected in the much lower signal associated with Ge outside of the core. In this case, the scanned nanowire was damaged by the electron beam irradiation presumably due to the presence of amorphous silica on the surface.<sup>171</sup>

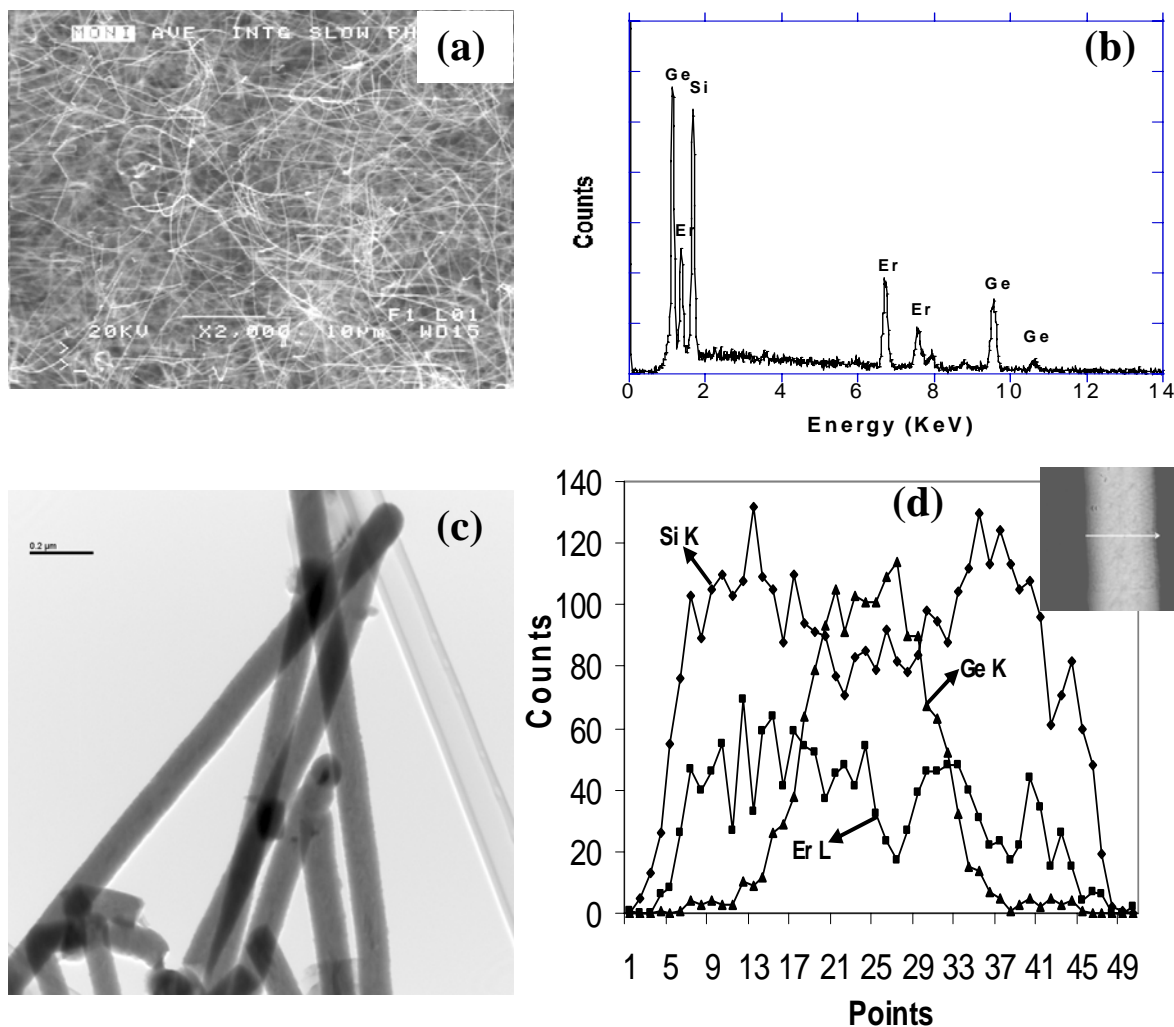


**Figure 55.** (a) SEM image of the “co-deposited Er&Si” Ge core NWs. (b) XEDS spectrum of the NWs shows the concentration of Er&Si is higher than that of “Sandwich” NW under similar preparation conditions. (c) TEM image of the NWs shows that the morphology of the NWs is smooth and uniform with thicker diameter than those of the other two NWs. (d) XEDS line scans of the NW shown in the inset indicates that the NW has a Ge-rich core and a Si&Er rich shell.

Figure 56 is the XEDS map of a  $\sim 50$  nm “co-deposited Er&Si” Ge core NWs, from which the Ge-rich core and Er & Si-rich shell can be clearly seen. The ‘bump’ on the mapped wire was likely caused by the recrystallization of the Ge NWs during the high temperature post-fabrication annealing process to enhance the photoluminescence intensity of the NWs. This XEDS map also confirms that the composition of the ‘bump’ is very similar to that of the straight part of the NW.

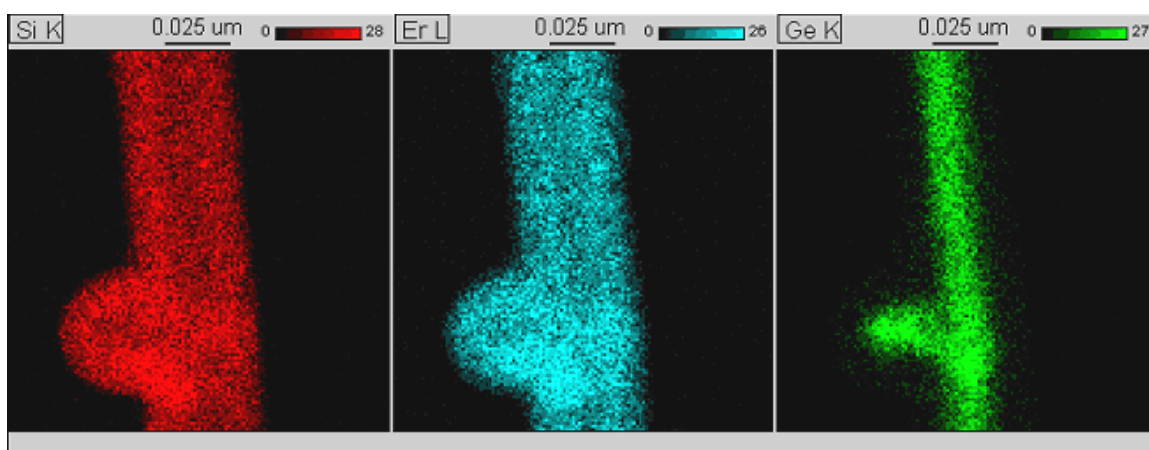


**Figure 56.** Elemental mapping of a single “co-deposited Er&Si” Ge core NW also shows that the core is Ge-rich and the Si&Er distribute uniformly on the core.

There are two distinct crystalline regions on the ‘co-deposited Si&Er’ NW, which are marked as areas 1 and 2 on the HRTEM image of the NWs annealed at 700 °C (Figure 57). One region (marked as 1) has a lattice constant of 3.19 Å corresponding to the (111) orientation of  $\text{Si}_{0.45}\text{Ge}_{0.55}$ . Another small region (marked as 2) has a lattice constant of 2.79 Å consistent with that of the (321) orientation of cubic  $\text{Er}_2\text{O}_3$  (2.82 Å, JCPDS-ICDD PDF No. 08-0050). This phenomenon appears presumably as the consequence of higher concentration of Er on the surface of the NW and the presence of adequate oxygen during the annealing

process. The outmost edge of the NW is amorphous with a width of ~5 nm, judging from the HRTEM image.

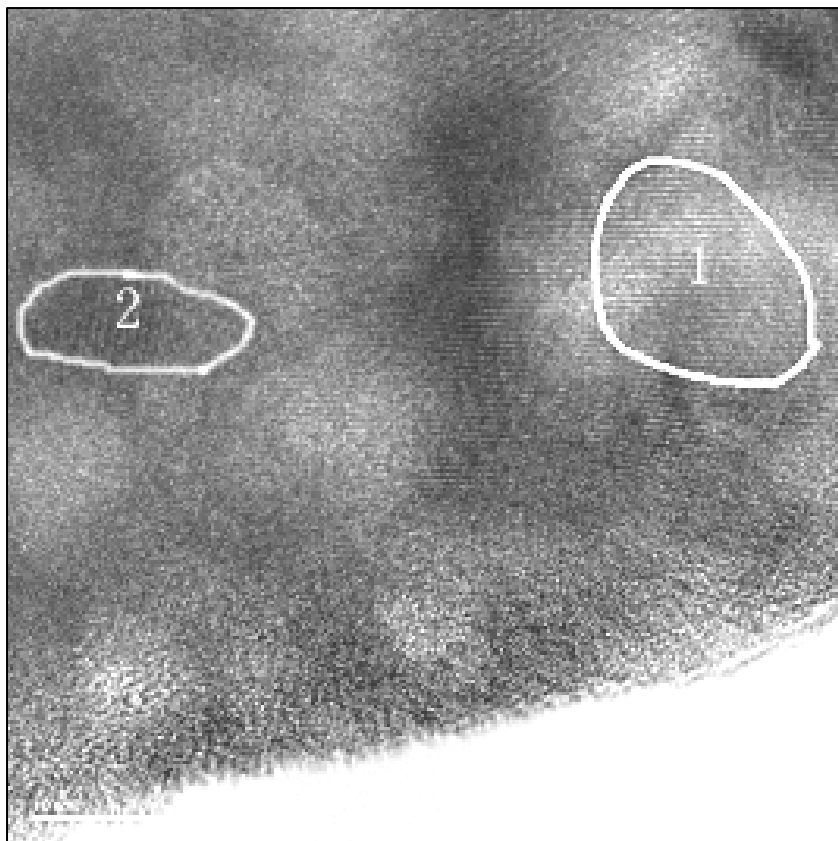


**Figure 57.** HRTEM of the NW (Most region on the NW (area 1) has a lattice constant of 3.19 Å corresponding to (111) orientation  $\text{Si}_{0.45}\text{Ge}_{0.55}$ , but some place (area 2) has a lattice constant of 2.79 Å close to that of (321) orientation cubic  $\text{Er}_2\text{O}_3$  (2.82 Å).

### 4.2.2 Micro-Raman Spectroscopy

The above nanowire samples were annealed at 600 °C or 700 °C in N<sub>2</sub> for 1 h. The evolution of crystallinity can be probed by Raman spectroscopy. In the crystalline random Si<sub>1-x</sub>Ge<sub>x</sub> system the peak position of the Ge-Ge optical phonon shifts linearly from 281 cm<sup>-1</sup> to 300 cm<sup>-1</sup> with increasing Ge mole fraction x.<sup>172</sup> At the same time, the Si-Si Raman-active mode decreases from 521 cm<sup>-1</sup> to 453 cm<sup>-1</sup>; the composition dependence of the corresponding Si-Ge peak position has been shown to fit the following polynomial equation (17):<sup>173</sup>

$$\nu(\text{Si-Ge}) (\text{cm}^{-1}) = 400.0 + 22.07x - 36.14x^2 + 83.73x^3 - 88.54x^4 \quad (17)$$

#### 4.2.2.1 'Sandwich' Structure

The Raman spectra of 'Sandwich' Structure Er-doped SiGe NWs annealed at 600 °C and 700 °C are shown in Figure 58. The spectrum obtained from a sample annealed at 600 °C has a strong peak at 295 cm<sup>-1</sup>, attributed to the phonon scattering associated with Ge-Ge vibrations. There are two other very weak broad peaks appearing at 387 cm<sup>-1</sup> and 494 cm<sup>-1</sup>, which are assigned to the phonon scattering of the Si-Ge and Si-Si vibrations, respectively. Use of equation 17 above leads to a Ge concentration of ~ 96%, which is close to the value derived from a HREM analysis (Si<sub>0.13</sub>Ge<sub>0.87</sub>) for NWs annealed at 600 °C. Upon annealing at 700 °C, the Ge-Ge peak remains at 295 cm<sup>-1</sup> but the Ge-Si and Si-Si peaks become sharper and shift to 392 cm<sup>-1</sup> and 483 cm<sup>-1</sup> respectively. The corresponding concentration of Ge is ~91% according to the above equation, which is somewhat consistent with an enhancement of the alloying process at higher temperatures. The intensity of the Si-Ge and Si-Si peaks also

increase as the result of higher temperature annealing that is helpful in relaxing strain and improving crystallinity in the sample.<sup>174</sup>

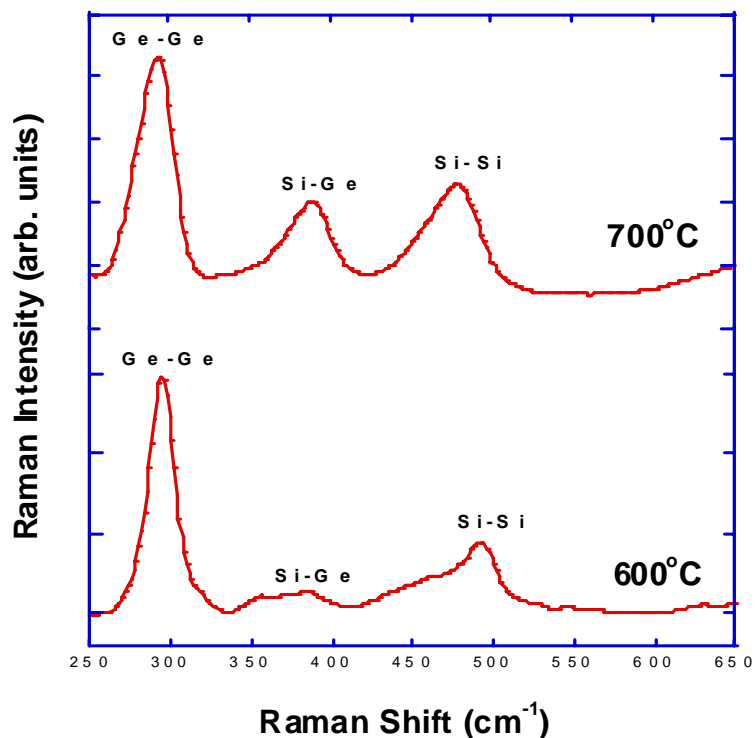


**Figure 58.** Raman spectra of the ‘Sandwich’ Structure Er-doped SiGe NWs annealed at 600 °C and 700 °C in N<sub>2</sub> for 1 h suggests that SiGe alloy is formed at 600 °C and highly crystalline SiGe alloy is obtained at 700 °C.

#### 4.2.2.2 ‘Er-Surface Enriched’ SiGe Structure

Raman spectra measured from this type of nanowire sample annealed at 600 °C and 700 °C in N<sub>2</sub> are shown in Figure 59. For the sample annealed at 600 °C, Ge-Ge, Si-Ge, and Si-Si phonon scattering peaks appear at 301, 394, and 497 cm<sup>-1</sup>, respectively, whereas the Si-Ge Raman shift of the NWs annealed at 700 °C appears at 407 cm<sup>-1</sup>. Calculated according to

the same equation above, the concentrations of Ge in the SiGe alloys are 90% and 50% for the NWs annealed at 600 °C and 700 °C, respectively. However, the above HRTEM data suggest that the concentration of Ge in the NWs annealed at 600 °C is 40%, due presumably to the heterogeneous structures of these wires. It is again reasonable to expect that a higher temperature is beneficial to forming an alloy between Si and Ge, and due to the lack of Er impurity barrier inserted between the Si shell and the Ge core in the case of ‘Sandwich’ NWs, more Si can diffuse into Ge core matrix to form alloys with higher concentration of Si for this type of NW.

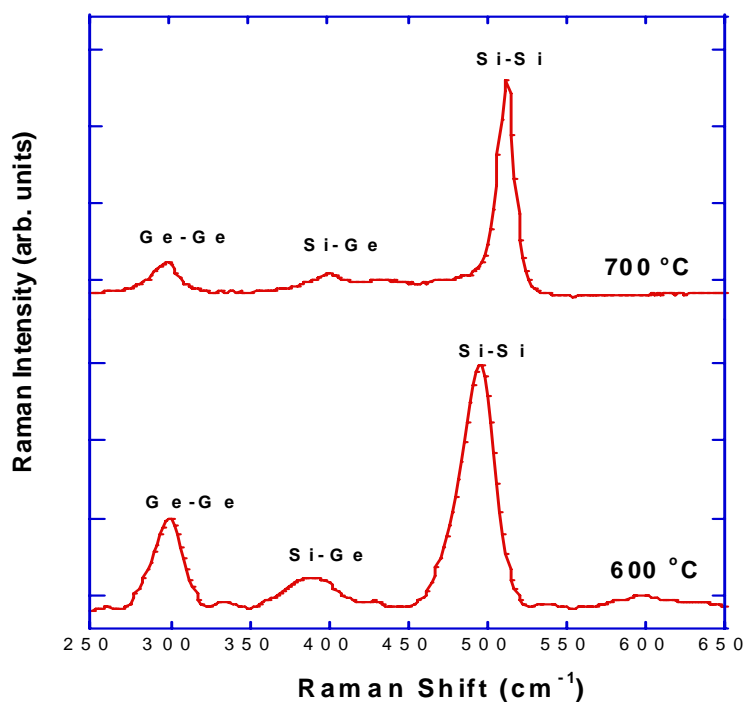


**Figure 59.** Raman spectra of ‘Er-Surface Enriched’ SiGe NWs annealed at 600 °C and 700 °C in N<sub>2</sub> for 1 h shows that Si-Ge phonon scattering peak shifts towards higher wavenumbers when the annealing temperature is increased.

#### 4.2.2.3 ‘co-deposited Si&Er’ Ge Core Structure

Raman spectra of the “co-deposited Si&Er” Ge core NWs annealed at 600 °C and 700 °C in N<sub>2</sub> for 1 h are shown Figure 60. For this type of sample, the extent of alloying is very sensitive to annealing temperature, as reflected in analysis by Raman spectroscopy. For the sample annealed at 600 °C in N<sub>2</sub>, only the Ge-Ge phonon scattering peak at 294 cm<sup>-1</sup> is obtained, inferring that the SiGe phase is either amorphous or not formed at all under these conditions. This is in stark contrast to NWs annealed at 700 °C in N<sub>2</sub> demonstrating a broad peak ranging from 280 cm<sup>-1</sup> to 400 cm<sup>-1</sup>; such a feature presumably originates from the heterogeneous Si<sub>1-x</sub>Ge<sub>x</sub> alloy with broad distribution of x values caused by this co-deposition fabrication method. This feature might also reflect the heterogeneous composition of the surface of these wires, i.e. polycrystalline SiGe and Er<sub>2</sub>O<sub>3</sub> domains. In addition, there also appears to be a weak Si-Si phonon peak present at ~517 cm<sup>-1</sup>.

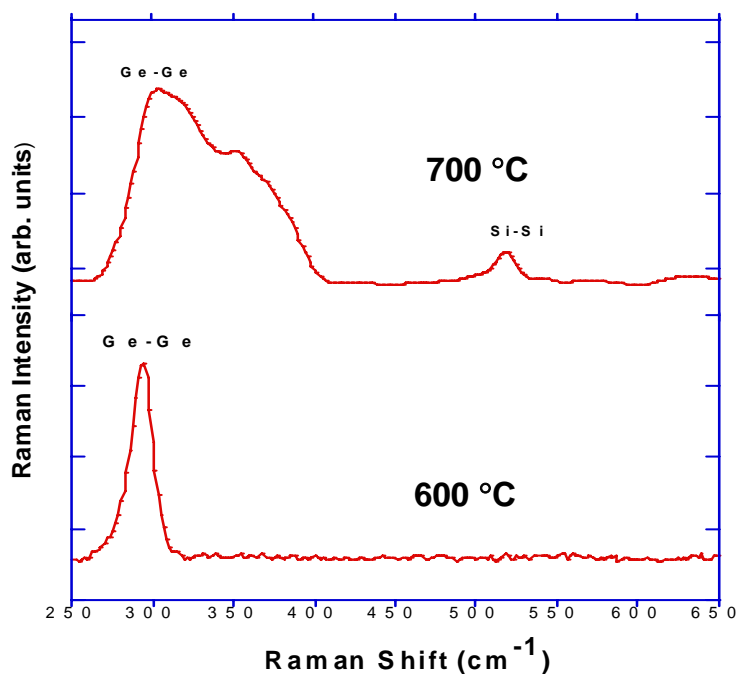


**Figure 60.** Raman spectra of the “co-deposited Si&Er” Ge core NWs annealed at 600 °C and 700 °C in N<sub>2</sub> for 1 h shows that there are crystalline Si-Si (517 cm<sup>-1</sup>) and broadened Si-Ge phonon scattering peaks for the sample annealed at 700 °C.

### 4.2.3 UV-visible Absorption Spectroscopy

The UV-visible absorption spectra of 3 types of Er-doped SiGe NWs suspended in ethylene glycol are shown in Figure 61. A typical absorption spectrum of “co-deposited Si&Er” Ge core NW reveals a broad absorption tail ranging from 300 nm to 600 nm (Figure 61a), which might be due to the presence of Si on the surface of Ge core NWs. A typical UV/visible absorption spectrum of ‘Sandwich’ structure Er-doped SiGe NWs shows that there is a broad absorption tail extending beyond the visible light range. The spectrum of “Er-surface Enriched” SiGe NWs demonstrates that they can absorb visible light less efficiently than other two types of NWs, which also originates from SiGe alloys in the NWs.

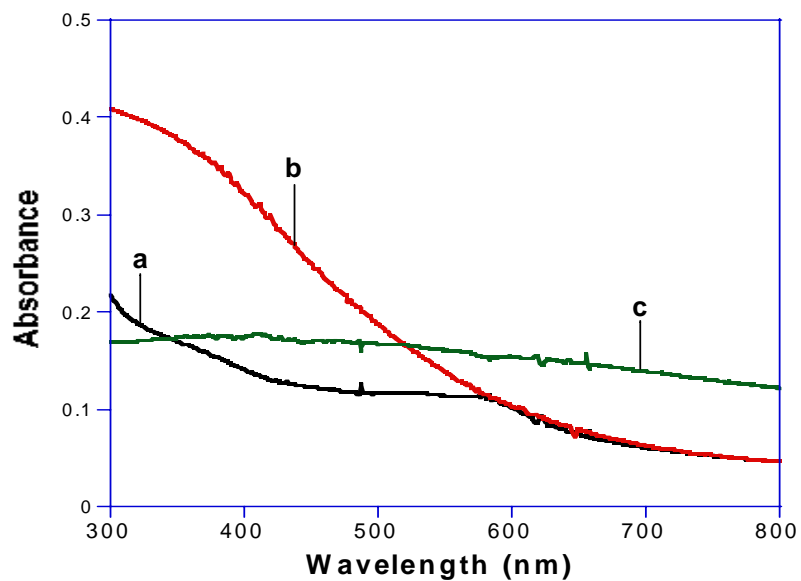


**Figure 61.** UV-visible absorption spectra of (a) “co-deposited Si&Er” Ge core NWs. (b) “Sandwich” structure Er-doped SiGe NWs. (c) “Er-surface Enriched” SiGe NWs. All NWs were annealed at 600 °C in N<sub>2</sub> and dispersed in ethylene glycol solution by sonication.

#### 4.2.4 EXAFS Measurements

It is very important to understand the coordination environment of the optically active  $\text{Er}^{3+}$  centers in a given host material since this environment will greatly affect the Er-related luminescence.<sup>34,79,148</sup> For example, it has been reported that Er-related luminescence can be greatly enhanced by co-doping with a series of impurities such as F, C, O, and N.<sup>34</sup> In the case of co-doping with oxygen, the formation of Er-O complexes not only reduces the room temperature quenching effect, but also enhances the solubility of Er ions in a given host materials, e.g. Si.<sup>34,116</sup> Recently, EXAFS spectroscopy has demonstrated to be an efficient method to investigate this coordination environment, as mentioned in Chapter 1. However, it is notable that these EXAFS structural data must be interpreted with some caution while attempting to determine the local coordination environment of luminescent  $\text{Er}^{3+}$  ions, because only a fraction of the erbium ions in a given host material are optically active.<sup>34,175</sup>

Figure 62 shows the pseudo-radial distribution functions (pseudo-RDF) obtained from the  $k^2$  weighted Fourier transformation of the EXAFS signals for all the Er-doped Ge NWs, Er-doped SiGe NWs, and  $\text{Er}_2\text{O}_3$ . The first peak of the pseudo-RDF for all samples appears at almost the same position as that of  $\text{Er}_2\text{O}_3$ , indicating that Er is coordinated to oxygen.<sup>148</sup> When Er is coordinated to other elements the position of the peak will be shifted to other values due to the difference in the interatomic distances.<sup>148</sup>

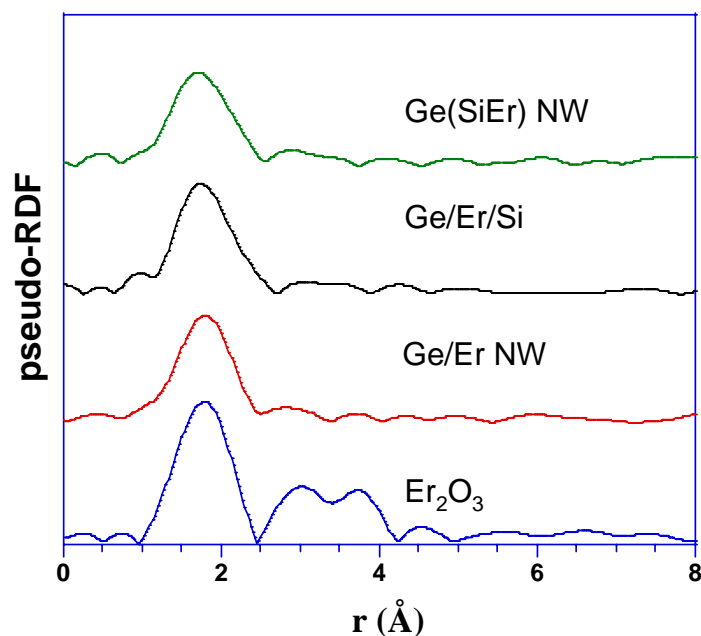


**Figure 62.** Pseudo-RDF of Er-doped Ge NWs, two types of Er-doped SiGe NWs, and  $\text{Er}_2\text{O}_3$ , which were obtained from the  $k^2$  weighted Fourier transformations of the EXAFS signals. Note: Ge/Er stands for the Er-doped Ge NW annealed at 600 °C in air for 1 h; Ge/Er/Si NW stands for ‘Sandwich’ structure  $\text{Er}^{3+}$ -doped SiGe NW annealed at 600 °C in  $\text{N}_2$  for 1 h; Ge(SiEr) stands for “co-deposited Si&Er” Ge core NW annealed at 600 °C in  $\text{N}_2$  for 1 h.

The pseudo-radial distribution functions for the first neighbor peak were then fitted by Professor Leandro R. Tessler of the State University of Campinas, using data collected at the Brazilian National Light Laboratory and the phases and amplitudes from the  $\text{Er}_2\text{O}_3$  standard to obtain the coordination number  $N$ , Er-O interatomic distance  $r$ , and Debye-Waller factor  $\sigma_j^2$ . Table 6 shows the EXAFS parameters obtained for all the samples studied.

The EXAFS data indicates that Er has a coordination number of 6 with oxygen in  $\text{Er}_2\text{O}_3$  standard, and the Er-O distance is 2.26 Å. Ideally, the erbium ion in  $\text{Er}_2\text{O}_3$  is located in

an octahedral coordination environment, the symmetry ( $O_h$ ) of which results in electric dipole forbidden transitions between  $Er^{3+}$  energy levels.<sup>176</sup> As a consequence, the Er-related PL intensity from  $Er_2O_3$  is very weak,<sup>176</sup> which is also consistent with our experimental results in the case of  $Er_2O_3$  nanofibers (to be described in Chapter 5).

For the Er-doped Ge NWs annealed at 600 °C in air for 1 h, the Er first coordinating neighbors are still composed of oxygen atoms. However, erbium has a higher coordination number of 8.1 and a longer Er-O bond length ( $r = 2.30 \text{ \AA}$ ) relative to those of  $Er_2O_3$  standard. For coordination number of 8, there are mainly 3 types of structures: cubic, square antiprism, and dodecahedron. If Er has a square antiprism ( $D_{4d}$ ) or dodecahedron ( $D_{2d}$ ) coordination environment, there will be no centers of symmetry, in which symmetry the transition between  $Er^{3+}$  energy levels should be partially electric dipole allowed.<sup>177</sup> As a consequence, Er-doped Ge NWs can emit much stronger Er-related luminescence than  $Er_2O_3$ . It has been reported that Er has a coordination number of 8.1 and an Er-O bond length of 2.30 Å in a 10% (atomic percentage) Er-doped  $GeO_2$  sol-gel glass.<sup>178</sup> The higher coordination number is mainly attributed to the angle distortion of the Ge-O-Ge linkage, which is caused by the introduction of impurity ions.<sup>178</sup> Due to the oxygen-rich annealing condition, the surface of these Ge NWs might be heavily oxidized, which makes our case similar to the Er-doped  $GeO_2$  glass. Furthermore, Shannon's radius ratio rule requires that the ratio of  $r^+/r^-$  ( $r^+$  = radius of a cation;  $r^-$  = radius of an anion) must be larger than 0.732 and less than 1 for the 8 coordination.<sup>178</sup> The theoretical radius ratio of  $Er^{3+}$  to  $O^{2-}$  is 0.817,<sup>178</sup> which completely satisfies this requirement. The larger Er-O bond length is presumably caused by the surface relaxation of Er-O interaction on the shell of this type of NW.

In the case of ‘Sandwich’ structure Er<sup>3+</sup>-doped SiGe NWs annealed at 600 °C in N<sub>2</sub> for 1 h, the Er coordination number (7.4) is smaller than that of Er-doped Ge NWs. Recall that Er probably has a higher solubility in Ge than in Si because Er preferentially diffuses into Ge-rich core, and no detectable Er is present in the Si-rich shell. Therefore, the erbium coordination environment in germanium should be most important while interpreting these EXAFS data. The smaller number is presumably related to the lower Er concentrations in ‘Sandwich’ NWs relative to Er-doped Ge NWs. Recall that the concentration of Er is typically ~2.6% in the center of ‘Sandwich’ NWs, while this concentration is typically 5.4% in the center of Er-doped Ge NWs. It has been reported that in the Er-doped GeO<sub>2</sub> glass Er possesses a smaller coordination number with oxygen when the erbium concentration is lower.<sup>178</sup> However, the large allowed coordination number error ( $\pm 0.7$ ) makes it difficult to interpret this difference in coordination number precisely.

Among these NWs, “co-deposited Si&Er” Ge core NWs annealed at 600 °C in N<sub>2</sub> for 1 h have the highest Er coordination number (8.7). This high coordination number is presumably due to the following two reasons: (1) the oxidation of the germanium in this type of NWs; and (2) the relative high Er concentration in the “co-deposited Si & Er” NWs. The oxidation occurred during the annealing process, and the relatively higher Er concentration is due to the enhanced Er solubility by this co-deposition method. Recall again that Er has a coordination number above 6 in Er-doped GeO<sub>2</sub> sol-gel glass, and higher the Er concentration is, larger the coordination number will be.<sup>178</sup> The large Debye-Waller factor for this type of NWs also suggests that the erbium ions have heterogeneous coordination environments.<sup>178</sup>

**Table 6.** Erbium coordination parameters (coordination number,  $N$ ; interatomic distance,  $r$ ; and Debye-Waller factor,  $\sigma_j^2$ ) for all the samples studied.

<b>Sample</b>	<b><math>N \pm 0.7</math></b>	<b><math>r \pm 0.02</math> (Å)</b>	<b><math>\sigma^2 \pm 0.0001</math> (Å<sup>2</sup>)</b>
Er <sub>2</sub> O <sub>3</sub>	6	2.26	Standard
Er-doped Ge NW	8.1	2.30	0.0058
Ge/Er/Si NWs	7.4	2.27	0.0043
Ge(SiEr) NWs	8.7	2.28	0.012

#### 4.2.5 The Impact of NW Structure and Post-Fabrication Annealing on the Near IR Light Emission

Figure 63 shows the room temperature photoluminescence (PL) spectra of all types of NWs. All NWs were annealed at 600 °C in N<sub>2</sub> unless otherwise noted. Laser power is 200 mW, and the excitation wavelength is 488 nm. The structure of a given NW greatly affects the light emission intensity at 1.54 μm, which originates from the intra-f-shell transition associated with the  $^4I_{13/2} \rightarrow ^4I_{15/2}$  levels in the Er<sup>3+</sup> centers. Overall, the strongest light emission from Er<sup>3+</sup> in these types of SiGe NWs is obtained from ‘co-deposited Si&Er’ on a Ge core NW (Figure 63a). ‘Sandwich’ structure Er<sup>3+</sup>-doped SiGe NWs have a modest emission intensity at 1540 nm after an appropriate annealing in N<sub>2</sub>, which is approximately 1/3 of the emission intensity from a similarly treated co-deposited NW (Figure 63c). For the case of “Er-surface enriched” SiGe NWs (Figure 63e), negligible light emission in the near IR is obtained, except in the cases of samples coated with a very thin silicon surface layer (~50 nm) and annealed in air instead of nitrogen; such samples yield much stronger near infrared light emission (Figure 63b). A typical near-IR emission spectrum for Er-doped Ge NWs is shown in Figure 63d for comparison.

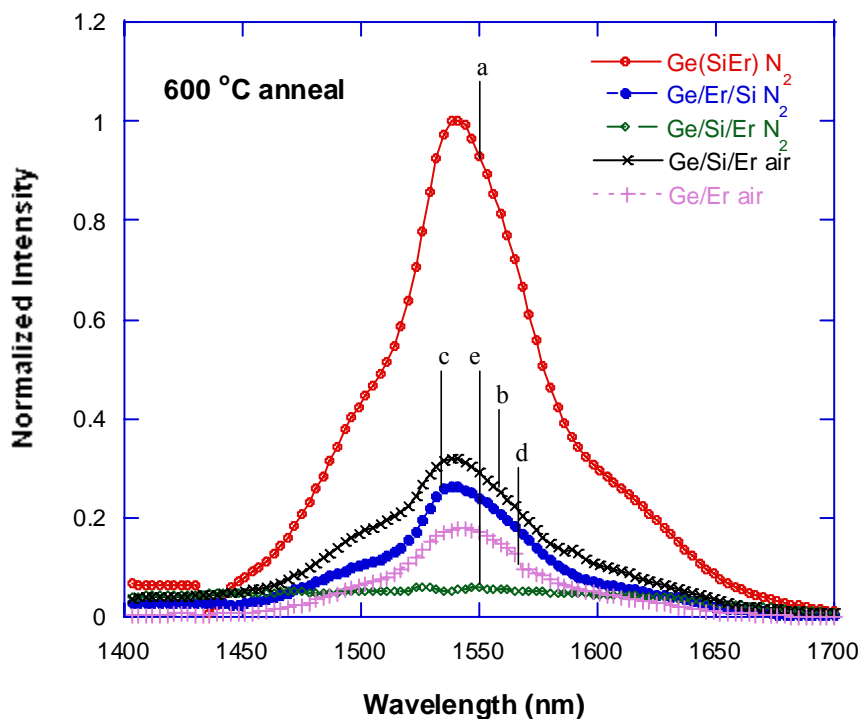


**Figure 63.** Room temperature photoluminescence (PL) spectra of all types of NWs. (a) PL of “co-deposited Si&Er” Ge core NW annealed in  $N_2$ . (b) PL of “Er-Surface Enriched” SiGe Structure NW annealed in  $N_2$ . (c) PL of “Sandwich” Structure NW annealed in  $N_2$ . (d) PL of Er-doped Ge NW annealed in air. (e) PL of “Er-Surface Enriched” SiGe Structure NW annealed in  $N_2$ . All NWs were annealed at 600 °C.

#### 4.2.5.1 Erbium & Silicon co-deposited Sample

Upon excitation at 488 nm, the as-prepared “co-deposited Si&Er” Ge core NW has very weak emission at 1.54  $\mu\text{m}$  (Figure 64e). However, the photoluminescence (PL) of these structures can be greatly enhanced by post-fabrication annealing in  $N_2$ . Such higher intensity light emission at 1.54  $\mu\text{m}$  can be achieved by annealing at elevated temperatures (e.g. from 600 °C to 700 °C) (Figure 64a & 64b). However, a ‘co-deposited’ NW sample annealed in

N<sub>2</sub> at 900 °C and above for 60 s emits with a significant lower intensity at 1.54 μm (Figure 64d).

Preliminary experiments also suggest that there is a reactant concentration dependence to the intensity of light emission observed for these types of structures. The magnitude of near IR PL also decreases if the co-deposition duration of Si and Er is extended from 1 h to 2 h (Figure 64c), likely a consequence of more extensive self-quenching from the additional Er<sup>3+</sup> ions present, along with a greater Si to Ge ratio in the annealed NWs. The former phenomenon is quite common for erbium, while the latter is in agreement with literature report that erbium-doped SiGe films with higher Ge content grown by molecular beam epitaxy (MBE) are less strained, resulting in a stronger PL intensity.<sup>179,180</sup> It is also notable that Er has very limited solubility in crystalline Si.<sup>34</sup> Therefore, a higher Si concentration could lead to a more serious clustering of Er ions, resulting in the quenching of the Er-related PL.

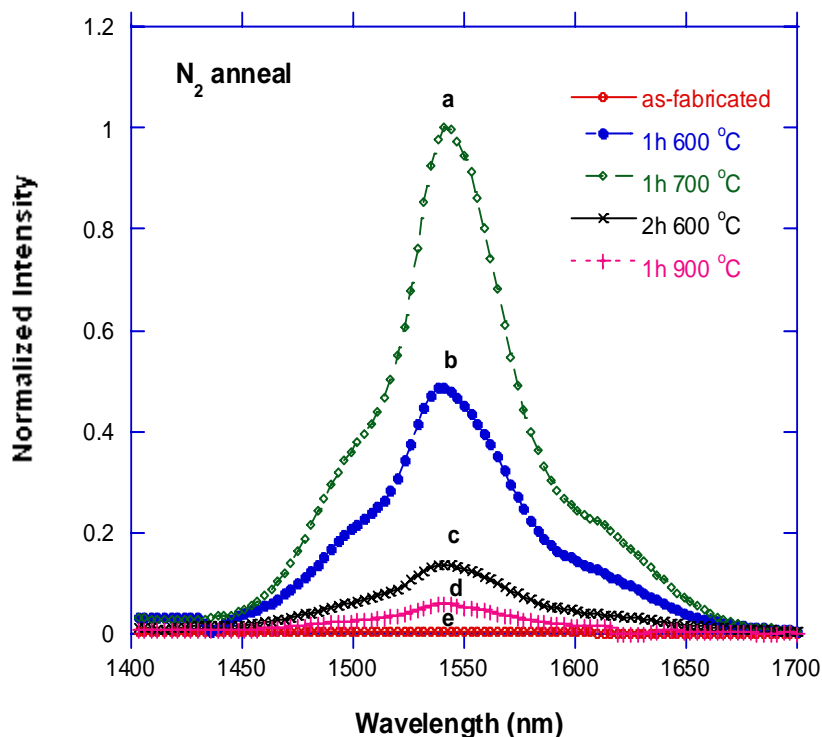


**Figure 64.** PL spectra of “co-deposited Si&Er” Ge core NWs. (a) PL of 1 h Si&Er co-deposition NW annealed in N<sub>2</sub> at 700 °C for 1 h. (b) PL of 1 h Si&Er co-deposition NW annealed in N<sub>2</sub> at 600 °C for 1 h. (c) PL of 2 h co-deposition NW annealed in N<sub>2</sub> at 600 °C for 1 h. (d) PL of 1 h Si&Er co-deposition NW annealed in N<sub>2</sub> at 900 °C for 1 h. (e) PL of as-fabricated NW. Note: 488 nm laser with a power of 200 mW was employed in all cases.

In an attempt to locate where the optically active Er<sup>3+</sup> ions are present, a buffered HF solution, known to be able to etch away Si and silicon oxide, was employed. In this case, the etch addresses two possibilities: (1) if the emitting Er<sup>3+</sup> centers are localized in an oxide-rich environment at the surface, such ions will be removed; (2) given literature precedents for enhanced dissolution reactivity of Si NWs in HF solutions,<sup>181</sup> it is also likely that erbium ions residing in a polycrystalline structural environment on the nanowire shell will also be

removed by this etch. Thus, when these ‘co-deposited’ NWs are exposed to a buffered HF solution, their color becomes darker due to the removal of the light-contrast oxide shell after etching. The light emission at 1.54  $\mu\text{m}$  vanishes completely, which suggests that the optically active Er centers lie inside the shell where higher concentrations of both Er and Si are located.

To further understand the underlying mechanism for the observed 1.54  $\mu\text{m}$  photoluminescence, photoluminescence excitation (PLE) measurements were carried out. Although a slight enhancement of Er-related PL was observed using a 488 nm laser excitation, no distinct increase of the Er-related PL was found upon excitation at 514 nm (Figure 65a). It can be inferred that carrier-mediated process dominates the process of producing light emission at 1.54  $\mu\text{m}$ .<sup>78</sup> It should be pointed out that erbium excitation efficiency related to carrier-mediated process is sensitive to light absorption by the sensitizers rather than to erbium energy levels. The near IR PL intensity is not saturated using an up to 1W laser pump power due to the relatively high concentration of optically active Er centers present in this type of NW.

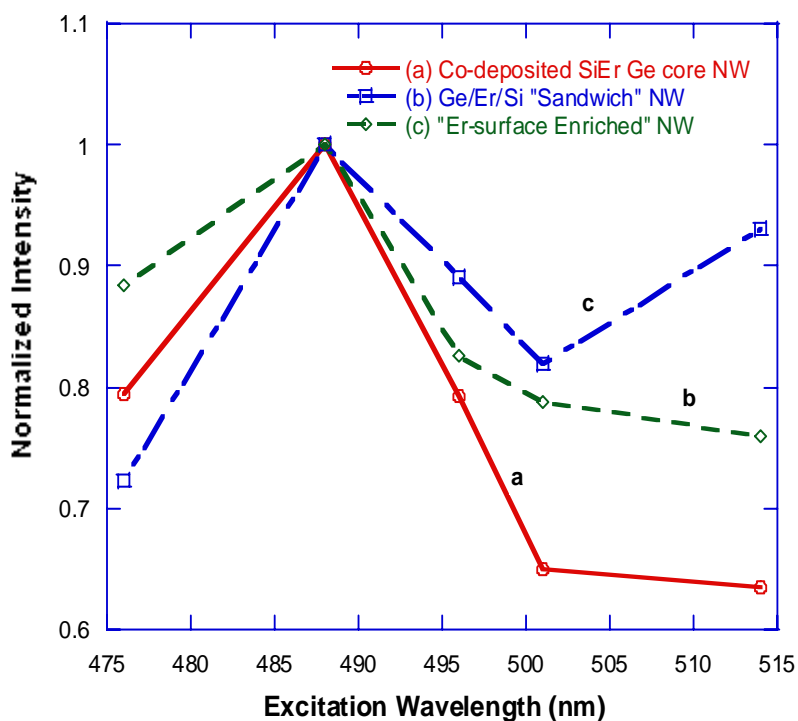


**Figure 65.** Excitation wavelength dependence of (a) “co-deposited Si&Er” Ge NW. (b) “Er-surface Enriched” SiGe NW. (c) “Sandwich” structure Er-doped SiGe NW.

#### 4.2.5.2 Sandwich Structure

Similar to the “co-deposited Si&Er” Ge core NWs, as-fabricated “Sandwich” structure SiGe NWs have no detectable emission without appropriate thermal annealing (Figure 66c). This ‘Sandwich’ NW can emit more than one order of magnitude stronger luminescence at 1.54  $\mu\text{m}$  after 600  $^{\circ}\text{C}$  anneal in  $\text{N}_2$  (Figure 66a). However, the PL intensity was quenched by  $\sim 70\%$  after higher temperature (700  $^{\circ}\text{C}$ ) annealing in  $\text{N}_2$  (Figure 66b). This is a different scenario than that of the co-deposited material, whereby a PL enhancement at 700  $^{\circ}\text{C}$  was observed. In the case of the sandwich geometry, it is clear from the XEDS linescans that Er does not diffuse into the Si surface layers (unlike the co-deposited phase);

thus upon annealing the erbium will form extended aggregates capable of strong Er-Er coupling interactions that will quench the photoluminescence, or diffuse into the crystalline Ge core that is non-emissive.

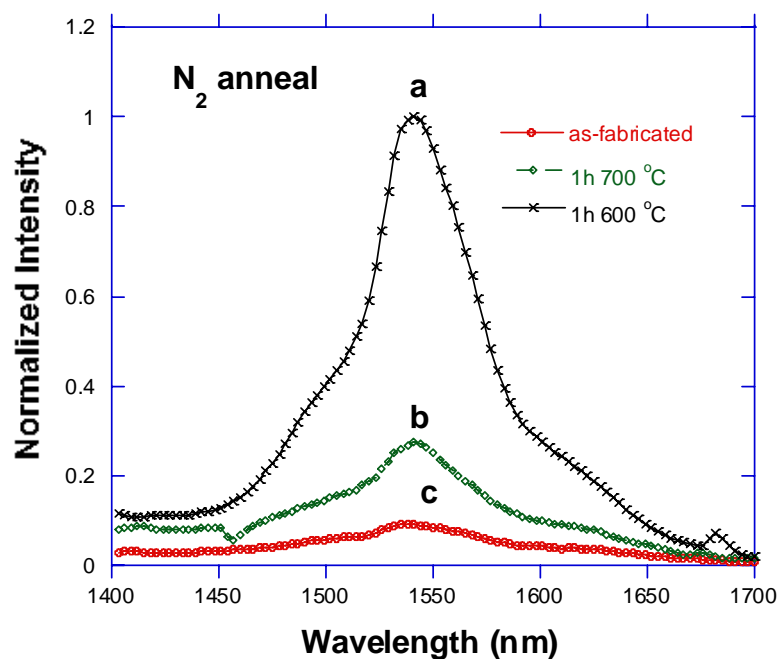


**Figure 66.** PL spectra of “Sandwich” structure Er-doped SiGe NW. (a) PL spectrum of the NW annealed at 600 °C for 1 h. (b) PL spectrum of the NW annealed at 700 °C for 1 h. (c) PL spectrum of the as-fabricated NW. Notes: 488 nm laser of 300 mW was used for excitation; and all samples were annealed in N<sub>2</sub>.

In a manner quite different from the ‘co-deposited Si&Er’ NWs, the PL intensity of ‘Sandwich’ NWs is significantly increased upon excitation at both 488 and 514 nm (Figure 65c), which implies that direct excitation mechanism is responsible for the luminescence at 1.54 μm.

#### 4.2.5.3 'Erbium Surface-Enriched' SiGe Nanowires

'Er-surface enriched' SiGe NWs provided the weakest emission at 1.54  $\mu\text{m}$  among all three types of NWs evaluated in this study. Very thick Si-rich SiGe wires ( $\sim 0.4 \mu\text{m}$  on average) were produced using the same fabrication conditions (in terms of reactant concentrations and reaction times) as that of 'co-deposited' and 'Sandwich' NWs. Although these 'Er-surface enriched' wires were annealed in air or  $\text{N}_2$  at 600  $^\circ\text{C}$  or 700  $^\circ\text{C}$ , nevertheless no measurable improvement in light emission was detected (Figure 67b). To reduce the extent of Er clustering formed on the surface of the NWs, the exposure time of the SiGe nanowire to the erbium precursor was shortened from 1 h to 0.5 h. This method, however, does not improve the efficiency of light emission from  $\text{Er}^{3+}$  ions whatsoever (Figure 67c). Because of a relatively high concentration of Er ions located on the surface of the NWs (e.g. 21%), it is assumed that clusters form, which can significantly reduce the population of erbium ions in the first excited state ( $^4\text{I}_{13/2}$ ) through various nonradiative Auger deexcitation processes such that only very weak PL at 1540 nm can be obtained.<sup>114</sup> High temperature annealing does not help in breaking down these erbium clusters (through diffusing the concentrated Er ions on the shell into the Si-rich matrix), due presumably to the low solubility of Er in Si.<sup>34,182</sup>

'Er-surface enriched' SiGe NWs with relative high concentrations of Ge were also fabricated by reducing the exposure time of  $\text{SiH}_4$  to the Ge NW core, e.g. the Si deposition time is reduced from 1 h to 10 minutes. Similar to the NW with high concentrations of Si, these 'Er-surface enriched' NWs with a correspondingly higher concentration of Ge has no emission after annealed in  $\text{N}_2$  at 600  $^\circ\text{C}$  and very weak emission after being annealed at 700  $^\circ\text{C}$  (Figure 67d). Changing the nature of the gaseous ambient to air results in enhancement of

the PL intensity of the NW by more than one order of magnitude (Figure 67a). This is a consequence of several synergistic factors. First, a thinner Si coating presumably facilitates the diffusion of Ge out into the Si layer, and after oxidation in air,  $\text{GeO}_x$  (or perhaps  $\text{SiGeO}_x$ ) with a tunable bandgap can form and assist in enhancing the PL performance through a carrier-mediated process.<sup>133</sup> It should also be noted that the co-doping of oxygen and erbium into crystalline Si greatly increases the amount of excitable Er ions and reduces the room temperature quenching process.<sup>175,183</sup>

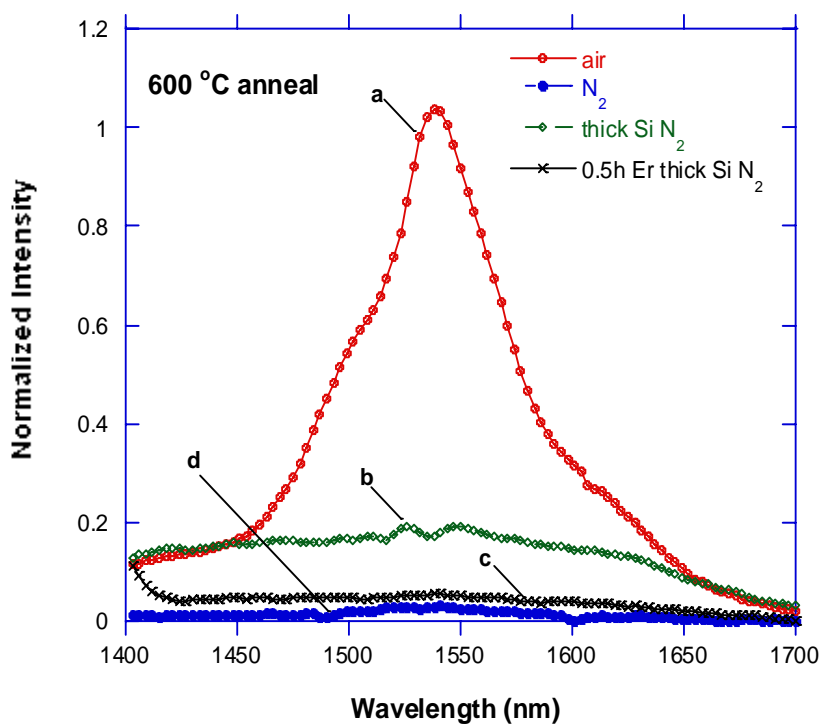


**Figure 67.** PL spectra of “Er-surface enriched” SiGe NW. (a) PL spectrum of the NW annealed in air. (b) PL spectrum of the NW with thicker Si coating and annealed in  $\text{N}_2$ . (c) PL spectrum of the NW with thicker Si coating and shorter (0.5 h) Er deposition time that was annealed in  $\text{N}_2$ . (d) PL spectrum of the NW annealed in  $\text{N}_2$ . All samples were annealed at  $600\text{ }^\circ\text{C}$ .

The PLE behavior of 'Er-surface enriched' SiGe NWs annealed in N<sub>2</sub> shows an enhanced emission intensity for 488 nm excitation relative to 476 nm, but with an overall diminution in PL intensity with the remaining wavelengths out to 514 nm (Figure 65b). This suggests that both carrier-mediated and direct excitation processes determine the light emission intensity of this type of NW structure.

## 4.3 Discussion

### 4.3.1 'Sandwich' Structure

In this type of sample, HRTEM lattice imaging, Raman analyses, and XEDS linescans point to an alloy structure that is clearly Ge-rich at the core, with some Si present (~10%). Hence, the presence of the  $\text{Er}^{3+}$  at the interface between Si and Ge does not inhibit Si diffusion into the core with annealing; however, the XEDS data suggests that the energy barrier for Er diffusion is significantly lower into the Ge layer than outward into the Si-rich surface layer. A clear compositional gradient does exist, as the surface cap appears amorphous and oxygen rich, with a total absence of erbium.

With particular regard to the erbium, the largest concentration of centers is localized at the boundary between the SiGe core and the Si oxide shell. The erbium coordination environment in this type of structure is greater than six fold and surrounded by oxygen, as determined by EXAFS. While it is possible with this type of geometry to achieve an emissive  $\text{Er}^{3+}$  environment, this relatively high concentration of rare earth ions at the boundary (~ 6%) is at a level capable of self-quenching. The weaker 1.54  $\mu\text{m}$  PL of this system (with respect to the two other configurations studied here) is consistent with this conclusion. Detectable emission, when activated by a necessary 600 °C anneal does follow an excitation pathway that involves direct excitation of the  $\text{Er}^{3+}$  ligand field levels associated with the  $^4\text{I}_{15/2} \rightarrow ^4\text{G}_{7/2}$  and  $^4\text{I}_{15/2} \rightarrow ^4\text{H}_{9/2}$  transitions, and not excitons originating from the SiGe phase. Extended anneals at higher temperatures (700 °C) only serve to facilitate clustering in this type of sample, with a corresponding drop in emission intensity at 1.54  $\mu\text{m}$ .

### 4.3.2 Erbium-Surface Rich Structure

The lack of a diffusion barrier between Ge and Si layers is presumed to facilitate intermixing of the two elements during annealing at 700 °C, and the comparable levels of each element present in the core ( $\sim\text{Si}_{0.6}\text{Ge}_{0.4}$ , suggested by Raman and HRTEM lattice spacings), are consistent with this conclusion. EXAFS data confirm that the erbium coordination environment in this type of structure is greater than six fold and surrounded by oxygen, which is beneficial to increasing its PL intensity due to the absence of octahedral coordination environment of Er.

Not surprisingly, this deposition sequence produces the greatest concentration of erbium at the outermost surface of the nanowire, and thus greater opportunities for clustering. This significant erbium fraction present at the surface is structurally reminiscent of the previously-studied Er-surface enriched Si nanowires, where a relatively high erbium fraction (>20%) and weak near IR emission is observed.<sup>80</sup>

The emission intensity at 1.54  $\mu\text{m}$  of these ‘Er-surface enriched’ SiGe NWs is quite weak when annealed in  $\text{N}_2$  at 600 °C (Figure 67b); the corresponding UV/visible absorption spectrum of this type of sample shows a weak absorption cross section, which inhibits possibility of any carrier-mediated participation process in the erbium photoluminescence. For these NWs annealed in air, however, the greater PL emission intensity at 1.54  $\mu\text{m}$  likely originates with the dominance of direct excitation of the rare earth ligand field states, as noted for the ‘sandwich’ architecture described above.

### 4.3.3 Erbium-Silicon co-deposited Structure

The structure of this type of nanowire, especially at the surface, is rather different than the two other varieties described in this chapter. HRTEM analyses suggest a coating of Si randomly-oriented nanocrystals that presumably ‘break up’ the erbium-erbium clustering present in the Er-surface enriched and sandwich nanowire structures. While simultaneous deposition of erbium and silicon onto the Ge NW core likely reduces opportunities for radial epitaxial growth, it nevertheless permits relatively higher fractions of optically-active rare earth to be introduced into this type of nanowire. Significant Si diffusion into the Ge core, and subsequent alloying, also takes place upon annealing. Based on HRTEM analyses, XEDS linescans, and EXAFS results, it appears that the erbium resides in a surface-enriched polycrystalline environment, surrounded by oxygen with a coordination number much greater than six. Such a non-centrosymmetric rare earth environment is necessary for parity purposes and the detection of strong emission.

Post-fabrication annealing can introduce oxygen impurities that assist in the formation of a non-centrosymmetric coordination environment for Er ions, necessary for yielding much stronger light emission.<sup>34</sup> Hence activation by heating at 600 or 700 °C is necessary in these samples; yet use of temperatures higher than these (e.g. 900 °C) result in a significantly diminished PL signal at 1.54  $\mu\text{m}$ , suggesting a clustering of erbium ions at temperatures closer to the recrystallization temperature of silicon (and an upper thermal threshold for PL activation).

In addition to relative PL intensity at 1.54  $\mu\text{m}$ , analysis of the emission intensity dependence on excitation wavelength finds an overall diminution with increasing excitation wavelength, consistent with carrier-mediated behavior. Strong absorption by this type of

sample well into the visible ( $> 600$  nm, detected by electronic absorption) is consistent with this conclusion as well.

Overall, this type of local erbium coordination closely resembles that found in erbium-doped silicon-rich silicon oxide films produced by CVD, co-sputtering, and related methods.<sup>76,122</sup> It is structures of this type that are showing promise in reported observations of optical gain,<sup>123</sup> and it is believed that this architecture may ideally prove useful in electroluminescent structures involving current transport through a Ge core NW with desirable carrier mobilities.

#### 4.4 Summary

Three structurally different Er-doped SiGe NWs have been prepared via altering the deposition sequence of Si and Er<sup>3+</sup> on a Ge NW core. XEDS linescans of ‘sandwich’ structure Er<sup>3+</sup>-doped SiGe NWs suggest that Er is preferentially diffused into Ge-rich SiGe core, and no detectable Er is present in the Si-rich shell. SiGe alloys can be formed by annealing this type of NWs at 600 °C for 1 h in N<sub>2</sub>, which is confirmed by the HRTEM imaging and Raman spectroscopy. “Er-surface Enriched” SiGe NWs possess a SiGe-rich core and an Er-rich shell. HRTEM imaging indicates that the core is composed of crystalline SiGe alloys, which is consistent with the corresponding Raman spectroscopy. In contrast with the other two types of Er-doped SiGe NWs, “co-deposited Si&Er” Ge NWs have a much higher Er concentration and a smoother surface morphology. XEDS elemental mapping suggests that the core is Ge rich and Si & Er are concentrated on the shell. HRTEM imaging indicates that the shell is mainly composed of crystalline SiGe alloys and some Er<sub>2</sub>O<sub>3</sub> precipitates.

EXAFS data show that Er has a coordination number of ~8 with oxygen in Er-doped Ge NWs and Er-doped SiGe NWs. Among three types of Er-doped SiGe NWs, “co-deposited Si&Er” Ge NWs emit the strongest Er-related luminescence due presumably to the presence of SiGe or SiGeO<sub>x</sub> nanocrystals that could serve as sensitizers for erbium to enhance the PL intensity through a carrier-mediated process. “Er-surface Enriched” SiGe NWs cannot emit luminescence at 1540 nm unless they have been annealed in air. This fact is attributed to the formation of SiGeO<sub>x</sub> under an oxygen-rich annealing condition. In the case of ‘sandwich’ structure Er<sup>3+</sup>-doped SiGe NWs, erbium ions can only be directly excited so that the emitted

luminescence is weaker than that of “co-deposited Si&Er” Ge NWs due to the lack of sensitizer.

The studies presented in this work are a clear example of how the relative timing of introducing a dopant or impurity center during semiconductor nanowire fabrication can alter element inter-diffusion during subsequent thermal treatment as well as the clustering of the optically-active impurity centers. The relative timing of introducing a dopant or impurity center can also affect the Er-related PL intensity and mechanism. When Er is deposited between Si layer and Ge core NW, a weak Er-related emission was obtained via the direct excitation of  $\text{Er}^{3+}$  ions; whereas a much stronger emission at 1540 nm was acquired via a carrier-mediated excitation when Si and Er were co-deposited on the Ge core NW.

*CHAPTER V.*

Emissive Erbium-Doped Group IV Oxide Nanofibers Derived  
from an Electrospinning Process

## 5.0 Introduction

As mentioned in Chapter 1, it is very important to fabricate free-standing erbium-doped 1-D nanofibers because they could be used as potential building blocks for generating complex nanoscale photonic devices such as waveguides and amplifiers. In addition, these 1-dimensional (1-D) Er-doped Group IV oxide nanofibers could also provide an alternative, well-defined experimental model analogous to oxidized Er-doped Ge and SiGe NWs so that the mechanism of erbium luminescence in these host materials could be further understood. In terms of bottom-up assembly methods, electrospinning has demonstrated to be an efficient technique to produce polymer nanofibers with a high yield, and it is known that sol-gel processes can be employed to fabricate Er-doped Group IV oxide film waveguides and amplifiers.<sup>184</sup> Therefore, combining the electrospinning technique with the sol-gel process is one possible route to obtain erbium-doped Group IV oxide nanofibers.

Since this fabrication method requires condensed phase reactions whereby reactants can be precisely weighted, the concentrations of erbium ions in the host materials can be easily controlled by adjusting the ratios of the erbium precursor to these Group IV oxide sol-gel precursors. Ideally, all  $\text{Er}^{3+}$  ions are left in the oxide matrixes after the reaction without any loss. In addition, erbium ions can be homogeneously dispersed in the host materials without a serious erbium clustering provided that the concentrations of  $\text{Er}^{3+}$  ions are below its solubility limit in a given host material. However, in the Er-doped Ge and SiGe NWs prepared by vapor transport reactions described in earlier chapters, most of the  $\text{Er}^{3+}$  ions are concentrated on the surface of these NWs. Although a high temperature post-annealing can help diffuse these concentrated  $\text{Er}^{3+}$  ions into these host materials, a certain amount of  $\text{Er}^{3+}$  ions are still clustered on the surface of these NWs. Furthermore, since the load of  $\text{Er}^{3+}$

incorporation relies on a kinetic entrapment process, some of the  $\text{Er}^{3+}$  ions present in the reactor were deposited on the inner wall of the reactors or carried away by the helium carrier gas so that the amount of erbium actually incorporated is more difficult to measure.

In terms of potential host materials for erbium ions, silica possesses multiple advantages including broad spectral transmission range, easy to clad, strong tolerance to harsh chemical environments, high resistance to laser damage, etc.<sup>142</sup> Especially, this host material is fully compatible with the silica-based optical fiber industry and has been successfully employed to fabricate 2-dimensional Er-doped film waveguides and amplifiers.<sup>112</sup>  $\text{SnO}_2$  also possesses several appropriate properties as an optical waveguide. First, it is highly optical transparent (80-90% transparency in the visible light region).<sup>143</sup> Secondly,  $\text{Er}^{3+}$  ions could substitute interstitial  $\text{Sn}^{4+}$  ions in the rutile  $\text{SnO}_2$  lattice so that the direct Er-Er coupling interaction would be much suppressed.<sup>144</sup> Thirdly,  $\text{SnO}_2$  is a wide band gap n-type semiconductor ( $E_g = 3.6$  eV) due to the presence of donor sites such as oxygen vacancies and interstitial  $\text{Sn}^{4+}$  ions, which means that an electroluminescence could be obtained from an Er-doped  $\text{SnO}_2$  sample via an electrical pumping.<sup>143</sup> Germanate based glasses also have potential applications in optical devices because of their low transmission loss in the infrared region.<sup>145</sup> These glasses also have good mechanical strength, high thermal stability, and high refractive index, which make them suitable candidates for optical fibers.<sup>146</sup> Recently, optical fibers based on undoped  $\text{GeO}_2$  glasses have been successfully used for high power laser delivery at  $2.94 \mu\text{m}$  (wavelength of the erbium substituted yttrium aluminium garnet laser).<sup>147</sup>

In this chapter, Er-doped Group IV oxide nanofibers with controllable erbium concentrations and tunable widths are first fabricated successfully via an electrospinning

approach that is assisted by a sol-gel process.  $\text{Er}_2\text{O}_3$  nanofibers were prepared as a control sample with an intention to compare their PL excitation properties with other nanofibers in order to further explore erbium luminescence mechanism. As-prepared nanofibers were then characterized using SEM, XEDS, TEM, and infrared (IR) spectroscopy. The crystalline Er-doped  $\text{SnO}_2$  fibers were also analyzed by these methods along with a more detailed characterization using X-ray diffraction (XRD), SAED, HRTEM and XEDS linescan analysis to identify their crystal structures and compositions. The near-IR photoluminescence properties of all Er-doped nanofibers were also investigated herein. Furthermore, the PL properties of Er-doped crystalline  $\text{GeO}_2$  nanowires prepared via a VLS synthetic route were compared with analogous Er-doped  $\text{GeO}_2$  nanofibers fabricated through an electrospinning method.

## 5.1 Experimental

### 5.1.1 Fabrication of Er-doped Group IV Oxide Nanofibers

Figure 68a shows a general overview of the procedures used for preparing  $\text{Er}_2\text{O}_3$ , Er-doped  $\text{SiO}_2$ ,  $\text{SnO}_2$ , and  $\text{GeO}_2$  nanofibers.  $\text{Er}_2\text{O}_3$  nanofibers were prepared for comparison with Er-doped oxide nanofibers in terms of near-IR photoluminescence. Erbium concentrations in these Group IV oxide nanofibers were controlled by varying the atomic ratio of erbium and Group IV oxide precursors.

*Fabrication of  $\text{Er}_2\text{O}_3$  nanofibers:* Polyvinylpyrrolidone (PVP, 0.60 g,  $M_w = 1.3$  M, Aldrich Chemical Company), dissolved in 2.5 ml absolute ethanol (AAPER Alcohol and Chemical Co.), was mixed well with 0.25 g of Er(III) *i*-propoxide (99.9%, Strem Chemicals) in a mixture of 1.0 ml absolute ethanol and 1.0 ml acetic acid (Mallinckrodt AR) by vortex shaking. PVP was selected as a templating polymer because it has good solubility in alcohols and water, which makes it compatible with the sol-gel process. Furthermore, PVP electrospun nanofibers have been well investigated as a model system by Xia's group as mentioned earlier in Chapter 1. The mixture was then loaded into a glass syringe equipped with a 21 gauge stainless steel needle. The needle was connected to a high voltage direct current (DC) supply using a metal clamp. A piece of aluminum foil was used to wrap the surface of a drum that serves as a grounding electrode to collect these nanofibers. The as-formed nanofibers were exposed to air for about a week in order to completely hydrolyze the organometallic precursors. A 25 kV accelerating voltage and a 15 cm working distance between the needle and the drum were used to run the electrospinning process. The electrospinning setup is illustrated in Figure 68b. As-fabricated nanofibers were annealed in

air at 500 °C or higher temperatures for 3 h to remove the PVP templates completely.<sup>106</sup> It is notable that a very thin layer of fibers is preferable for the thermal annealing process, as otherwise the fibers will be partially fused together to form bundles after such an annealing.

*Fabrication of Er-doped SiO<sub>2</sub> nanofibers:* To prepare 4.1% (atomic percentage) Er-doped SiO<sub>2</sub> nanofibers, 0.12 g Er(III) *i*-propoxide and 1.8 g tetraethyl orthosilicate (TEOS, 98%, Aldrich Chemical Company) were dissolved in a mixture of 1.0 ml ethanol and 1.0 ml acetic acid, which were mixed well with 0.61 g PVP in 2.5 ml ethanol. The remaining experimental conditions are the same as those used for the preparation of Er<sub>2</sub>O<sub>3</sub> nanofibers.

*Fabrication of Er-doped GeO<sub>2</sub> nanofibers:* To prepare 2.0% (atomic percentage) Er-doped GeO<sub>2</sub> nanofibers, 0.02 g Er(III) *i*-propoxide and 0.81 g tetraethoxy germane (Gelest, Inc.) were dissolved in a mixture of 1.0 ml methanol (AAPER Alcohol and Chemical Co.) and 0.5 ml acetic acid, which was further mixed well with 0.30 g PVP in 1.2 ml methanol. This mixture was then used to prepare electrospun nanofibers using a 20 kV accelerating voltage. The other experimental conditions are the same as those used for the preparation of Er<sub>2</sub>O<sub>3</sub> nanofibers.

*Fabrication of Er-doped SnO<sub>2</sub> nanofibers:* To prepare 4.0% (atomic percentage) Er-doped SnO<sub>2</sub> nanofibers, 0.030 g Er(III) *i*-propoxide and 0.90 g Sn(IV) *t*-butoxide (Gelest, Inc.) dissolved in a mixture of 1.0 ml ethanol and 1.0 ml acetic acid were mixed well with 0.30 g PVP in 1.2 ml ethanol. Again, the other experimental conditions are the same as those used for the preparation of Er<sub>2</sub>O<sub>3</sub> nanofibers. Pure SnO<sub>2</sub> nanofibers were prepared in the same way, except that no erbium precursor was added.

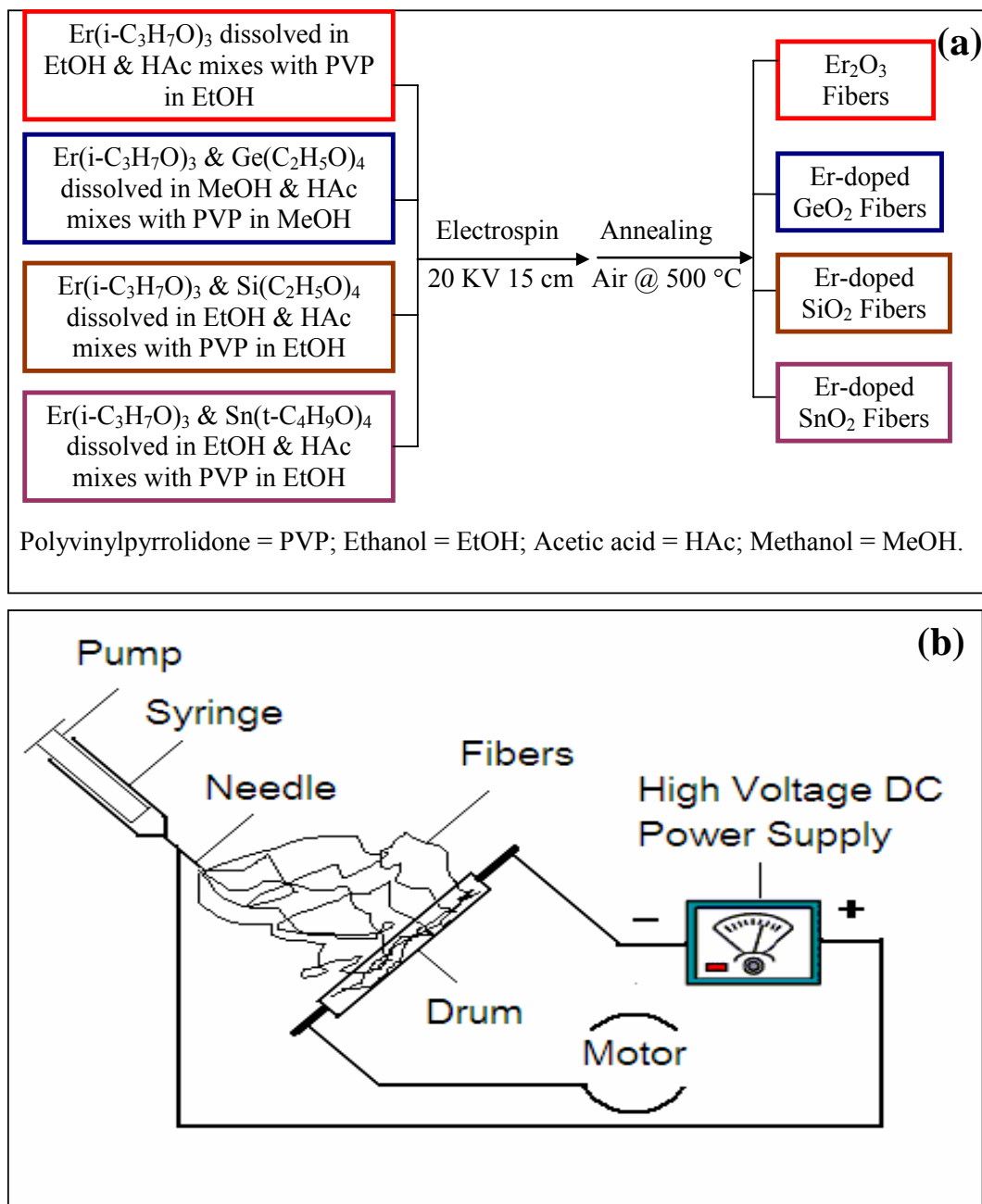


**Figure 68:** (a) General procedures for fabricating Er<sub>2</sub>O<sub>3</sub>, Er-doped SiO<sub>2</sub>, GeO<sub>2</sub>, and SnO<sub>2</sub> nanofibers. (b) Schematic diagram of an electrospinning setup.

### 5.1.2 Preparation of Nanofiber Arrays

Two strategies were developed to obtain nanofiber arrays, which are illustrated in Figure 69. Arrays of  $\text{Er}_2\text{O}_3$ , Er-doped  $\text{SiO}_2$ , and PVP nanofibers have been successfully prepared using these two strategies. In the case of the fabrication of PVP nanofiber arrays, 0.60 g PVP dissolved in a mixture of 2.2 ml methanol and 0.5 ml acetic acid was used as a solution for electrospinning. PVP nanofibers were explored as a model system to find feasible strategies to obtain other types of nanofiber arrays. It is relatively cheap and convenient to prepare PVP nanofiber arrays, because no expensive and air sensitive inorganic precursors are required.

In strategy 1, the setup and experimental conditions are the same as those described above. Aligned nanofiber arrays can only be found in the area between the wood support and the metal clamp or across the gap on the metal motor as shown in Figure 69a. The nanofiber arrays were then transferred to a piece of Si wafer for SEM or optical microscopy measurements. It is noteworthy that there are no aligned nanofiber arrays found on the grounding drum.

In strategy 2 (Figure 69b), the setup is similar to that in strategy 1, except that a different grounding electrode design is used. The grounding electrode is composed of two pieces of  $5 \times 15$  mm p-type Si (100) wafers that were placed on top of a 2.5 cm insulating quartz disc (G. M. Associates, Inc.). The distance between the needle and the quartz disc is 7.5 cm, and the accelerating voltage is 8 kV. Typically, the electrospinning time is 10 seconds. Other experimental conditions for electrospinning are the same as those used in strategy 1. Nanofiber arrays can be obtained across the insulating gap bridging these two pieces of Si wafers.

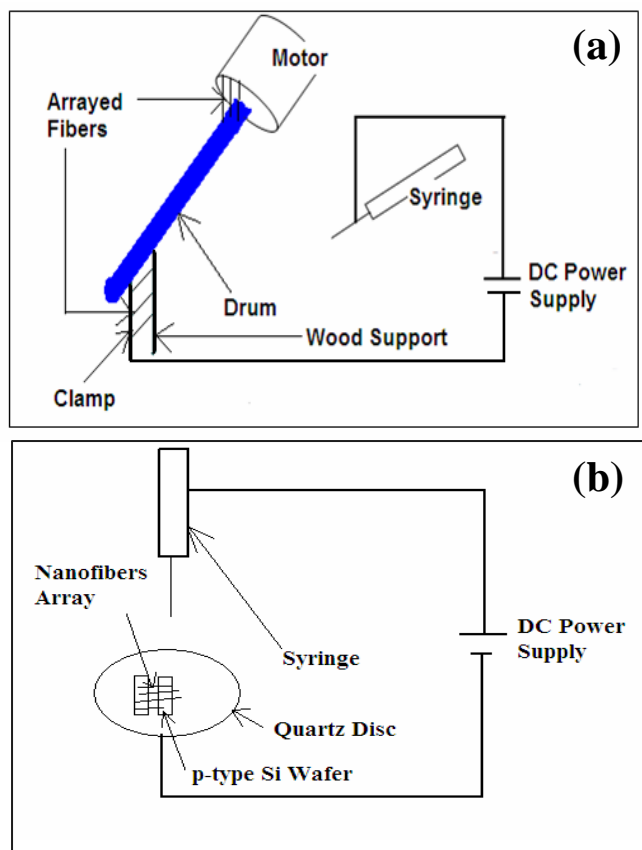


**Figure 69.** Schematic illustrations of the electrospinning setups for (a) Strategy 1 and (b) Strategy 2.

### 5.1.3 Fabrication of Crystalline Er-doped GeO<sub>2</sub> NWs

Similar to Er-doped Ge NWs, a two-step process was used to fabricate crystalline Er-doped GeO<sub>2</sub> NWs. First, using the fabrication methods described in Chapter 3, crystalline GeO<sub>2</sub> NWs were prepared via a VLS synthetic route that was assisted by a carbothermal reduction reaction to provide the vapor source. In the second step, Er<sup>3+</sup> ions were deposited on GeO<sub>2</sub> NWs using the same chemical vapor deposition (CVD) method as that for coating Ge NWs with Er<sup>3+</sup> ions, also described in the earlier chapter.

*Crystalline GeO<sub>2</sub> Nanowires Synthesis:* Figure 70a illustrates the reactor design for preparing crystalline GeO<sub>2</sub> nanowires using a vapor phase method. Quartz tubing with a 20 mm inner diameter (I.D) was used to build the reactor that was sealed at one end and left open at another end with a hole of the size of 18 gauge needle. In a typical reaction, an alumina boat containing a mixture of 0.0470 g carbon (J. T. Baker) and 0.1989 g GeO<sub>2</sub> powder (99.999%, Alfa Inorganics, Inc.) in a C:Ge molar ratio of 2:1 was placed in the reactor. A 5 x 15 mm p-type Si wafer piece deposited with sputtered Au islands was attached vertically to the side of another alumina boat that was positioned in the quartz tube reactor approximately 2 cm from the edge of the oven. The boat containing a mixture of carbon and GeO<sub>2</sub> was heated by a 30 cm ceramic oven at 940 °C for 15 minutes. The growth temperature of the GeO<sub>2</sub> NWs is ~ 563 °C, close to that of the above-mentioned Ge NWs. At the end of the reaction period, thick pink fluffy films can be easily seen on the Si wafer. It should be noted that GeO<sub>2</sub> NWs can only be obtained in the dark region shown in Figure 70b.

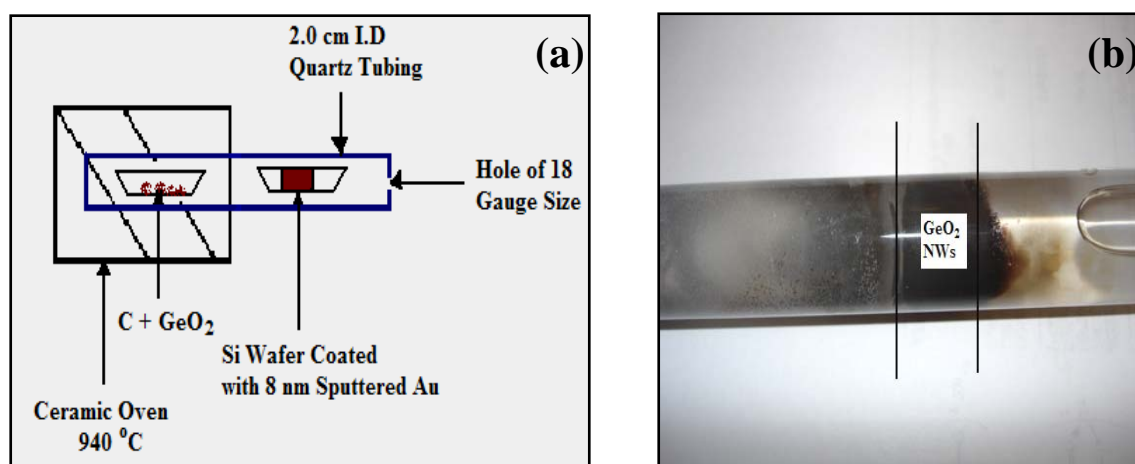


**Figure 70.** (a) Reactor design for the fabrication of GeO<sub>2</sub> nanowires. (b) Optical image of the reactor showing that GeO<sub>2</sub> NWs can only be obtained in the dark region between two lines.

*Preparation of Er-doped GeO<sub>2</sub> Nanowires:* As-formed GeO<sub>2</sub> NWs were deposited with erbium using the same setup and experimental conditions as those for doping Ge NWs with erbium ions as described in Chapter 3. As-formed Er-doped GeO<sub>2</sub> NWs were annealed at 600 °C in air for 1 h to obtain near-IR photoluminescence.

#### **5.1.4 Instrumentation**

Structural characterization of nanofiber samples was performed using several different electron-microscopes: a JEOL JEM-3010 TEM, a JEOL JEM-2010F STEM, a JEOL JSM-6100 SEM, and a Philips EM300. The JEM-3010 TEM at the University of Illinois-Chicago, operating at 300 kV, was used to record TEM and high resolution TEM images, as well as SAED patterns. The JEM-2010F STEM at the University of Illinois-Chicago is a field emission TEM which operates in both transmission and scanning transmission modes. It has a probe size of 1 nm that was used for point elemental analysis. High angle annular dark field (HAADF) images were obtained using an annular detector attached to this STEM. A JEOL JSM-6100 SEM equipped with a XEDS analysis system at Texas Christian University operating at 20 kV was used to record SEM images and perform elemental analyses of macroscopic nanofiber samples. A Philips EM300 operating at 60 kV at Texas Christian University was also used to take TEM measurements. Specimens for TEM characterization were prepared by dispersing the sample with a 10 µL drop of 2-propanol and then placing the drop onto a copper grid.

A Hummer VII sputtering system (Anatech, Ltd.) at Texas Christian University was used to coat selected Si wafers with gold films. Infrared spectra were collected using a MIDAC M4000 FT-IR spectrometer with a resolution of 4 cm<sup>-1</sup> at TCU.

X-ray diffraction (XRD) patterns were collected using a PW Philips diffractometer operating at 35 kV and 30 mA. Copper  $K\alpha$  irradiation with a wavelength of 1.54056 Å was used as an X-ray source. The angle  $2\theta$  ( $\theta$  = Bragg diffraction angle) ranges from 20 to 110° with a step rate of 0.02° per 3 seconds for each measurement. Low resolution ( $\pm 4$  nm) near-IR photoluminescence (PL) spectra were obtained using the system described in Chapter 3.

## 5.2 Results and discussion

### 5.2.1 $\text{Er}_2\text{O}_3$ Nanofibers

Figures 4a-4c show the SEM images of as-formed  $\text{Er}_2\text{O}_3/\text{PVP}$  fibers and the fibers annealed at 500 °C and 700 °C in air for 3 h. It can be easily seen that the as-formed nanofibers are smooth and uniform (Figure 71a). In order to obtain pure inorganic fibers, a high temperature anneal is employed to remove the organic PVP templates. It was found that the structure of the nanofibers was maintained after being annealed at 500 °C in air for 3 h (Figure 71b). After being annealed at 700 °C in air for 3 h, however, the nanofibers were partially deformed with some interfiber connections formed as shown in Figure 71c. Figure 71d shows the XEDS spectrum of an  $\text{Er}_2\text{O}_3$  nanofiber sample, which was taken using the XEDS system attached to the JEOL JSM-6100 SEM at TCU. The spectrum suggests that this sample is composed of pure erbium oxide. Since the XEDS cannot detect elements lighter than fluorine due to the existence of a filtering window, the oxygen peak is not observed. As it is necessary to coat a 10 nm Au layer on the sample to obtain clearer SEM images, a corresponding Au peak in the XEDS spectrum is observed.

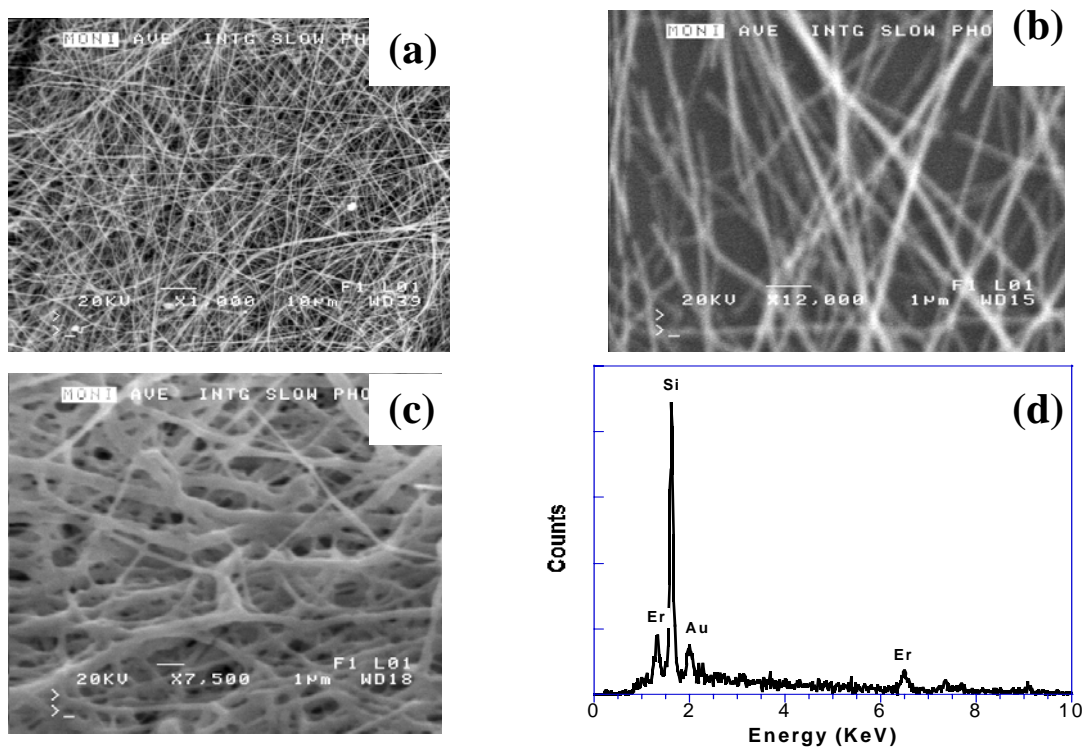


**Figure 71.** SEM images of (a) as-formed Er<sub>2</sub>O<sub>3</sub>/PVP fibers, (b) the fibers annealed at 500 °C for 3 h in air, and (c) the fibers annealed at 700 °C for 3 h in air. (d) XEDS spectrum of Er<sub>2</sub>O<sub>3</sub> nanofibers.

Figure 72 shows the diameter distributions of as-formed Er<sub>2</sub>O<sub>3</sub>/PVP nanofibers and the nanofibers annealed at 500 °C in air for 3 h. The average diameter of the nanofibers has been reduced from 345 nm to 180 nm (by 48%) due to removal of PVP templates.<sup>106</sup>

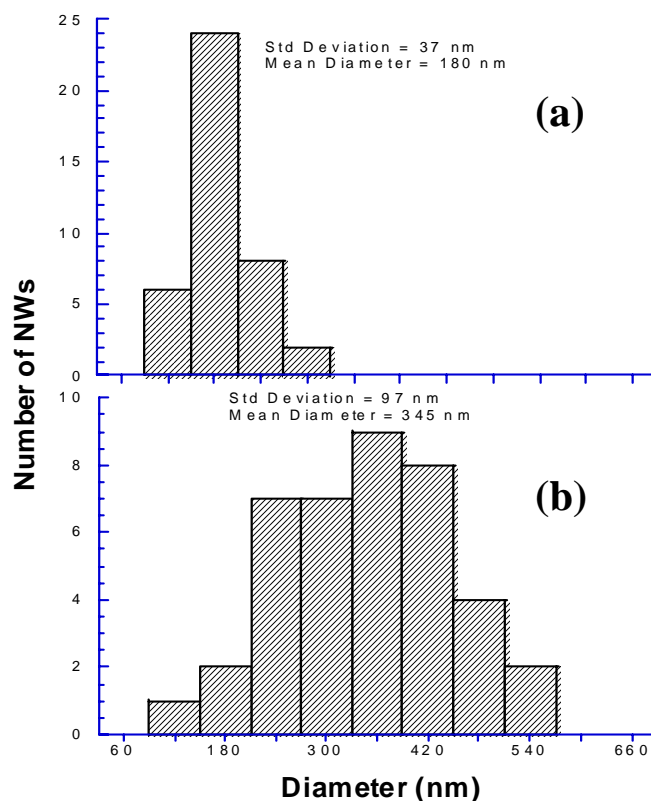


**Figure 72.** Diameter distributions of (a) Er<sub>2</sub>O<sub>3</sub> nanofibers annealed at 500 °C in air for 3 h; (b) as-formed Er<sub>2</sub>O<sub>3</sub>/PVP nanofibers.

### 5.2.2 Er-doped SiO<sub>2</sub> Nanofibers

Figure 73a shows the SEM image of as-prepared Er-doped SiO<sub>2</sub>/PVP fibers. In general, there are two types of fibers in terms of diameter. The thicker fibers are formed during the process of pushing the pump of the syringe to eject the viscous solution. This SEM image also shows that the fibers have smooth surfaces. Figure 73b is the SEM image of Er-doped SiO<sub>2</sub> nanofibers annealed at 800 °C for 3 h. The diameters of these annealed fibers have been greatly reduced, due probably to the removal of the organic PVP templates and the rearrangement of the silica matrix. Figure 73c is a typical TEM image of an Er-doped SiO<sub>2</sub>

nanofiber annealed at 700 °C in air for 3 h, showing that the nanofiber has a diameter of about 73 nm. The XEDS spectrum of Er-doped SiO<sub>2</sub> nanofibers (Figure 73d) confirms the presence of both erbium and silicon with an atomic ratio of around 1:50. A layer of 10 nm Au was also coated on the sample to obtain clearer SEM images, which is reflected in its XEDS spectrum.

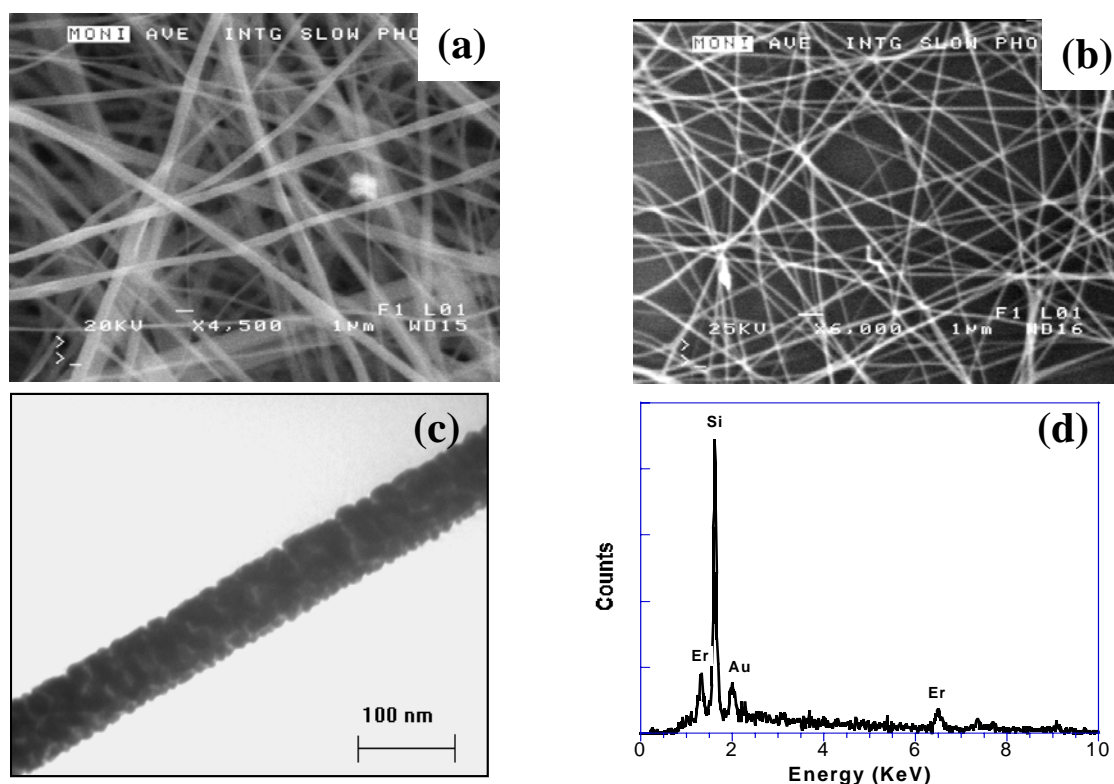


**Figure 73.** SEM images of (a) as-prepared Er-doped SiO<sub>2</sub>/PVP nanofibers and (b) the nanofibers annealed at 800 °C for 3 h in air. (c) TEM image of the fibers annealed at 700 °C in air for 3 h (from a Phillips EM300). (d) XEDS spectrum of the nanofibers confirms the presence of both Si and Er with an atomic ratio of ~50:1.

Figure 74 shows the diameter distributions of 2 at. % Er-doped SiO<sub>2</sub> nanofibers and the nanofiber sample annealed at 700 °C in air for 3 h. The average diameter has been reduced by 55% after the 700 °C anneal. Er-doped SiO<sub>2</sub> nanofibers with various concentrations of Er<sup>3+</sup> ions were simply prepared by adding different amount of erbium precursor in a given amount of TEOS solution. The concentration of erbium ions does not affect the general morphology of the fibers in terms of diameter, due to its relatively low concentration.

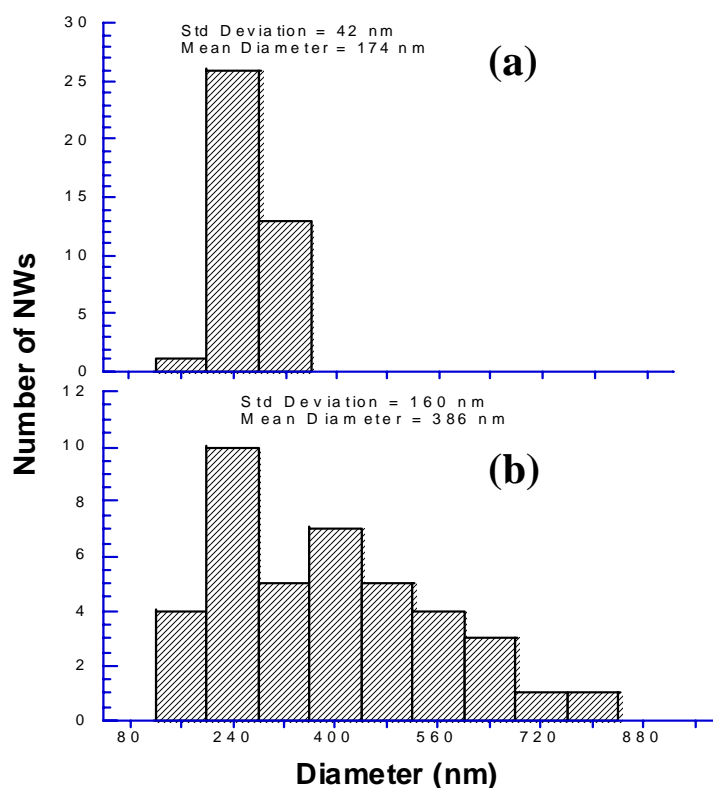


**Figure 74.** Diameter distributions of (a) a 2% Er-doped SiO<sub>2</sub> nanofiber sample annealed at 500 °C in air for 3 h; (b) as-formed 2% Er-doped SiO<sub>2</sub>/PVP nanofibers.

## 5.2.3 Er-doped GeO<sub>2</sub> Nanofibers

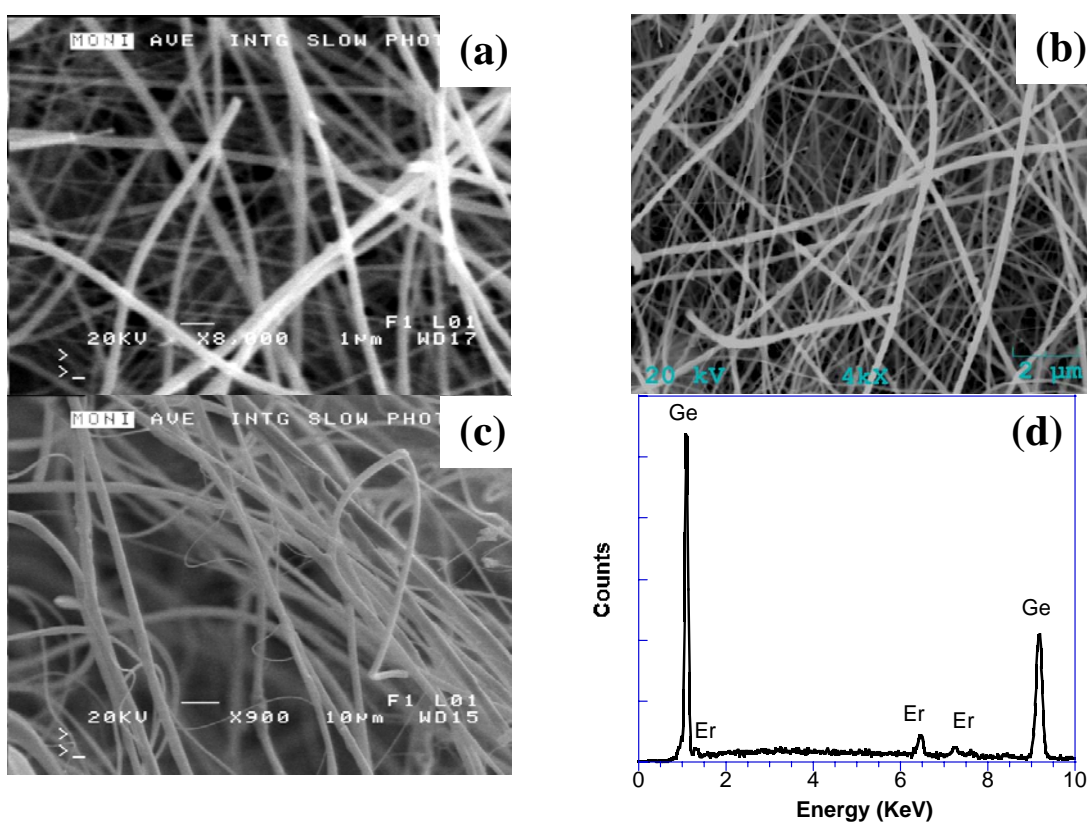
### 5.2.3.1 Characterization

Figure 75a shows the SEM image of as-prepared Er-doped GeO<sub>2</sub>/PVP fibers. The as-prepared fibers are smooth and uniform with a typical diameter of ~210 nm. Figure 75b is the SEM image of the fibers annealed at 500 °C for 3 h in air. It can be seen that the surfaces of these fibers remain smooth. However, after annealing the color of the fibers became grayish rather than whitish as in the case of Er<sub>2</sub>O<sub>3</sub> nanofibers. This grayish color is probably caused by the presence of residual GeO<sub>x</sub> that was formed by the carbothermal reducing reaction between the carbon (produced after the decomposition of PVP polymer) and the germanium (IV) precursor.<sup>153</sup> To fabricate Er-doped GeO<sub>2</sub> nanofibers, an appropriate solvent must be chosen, as otherwise only microfibers could be obtained. For example, if ethanol instead of methanol is used as the solvent, the solution will be too viscous to be suitable for electrospinning, and fibers of micron size in diameter were obtained as shown in Figure 75c. It is notable that the viscosity is a critical factor that can greatly affect the morphology of electrospun nanofibers.<sup>106</sup> No fibers can be obtained when the viscosity is below a critical value, and a higher viscosity can result in the formation of thicker electrospun fibers.<sup>99</sup> When the particles in a polymer solution are treated as spheres, Einstein's relationship for the viscosity can be applied:<sup>185</sup>

$$\eta/\eta_o = 1 + 2.5\phi \quad (18)$$

where  $\eta$  is the viscosity of a polymer solution,  $\phi$  is volume fraction of the polymer, and  $\eta_o$  is the viscosity of a solvent. It is known that methanol is much less viscous than ethanol (0.59

mPa·s vs. 1.2 mPa·s at 20°).<sup>186</sup> Therefore, according to the above equation, the solution of PVP/GeO<sub>2</sub> sol-gel in methanol should be less viscous than that in ethanol. As a consequence, thicker fibers were obtained using ethanol as a solvent. The XEDS spectrum (Figure 75d) confirms that there is ~4% erbium in the GeO<sub>2</sub> nanofibers, where Ge-L $\alpha$  and Er-L $\alpha$  peaks lie at 1.2 and 6.9 KeV, respectively.



**Figure 75.** SEM images of (a) as-prepared Er-doped GeO<sub>2</sub>/PVP fibers using methanol as a solvent. (b) The fibers annealed at 500 °C for 3 h in air. (c) As-prepared Er-doped GeO<sub>2</sub>/PVP fibers using ethanol as solvent. (d) XEDS spectrum of ~4% Er-doped GeO<sub>2</sub> nanofibers.

The diameter distributions of as-formed 2% (atomic percentage) Er-doped GeO<sub>2</sub> nanofibers and the annealed ones are shown in Figure 76. The average diameter was found to

be reduced from 618 nm to 388 nm after a 500 °C annealing in air for 3 h, which corresponds to a 37% reduction in diameter.

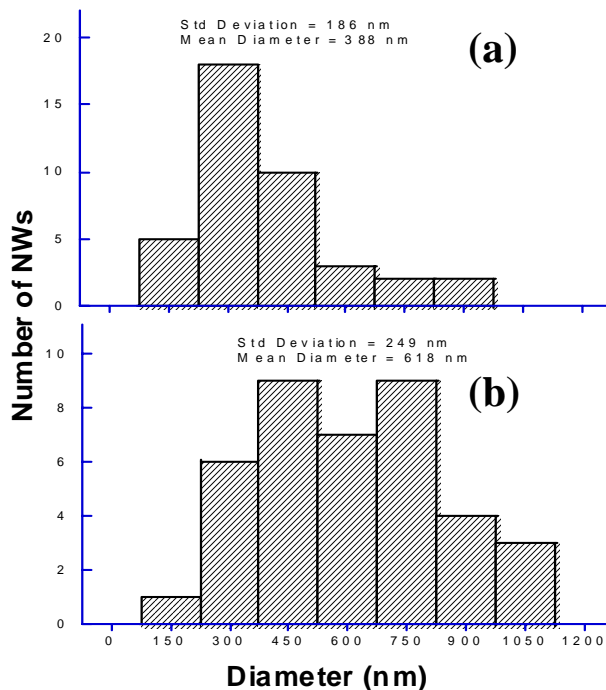


**Figure 76.** Diameter distributions of (a) 2% Er-doped GeO<sub>2</sub>/PVP nanofibers annealed at 500 °C in air for 3 h. (b) As-formed 2% Er-doped GeO<sub>2</sub>/PVP nanofibers.

### 5.2.3.2 Effect of Annealing Temperatures

Er-doped GeO<sub>2</sub> fibers annealed at various temperatures have quite different colors and morphologies. The fibers annealed at 500 and 700 °C are dark and light grayish, respectively. However, the color of the fibers annealed at 900 °C is white. It is known that GeO has a dark color and sublimates at 710 °C.<sup>187</sup> It is possible that some GeO<sub>x</sub> formed by the carbothermal reducing reaction during annealing process might be trapped in the host materials when the temperature is lower than the sublimation point of GeO. As a

consequence, the fibers annealed at 500 and 700 °C appear dark. When the annealing temperature is above the sublimation point of GeO, GeO<sub>x</sub> becomes more volatile such that much less GeO<sub>x</sub> could be trapped in the host materials and only white GeO<sub>2</sub> is left. It is also possible that GeO<sub>x</sub> tends to be completely oxidized into GeO<sub>2</sub> at higher temperatures so that the fibers appear whitish in terms of appearance.

It was also found that the morphologies of Er-doped GeO<sub>2</sub> nanofibers changed drastically along with increasing annealing temperatures. Figure 77 shows the SEM images of Er-doped GeO<sub>2</sub> nanofibers annealed at 500, 700, and 900 °C for 3 h in air. The fibers can maintain their morphology after being annealed at 500 °C, and started to grow thicker when they were annealed at 700 °C. The formation of thick nanofibers is probably due to an Ostwald ripening effect, that is, small islands grow into larger islands due to the chemical potential differences between islands.<sup>188</sup> The fibers were totally fused together, and no individual fibers can be observed after being annealed at 900 °C. The presence of impurities, such as erbium ions might result in the decrease of the melting point of GeO<sub>2</sub>, which leads to the fusion of the fibers at the temperature below the melting point of GeO<sub>2</sub> (1115 °C).

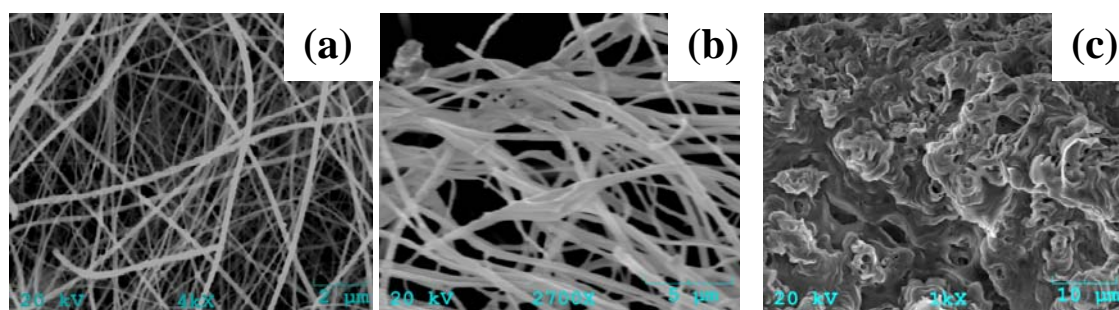


**Figure 77.** SEM images of Er-doped GeO<sub>2</sub> nanofibers annealed at (a) 500 °C; (b) 700 °C; and (c) 900 °C in air for 3 h.

### 5.2.3.3 FT-infrared (IR) Vibrational Spectroscopy

FT-IR spectra of Er-doped GeO<sub>2</sub> nanofibers annealed at various temperatures are shown in Figure 78. All spectra have a weak peak at  $\sim 432\text{ cm}^{-1}$  in the low frequency region, which is attributed to trace amounts of the rutile phase GeO<sub>2</sub>.<sup>189</sup> The absence of a C=O stretching vibration at  $1660\text{ cm}^{-1}$  means that the PVP polymer has been completely removed by this thermal annealing process.<sup>190</sup> The FT-IR spectrum of the fiber sample annealed at  $900\text{ }^{\circ}\text{C}$  matches well that of standard quartz phase GeO<sub>2</sub>,<sup>189</sup> which suggests that this sample has been completely oxidized. Three peaks at  $517$ ,  $550$ , and  $586\text{ cm}^{-1}$  are from the O-Ge-O bending vibrations, and another two peaks at  $872$  and  $962\text{ cm}^{-1}$  are from the asymmetric and symmetric O-Ge-O stretching vibrations, respectively.<sup>191</sup> For the Er-doped GeO<sub>2</sub> fibers annealed at  $500\text{ }^{\circ}\text{C}$  and  $700\text{ }^{\circ}\text{C}$ , their FT-IR spectra only show two broad peaks in the ranges of  $550\text{-}650\text{ cm}^{-1}$  and  $800\text{-}950\text{ cm}^{-1}$ , which indicates that they might be composed of amorphous GeO<sub>2</sub> or GeO<sub>x</sub>.<sup>192</sup>

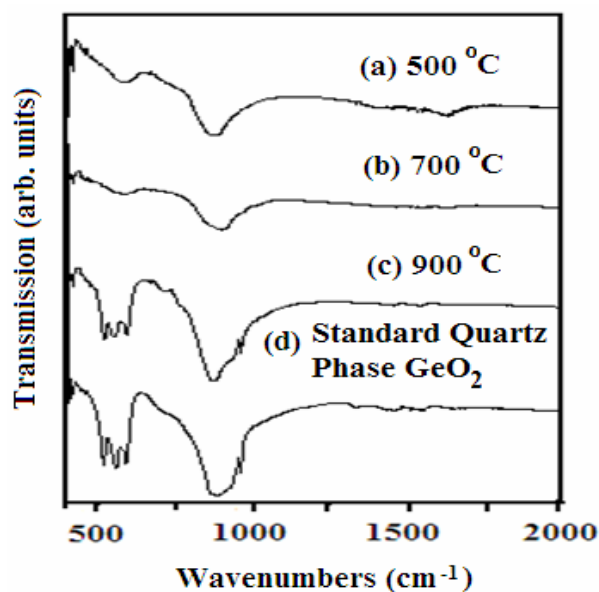


**Figure 78.** FT-IR spectra of Er-doped GeO<sub>2</sub> nanofibers annealed in air for 3 h at (a) 500 °C; (b) 700 °C; (c) 900 °C; and (d) Standard quartz phase GeO<sub>2</sub>.

#### 5.2.4 Er-doped SnO<sub>2</sub> Nanofibers

Er-doped SnO<sub>2</sub> nanofibers were structurally characterized using SEM, TEM, HRTEM, SAED, XEDS linescans, and XRD. XRD and TEM imaging were also employed to study the effects of anneal temperature and the presence of erbium on the morphology of these nanofibers and the sizes of SnO<sub>2</sub> nanocrystals.

##### 5.2.4.1 Characterization

A SEM image of as-prepared Er-doped SnO<sub>2</sub>/PVP fibers is shown in Figure 79a. In general, there are two types of fibers, that is, one type is about 500 nm in diameter, and another type is about 200 nm in diameter. After annealing, the diameters of these fibers do not change as much as those of the above nanofibers (Figure 79b). Figure 79c shows the

TEM image of an Er-doped SnO<sub>2</sub> nanofiber annealed at 900 °C for 3 h in air, which was recorded using the JEM-3010 TEM at the University of Illinois-Chicago. This fiber has a diameter of ~590 nm and is composed of lots of nanoparticles. An XEDS spectrum of 4% (atomic percentage) Er-doped SnO<sub>2</sub> fibers (Figure 79d) confirms the presence of Sn and Er, where the Sn-L $\alpha$  and Er-M $\alpha$  peaks lie at 3.5 and 1.4 KeV, respectively.

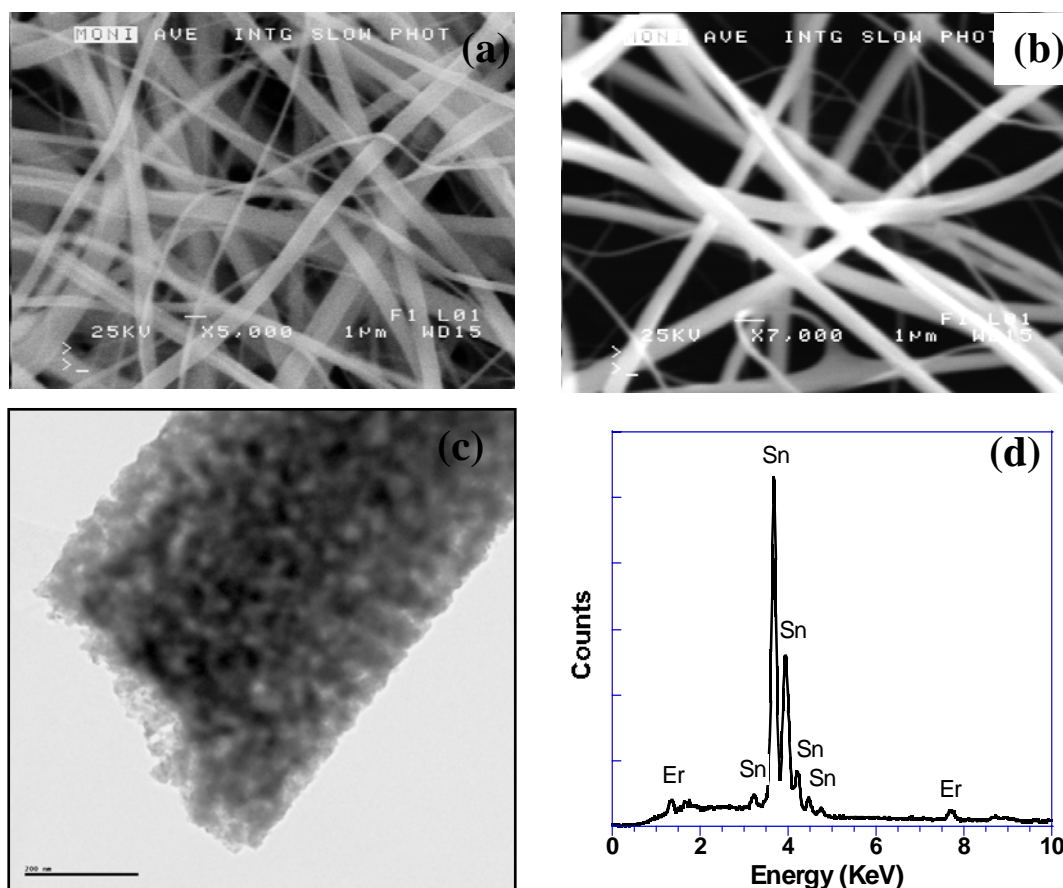


**Figure 79.** SEM images of (a) As-prepared 4% (atomic percentage) Er-doped SnO<sub>2</sub> nanofibers; (b) the fibers annealed at 800 °C for 3 h in air; (c) TEM image of a 4% Er-doped SnO<sub>2</sub> nanofiber with a diameter of 590 nm (scale bar = 200 nm); (d) XEDS spectrum of a 4% Er-doped SnO<sub>2</sub> nanofiber sample confirming the presence of Er and Sn.

Figure 80 shows the diameter distributions of as-formed 4% (atomic percentage) Er-doped SnO<sub>2</sub> nanofibers and the annealed ones. It was found that the nanofibers only have a 28% reduction in diameter, which is much smaller than the reduction in the cases of Er-doped SiO<sub>2</sub> and Er<sub>2</sub>O<sub>3</sub> nanofibers (~50%). This result is due to the difference in the ratios of PVP polymer to oxide precursor and the relative higher atomic number of tin than silicon.<sup>106</sup>

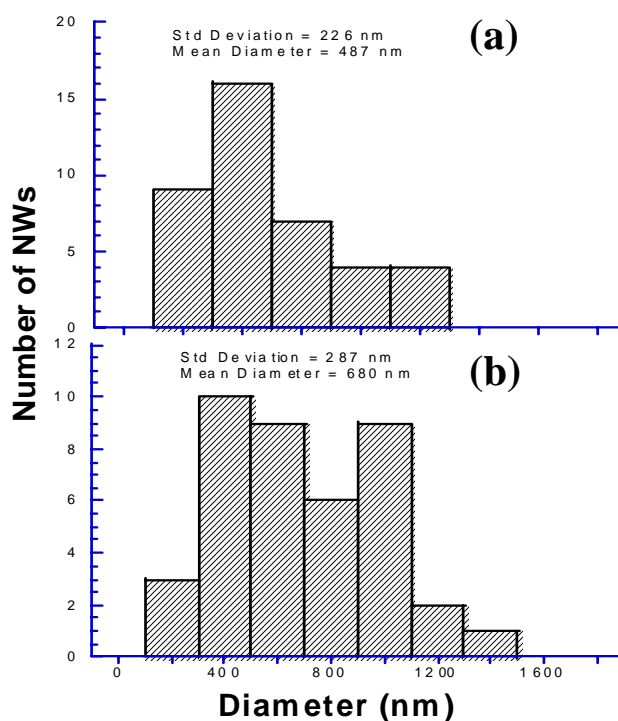


**Figure 80.** Diameter distributions of (a) 4% Er-doped SnO<sub>2</sub>/PVP nanofibers annealed at 700 °C in air for 3 h. (b) As-formed 4% Er-doped SnO<sub>2</sub>/PVP nanofibers.

#### 5.2.4.2 SAED, HRTEM and XEDS Linescan Analysis

Selected-area electron diffraction (SAED), HRTEM and XEDS linescans were used to further investigate the structure and composition of Er-doped SnO<sub>2</sub> nanofibers. Figure 81a shows the SAED pattern obtained from a single fiber shown in the inset. This SAED pattern

is consistent with a polycrystalline structure. The inner 6 diffraction rings in turn are from (110), (101), (200), (211) and (301) crystal planes of tetragonal SnO<sub>2</sub>, which are assigned according to their calculated d-spacing values. Figure 81b shows the HRTEM image of an Er-doped SnO<sub>2</sub> fiber annealed at 900 °C for 3 h in air. The lattice image shows that the nanocrystals have a d-spacing value 3.389 Å in the circled areas, which is a 1.3% deviation from the standard value (3.347 Å for (110) crystal plane of tetragonal SnO<sub>2</sub>, JCPDS-ICDD PDF No. 41-1445). The HRTEM image also shows that a typical size of SnO<sub>2</sub> nanocrystals is about 10 nm.

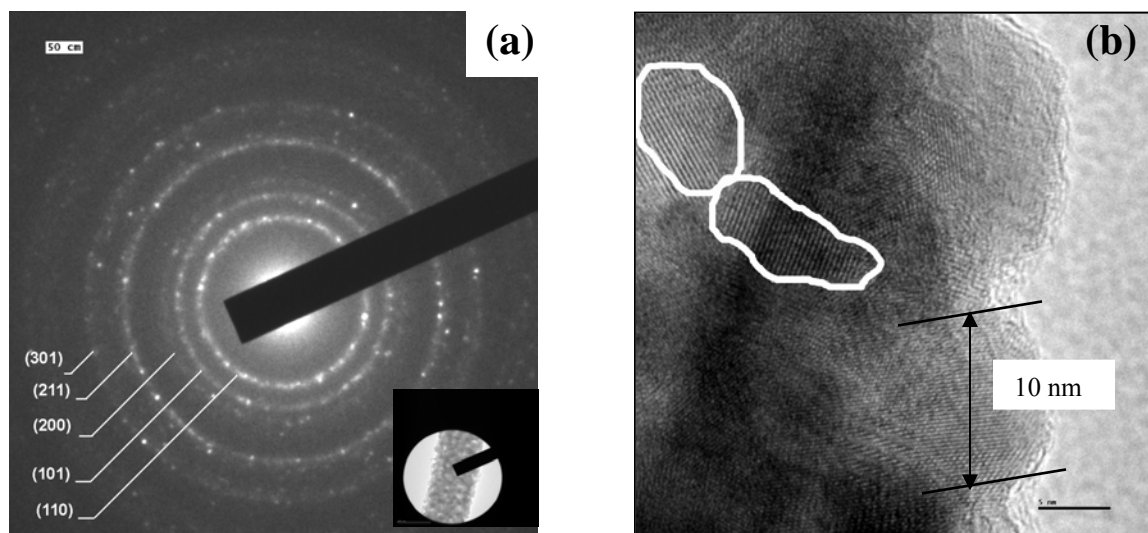


**Figure 81.** (a) SAED pattern obtained from a single Er-doped SnO<sub>2</sub> fiber shown in the inset (Scale bar = 200 nm). (b) HRTEM images of SnO<sub>2</sub> nanocrystals in an Er-doped SnO<sub>2</sub> nanofiber showing that the nanocrystals have a d-spacing value of 3.347 Å (scale bar = 5 nm).

Note: All Er-doped SnO<sub>2</sub> nanofibers have been annealed at 900 °C in air for 3 h.

Figure 82b presents the XEDS linescans across a ~60 nm Er-doped SnO<sub>2</sub> nanofiber

shown in Figure 82a. The nanofiber has been annealed at 900 °C in air for 3 h. The linescans suggest that erbium ions are uniformly distributed among the SnO<sub>2</sub> host matrix without significant clustering of Er<sub>2</sub>O<sub>3</sub>.

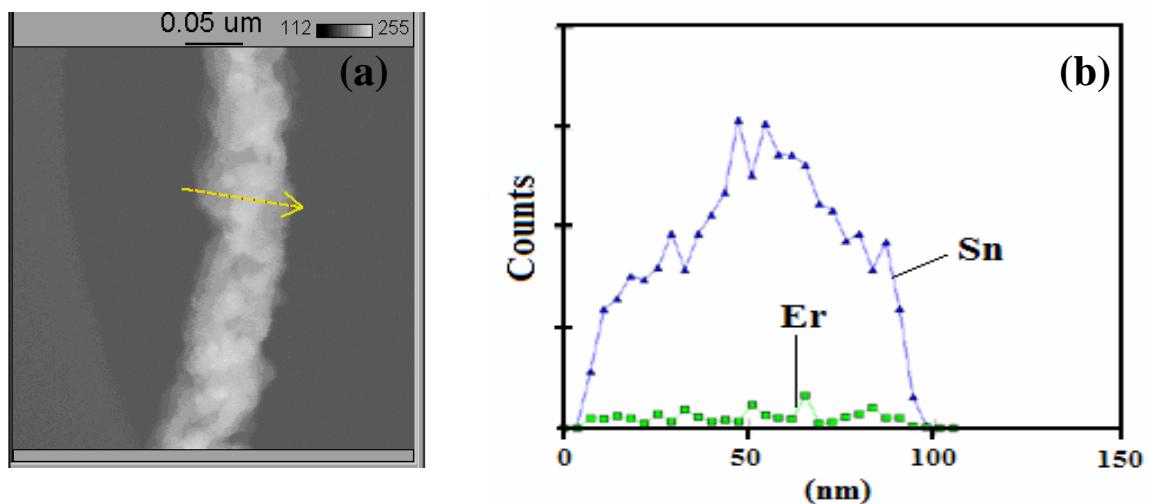


**Figure 82.** (a) High angle annular dark field (HAADF) image of an Er-doped SnO<sub>2</sub> nanofiber that was annealed at 900 °C for 3 h in air. (b) XEDS linescans across the fiber shown in Figure 72a.

#### 5.2.4.3 X-ray Diffraction

Figure 83a shows the XRD patterns of 4% (atomic percentage) Er-doped SnO<sub>2</sub> nanofiber sample annealed at 900 °C in air for 3 h. Sharp diffraction peaks indicate that the sample was well-crystallized, and all peaks match well those of the standard tetragonal phase of SnO<sub>2</sub> (ICDD PDF # 41-1445). Figure 83b is the XRD patterns of 4% (atomic percentage) Er-doped SnO<sub>2</sub> nanofiber sample annealed at 1000 °C in air for 3 h. It is notable that two new peaks appear at 29.58° and 58.64°, which are from the (222) and (622) crystal planes of bcc

(body centered cubic)  $\text{Er}_2\text{O}_3$  (ICDD PDF # 08-0050). This indicates that erbium ions are starting to precipitate at a 1000 °C annealing temperature.

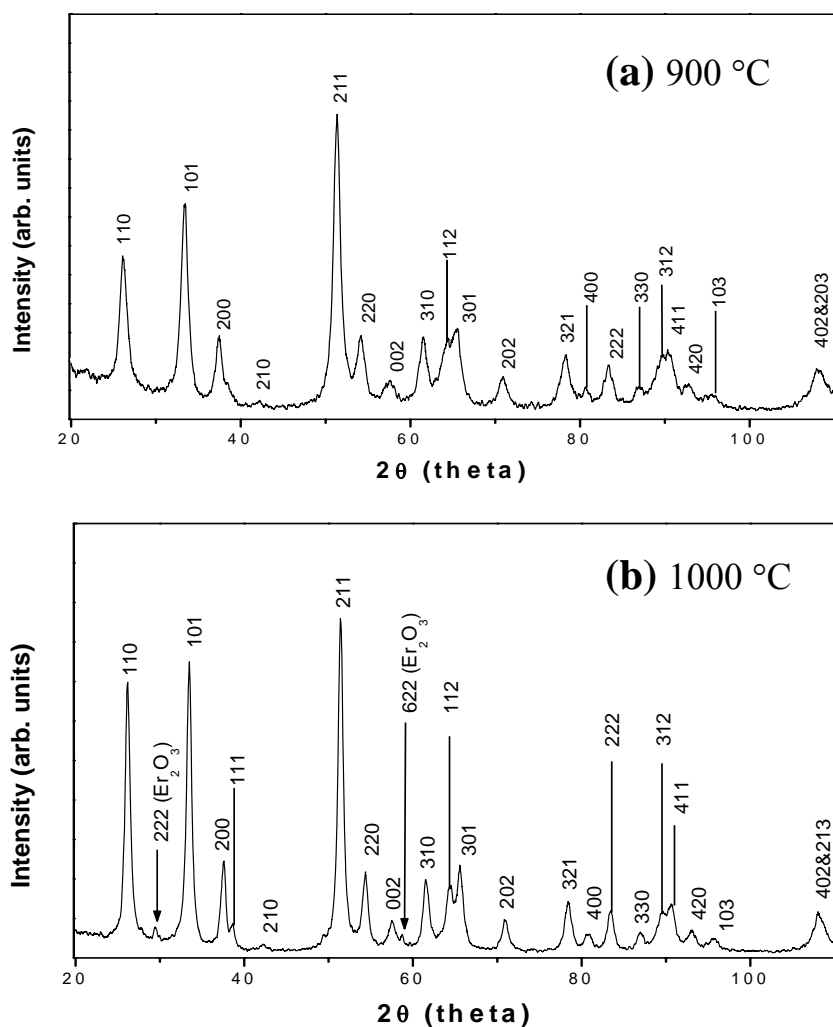


**Figure 83.** XRD patterns of 4% Er-doped  $\text{SnO}_2$  nanofibers annealed in air for 3 h at (a) 900 °C and (b) 1000 °C.

#### 5.2.4.4 Effect of Annealing Temperatures on the Size of $\text{SnO}_2$ Nanocrystals

X-ray diffraction and a Philips EM300 TEM were used to investigate the effect of annealing temperatures on the size of  $\text{SnO}_2$  nanocrystals in Er-doped  $\text{SnO}_2$  nanofibers. Figure

84 shows the XRD patterns of Er-doped SnO<sub>2</sub> nanofibers annealed at various temperatures ranging from 500 to 1000 °C. The full widths at half maximum peak value (FWHM) are decreasing along with increasing annealing temperatures, which means that the average grain diameter of SnO<sub>2</sub> nanocrystals in the fiber is increased after being annealed at a higher annealing temperature.

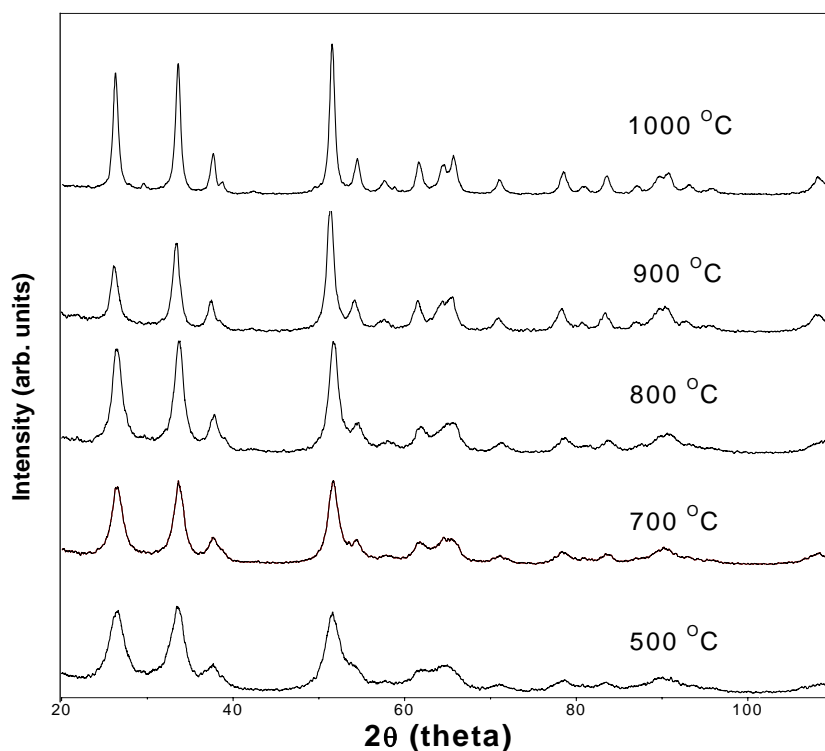


**Figure 84.** XRD patterns of a 4% (atomic percentage) Er-doped SnO<sub>2</sub> nanofiber sample annealed at various temperatures ranging from 500 to 1000 °C showing that FWHMs are decreasing along with increasing annealing temperatures.

Table 7 presents the average diameters of SnO<sub>2</sub> nanocrystals in Er-doped SnO<sub>2</sub> nanofibers that were annealed at temperatures ranging from 500 to 1000 °C. The average

diameters were calculated using the classical Scherrer formula represented by equation (19):<sup>193,194</sup>

$$D (HKL) = K \lambda / (\beta \cos\theta) \quad (19)$$

where D is the average diameter of nanocrystals, HKL is Miller indices of the crystal planes, K is the shape factor (0.90),  $\lambda$  is the wavelength of the X-ray (1.54178 Å),  $\beta$  is FWHM of the peak at the diffraction angle, and  $\theta$  is diffraction angle. The (110) diffraction peak was used to calculate the average diameters of SnO<sub>2</sub> nanocrystals. The average diameter of SnO<sub>2</sub> nanocrystals is only 3.27 nm when the annealing temperature is 500 °C, whereas the average diameter is increased to 13.3 nm after being annealed at 1000 °C.

**Table 7.** Average diameters of SnO<sub>2</sub> nanocrystals in Er-doped SnO<sub>2</sub> fibers that were annealed at temperatures ranging from 500 to 1000 °C (Scherrer's formula and (110) diffraction peak were used to calculate these diameters.).

Annealing Temperature (°C)	FWHM (110)	D(110) (Å)
500	2.50°	32.7
700	1.49°	54.8
800	1.21°	67.5
900	1.00°	81.7
1000	0.616°	133

TEM imaging was employed to measure the size of SnO<sub>2</sub> in the fibers qualitatively.

Figure 85 shows the TEM images of 4% Er-doped SnO<sub>2</sub> nanofibers annealed at 500, 700, 800, 900 and 1000 °C. The edges of these fibers are getting rougher and rougher along with increasing annealing temperatures due to the formation of bigger SnO<sub>2</sub> nanocrystals, which again is consistent with an Ostwald ripening mechanism.<sup>188</sup> These results are also consistent with the above XRD characterization.

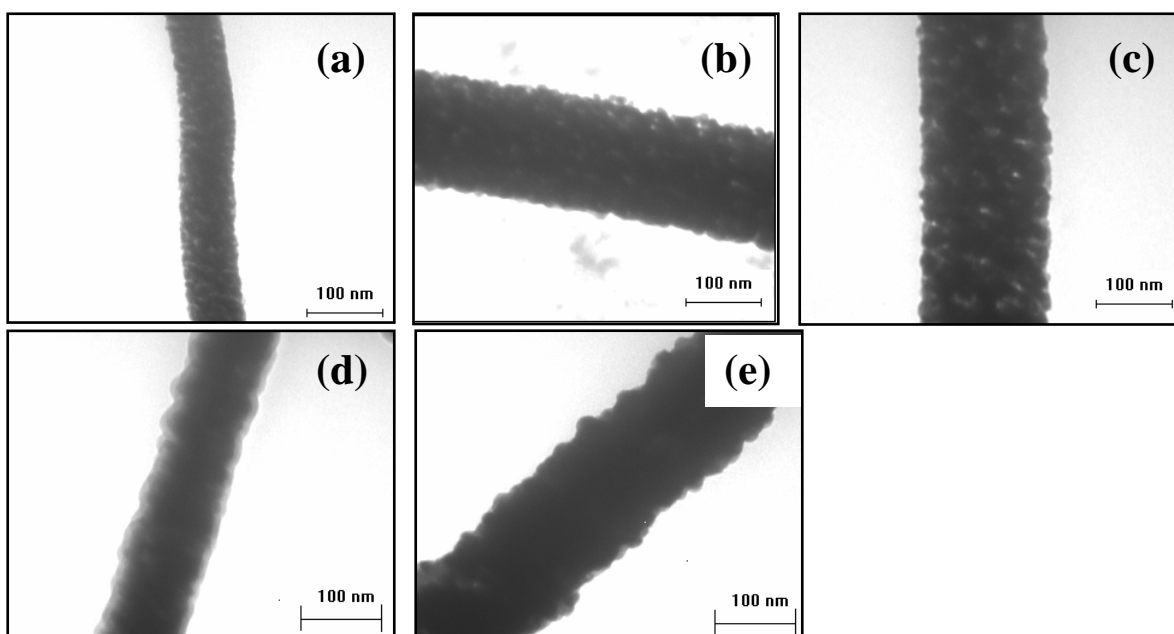


**Figure 85.** TEM images of 4% Er-doped SnO<sub>2</sub> nanofibers annealed at (a) 500 °C; (b) 700 °C; (c) 800 °C; (d) 900 °C; and (e) 1000 °C.

#### 5.2.4.5 Effect of the Presence of Er<sup>3+</sup> Ions on the Size of SnO<sub>2</sub> Nanocrystals

XRD and TEM imaging were also used to investigate the effect of erbium ions on the size of SnO<sub>2</sub> nanocrystals in the fibers. Figure 86 shows the XRD patterns of pure SnO<sub>2</sub> and Er-doped SnO<sub>2</sub> nanofibers that were annealed at 1000 °C in air for 3 h. The diffraction peaks of pure SnO<sub>2</sub> nanofibers are sharper than those of Er-doped SnO<sub>2</sub> nanofibers, which means

that the average size of SnO<sub>2</sub> nanocrystals in pure SnO<sub>2</sub> nanofibers is larger.<sup>194</sup> Table 8 shows the average diameters of SnO<sub>2</sub> nanocrystals for these two nanofiber samples calculated using the above Scherrer formula. The average size of SnO<sub>2</sub> nanocrystals is about 30.0 nm in pure SnO<sub>2</sub> fibers that were annealed at 1000 °C, whereas the value is only ~13.3 nm for 4% Er-doped SnO<sub>2</sub> fibers annealed at the same temperature. This fact suggests that the presence of erbium ions can greatly increase the number of nucleation sites for the growth of SnO<sub>2</sub> nanocrystals resulting in the formation of smaller nanocrystals. It is also possible that erbium ions on the surface of these SnO<sub>2</sub> nanocrystals can serve as a diffusion barrier so that the growth of larger particles is suppressed.

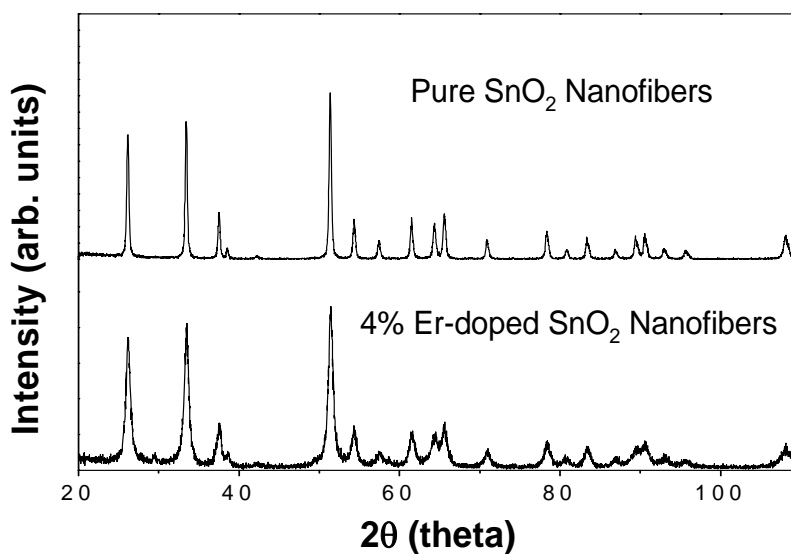


**Figure 86.** XRD patterns of pure SnO<sub>2</sub> nanofibers and 4% (atomic percentage) Er-doped SnO<sub>2</sub> nanofibers. Note: both fibers were annealed at 1000 °C in air for 3 h.

**Table 8.** Average diameters of SnO<sub>2</sub> nanocrystals in pure and Er-doped SnO<sub>2</sub> nanofibers calculated using Scherrer formula and (110) diffraction peak. Note: both samples were annealed at 1000 °C in air for 3 h.

Sample	FWHM (110)	D(110) (Å)
Pure SnO <sub>2</sub> fibers	0.296°	300
4% Er-doped SnO <sub>2</sub> fibers	0.616°	133

TEM images of pure SnO<sub>2</sub> and 4% Er-doped SnO<sub>2</sub> nanofibers annealed at 1000 °C in air for 3 h are shown in Figure 87. A typical size of SnO<sub>2</sub> nanocrystals in pure nanofibers is ~36 nm, which is very close to the value (30 nm) calculated using Scherrer formula above. The size of nanocrystals in Er-doped SnO<sub>2</sub> nanofibers is clearly much smaller than that in pure SnO<sub>2</sub> nanofibers.

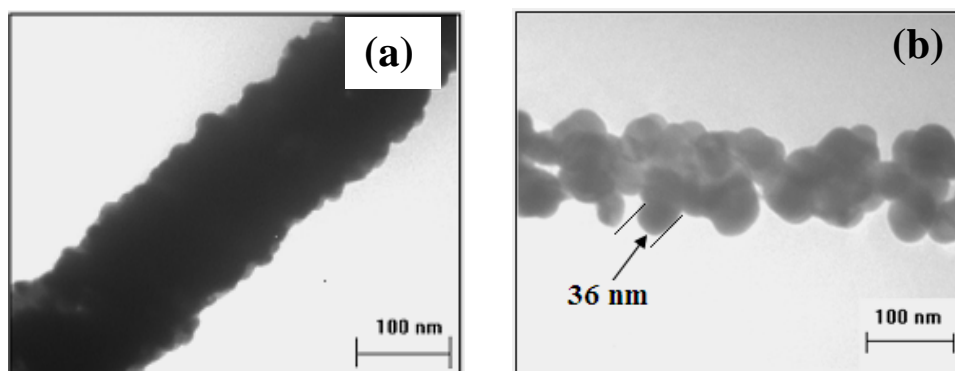


**Figure 87.** TEM images of (a) 4% Er-doped SnO<sub>2</sub> nanofibers. (b) Pure SnO<sub>2</sub> nanofibers. All fibers were annealed at 1000 °C in air for 3 h.

### 5.2.5 Effect of PVP Concentration on the Diameter of Er-doped SnO<sub>2</sub> Nanofibers

The concentrations of PVP solution were varied to investigate their effects on the diameter of Er-doped SnO<sub>2</sub> nanofibers. Figure 88a and Figure 88b are the SEM images of 4% (atomic percentage) Er-doped SnO<sub>2</sub> nanofibers that were prepared using a 0.30 g PVP/1.2 ml ethanol solution and a 0.20 g PVP/1.2 ml ethanol solution, respectively. These nanofibers were annealed at 800 °C in air for 3 h before SEM measurements. The nanofibers prepared using a 0.3 g PVP/1.2 ml ethanol solution are almost two times thicker on average than those prepared using a 0.2 g PVP/1.2 ml ethanol solution. This phenomenon suggests that a more viscous solution can lead to the formation of thicker Er-doped SnO<sub>2</sub> nanofibers.<sup>106</sup> Recall that according to the above Einstein equation, the lower the volume fraction of a given polymer, the less viscous the polymer solution will be, provided that the same solvent is used. Figure 88c shows the diameter distribution of Er-doped SnO<sub>2</sub> nanofibers shown in Figure 88b. These nanofibers have an average diameter of 203 nm, which is much thinner than those fibers shown in Figure 88a (487 nm on average). The concentration of polymer solution is one of the most important factors that could affect the diameters of electrospun nanofibers.<sup>106</sup> It has been reported that the average diameter of TiO<sub>2</sub>/PVP nanofibers can be reduced from 100 nm to 50 nm while the PVP polymer concentration was decreased from 0.04 g/ml to 0.02 g/ml.<sup>106</sup>

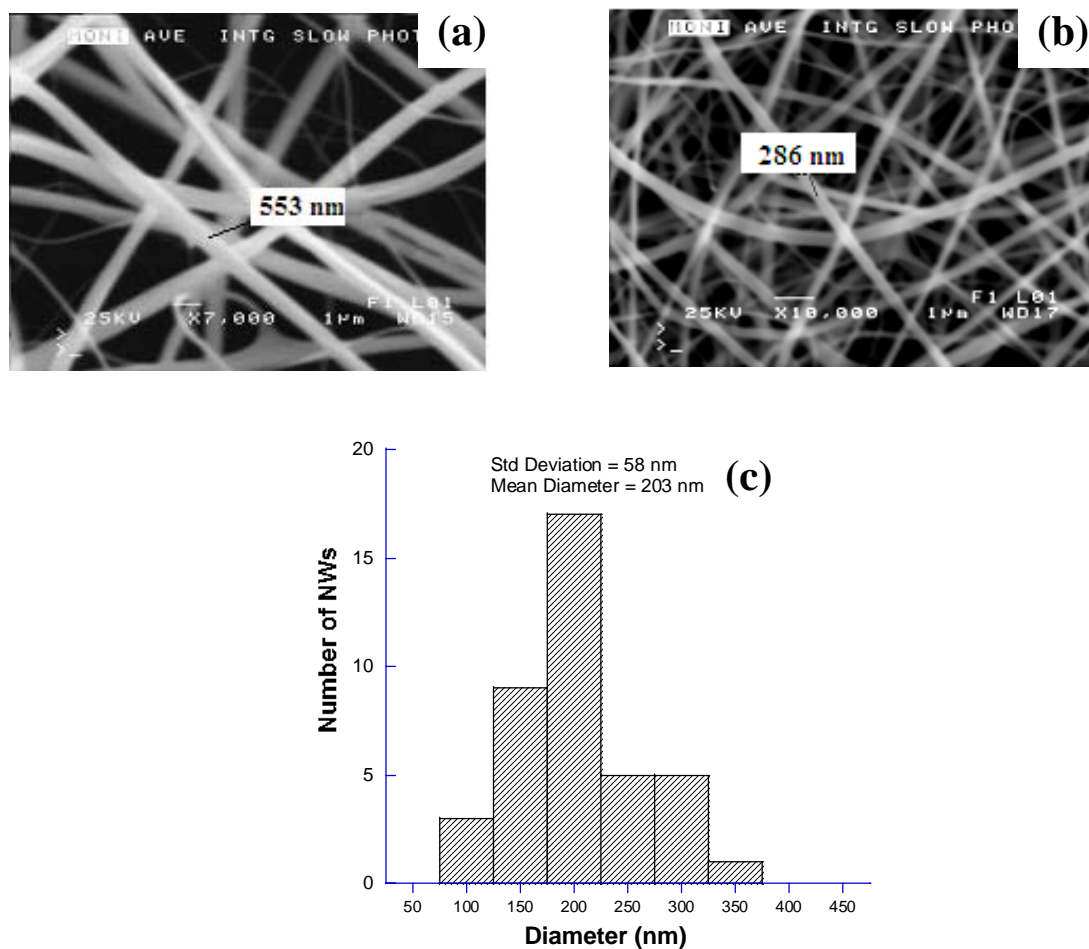


**Figure 88.** SEM images of 4% (atomic percentage) Er-doped SnO<sub>2</sub> nanofibers that were prepared using (a) a 0.3 g PVP/1.2 ml ethanol solution; (b) a 0.2 g PVP/1.2 ml ethanol solution. (c) Diameter distribution of the nanofibers shown in Figure 88b.

## 5.2.6 Nanofiber Arrays

Figure 89 shows the SEM and optical images of the arrays of PVP, Er<sub>2</sub>O<sub>3</sub>/PVP, and Er-doped SiO<sub>2</sub>/PVP fibers prepared using the two approaches described in the experimental section of this chapter. It can be easily seen that most fibers were well aligned and parallel to each other; however, some fibers are disordered, probably due to disturbances such as the

manual pumping of the syringe and fluctuations in local air currents during the electrospinning process. As-mentioned in Chapter 1, the arrays are directed by two kinds of electrostatic interactions. One is the repulsive force between the charged fibers and another one is the Coulomb attraction force between the positively charged fibers and the negatively charged grounding electrodes. In our case, the grounding devices are wood support & metal clamp, and p-type Si wafers. It should be pointed out that the arrays of fibers can only be produced across the insulating gap between two grounding devices. Furthermore, theoretically, these two approaches to array fibers could be applied to obtain other types of fiber arrays, such as Er-doped  $\text{SnO}_2$  and  $\text{GeO}_2$  nanofibers.

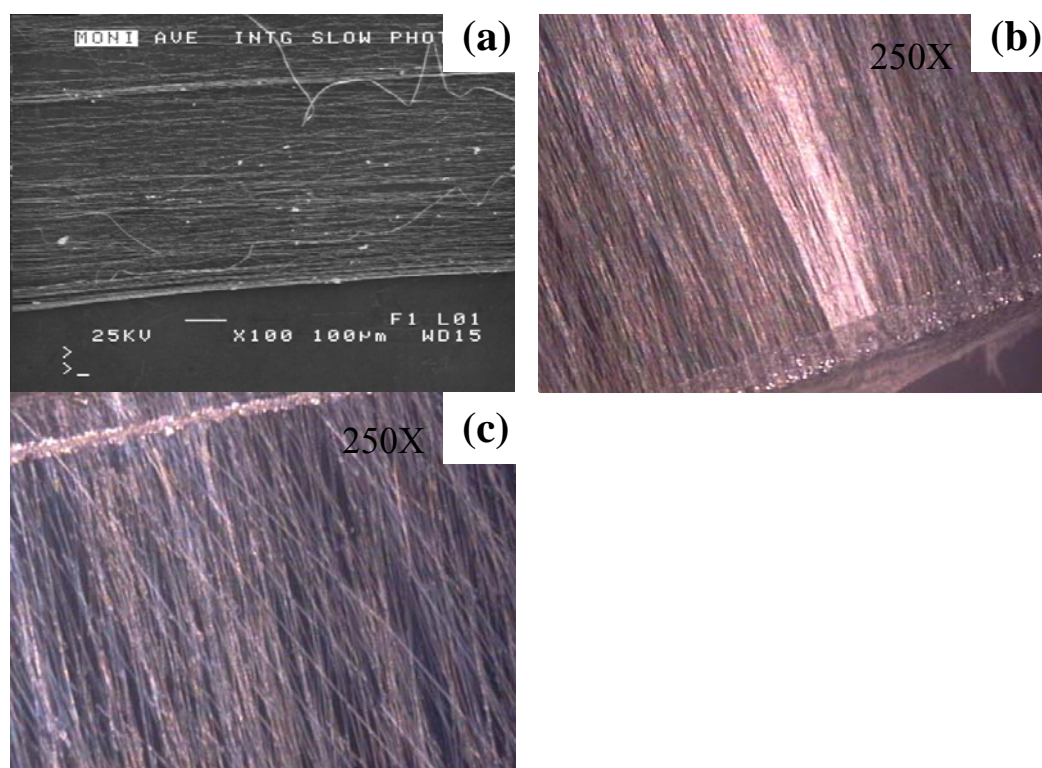


**Figure 89.** (a) SEM image of an Er-doped  $\text{SiO}_2$  nanofiber array. Optical images of (b) a PVP fiber array (250X) and (c) an  $\text{Er}_2\text{O}_3/\text{PVP}$  fiber array (250X).

### 5.2.7 Er-doped Crystalline GeO<sub>2</sub> NWs

To further understand the mechanism of erbium luminescence in Er-doped Ge NWs, we prepared Er-doped crystalline GeO<sub>2</sub> NWs and compared their near-IR PL properties with those of Er-doped GeO<sub>2</sub> nanofibers and Ge NWs.

#### 5.2.7.1 Characterization

Figure 90a shows the SEM image of as-prepared GeO<sub>2</sub> nanowires prepared through a vapor transport method combined with a carbothermal reduction reaction. A Si wafer coated with an 8 nm thick sputtered Au film was used as substrate, and the reaction time was 30 minutes. These GeO<sub>2</sub> nanowires have diameters ranging from 1 to 8 μm and lengths up to hundreds of microns. Figure 90b is the SEM image of the GeO<sub>2</sub> NWs prepared using a 15 minute reaction time. The typical diameter of these nanowires is reduced to ~120 nm, while their lengths are shortened to tens of microns. In general, shorter reaction times lead to the formation of thinner and shorter GeO<sub>2</sub> nanowires. Figure 90c shows the SEM image of GeO<sub>2</sub> NWs produced on the most front part of the Si wafer. These NWs are much thicker than those produced on the back part of the Si wafer due to the existence of an intrinsic temperature gradient in the reactor. The front part is hotter than the back part because of the former's proximity to the ceramic oven. Therefore, the gold catalysts on the front part of the wafer can grow larger resulting in the formation of thicker NWs in accordance to the VLS mechanism. These thicker NWs (Figure 90c) have diameters and lengths range from 1 to 2 μm and 10 to 20 μm, respectively. A TEM image of a typical GeO<sub>2</sub> nanowire recorded using a Philips EM300 TEM is shown in Figure 90d. The nanowire has a diameter of ~62 nm and

the presence of a catalyst on the tip of the NW implies that the NW was grown via a VLS synthetic route.

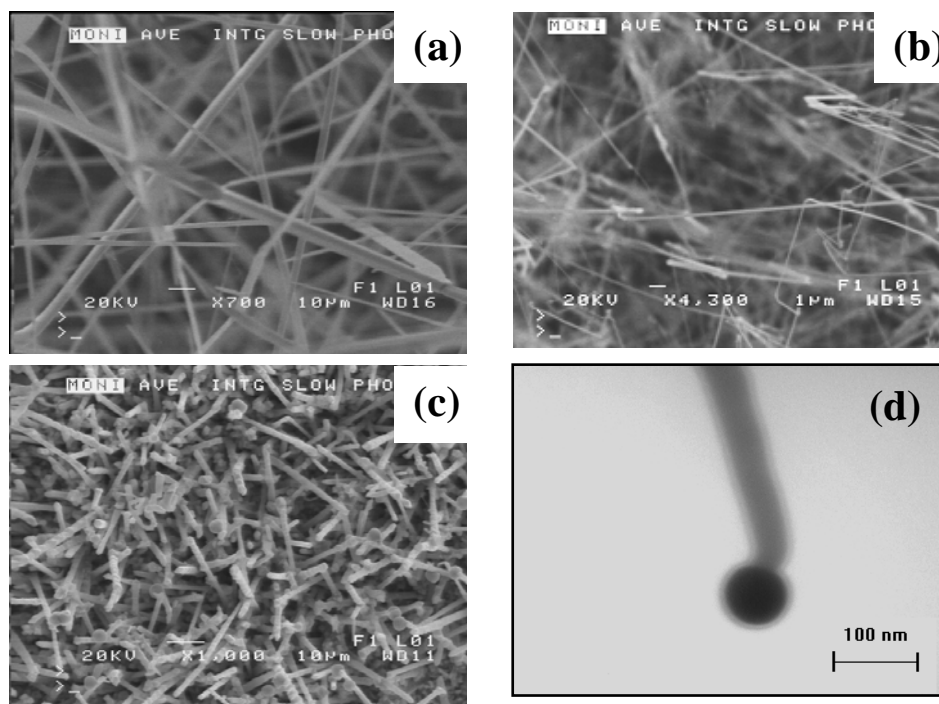


**Figure 90.** SEM images of (a) GeO<sub>2</sub> NWs grown using a 30 minute reaction time; (b) GeO<sub>2</sub> NWs grown using a 15 minute reaction time; and (c) the most front part of the sample prepared using a 30 minute reaction time. (d) TEM image of a typical GeO<sub>2</sub> NW with a catalyst on its tip (dark contrast). Note: all GeO<sub>2</sub> NWs were prepared at 940 °C on a piece of Si wafer that was coated with an eight nm thick Au film.

Figure 91a shows the SEM image of Er-doped GeO<sub>2</sub> NWs that were exposed to erbium vapor for 1 h. The diameters of the NWs are very close to those of the GeO<sub>2</sub> NWs due to the thin coating of erbium. The corresponding XEDS spectrum (Figure 91b) suggests that the erbium concentration is about 8.5% (atomic percentage), which is close to that of the Er-doped Ge NWs (~5.4% in the middle of the NW) as described in Chapter 3.

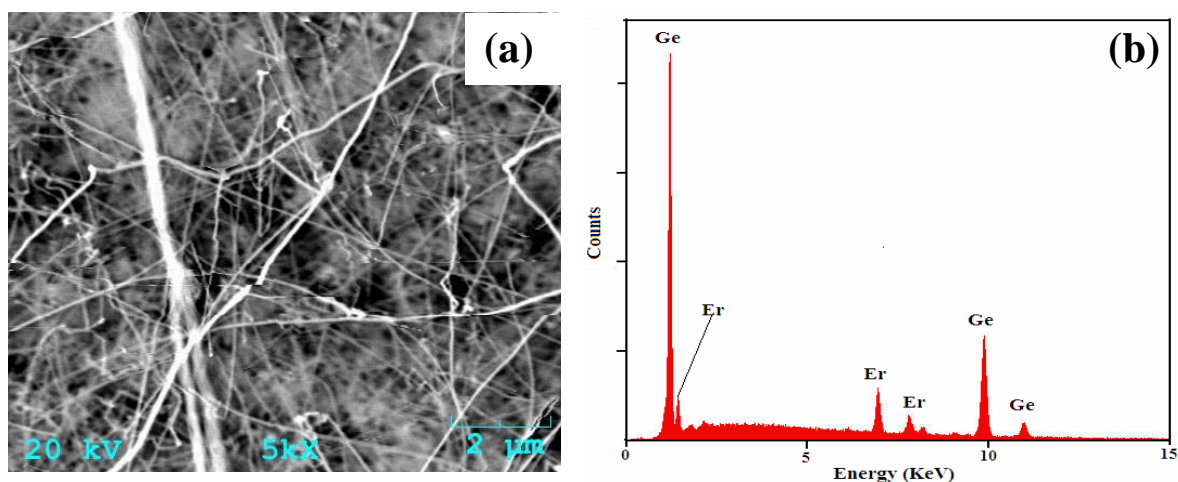


**Figure 91.** (a) SEM image of Er-doped GeO<sub>2</sub> NWs that were exposed to erbium vapor for 1 h. (b) The XEDS spectrum of the sample shown in Figure 86a.

### 5.2.7.2 XRD

XRD patterns of as-formed GeO<sub>2</sub> nanowires are shown in Figure 92. All diffraction peaks match well those of the standard hexagonal germanium dioxide except for the peak at  $2\theta$  of  $69.1^\circ$ , which is from the Si (100) wafer (ICDD PDF # 36-1463, GeO<sub>2</sub>; ICDD PDF # 27-1402, Si). The sharp diffraction peaks indicates that these nanowires are highly crystallized. The diffraction intensity ratio of (101) to (102) for this sample is about 11:1; this is much higher than the 5:1 ratio for the standard hexagonal GeO<sub>2</sub>, which suggests that the GeO<sub>2</sub> NWs might have a preferred (101) growth direction.<sup>195</sup>

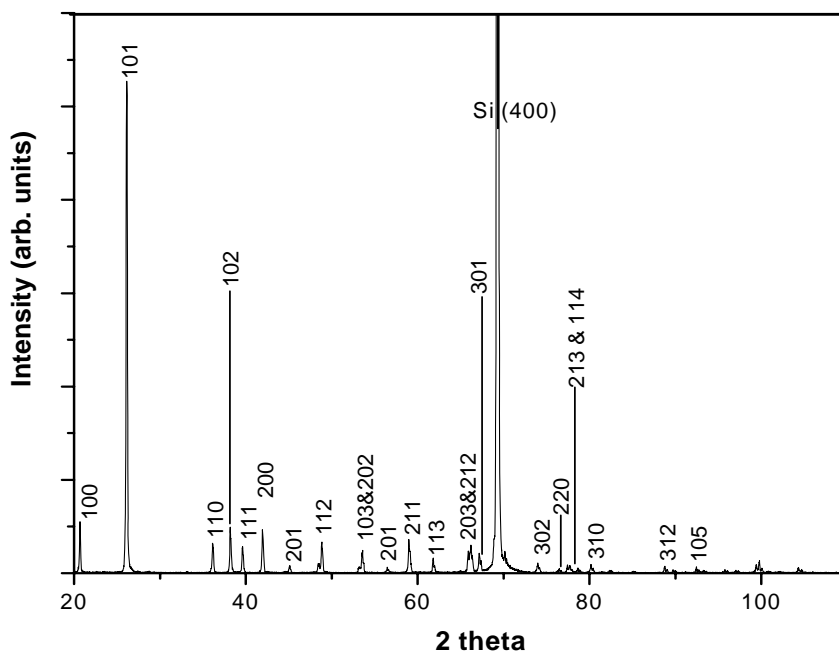


**Figure 92.** X-ray diffraction (XRD) pattern of as-formed  $\text{GeO}_2$  NWs prepared using a 15 minute reaction time. The diffraction peak at  $69.1^\circ$  is from the single crystal Si (100) wafer.

### 5.2.7.3 Effect of Si Wafer Position on the Morphology of $\text{GeO}_2$ NWs

It was found that the position of the Si wafer coated with a Au film can greatly affect the morphology of the as-formed  $\text{GeO}_2$  NWs. Figure 93a shows the SEM image of a sample grown on a Si wafer that was placed on an alumina boat. No wires can be obtained on the wafer; however, some long thick wires can be found growing on the edges of Si wafer as shown in Figure 93b. This phenomenon might be related to the critical germanium oxide vapor concentration around the edges of the wafer, which is crucial to the growth of  $\text{GeO}_2$  nanowires.<sup>153</sup> Figure 93c is the SEM image of  $\text{GeO}_2$  NWs produced on a Si wafer that was positioned inside an alumina boat. These nanowires have lots of beads growing on their surfaces. This type of structure is likely caused by the presence of a relatively higher

germanium oxide vapor concentration in the boat. When the vapor supply is more than enough for the growth of GeO<sub>2</sub> NWs, some GeO<sub>2</sub> vapor will deposit on the surface of these NWs to form beads. However, when a Si wafer was attached to the side walls of an alumina boat, much higher yields of GeO<sub>2</sub> nanowires without dots can be obtained as shown in Figure 93d.

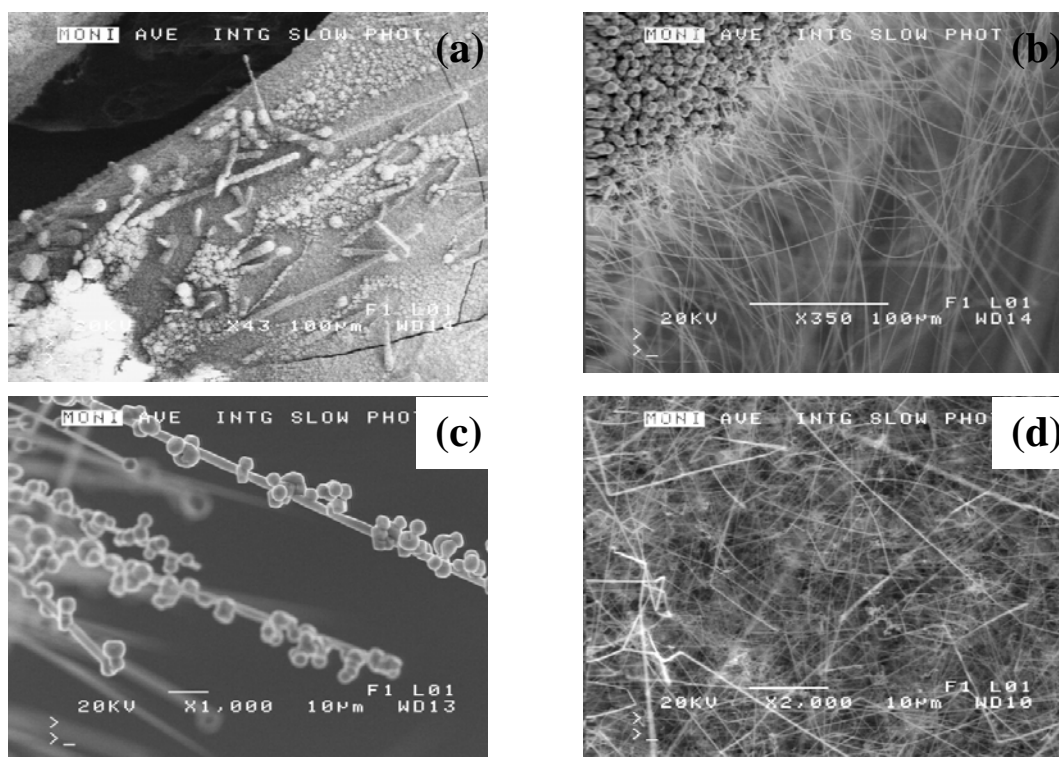


**Figure 93.** SEM images of (a) a sample produced on a Si wafer that was placed *on* an alumina boat; (b) GeO<sub>2</sub> NWs grown on the edge of a Si wafer that was placed on an alumina boat; (c) GeO<sub>2</sub> NWs grown on a Si wafer that was positioned *inside* an alumina boat; and (d) GeO<sub>2</sub> NWs grown on a Si wafer that was placed on the *side* of an alumina boat.

### 5.2.8 Near-IR Photoluminescence

The near-IR photoluminescence properties of those four types of nanofibers with different erbium concentrations and under various annealing conditions were systematically investigated. Furthermore, the PL excitation spectrum of Er-doped GeO<sub>2</sub> NWs prepared via a VLS synthetic route is compared with those of Er-doped Ge NWs and GeO<sub>2</sub> nanofibers that were prepared through an electrospinning approach to investigate their similarity and difference in structure and composition.

#### 5.2.8.1 Near-IR PL of Er<sub>2</sub>O<sub>3</sub>, Er-doped SiO<sub>2</sub>, GeO<sub>2</sub>, and SnO<sub>2</sub> nanofibers

Figure 94 shows the PL comparison of Er<sub>2</sub>O<sub>3</sub>, Er-doped SiO<sub>2</sub>, GeO<sub>2</sub>, and SnO<sub>2</sub> nanofibers. All Er-doped nanofibers were annealed at 700 °C, except for Er<sub>2</sub>O<sub>3</sub> fibers, which were annealed at 500 °C (Er<sub>2</sub>O<sub>3</sub> nanofibers were partially fused together at the higher annealing temperature of 700 °C.). It should be noted that all as-formed nanofibers are not emissive unless they have been annealed at high temperatures. This is due to the presence of organic PVP fibers that could quench the PL through the resonant energy transfer from excited Er<sup>3+</sup> ions to C-H vibrations.<sup>114,196</sup> Meanwhile, high temperature annealing can also help diffuse the erbium ions uniformly into the host matrix so that Er-Er interactions are relieved.<sup>197</sup> Among these four types of nanofibers, Er<sub>2</sub>O<sub>3</sub> nanofibers emit the weakest luminescence at 1.54 μm due to the high concentration of erbium ions present in this type of fiber. High erbium concentrations can also cause serious up-conversion and excited state absorption effects resulting in the decrease of the PL intensity.<sup>114,117</sup> Furthermore, erbium ions in crystalline Er<sub>2</sub>O<sub>3</sub> have an octahedral coordination environment, in which the 4f-4f transitions are forbidden resulting in weak Er-related emission. Er-doped SiO<sub>2</sub> and SnO<sub>2</sub>

nanofibers both can emit luminescence at 1540 nm with a medium intensity. However, the PL intensity of Er-doped SiO<sub>2</sub> fibers is stronger than that of Er-doped SnO<sub>2</sub> fibers when both fibers are annealed at 700 °C. Er-doped GeO<sub>2</sub> fibers emit the strongest luminescence at 1.54 μm among these 4 types, which is about 10 times stronger than that of Er-doped SiO<sub>2</sub> nanofibers. This strong increase in PL intensity is likely related to the presence of GeO<sub>x</sub>, which will be discussed in detail later.

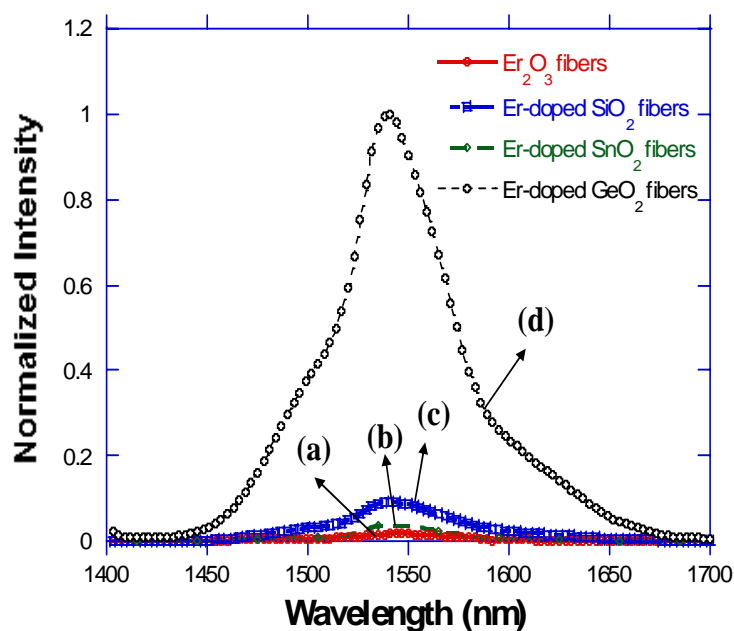
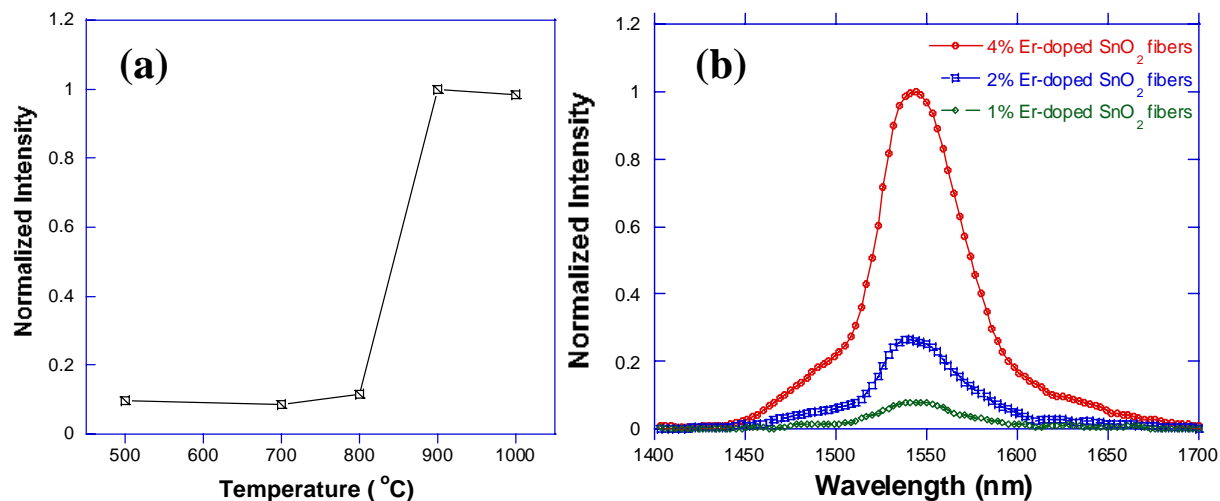


**Figure 94.** PL comparison of all four types of nanofibers (a) Er<sub>2</sub>O<sub>3</sub>; (b) Er-doped SnO<sub>2</sub>; (c) Er-doped SiO<sub>2</sub>; (d) Er-doped GeO<sub>2</sub>. Note: all Er-doped nanofibers were annealed at 700 °C except for Er<sub>2</sub>O<sub>3</sub> nanofibers, which were annealed at 500 °C.

Figure 95a shows the normalized 1540 nm PL intensities of a 4% Er-doped SnO<sub>2</sub> nanofiber sample annealed at various temperatures. The sample does not emit strong luminescence at 1540 nm until it is annealed at 900 °C. The PL intensity of the sample

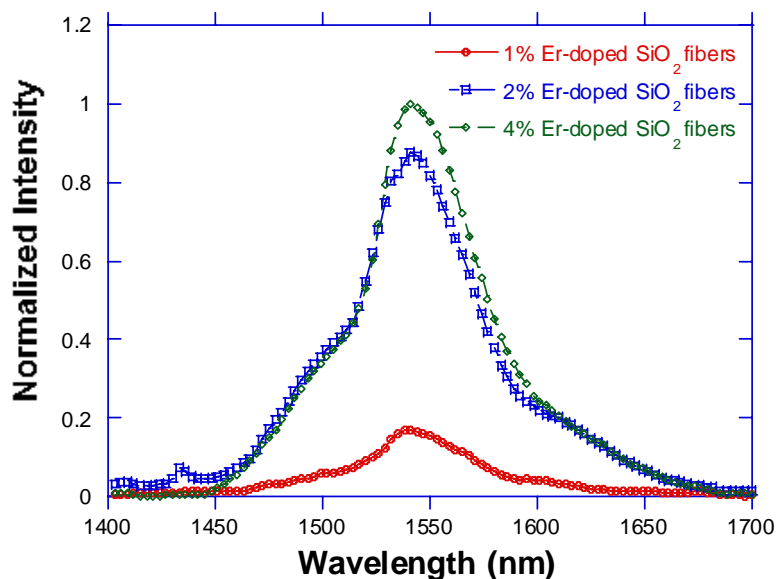
annealed at 900 °C is almost 10 times stronger than that of the sample annealed at 800 °C. A higher temperature annealing is critical to enhancing the luminescence because it can help remove most residual hydroxy groups introduced during the sol-gel process.<sup>198</sup> It was reported that excited  $\text{Er}^{3+}$  ions can de-excite through a resonant energy transfer to O-H vibrations resulting in the quenching of the erbium PL.<sup>198</sup> It is also possible that erbium ions can substitute for interstitial  $\text{Sn}^{4+}$  ions at such a high annealing temperature so that the direct Er-Er interaction could be suppressed resulting in a significant enhancement of PL intensity.<sup>144</sup> However, PL intensity of the fibers annealed at 1000 °C decreases by ~5% (relative to the fibers annealed at 900 °C), due to the precipitation of erbium ions as confirmed by our XRD data (Figure 83).

Figure 95 (b) shows the PL spectra of Er-doped  $\text{SnO}_2$  nanofibers with concentrations ranging from 1 to 4 atomic percentages. It was found that the PL intensity of the fibers with a 4% Er concentration is almost 5 times stronger than the fibers with a 2% Er concentration. No concentration-related quenching effect is observed, which suggests that  $\text{Er}^{3+}$  ions have a relatively higher solubility in  $\text{SnO}_2$ . This observation is also consistent with our XEDS linescan analysis (Figure 82) that confirms that there is no significant erbium clustering in a 4% Er-doped  $\text{SnO}_2$  nanofiber sample.



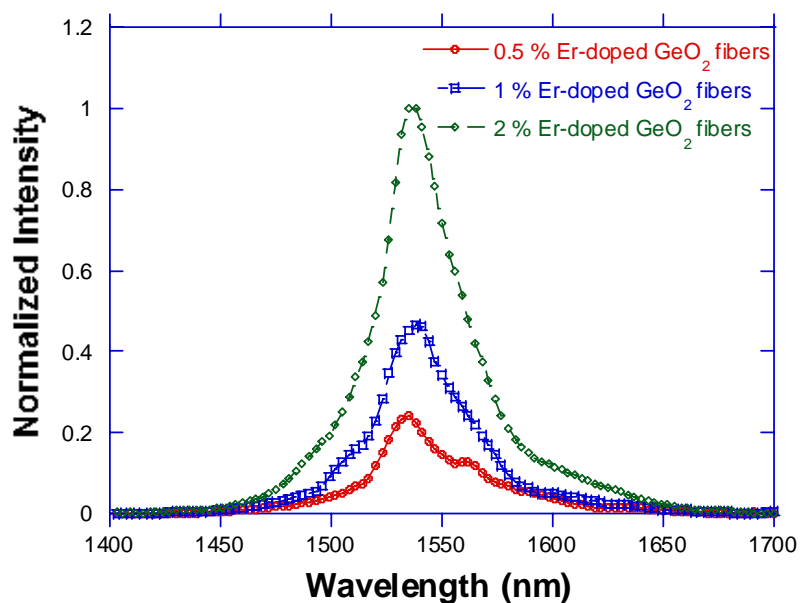
**Figure 95.** (a) Normalized 1540 nm PL intensities of a 4% Er-doped SnO<sub>2</sub> nanofiber sample annealed at various temperatures. (b) PL spectra of Er-doped SnO<sub>2</sub> nanofiber samples with erbium concentrations ranging from 1 to 4% (atomic percentage). Note: All fibers were annealed at 900 °C in air for 3 h.

Figure 96 shows the PL spectra of the Er-doped SiO<sub>2</sub> nanofibers with erbium concentrations ranging from 1-4%. When the erbium concentration is increased from 1 to 2%, the PL intensity is enhanced by almost 4 times due to the presence of increased amount of optically active Er<sup>3+</sup> ions. However, the PL intensity of Er-doped SiO<sub>2</sub> fibers with a 4% erbium concentration is only 10% higher than that of the fibers with a 2% Er concentration. This phenomenon is probably related to the relatively lower solubility of Er<sup>3+</sup> ions in the silica host. At higher erbium concentrations, a certain amount of Er<sup>3+</sup> ions will precipitate from the host matrix and become optically inactive.<sup>117,199</sup> As a consequence, the PL intensity does not increase linearly when the erbium concentration is increased.



**Figure 96.** PL spectra of Er-doped SiO<sub>2</sub> nanofibers with erbium concentrations ranging from 1 to 4% (atomic percentage). Note: All fibers were annealed at 700 °C in air for 3 h.

Figure 97 shows the PL spectra of Er-doped GeO<sub>2</sub> nanofibers with erbium concentrations ranging from 0.5 to 2% (atomic percentage). It is found that the PL intensity is almost linearly increased along with increasing erbium concentrations, which also suggests that there is no significant precipitation of erbium ions in this concentration range. The sharp peak indicates that erbium ions are located in a relatively homogeneous coordination environment.<sup>113</sup>



**Figure 97.** PL spectra of Er-doped GeO<sub>2</sub> nanofibers with erbium concentrations ranging from 0.5 to 2% (atomic percentage). Note: All fibers were annealed at 500 °C in air for 3 h.

PL excitation spectra were also employed to further investigate the mechanism of erbium luminescence in these fibers (Figure 98a). In the cases of Er<sub>2</sub>O<sub>3</sub>, Er-doped SnO<sub>2</sub> and SiO<sub>2</sub> nanofibers, 488 nm and 514 nm laser lines can excite the erbium ions more efficiently, which means that the erbium ions in these nanofibers are directly excited.<sup>78,137</sup> In stark contrast to other three types of nanofibers, the PL excitation spectra of Er-doped GeO<sub>2</sub> nanofibers are strongly annealing temperature-dependent as shown in Figure 98b. For the Er-doped GeO<sub>2</sub> nanofibers annealed at 700 °C, the PL intensity excited at 476 nm is ~76% of the value at 488 nm, and stronger than the emission magnitude when excited at 514 nm. This result implies that a carrier-mediated process is responsible for the erbium luminescence in this sample.<sup>78,137</sup> However, the PL excitation spectrum of the Er-doped GeO<sub>2</sub> nanofibers annealed at 900 °C is quite different from that of the sample annealed at 700 °C, which

shows that at higher annealing temperature the 514 nm and 488 nm laser lines can excite the  $\text{Er}^{3+}$  ions much more efficiently. The PL intensity excited at 476 nm is only ~5% of the value excited at 488 nm, and also much weaker than the emission magnitude when excited at 514 nm. This result suggests that erbium ions in this sample are in a more insulating environment and thus only capable of being excited at certain wavelengths correlated to selected ligand field transitions of  $\text{Er}^{3+}$ .

This difference in the PL excitation spectra is presumably caused by the presence of  $\text{GeO}_x$ . When the nanofibers are annealed at relatively lower temperatures such as 700 °C, some incompletely oxidized  $\text{GeO}_x$  remains and so be trapped in the nanofiber matrix. This  $\text{GeO}_x$  can serve as a sensitizer to excite erbium ions via a carrier-mediated process.<sup>137</sup> When annealed at higher temperatures such as 900 °C, however,  $\text{GeO}_x$  could be completely oxidized into  $\text{GeO}_2$  resulting in the absence of sensitizers. Therefore, erbium ions can only be directly excited in this sample.

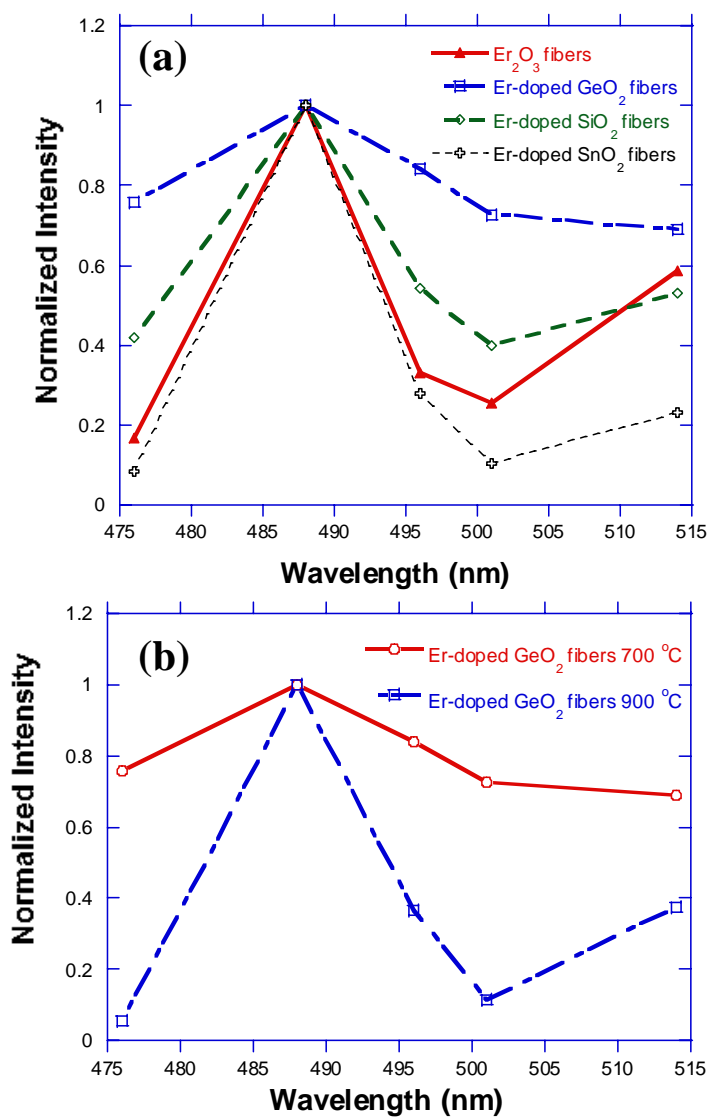


**Figure 98.** (a) PL excitation spectra of Er<sub>2</sub>O<sub>3</sub>, Er-doped SnO<sub>2</sub>, SiO<sub>2</sub>, and GeO<sub>2</sub> nanofibers (all Er-doped nanofibers were annealed at 700 °C except that Er<sub>2</sub>O<sub>3</sub> nanofibers were annealed at 500 °C.). (b) PL excitation spectra of Er-doped GeO<sub>2</sub> nanofibers annealed at 700 and 900 °C.

### 5.2.8.2 PL Excitation Spectra of Er-doped Ge NWs, GeO<sub>2</sub> NWs, and GeO<sub>2</sub> Nanofibers

Figure 99 presents a typical near-IR PL of Er-doped GeO<sub>2</sub> NWs showing that these NWs can emit strong luminescence at 1540 nm.

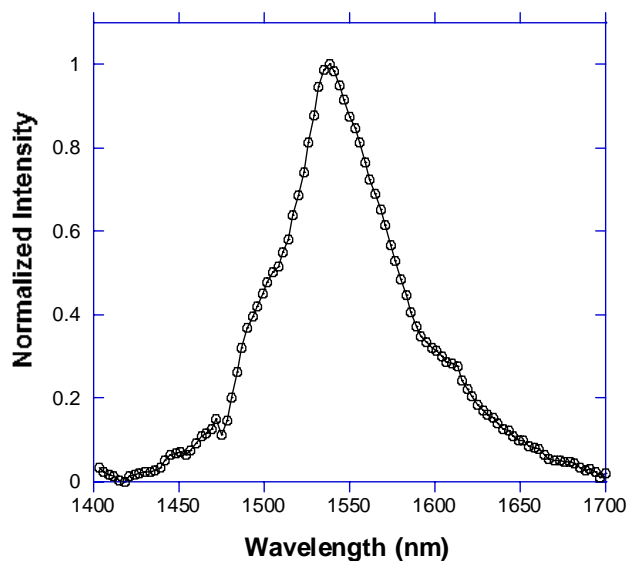


**Figure 99.** A typical near-IR photoluminescence of Er-doped GeO<sub>2</sub> nanowires that have been annealed at 600 °C in air for 1 h and exposed to erbium vapor for 1 h.

Figure 100 presents the PL excitation spectra of Er-doped Ge NWs, GeO<sub>2</sub> NWs, and Er-doped GeO<sub>2</sub> nanofibers. Er-doped Ge and GeO<sub>2</sub> NWs have been exposed to erbium vapor for 1 h and annealed at 600 °C in air for 1 h. The 2% Er-doped GeO<sub>2</sub> nanofibers have been annealed at 700 or 900 °C in air for 3 h. It can be seen that the PL excitation spectra of Er-doped Ge NWs, GeO<sub>2</sub> NWs, and GeO<sub>2</sub> nanofibers annealed at 700 °C are very similar. They all have a maximum intensity when excited at 488 nm and the PL intensity excited at 476 nm is very close to that excited at 488 nm. These results suggest that erbium ions in these NWs and nanofibers are excited through a common carrier-mediated process that is assisted by GeO<sub>x</sub>. It is noteworthy that since the as-prepared GeO<sub>2</sub> NWs show a pink color, it is possible

that these NWs have some  $\text{GeO}_x$  present.<sup>153</sup> However, Er-doped  $\text{GeO}_2$  nanofibers annealed at 900 °C emit very weak luminescence when excited at 476 nm and much stronger luminescence when excited at 488 and 514 nm, which implies that erbium ions are directly excited in this type of sample.

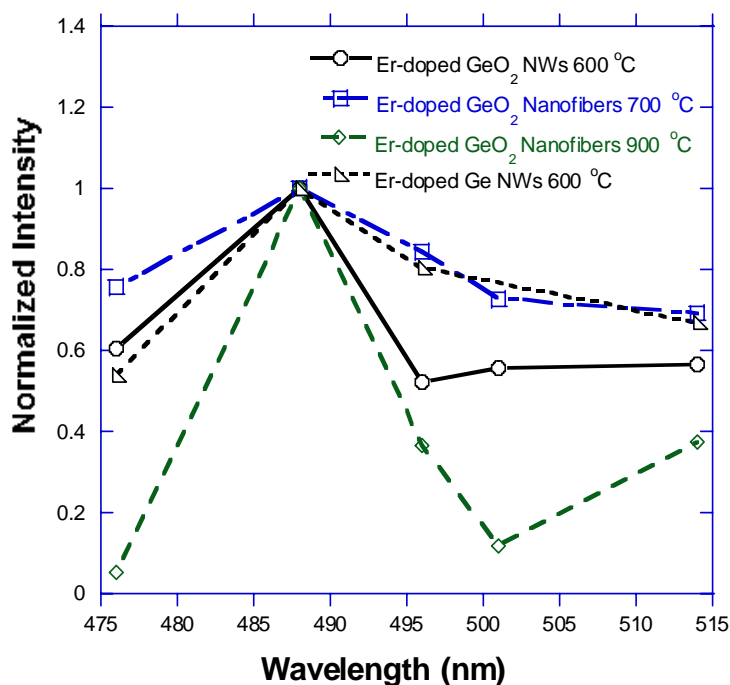


**Figure 100.** PL excitation spectra of Er-doped Ge NWs,  $\text{GeO}_2$  NWs, and Er-doped  $\text{GeO}_2$  nanofibers. Note: Er-doped Ge NWs and  $\text{GeO}_2$  NWs have been annealed at 600 °C in air for 1 h, and the 2% Er-doped  $\text{GeO}_2$  nanofibers have been annealed at 700 °C and 900 °C in air for 3 h.

### 5.3 Summary

In summary, a facile method that combines the advantages of both electrospinning techniques and sol-gel processing has been developed to fabricate Er-doped Group IV oxide nanofibers with various erbium concentrations, diameters, and host identity of Group IV elements. Thinner inorganic fibers have also been prepared using a diluted PVP polymer solution.

Er-doped SnO<sub>2</sub> nanofibers were composed of tin dioxide nanocrystals, most of which possess a (110) orientation. The presence of erbium ions will greatly reduce the average diameter of SnO<sub>2</sub> nanocrystals, whereas higher temperature anneal will increase the average diameter of the nanocrystals.

Among all four types of fibers, Er<sub>2</sub>O<sub>3</sub> fibers emit very weak luminescence, and the PL intensity of Er-doped GeO<sub>2</sub> fibers is almost 10 times stronger than that of Er-doped SiO<sub>2</sub> fibers. Er-doped SnO<sub>2</sub> fibers do not demonstrate strong PL until the annealing temperature is increased to 900 °C. PL of Er<sub>2</sub>O<sub>3</sub>, Er-doped SnO<sub>2</sub>, and Er-doped SiO<sub>2</sub> fibers arise from the direct excitation of erbium ions, whereas a carrier-mediated process is the underlying reason for the erbium photoluminescence in Er-doped GeO<sub>2</sub> nanofibers that are annealed at relatively lower annealing temperatures.

For comparison, crystalline Er-doped GeO<sub>2</sub> NWs were prepared via a VLS synthetic route. The PL excitation spectrum of Er-doped GeO<sub>2</sub> NWs is quite similar to those of Er-doped Ge NWs and Er-doped GeO<sub>2</sub> nanofibers annealed at low temperatures, suggesting that the excitation of erbium ions in these types of NWs and nanofibers is assisted by GeO<sub>x</sub> through a carrier-mediated process.

*CHAPTER VI.*

GeO<sub>x</sub> as a Broad Band Sensitizer for Er-doped SnO<sub>2</sub>

Nanofibers

## 6.0 Introduction

As mentioned in Chapter 1, an  $\text{Er}^{3+}$  ion has a very small absorption cross section (typically on the order of  $10^{-21} \text{ cm}^2$ ) for stimulated emission, and can only be directly excited in the case of an Er-doped  $\text{SiO}_2$  amplifier. In order to further enhance the PL intensity at 1540 nm, sensitizers such as Si nanocrystals and  $\text{Ag}^+$  ions that have much larger absorption cross sections than  $\text{Er}^{3+}$  ions are employed to excite  $\text{Er}^{3+}$  ions more efficiently via a carrier-mediated process. In the case of Er-doped  $\text{SiO}_2$  films containing Si NCs, the PL intensity can be increased by two orders of magnitude compared with Er-doped  $\text{SiO}_2$ , given that Er-concentrations are same in these two samples.<sup>200</sup>

As mentioned in Chapter 5,  $\text{SnO}_2$  is a highly optical transparent n-type semiconductor with a wide band gap of 3.6 eV at 300 K. Such semiconducting character suggests that it should be possible to achieve electroluminescence from an Er-doped  $\text{SnO}_2$  nanofiber sample via electrical pumping. However,  $\text{Er}^{3+}$  ions can only be directly excited in such Er-doped  $\text{SnO}_2$  nanofibers. In order to obtain more efficient electroluminescence, an effective sensitizer is required to further enhance their Er-related PL intensity. In the previous chapters,  $\text{GeO}_x$  has been identified as an efficient sensitizer for erbium ions. Therefore, it is logical to introduce  $\text{GeO}_x$  into Er-doped  $\text{SnO}_2$  nanofibers for the deliberate purpose of producing a carrier-mediated excitation enhancement pathway into a conductive host.

In this chapter, a vapor transport method was employed to introduce various amounts of  $\text{GeO}_x$  into the Er-doped  $\text{SnO}_2$  nanofibers. The compositions and structures of these NWs were characterized using TEM, SEM, X-ray energy dispersive spectroscopy (XEDS), and Micro-Raman spectroscopy. Importantly, micro-Raman spectroscopy confirms the presence

of elemental tin in these nanofibers. Interestingly, a longer Ge deposition time (1 h) on Er-doped SnO<sub>2</sub> or SnO<sub>2</sub> nanofibers can lead to the formation of Ge nanorods on these nanofibers, which were confirmed by SEM and XEDS analysis. Both room and low temperature photoluminescence (PL) properties of Er-doped SnO<sub>2</sub> nanofibers sensitized by GeO<sub>x</sub> are also investigated.

## 6.1 Experimental

### 6.1.1 Deposition of Ge on Er-doped SnO<sub>2</sub> Nanofibers

The starting material, Er-doped SnO<sub>2</sub> nanofibers, was prepared using the procedures described in Chapter 5. As-prepared nanofibers were annealed at 500 °C in air for 3 h to remove the PVP templates. These annealed Er-doped SnO<sub>2</sub> nanofibers were then deposited with Ge using the reactor design shown in Figure 101. In a typical reaction, an alumina boat containing a mixture of ~25 mg germanium powder (Strem) and 10 mg carbon (J.T. Baker) was placed in the reactor. A 2% Er-doped SnO<sub>2</sub> nanofiber sample of 5 mm × 20 mm dimension was placed on another alumina boat that was positioned in the 20 mm I.D quartz tube reactor approximately 2 cm from the edge of a 30 cm long ceramic oven. The nanofiber sample was covered with a piece of Si wafer to prevent it from being blown from the boat by helium carrier gas. The boat containing a given C:Ge mixture was heated at 1000 °C for 15 minutes under the protection of helium at a flow rate of 3000 sccm. The temperature of Ge deposition is ~590 °C, slightly higher than that for the growth of Ge NWs (~560 °C). After the deposition was completed, the front part and the back part of the sample became black and yellow, respectively.

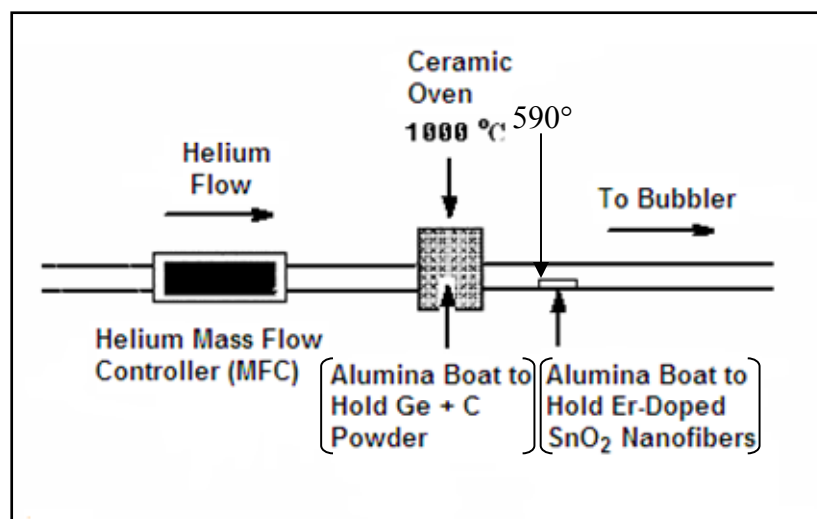


**Figure 101.** Reactor design for depositing Ge on Er-doped SnO<sub>2</sub> nanofibers.

### 6.1.2 Growth of Ge Nanorods on SnO<sub>2</sub> and Er-doped SnO<sub>2</sub> Nanofibers

SnO<sub>2</sub> nanofibers and Er-doped SnO<sub>2</sub> nanofibers were prepared according to the procedures described in Chapter 5. As-formed nanofibers were annealed at 500 °C in air for 3 h to remove PVP templates before the deposition of Ge. The reactor design for growing Ge nanorods on SnO<sub>2</sub> and Er-doped SnO<sub>2</sub> nanofibers is same as that shown in Figure 101. However, a longer time Ge deposition time (1 h) was used to obtain nanorods on these nanofibers.

### 6.1.3 Instrumentation

Structural characterization of all samples was performed using JEOL JSM-6100 SEM and Philips EM300 TEM at Texas Christian University. A JEOL JSM-6100 SEM equipped with a XEDS analysis system operated at 20 kV was used to record SEM images and perform elemental analyses. A Philips EM300 TEM operated at 60 kV was used to acquire TEM

images. Specimens for TEM characterization were prepared by dispersing the sample with a 20  $\mu\text{L}$  drop of 2-propanol and then placing the drop onto a copper grid.

Raman spectra were recorded using a standard Raman micro-imaging system located in Dr. Zerda's lab at Texas Christian University, as described in Chapter 3.

Low resolution ( $\pm 4$  nm) near-IR photoluminescence (PL) spectra were obtained using the system as described in Chapter 3. Excitation was provided by available lines of a Coherent Ar<sup>+</sup> laser and a 5 mW green laser pointer with a wavelength of 532 nm. An Oxford Instruments Microstat N cryostat equipped with a vacuum pump and a temperature controller was used to obtain low temperatures ranging from 100 to 300 K. The cryostat was cooled by continuously flowing liquid nitrogen and has a quartz optical access window with a diameter of 10 mm.

## 6.2 Results and Discussion

### 6.2.1 Characterization

In order to discuss the data properly, it is useful to define what is meant by the terms of the front, middle, and back parts of the sample (illustrated in Figure 102). For a typical sample that is 10 mm in length, the front part of the sample is closest to the ceramic oven, which accounts for ~10% of the sample. The middle part of the sample is somewhat less close to the oven, which accounts for ~20% of the sample. The back part of the sample is far away from the oven, which accounts for ~70% of the sample.

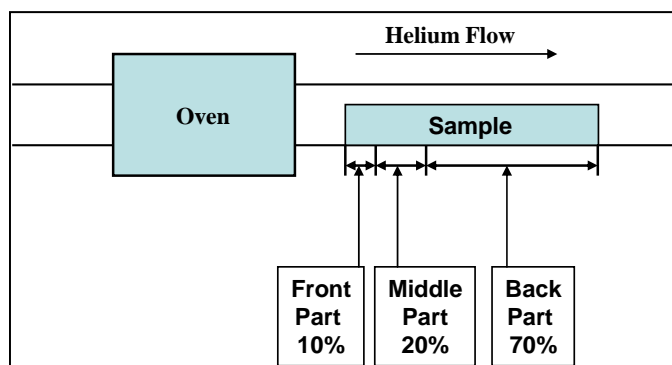


**Figure 102.** Illustration of the front, middle, and back parts of an Er-doped SnO<sub>2</sub> sample deposited with Ge.

Figure 103 shows the SEM images and XEDS spectra of the front and middle parts of a 2% Er-doped SnO<sub>2</sub> nanofiber sample that was exposed to Ge vapor for 15 minutes. The front part of the sample at a temperature of 590 °C was partially melted during the deposition of Ge as shown in Figure 103a. The corresponding XEDS spectrum (Figure 103c) indicates that the atomic percentage of Ge and Sn are ~48% and ~51%, respectively, in this part of the

sample. In contrast to the front part of the sample, the middle part of the sample still possesses a nanofiber morphology (Figure 103b). The corresponding XEDS spectrum (Figure 103d) confirms that these nanofibers are composed of 56% Ge, 43% Sn, and 1% Er. The relative concentration of erbium is lowered from 2% to 1% after the deposition due to the introduction of Ge. It is notable that either of these two parts of the sample can emit almost two orders of magnitude stronger near-IR luminescence relative to the starting material, 2% Er-doped  $\text{SnO}_2$  nanofibers.

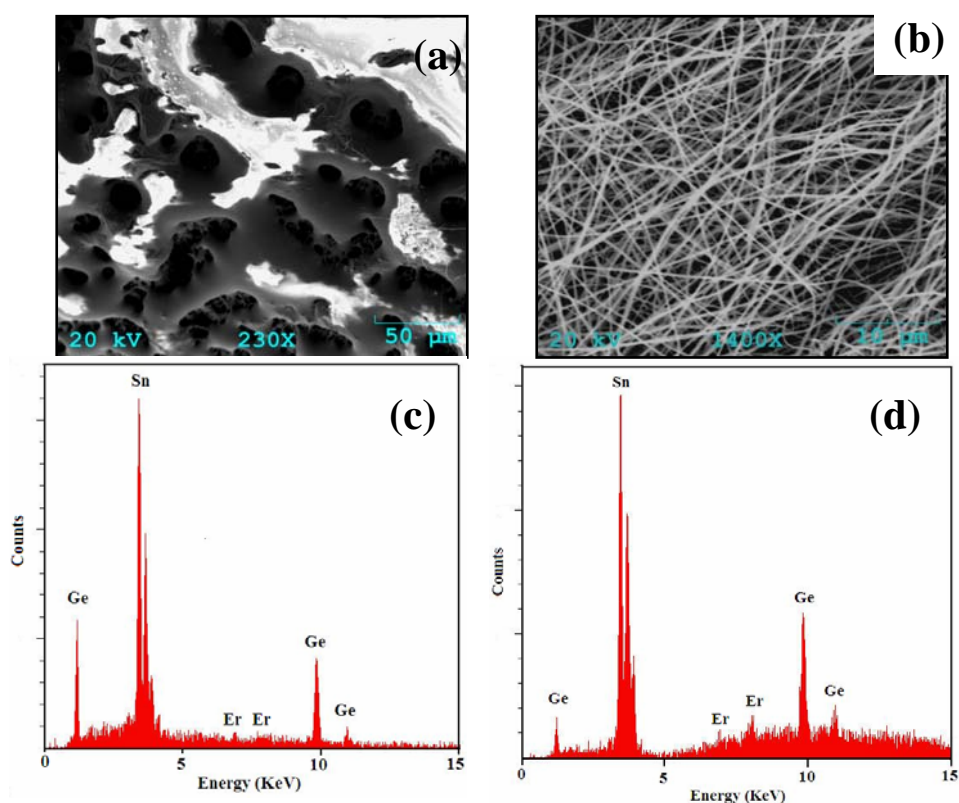


**Figure 103.** SEM images of (a) the front part and (b) the middle part of the sample; XEDS spectra of (c) the front part and (d) the middle part of the sample. The sample is composed of 2% Er-doped  $\text{SnO}_2$  nanofibers that were exposed to Ge vapor for 15 minutes.

After the deposition of Ge, it was observed that the front and middle parts of the sample became shiny black and yellow, respectively. Furthermore, the nanofibers in the front part of the sample were melted together at a temperature far below the melting points of both Ge (938 °C) and SnO<sub>2</sub> (1127 °C) (recall that the deposition temperature is only 590 °C). One possible explanation for these observations is for tin dioxide to be reduced by germanium at high temperatures to form metallic tin, as represented by equation (20):



It is known that elemental tin has a very low melting point (232 °C). As a consequence, the front part of the sample is melted after the deposition of Ge. However, because the temperature of the back part of the sample is presumably lower than that of the front part, the reduction to elemental tin will not take place. As a consequence, the morphology of these nanofibers is maintained.

TEM was also used to characterize the Er-doped SnO<sub>2</sub> nanofiber samples deposited with Ge. Figure 104a shows the TEM image of the front part of the sample. This section is mainly composed of melted film-like platelets, which is consistent with the above SEM imaging results. However, the back part of the sample consists of nanofibers with lots of nanoparticles present on their surfaces (Figure 104b). It is assumed that these particles are composed of GeO<sub>x</sub> or a mixture of Ge and GeO<sub>x</sub>.

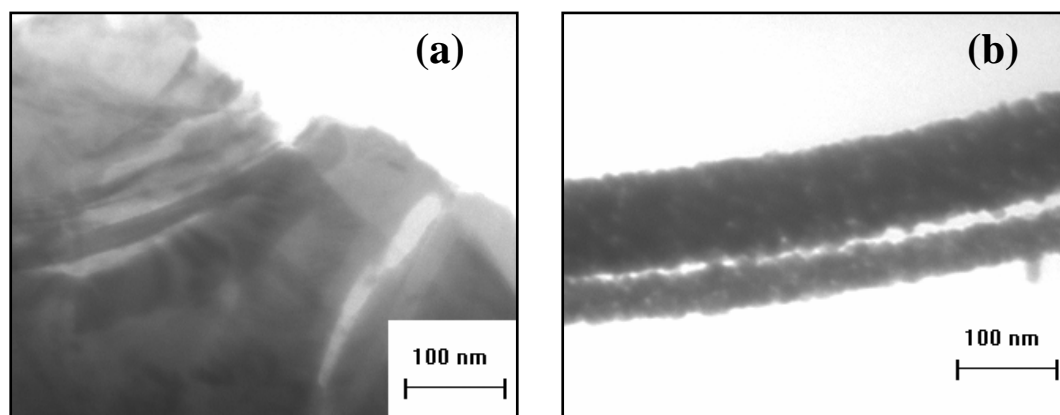


**Figure 104.** TEM images of (a) the front part of the sample (b) the back part of the sample. The sample is composed of 2% Er-doped SnO<sub>2</sub> nanofibers that were exposed to Ge vapor for 15 minutes.

### 6.2.2 Growth of Ge Nanorods on SnO<sub>2</sub> and Er-doped SnO<sub>2</sub> Nanofibers

Er-doped SnO<sub>2</sub> nanofiber samples were exposed to Ge vapor for longer times, including up to 1 h, to investigate the effect of Ge concentration on the photoluminescence intensity. Surprisingly, it was found that Ge nanorods can be grown on Er-doped SnO<sub>2</sub> nanofibers. Figure 105a is the SEM image of 4% Er-doped SnO<sub>2</sub> nanofibers exposed to Ge vapor for 1 h, showing that lots of short nanorods were grown on the surface of Er-doped SnO<sub>2</sub> nanofibers. Figure 105b is the magnified SEM image of the fiber shown in Figure 105a. These nanorods are ~1 μm long and ~100 nm in diameter. One may speculate that the round balls on the tips of these nanorods might be tin catalysts that were produced by the Ge reducing reaction as represented by equation (20). Some thicker nanorods can also be found to grow on the Er-doped SnO<sub>2</sub> nanofibers as shown Figure 105c. It is very difficult to control the yield and diameters of these Ge nanorods due to the complexity of a given nanofiber

network. The surface of this network is not even so that Ge vapor concentration around each nanofiber is variable, which makes the uniform growth of Ge nanorods challenging. A XEDS spectrum (Figure 105d) confirms the presence of significant amount of Ge (45%), Sn (52%), and a trace amount of Er (3%) in these nanofibers.

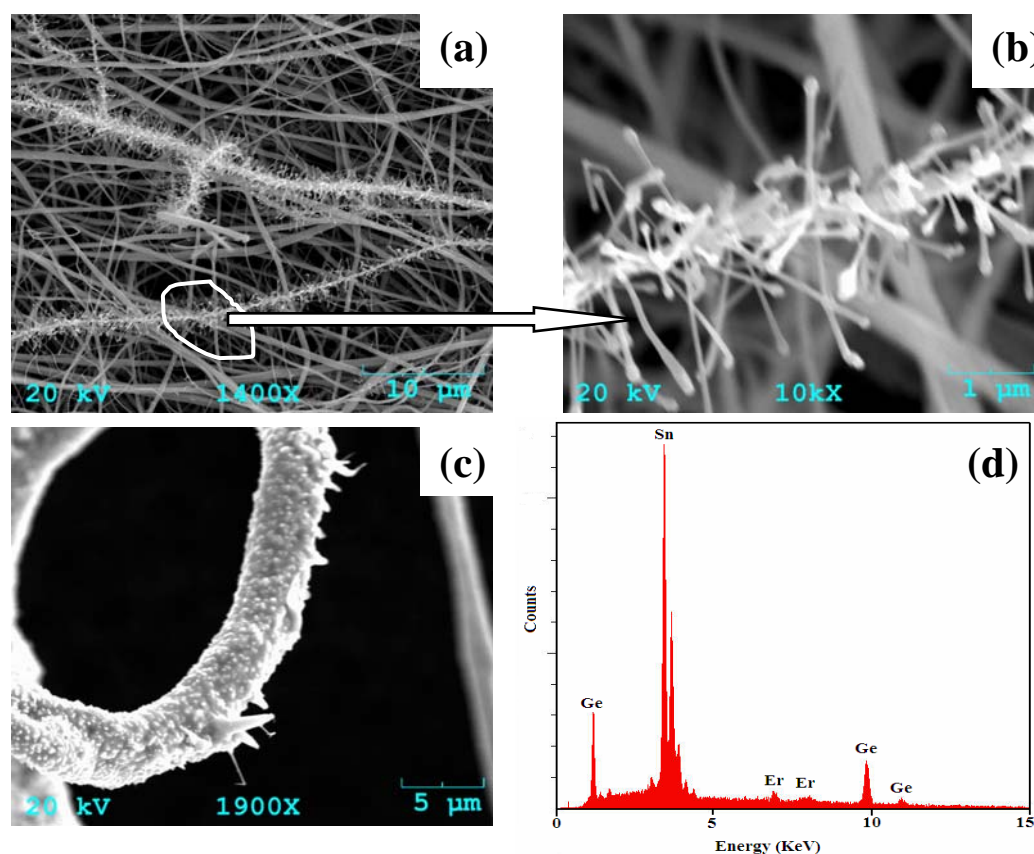


**Figure 105.** (a) Low magnification and (b) high magnification SEM images of thin Ge nanorods grown on the sample; (c) SEM image of thicker Ge nanorods grown on the sample; (d) XEDS spectrum of the sample. The sample is composed of 4% (atomic percentage) Er-doped SnO<sub>2</sub> nanofibers that were exposed to Ge vapor for 1 h.

Ge nanorods can also be grown on the surface of pure SnO<sub>2</sub> nanofibers. Figure 106a is a low magnification SEM image of the front part of a pure SnO<sub>2</sub> nanofiber sample that was exposed to Ge vapor for 1 h, showing that lots of Ge microrods and a few nanorods were produced on the melted SnO<sub>2</sub> nanofibers in the front part of the sample. Figure 106b shows a high magnification SEM image of these microrods in the circled area that are about 10 μm long and have a broad distribution of diameters ranging from several hundred nanometers to several microns. Recall that the size of SnO<sub>2</sub> nanocrystals in pure SnO<sub>2</sub> nanofibers is much larger than that in Er-doped SnO<sub>2</sub> nanofibers, as described in Chapter 5. As a consequence, the tin nanoparticles formed by the Ge reducing reaction should be correspondingly larger in pure SnO<sub>2</sub> nanofibers. In accordance with the VLS mechanism, a bigger catalyst particle will lead to the formation of a thicker nanorod. A XEDS spectrum of these microrods (Figure 106c) confirms that the microrods are mainly composed of Ge (96.2%, atomic percentage) and trace amount of Sn (3.3%, atomic percentage). The XEDS spectrum was collected from the circled area shown in the inset of Figure 106c.

Sn<sub>x</sub>Ge<sub>1-x</sub> alloy is a simple eutectic system with a eutectic temperature of ~231 °C. According to the VLS mechanism, Sn-catalyzed growth of Ge NWs could be initiated at 590 °C because this temperature is above the eutectic temperature of Sn<sub>x</sub>Ge<sub>1-x</sub> alloy. Furthermore, it has been reported that GeSn alloy quantum wires can be obtained by annealing a 15 nm thick film of Ge<sub>0.95</sub>Sn<sub>0.05</sub> alloys grown epitaxially on a Ge (100) substrate.<sup>201</sup> The formation of these quantum wires is presumably due to the diffusion of Ge to one facet of a Sn island, which possesses a relatively lower chemical potential.<sup>201</sup> Therefore, it is very possible that Sn can serve as a catalyst to help grow Ge NWs.

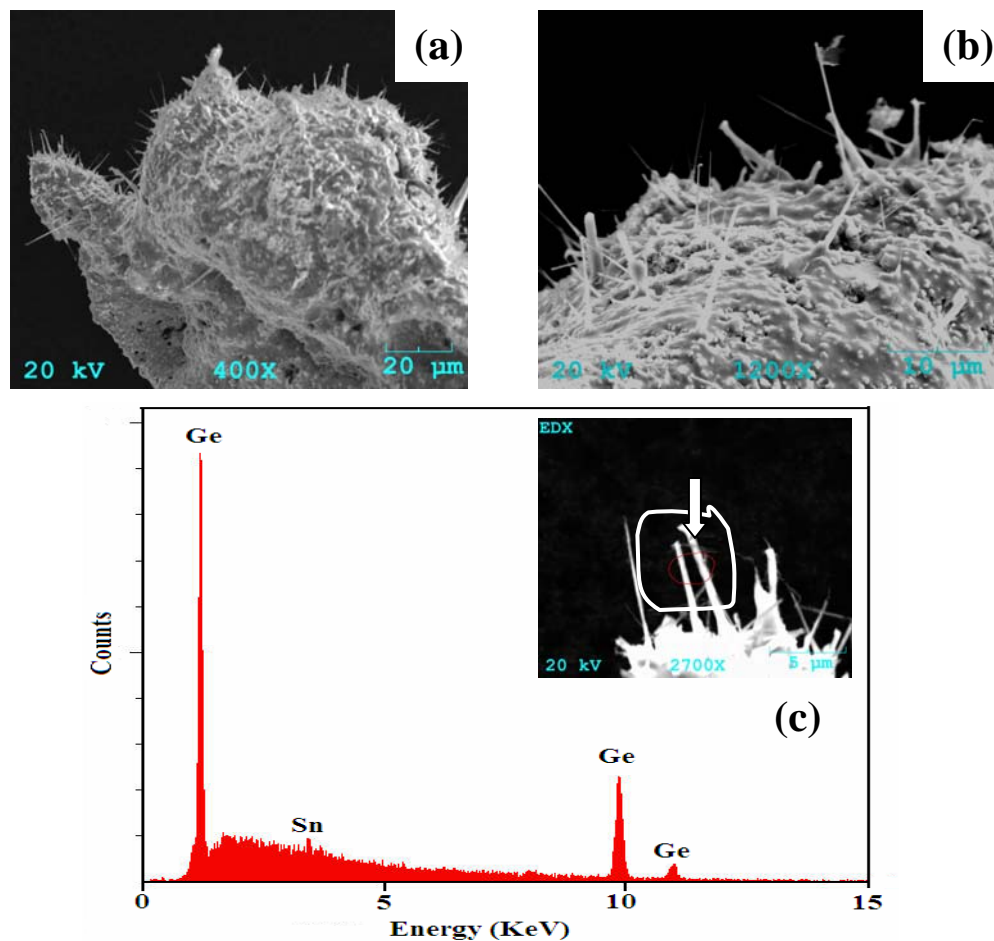


**Figure 106.** (a) Low magnification and (b) high magnification SEM images of Ge microrods grown on pure SnO<sub>2</sub> nanofibers; (c) A XEDS spectrum collected from the circled area shown in the inset. Inset: SEM image of Ge microrods grown on pure SnO<sub>2</sub> nanofibers. Note: The nanofibers were exposed to Ge vapor for 1 h.

### 6.2.3 Micro-Raman Spectroscopy

It was assumed above that Ge can reduce SnO<sub>2</sub> at high temperature to form Sn and GeO<sub>x</sub>. The formation of Sn leads to the deformation of the front part of pure SnO<sub>2</sub> and Er-doped SnO<sub>2</sub> nanofibers. The as-formed tin nanoparticles could be employed to catalyze the

growth of Ge nanorods on these nanofibers via the well-known VLS synthetic route. However, more direct proof must be provided to support this assumption. As mentioned in Chapter 3, Raman spectroscopy is an efficient technique used to investigate vibrational, rotational, and other low-frequency modes of condensed phase materials. Different substances have different characteristic Raman shift values, which can be used for compositional analysis and phase identification. For example, crystalline cubic Ge and cubic  $\alpha$ -Sn have different characteristic Raman peaks at  $298\text{ cm}^{-1}$  and  $196\text{ cm}^{-1}$ , respectively.<sup>202,203</sup> Therefore, Raman spectroscopy was chosen to investigate the composition and solid phase changes after the deposition of Ge on pure  $\text{SnO}_2$  and Er-doped  $\text{SnO}_2$  nanofibers.

Figure 107 shows the micro-Raman spectra of  $\text{SnO}_2$  and Er-doped  $\text{SnO}_2$  nanofibers deposited with Ge for 15 minutes. A Raman spectrum of the back part of  $\text{SnO}_2$  nanofiber sample deposited with Ge is shown in Figure 107a. The strongest peak at  $630\text{ cm}^{-1}$  is from a typical  $A_{1g}$  vibrational mode of tetragonal  $\text{SnO}_2$  nanocrystals.<sup>204</sup> Other weaker phonon scattering peaks of tetragonal  $\text{SnO}_2$  were not observed due presumably to the dimensions or poor crystallinity of the sample (recall that the deposition temperature is only  $590\text{ }^\circ\text{C}$ , and the XRD peaks of the Er-doped  $\text{SnO}_2$  nanofibers annealed at  $500\text{ }^\circ\text{C}$  are very broad, which is correlated to a poor crystallinity).<sup>204</sup> Another broad peak centered at  $240\text{ cm}^{-1}$  is presumably from amorphous Ge, known to possess a broad Raman peak ranging from  $220$  to  $300\text{ cm}^{-1}$ .<sup>202</sup> These observations suggest that Ge did not react with  $\text{SnO}_2$  in the back part of the sample.

However, the Raman spectrum of the front part of a  $\text{SnO}_2$  nanofiber sample deposited with Ge (Figure 107b) is quite different from that of the back part. The two sharp Raman peaks located at  $194\text{ cm}^{-1}$  and  $364\text{ cm}^{-1}$  are from the first- and second-order phonon scattering peaks of  $\alpha$ -Sn nanoparticles, respectively. It has been reported that Si nanocrystals have first-

and second-order phonon scattering peaks ranging from 495 to 520  $\text{cm}^{-1}$ , and 915 to 975  $\text{cm}^{-1}$ , respectively, depending on the size of Si nanocrystals,<sup>205</sup> which is similar to our case. This large deviation of the second-order phonon scattering peak from the theoretical value is probably due to the enhanced electron-phonon coupling in a quantum-confined nanostructure.<sup>205</sup> The front part of a 2% Er-doped  $\text{SnO}_2$  nanofiber sample deposited with Ge has a very similar Raman spectrum to that of the front part of pure  $\text{SnO}_2$  nanofiber sample deposited with Ge for a similar duration. The first- and second-order phonon scattering peaks of  $\alpha$ -Sn are at 195 and 360  $\text{cm}^{-1}$ , respectively (Figure 107c). These results strongly support the previous assumption that Ge can reduce  $\text{SnO}_2$  to form Sn and  $\text{GeO}_x$ .

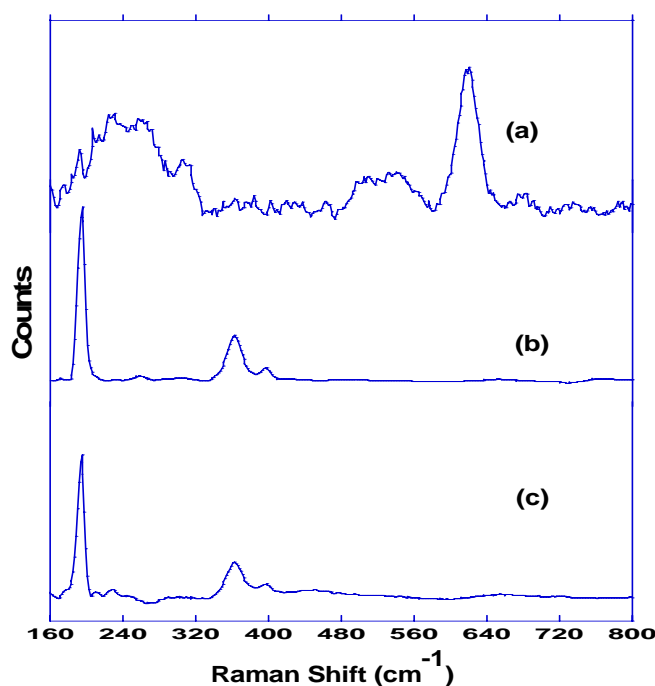


**Figure 107.** Raman spectra of (a) the back part and (b) the front part of a  $\text{SnO}_2$  nanofiber sample deposited with Ge for 15 minutes; (c) the front part of a 2% Er-doped  $\text{SnO}_2$  nanofiber sample deposited with Ge for 15 minutes.

#### 6.2.4 Room and Low Temperature Photoluminescence

Figure 108 shows the room temperature photoluminescence (PL) spectra of a 2% Er-doped SnO<sub>2</sub> nanofiber sample annealed at 900 °C for 3 h in air, followed by deposition with Ge at 590 °C for 15 minutes. The power and wavelength of the laser are 100 mW and 488 nm, respectively. It was found that the strongest light emission at 1540 nm is obtained from the front part of the nanofiber sample deposited with Ge (Figure 108a). The middle part of the sample deposited with Ge emits with ~15% weaker intensity relative to the front part of the sample (Figure 108b). The Er-related light emission from a 2% Er-doped SnO<sub>2</sub> nanofiber sample annealed at 900 °C in air for 3 h is shown in Figure 108c for comparison. It can be easily seen that the PL intensity at 1540 nm has been increased by almost 2 orders of magnitude after the Ge deposition compared with a 2% Er-doped SnO<sub>2</sub> nanofiber sample annealed under the same conditions. If compared with a 2% Er-doped SnO<sub>2</sub> nanofiber sample annealed at 800 °C, the PL intensity has been increased by almost 3 orders of magnitude. Recall that the PL intensity of a 2% Er-doped SnO<sub>2</sub> nanofiber sample annealed at 800 °C is 10 times weaker than that of the sample annealed at 900 °C (Chapter 5). This huge enhancement in emission intensity is closely related to the compositions of these samples. The Raman spectra presented above suggest that the front part of the sample deposited with Ge is composed of elemental Sn and amorphous GeO<sub>x</sub> that were produced through Ge reduction of the SnO<sub>2</sub>. The as-formed GeO<sub>x</sub>, with a broad band gap ranging from 0.75-5.0 eV, can serve as a sensitizer to harvest photons efficiently and transfer the energy to erbium ions.<sup>130,133</sup> Such a carrier-mediated process would result in a significant enhancement in the PL intensity.

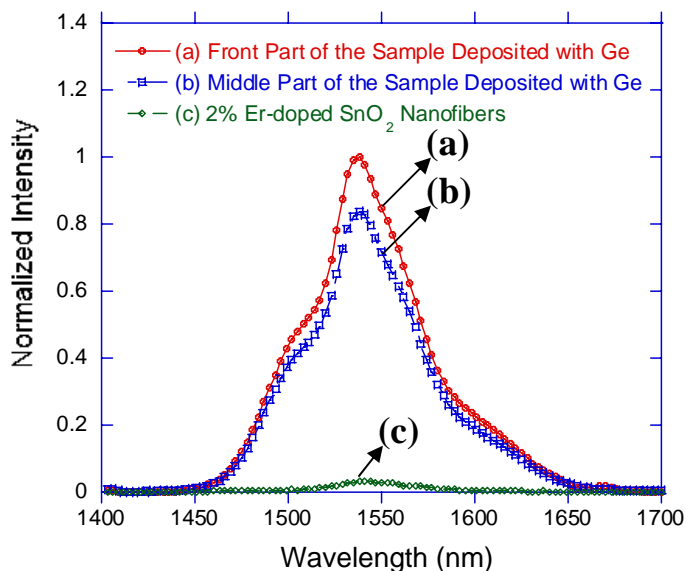


**Figure 108.** PL spectra of (a) front part and (b) back part of a 2% Er-doped SnO<sub>2</sub> nanofiber sample exposed to Ge vapor for 15 minutes; (c) a 2% Er-doped SnO<sub>2</sub> nanofiber sample annealed at 900 °C for 3 h in air. Note: The spectra of (a)-(c) were collected using a 488 nm laser of 100 mW.

To investigate the effect of excitation wavelength on the excitation efficiency of erbium ions in the Er-doped SnO<sub>2</sub> nanofibers deposited with Ge, a 532 nm green laser was chosen as an optical pump. It is known that 532 nm photons cannot be absorbed efficiently by Er<sup>3+</sup> ions via a direct excitation mode.<sup>112</sup> If such a wavelength could excite the Er<sup>3+</sup> ions in this sample, it can be inferred that there must be a sensitizer present in the sample, which can help excite Er<sup>3+</sup> ions via a carrier-mediated process. Figure 109 shows the PL spectrum of the front part of the sample deposited with Ge at 590 °C for 15 minutes excited using a very low excitation power (5 mW) of a 532 nm laser line. The intense peak at 1540 nm suggests that

the light emission from this sample must have been assisted by a carrier-mediated process.

This result further confirms that  $\text{GeO}_x$  is an effective sensitizer for erbium ions.

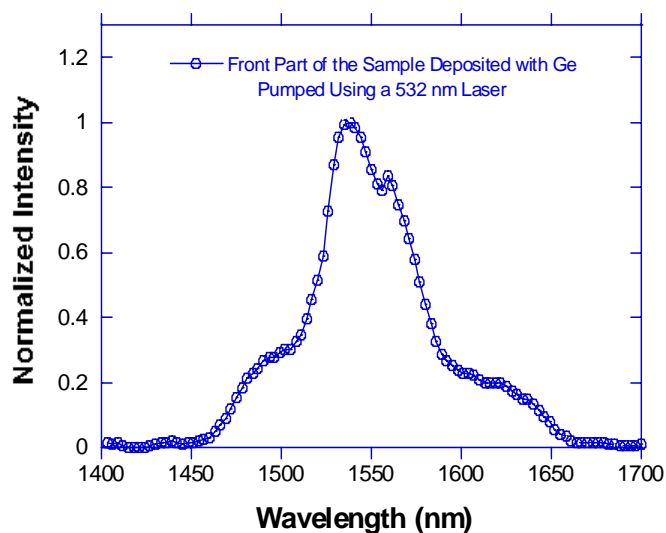


**Figure 109.** PL spectrum of the front part of a 2% Er-doped  $\text{SnO}_2$  nanofiber sample exposed to Ge vapor for 15 minutes excited using a 532 nm green laser of 5 mW.

PL excitation measurements were also carried out to further understand the underlying mechanism for this  $\text{GeO}_x$ -sensitized enhancement in PL intensity. Figure 110a shows the PL excitation spectrum of the front part of a 2% Er-doped  $\text{SnO}_2$  nanofiber sample deposited with Ge for 15 minutes. Although the PL intensity obtained using a 488 nm excitation line is  $\sim 20\%$  stronger than that using 476 nm excitation, no distinct increase of the Er-related PL was found upon excitation at 514 nm, which means that a carrier-mediated process assists the light emission process of  $\text{Er}^{3+}$  ions.<sup>78,79</sup> The PL excitation spectrum of the middle part of a 2% Er-doped  $\text{SnO}_2$  nanofiber sample (Figure 110b) shows that the PL intensity obtained using 488 nm excitation is  $\sim 30\%$  higher than that using a 476 nm excitation line. It can be inferred from this result that the light emission at 1540 nm is from

both direct and carrier-mediated excitations of erbium ions. In stark contrast to the above two samples, a 2% Er-doped SnO<sub>2</sub> nanofiber sample annealed at 900 °C and lacking the GeO<sub>x</sub> sensitizer emits much stronger luminescence at 1540 nm using 488 nm and 514 nm laser wavelengths (Figure 110c), which is characteristic of a direct excitation of erbium ions in this material.

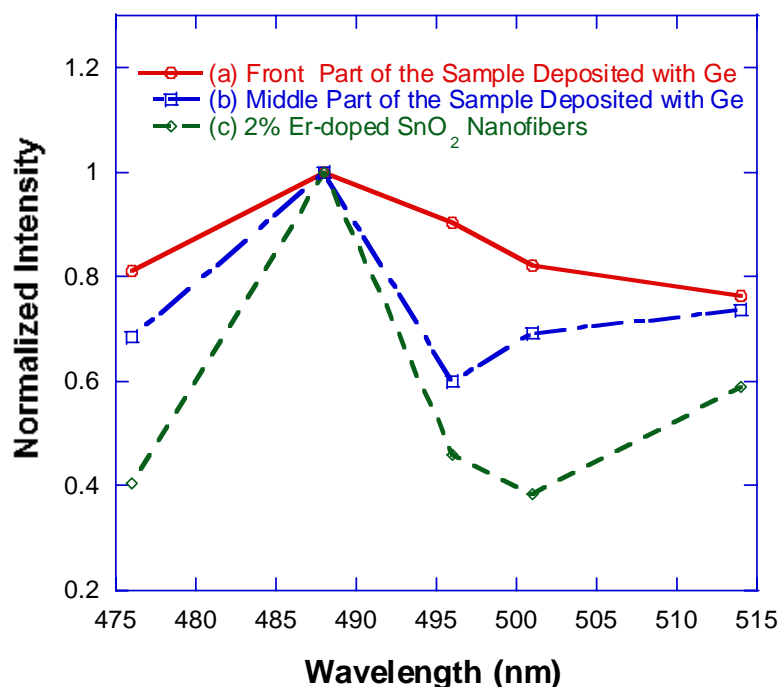


**Figure 110.** PL excitation spectra of (a) the front part and (b) the back part of an Er-doped SnO<sub>2</sub> nanofiber sample that was exposed to Ge vapor for 15 minutes; (c) an Er-doped SnO<sub>2</sub> nanofiber sample that was annealed at 900 °C in air for 3 h. (Note: Erbium concentration is 2% in all samples.)

Low temperature PL measurements were also carried out on those above samples to investigate the effect of temperature on their PL intensity. The temperatures range from 100 to 300 K in all cases. Figure 111a shows the low temperature PL spectrum of the front part of

the sample deposited with Ge for 15 minutes. The PL intensity at 1540 nm is reduced by ~60% while the temperature is increased from 100 to 300 K. However, the low temperature PL spectrum of the back part of the sample deposited with Ge for 15 minutes (Figure 111b) shows that the PL intensity at 1540 nm has only been reduced by ~35% when the temperature is increased from 100 to 300 K. In the case of Er-doped SnO<sub>2</sub> nanofibers, the PL intensity is reduced by ~40% (Figure 111c), which is similar to the case of the back part of the sample. These results are believed to be consistent with the differences in their respective compositions. Recall that the front part of the sample is composed mainly of Sn and GeO<sub>x</sub>, while the back part of the sample consists of SnO<sub>2</sub> and amorphous Ge.

It is noteworthy that the room temperature quenching effects of the Er-related luminescence are different when Er<sup>3+</sup> ions are located in different host materials.<sup>116,206-208</sup> In the case of Er-doped SiO<sub>2</sub> (a direct excitation host), the Er-related PL intensity decreases only by ~20% while the temperature is increased from 100 K to 300 K because Er ions are located in a relatively insulating environment.<sup>206,207</sup> In contrast, Er-doped bulk crystalline Si has a much more serious room temperature quenching effect, whose Er-related luminescence can be decreased by a two orders of magnitude when the temperature is increased from 100 to 300 K.<sup>116</sup> This significant room temperature quenching effect is closely related to the following two deactivation processes:<sup>116</sup> one is the reduction in the excitation rate of Er<sup>3+</sup> ions at the ground state due to the detrapping of excitons (excited electron and hole pairs) at Er-related defects, and another one is an increased de-excitation rate of excited Er<sup>3+</sup> ions due to the enhanced energy backtransfer rate from the excited Er<sup>3+</sup> ions to host materials.<sup>119</sup> It is also notable that in the case of Er-doped Si nanocrystals (a carrier-mediated excitation assisted by the sensitizer, Si NCs), the PL intensity can only be reduced by ~50% while the

temperature is elevated from 100 to 300 K.<sup>208</sup> This result is probably related to a suppressed Auger de-excitation process, including a reduced backtransfer rate from excited  $\text{Er}^{3+}$  ions at the first excited level to these nanocrystals.<sup>208</sup> In our case, the relative higher room temperature quenching effect of the front part of the sample is presumably related to an increased energy backtransfer rate from the excited  $\text{Er}^{3+}$  ions to  $\text{GeO}_x$  host at an elevated temperature compared with the back part of the sample and Er-doped  $\text{SnO}_2$  nanofiber sample.

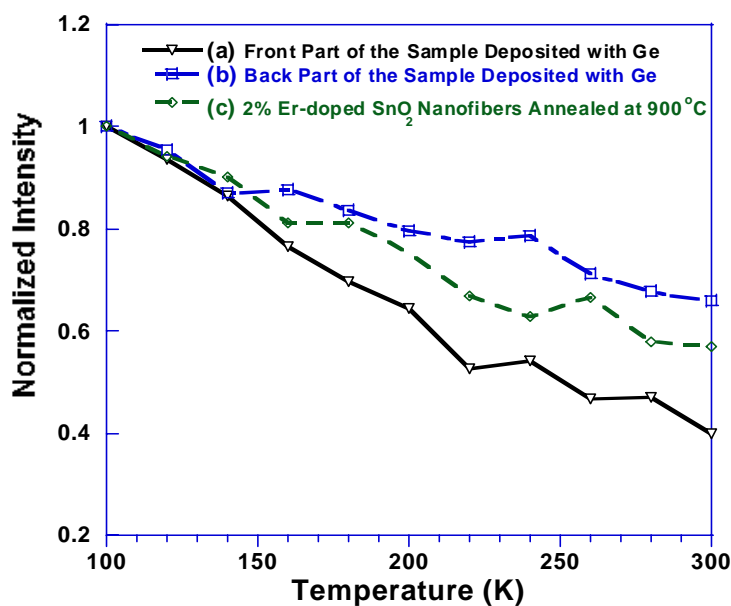


**Figure 111.** Low temperature PL spectra of (a) the front part and (b) the back part of a 2% Er-doped  $\text{SnO}_2$  nanofiber sample exposed to Ge vapor for 30 minutes; and (c) a 2% Er-doped  $\text{SnO}_2$  nanofiber sample annealed at 900 °C in air for 3 h.

### 6.3 Summary

Er-doped SnO<sub>2</sub> nanofibers deposited with Ge was prepared via a simple and straightforward vapor transport method. As-prepared nanofibers were characterized using SEM, TEM, XEDS and Raman spectroscopy. In terms of morphology, the front part of the nanofiber sample is composed of film-like platelets; the middle and back part of the sample consists of nanofibers with lots of small nanoparticles on their surfaces. Raman spectra confirm that SnO<sub>2</sub> can be reduced by Ge vapor in the front part of the sample at a relatively high temperature to form elemental Sn. In contrast, the back part of the sample is mainly composed of amorphous Ge and SnO<sub>2</sub>, which means that Ge cannot reduce SnO<sub>2</sub> under these conditions. Interestingly, Ge nanorods can be prepared on the surface of both SnO<sub>2</sub> and Er-doped SnO<sub>2</sub> nanofibers using a 1 h Ge deposition time. Presumably, the Ge nanorods were grown via a VLS synthetic route, with the as-formed Sn nanoparticles serving as catalysts.

In terms of emissive properties, it was found that the front and middle part of these nanofibers that were deposited with Ge for 15 minutes can emit ~2 orders of magnitude stronger room temperature luminescence at 1540 nm when compared with 2% Er-doped SnO<sub>2</sub> nanofibers that were annealed at 900 °C in air for 3 h. The PL excitation spectra of these nanofibers deposited with Ge suggest that the luminescence is from a GeO<sub>x</sub>-mediated excitation of erbium ions, which is different from the direct excitation of erbium ions in the case of Er-doped SnO<sub>2</sub> nanofibers. The temperature dependent PL spectra indicate that the front part and the back part of the sample have different room temperature quenching rates due probably to their difference in compositions. Thus, the sum of these results point to the

fact that  $\text{GeO}_x$  is an effective sensitizer for erbium ions. This sensitizer could be applied to other Er-doped materials to further enhance their PL intensity at 1540 nm.

*CHAPTER VII.*

Gold-Induced Self-Assembly of Germanium Micropatterns  
and Their Use as Nanowire Templates

## 7.0 Introduction

Germanium is a very important Group IV semiconductor with an indirect band gap of 0.66 eV and high carrier mobilities relative to silicon. It becomes an important electronic material since it can alloy with Si to form  $\text{Si}_x\text{Ge}_{1-x}$  which can be used to build super-high-frequency transistors that are routinely in use. A heterojunction bipolar SiGe transistor operating at 510 GHz was realized recently by the cooperative efforts of Georgia Tech and IBM as shown in Table 9.<sup>209</sup>

**Table 9.** Transistor performance summary at 300, 77, and 4.5 K for a  $0.12 \times 10 \mu\text{m}^2$  SiGe emitter (adapted from ref. 209).

Temperature (K)	300	77	4.5
Peak $f_T$ (GHz)	352	456	510

Micropatterned Ge has potential applications in the various fields of photonics and chemical sensors.<sup>210,211</sup> Owing to its high dielectric constant, micropatterned Ge is a good candidate for photonic band gap materials, within which a certain light frequency band is not allowed to propagate. Miguez et al. prepared patterned macroporous Ge inverse opals using silica opals as templates.<sup>210</sup> In their approach, submicron silica spheres first self-organize into a face-centered cubic lattice.  $\text{Ge}(\text{OCH}_3)_4$  (tetramethoxygermane) is then infiltrated into the void lattice of silica opals followed by a hydrolysis process to form  $\text{GeO}_2$ . The  $\text{GeO}_2$  is reduced to Ge by hydrogen gas at 550 °C. Finally, the silica templates are removed by a HCl

etching method to obtain Ge inverse opals. Figure 112 shows the low magnification SEM image of a germanium inverse opal showing a long range order is preserved.

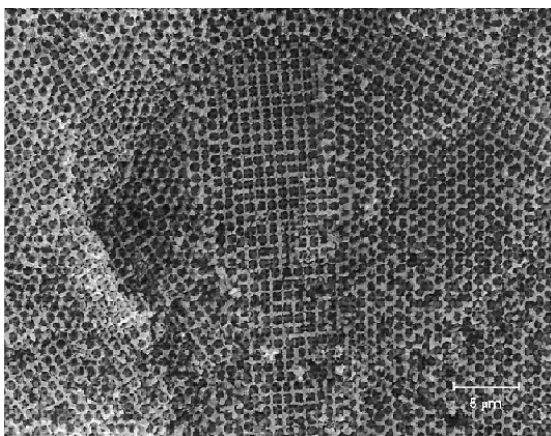


**Figure 112.** SEM image of a germanium inverse opal showing that a long range order is preserved. (Scale bar = 5  $\mu\text{m}$ , adapted from ref. 210.)

Furthermore, Ge micropatterns can also be used as templates to selectively grow nanoscale structures such as nanowires and nanodots on them so that they can be further functionalized.

Micropatterned materials of metals and dielectrics also have broad applications in microelectronic, optical and magnetic recording devices, and biochips/sensors.<sup>212-215</sup> For one example, a patterned array of discrete nanomagnets can be used to store data in a hard drive. Figure 113 shows the SEM image of a patterned Co/Pd nano-island array that was fabricated using a very complex ion beam proximity lithography (IBPL) method. Although the patterned surfaces could be fabricated through ‘top-down’ lithography techniques as mentioned above, nevertheless they are limited by cost and processing time.<sup>214</sup>

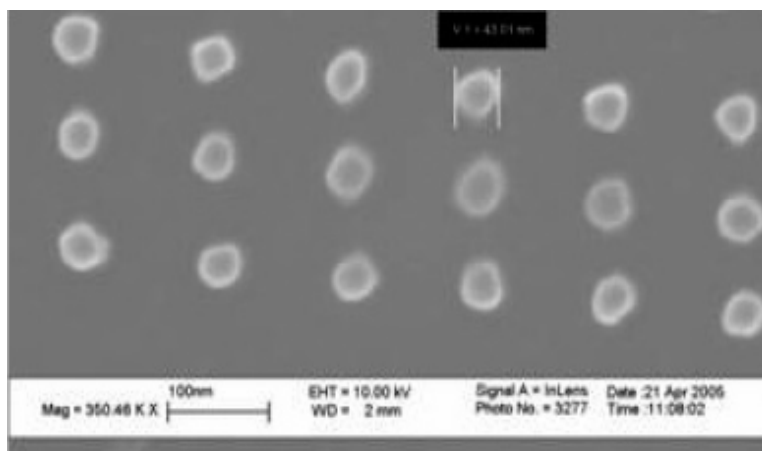


**Figure 113.** SEM image of 43 nm Co/Pd nano-island array fabricated using the IBPL method (adapted from ref. 214).

In this chapter, a facile self-assembly method relying on a Au-assisted thermal annealing process was employed to obtain rectangular and square Ge micropatterns. As a demonstration of their utility in possible patterning of biomaterials, the Ge micropatterns were used as templates to fabricate 1-D calcium carbonate nanowires via an electrochemical deposition method using simulated body fluid (SBF) or aqueous solution of  $\text{CaCl}_2 \cdot 2\text{H}_2\text{O}$  &  $\text{NaHCO}_3$  as electrolytes. As another proof of their possible applications in the field of electronic materials, the micropatterns were also used as templates to fabricate patterned silicon nanowires through a VLS synthetic route.

## 7.1 Experimental

### 7.1.1 Fabrication of Germanium Micropatterns

Germanium micropatterns were fabricated through a facile thermal annealing of Au-coated Ge (100) wafer pieces. Figure 114 shows the reactor design for obtaining these micropatterns. An n-type Ge (100) wafer was sonicated for 10 minutes in absolute methanol (Pharmco-AAPER, Inc.) followed by a 10 minute wash in boiling dichloromethane (Pharmco Product, Inc.). The wafer was then sonicated for 10 minutes in absolute methanol again to remove residual organic species. To remove the oxide layer, the wafer was immersed in a solution with a 1:4 volume ratio of concentrated  $\text{NH}_4\text{OH}$  (VWR) to  $\text{H}_2\text{O}$  for 5 minutes. The wafer was then rinsed thoroughly using de-ionized (DI) water and blown dry using nitrogen gas. In the next step, a layer of 3 nm Au was sputtered on the as-cleaned Ge wafer that was then placed on an alumina boat in a quartz tube reactor. After a 4 h anneal at  $830^\circ\text{C}$  in helium gas (Praxair, UHP grade), rectangular or square patterns can be formed on the Ge wafer surface.

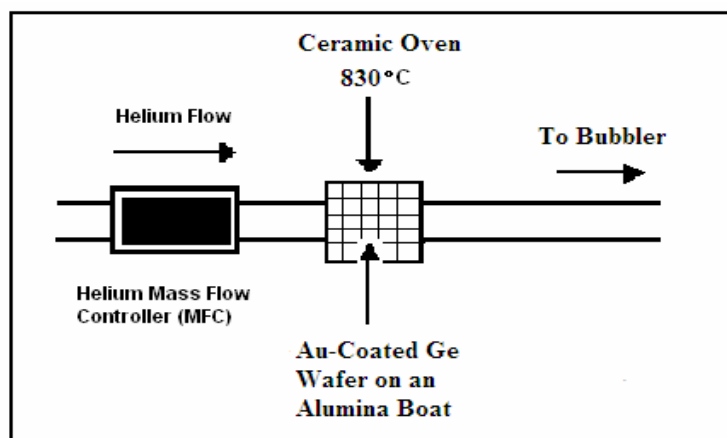


**Figure 114.** Reactor design for fabricating Ge micropatterns.

### 7.1.2 Preparation of CaCO<sub>3</sub> Nanowires Using Ge Micropatterns as Templates

An electrochemical deposition method was employed to fabricate calcium carbonate nanowires using this micropatterned Ge as a template. The diagram of the setup is shown in Figure 115. A platinum foil is used as anode, and a micropatterned Ge (100) wafer serves as cathode. Simulated body fluid (SBF) or an aqueous CaCl<sub>2</sub>·2H<sub>2</sub>O & NaHCO<sub>3</sub> solution was used as electrolyte solution. Simulated body fluid (SBF) solution was prepared according to a literature method.<sup>216</sup> To describe it briefly, reagent grade CaCl<sub>2</sub>·2H<sub>2</sub>O, Na<sub>2</sub>SO<sub>4</sub>, NaCl, KCl, MgCl<sub>2</sub>·6H<sub>2</sub>O, NaHCO<sub>3</sub> and K<sub>2</sub>HPO<sub>4</sub> were dissolved in a buffer solution of tris(hydroxymethyl)aminomethane and HCl with a final pH value of ~7.20. The corresponding molar ionic concentrations (mM) are listed as follows: Ca<sup>2+</sup> 2.5; HPO<sub>4</sub><sup>2-</sup> 1.0; K<sup>+</sup> 5.0; Na<sup>+</sup> 142.0; Mg<sup>2+</sup> 1.5; Cl<sup>-</sup> 147.8; HCO<sub>3</sub><sup>-</sup> 4.2; and SO<sub>4</sub><sup>2-</sup> 0.5. The pH value of the SBF solution is ~7.20. An aqueous CaCl<sub>2</sub>·2H<sub>2</sub>O & NaHCO<sub>3</sub> solution was prepared by dissolving 0.0918 g CaCl<sub>2</sub>·2H<sub>2</sub>O (Aldrich) and 0.0900 g NaHCO<sub>3</sub> (Sigma-Aldrich) in the appropriate amount of deionized (DI) water to make a total solution of 250 ml whose pH value is 7.81. The molar ionic concentrations (mM) of Ca<sup>2+</sup> and HCO<sub>3</sub><sup>-</sup> in the solution are 2.5 and 4.3, respectively, which are similar to those in SBF solution. Typically, the distance between the two electrodes is 1 mm, and the current density is 1.3 mA/cm<sup>2</sup>. Calcium carbonate nanowires were produced on the Ge micropatterns across the meniscus line after a 10 minute electrochemical deposition period. A p-type silicon (100) wafer was cleaned using acetone, H<sub>2</sub>SO<sub>4</sub>/H<sub>2</sub>O<sub>2</sub> solution, and rinsed with DI water thoroughly before it was sputtered with gold and then used for the electrochemical growth of calcium carbonate cubes, which is used in a control experiment.

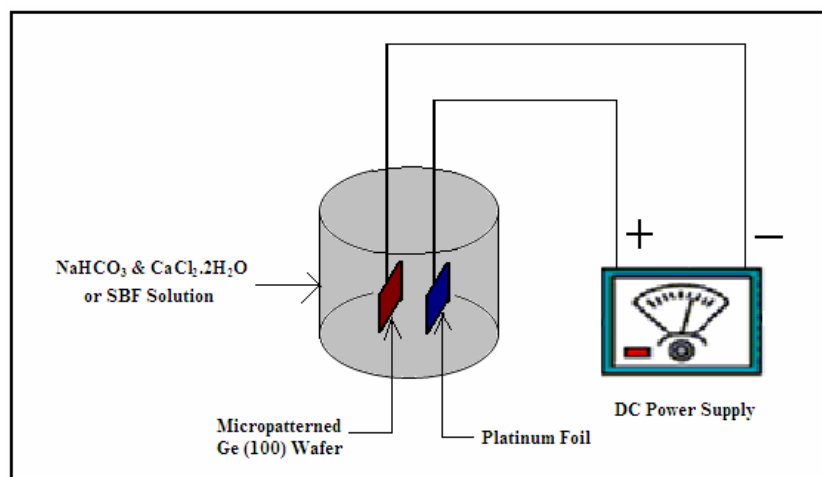


**Figure 115.** Diagram of the device for fabricating calcium carbonate nanowires using Ge micropatterns as templates.

### 7.1.3 Preparation of Si Nanowires Using Ge Micropatterns as Templates

Si nanowires were prepared using a VLS synthetic route using Ge micropatterns as templates. Figure 116 presents the diagram of the setup for fabricating Si nanowires. To fabricate Si nanowires, the micropatterned Ge (100) wafer was loaded into an alumina boat, which was then placed in the center of a quartz tube reactor heated by a 6 inch long oven. After 1 hour annealing at 600 °C, 30 sccm SiH<sub>4</sub> was then introduced into the system (0.5% in UHP grade He), which was further diluted with an additional 3000 sccm helium. The Si nanowire growth was carried out at 600 °C for 5 or 10 minutes. The silane gas flow was then turned off, and reactor was cooled down to room temperature naturally. Brown films of Si nanowires were produced on the Ge micropattern areas.

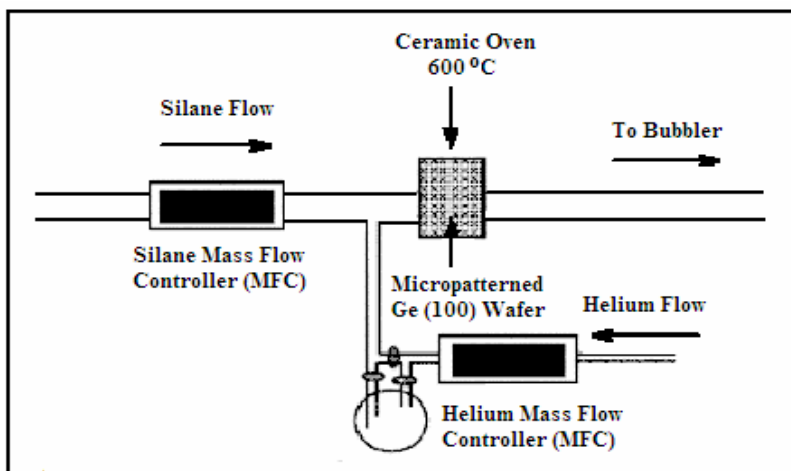


**Figure 116.** Diagram of the reactor design for fabricating Si nanowires using Ge micro-patterns as templates.

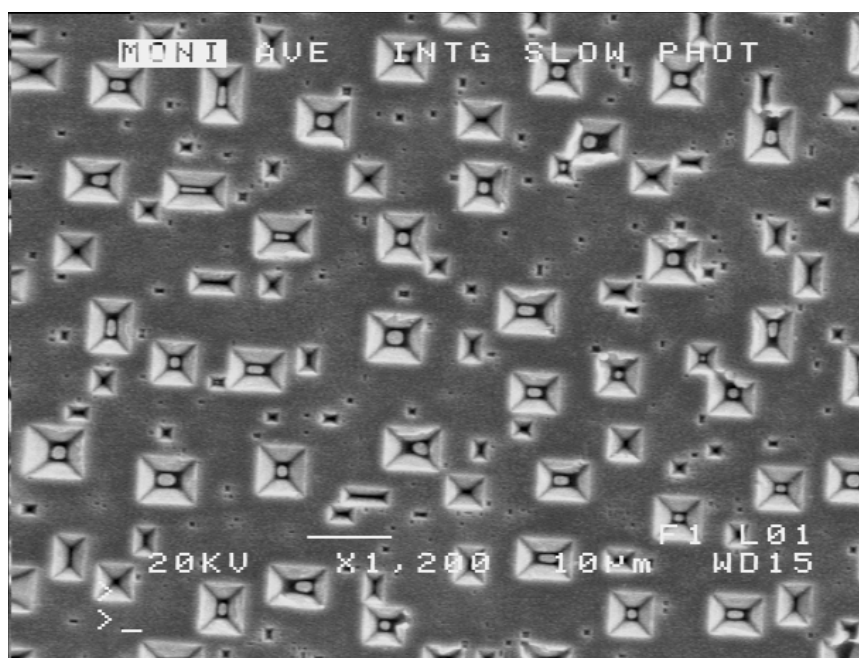
#### 7.1.4 Instrumentation

Structural characterization of micro-patterned germanium wafers, calcium carbonate structures and silicon nanowires was performed using a JEOL JSM-6320F field emission scanning electron microscope (SEM) at the University of Illinois-Chicago and a JEOL JSM-6100 SEM at Texas Christian University with an X-ray energy dispersive spectroscopy (XEDS) analyzing system attached. A Philips 300 Transmission Electron Microscope (TEM) at TCU was used to examine the morphology of calcium carbonate nanowires. Raman spectra were recorded using a Raman micro-imaging system in the laboratory of Prof. Zerda at the Physics Department of TCU (as described in Chapter 3). A Keithley Model 236 source-measure unit was employed to apply bias in the electrochemical deposition experiments.

## 7.2 Results and Discussion

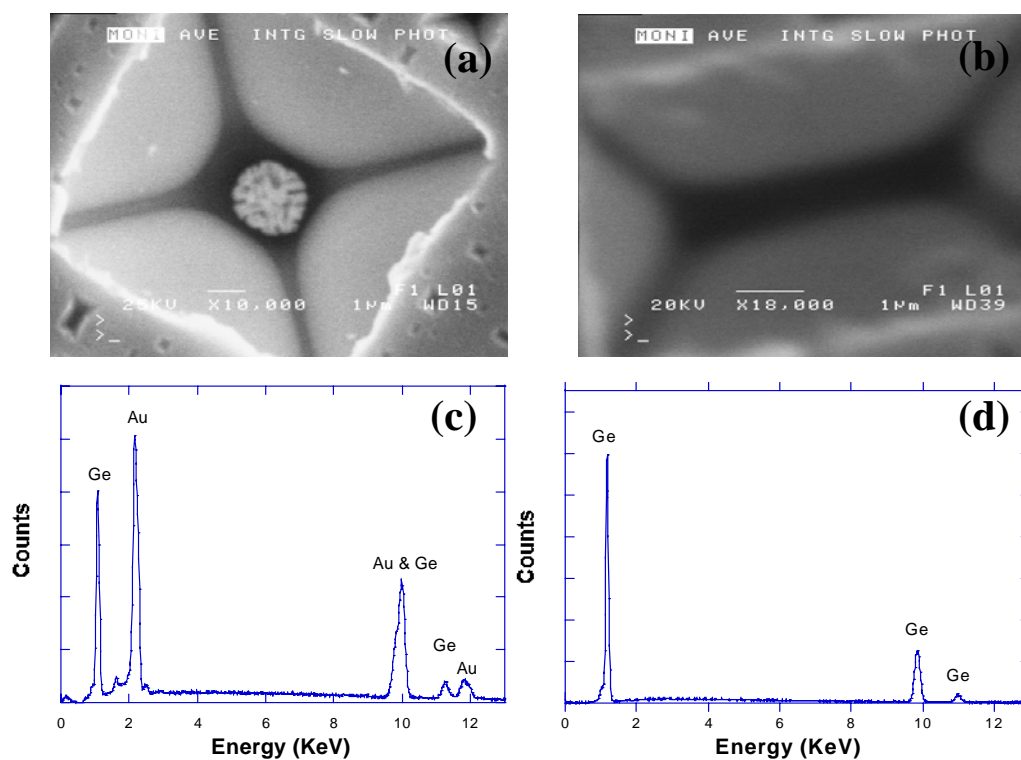
### 7.2.1 Characterization of Ge Micropatterns

Figure 117 shows the SEM image of germanium micropatterns fabricated through annealing an n-type Ge (100) wafer coated with a 3 nm thick Au film at 830 °C for 4 h in 3000 sccm flow rate helium gas. Generally, there are two types of micropatterns on the annealed Ge wafer, that is, one type is square, and another one is rectangular. It was also found that some neighboring corners of the micropatterns are in contact. The edges of these micropatterns are parallel or perpendicular to each other and their widths range from 10  $\mu\text{m}$  to less than 1  $\mu\text{m}$ .



**Figure 117.** SEM image of germanium micropatterns fabricated through annealing a 3 nm Au-coated n-type Ge (100) wafer at 830 °C for 4 h in helium gas.

Figure 118 presents the SEM images and XEDS spectra of the micropatterns with and without an island feature residing in the center. Figure 118a shows that the island residing in the center of a micropattern has a multifaceted structure. A XEDS spectrum (Figure 118c) collected from the multifaceted island indicates that the island is composed of Au and Ge, with Ge-L $\alpha$  and Au-M $\alpha$  peaks detected at 1.2 and 2.1 KeV, respectively. The Ge-K $\alpha$  and Au-L $\alpha$  peaks, known to lie at 9.9 and 9.7 KeV, respectively, are strongly overlapping and thus difficult to distinguish in this case. However, the XEDS spectrum (Figure 118d) carried out on the micropattern without such an island (Figure 118b) shows that there are no detectable Au signals present.



**Figure 118.** SEM images of (a) a Ge micropattern with a multifaceted island in the center, (b) a Ge micropattern without island in the center, and XEDS spectra (c) and (d) collected from the micropatterns shown in (a) and (b), respectively.

### 7.2.2 Factors Affecting the Morphology of Ge Micropatterns

SEM images of an as-cleaned Ge wafer, an annealed Ge wafer, and an annealed Au-coated Ge wafer are shown in Figure 119. It was found that the coating of Au on a Ge (100) wafer is necessary to form Ge micropatterns. An as-cleaned Ge (100) wafer has a smooth surface and the annealed Ge (100) wafer has irregular micropatterns on its surface, whereas regular germanium micropatterns can be obtained through annealing Au-coated Ge (100) wafer.

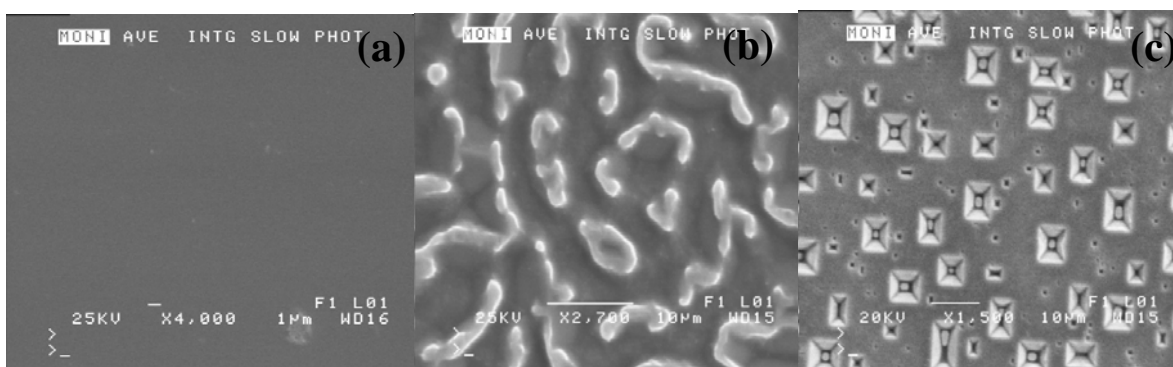


**Figure 119.** SEM images of (a) as-cleaned Ge (100) wafer, (b) Ge (100) wafer after being annealed at 830 °C for 4 h, and (c) 3 nm thick Au-coated Ge (100) wafer after being annealed at 830 °C for 4 h.

To further explore the factors which could affect the morphology of Ge micropatterns, a series of experiments were performed varying annealing temperatures, thicknesses of Au coating, annealing times, and helium flow rates. Figure 120 shows the SEM images of 8 nm thick Au-coated Ge (100) wafers annealed at various temperatures for the same amount of time. It is interesting to find that annealing temperatures can dramatically affect the

morphology of Ge micropatterns. At lower temperatures, such as 400 °C, no square or rectangular micropatterns can be produced. When the annealing temperature is elevated to 600 °C, small irregular micropatterns with rough edges start to appear. However, much more regular micropatterns are obtained when the annealing temperature is increased to 830 °C. In general, a higher temperature is beneficial to forming more distinct and regular Ge micropatterns, presumably due to the low eutectic point of AuGe (361 °C) and higher alloy mobility at higher temperatures.

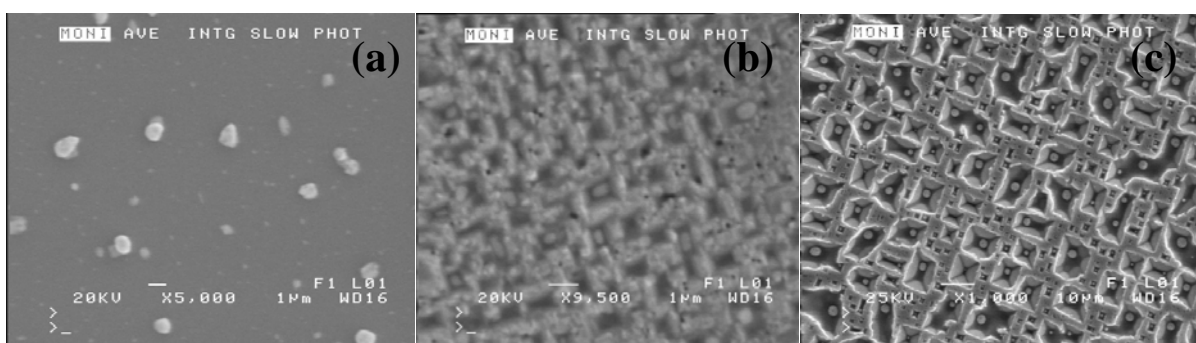


**Figure 120.** SEM images of 8 nm thick Au-coated Ge (100) wafer annealed for 4 h at (a) 400 °C, (b) 600 °C and (c) 830 °C.

The thickness of the Au coating was found to be another critical factor that could affect the morphology of Ge micropatterns. Figure 121 presents the SEM images of Ge micropatterns obtained through the annealing of a Ge wafer coated with different thicknesses of Au film, which range from 3 to 20 nm. Thinner Au coatings, e.g. 3 nm Au, are beneficial to forming much more regular Ge micropatterns. The micropatterns obtained through annealing a 20 nm Au-coated Ge (100) wafer are much less regular in terms of the uniformity of the surface of these micropatterns, and some AuGe alloys are residing atop the edges of

those micropatterns. In general, the thinner the Au coating, more regular the Ge micropattern will be. Given that Ge concentration is below 28% (by weight) in these AuGe alloys, a higher concentration of Au can lead to the formation of alloys with a higher melting point (according to Au-Ge binary phase diagram).<sup>93</sup> Therefore, thick gold coatings can reduce the mobility of AuGe alloys by increasing their melting points, which is probably deleterious to the formation of regular patterns.

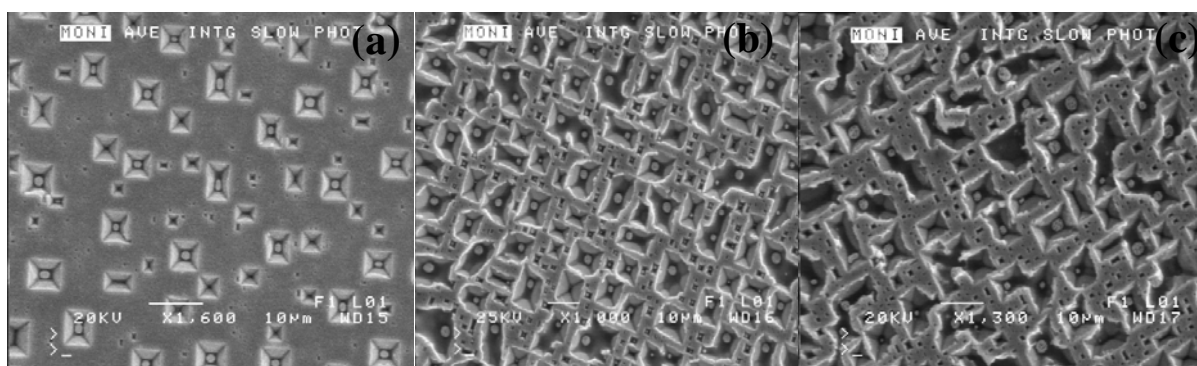


**Figure 121.** SEM images of Ge micropatterns obtained through annealing (100) Ge wafer coated with (a) 3 nm Au, (b) 8 nm Au, and (c) 20 nm Au.

Figure 122 shows the SEM images of Au-coated Ge (100) wafers annealed for different times and using various helium flow rates. When the annealing time is increased from 4 to 6 h, the center of the wafer possesses irregular patterns, whereas the edges of the wafer have more distinct square or rectangular micropatterns relative to those of the wafer annealed for 4 h. It is notable that far fewer AuGe islands were left in the middle of those micropatterns after longer time anneals. AuGe alloys are in the liquid state at 830 °C because the eutectic temperature of AuGe is only 361 °C, so the helium carrier gas would blow away more liquid AuGe alloys in longer reaction times, which leads to the reduction of the number

of AuGe islands left in the Ge micropatterns. When a slower helium flow rate was employed to anneal the wafer, the obtained Ge micropatterns are not very different from those prepared using a higher helium flow rate. However, wafers annealed using a slower He flow rate are more whitish in appearance, probably related to a higher degree of oxidation.

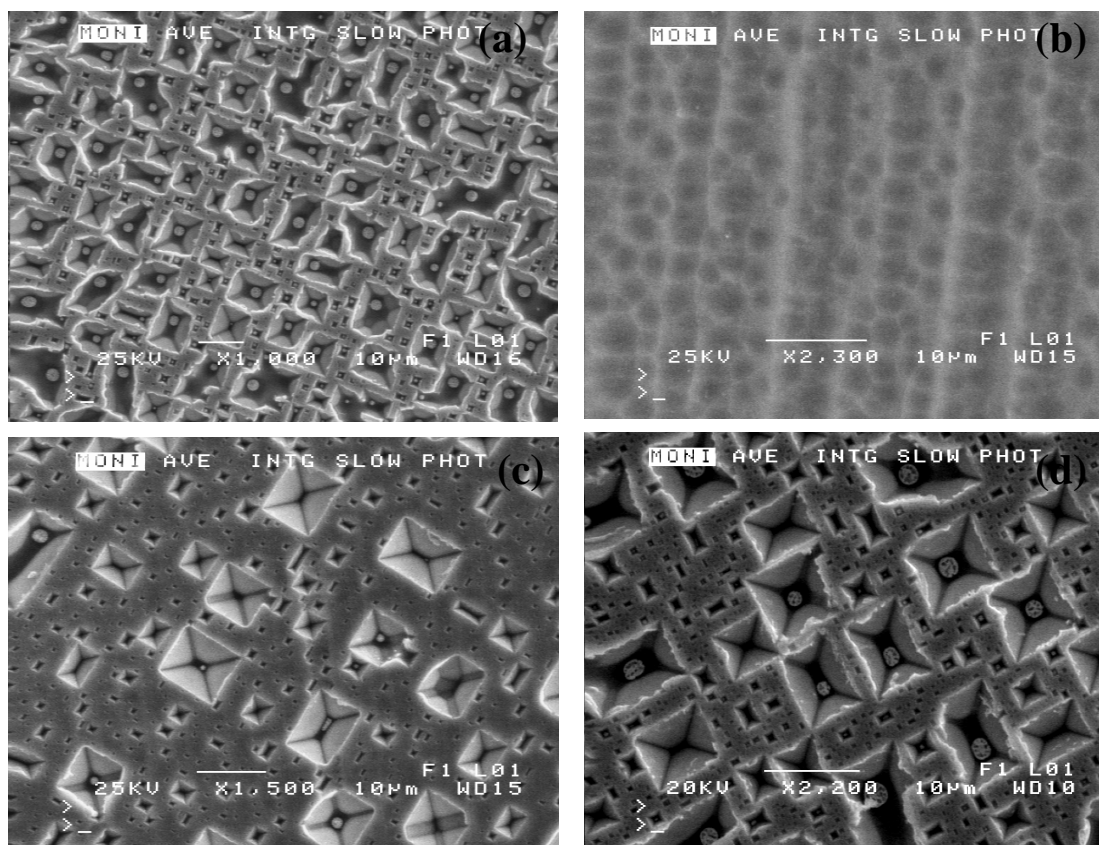


**Figure 122.** SEM images of (a) Au-coated Ge wafer annealed for 4 h using a 3000 sccm helium flow rate, (b) the center and (c) the edge of Au-coated Ge wafer annealed for 6 h using a 3000 sccm helium flow rate, and (d) Au-coated Ge wafer annealed for 4 h using a 1500 sccm helium flow rate. (All wafers were coated with 8 nm Au and annealed at 830 °C.)

### 7.2.3 Possible Mechanism Underlying the Formation of Ge Micropatterns

Figure 123 illustrates 3 typical examples of patterned Ge and Ge-containing alloys developed by other groups. Gray et al. reported that square nanoscale pits of  $\text{Si}_{0.7}\text{Ge}_{0.3}$  could be heteroepitaxially self-assembled on Si (001) wafer using a molecular beam epitaxy (MBE) growth method combined with thermal annealing.<sup>217</sup> They believe that the formation of these pits is driven by a strain relief process under appropriate kinetically-limited growth conditions. The strain originates from the 4% lattice mismatch between Si and Ge. Sun et al. found that square or rectangular  $\text{Co}_5\text{Ge}_7$  islands can grow epitaxially on Ge (001) wafers. They suggested that the strain caused by 2.3 % lattice misfit between a  $\text{Co}_5\text{Ge}_7$  alloy and the Ge substrate leads to the formation and enlargement of the islands.<sup>218</sup> Fang et al. found that germanium pores with  $\langle 111 \rangle$  and  $\langle 100 \rangle$  growth directions could be prepared by anodic electrochemical etching of n-type Ge (100) wafer in a 5% HCl aqueous electrolyte.<sup>219</sup> It is proposed that the nucleation of Ge pores is caused by the leakage current at the junction between Ge wafer and electrolyte, which is initiated by local defects such as dislocations.

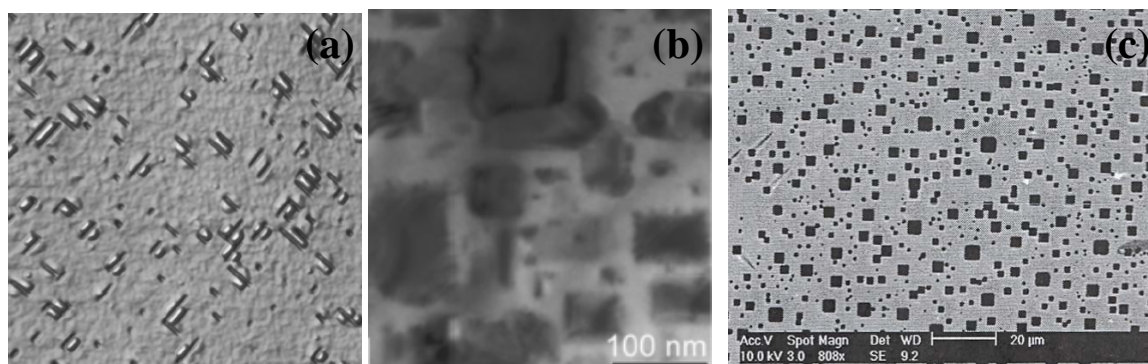


**Figure 123.** (a) a  $4 \times 4 \mu\text{m}$  atomic force microscopy (AFM) image of a 5-nm-thick  $\text{Si}_{0.7}\text{Ge}_{0.3}$  sample grown using MBE method and annealed at  $550 \text{ }^\circ\text{C}$  *in situ* for 1 h (adapted from ref. 217). (b) TEM images of  $\text{Co}_5\text{Ge}_7$  islands on a backside-polished Ge wafer (adapted from ref. 218). (c) SEM image of Ge pores with a (100) orientation made by anodic electrochemical etching of n-type Ge (100) wafer in 5% HCl aqueous electrolyte at  $20 \text{ }^\circ\text{C}$  with a current density of  $0.5 \text{ mA/cm}^2$  (adapted from ref. 219).

However, the exact mechanism for the formation of Ge pores does not lend itself to a simple explanation.<sup>219</sup> In our case, we believe that Au atoms first diffuse into the Ge substrate at the  $830 \text{ }^\circ\text{C}$  annealing temperature, which will cause strain due to the huge lattice misfit between Au ( $a=0.408 \text{ nm}$ ) and Ge ( $a=0.566 \text{ nm}$ ). To relieve such a strain, AuGe alloys will self-assemble on the four edges and the center of those micropatterns, which is thermodynamically more favorable.<sup>217,218</sup> Furthermore, AuGe alloys on both the edges and the center are so mobile at  $830 \text{ }^\circ\text{C}$  that they can be carried away by the helium carrier gas resulting in the absence of AuGe islands in some micropatterns after longer time anneals. In contrast, however, relatively large amounts of AuGe alloy remain on the edges and centers of those micropatterns at lower annealing temperatures, e. g.  $600 \text{ }^\circ\text{C}$  (as shown in Figure 120).

It should be pointed out that this thermodynamic process requires a critical annealing temperature, below which no patterns could be formed (e. g. 400 °C). As to the loss of Ge during the formation of these micropatterns, we believe that it is related to both the volatility of germanium suboxides and the high mobility of liquid AuGe alloys at such high annealing temperatures.<sup>154</sup>

#### 7.2.4 Growth Directions of the Sidewalls of Ge Micropatterns

To further understand the mechanism underlying the formation of Ge micropatterns, the growth directions of the sidewalls of these micropatterns were determined via an analysis of Ge crystallography combined with SEM measurements.<sup>220</sup> Figure 124 shows the SEM images and simulated projections of plan-view and vertical-view of Ge micropatterns and  $\langle 111 \rangle$  &  $\langle 101 \rangle$  families of cubic Ge. The single crystal Ge (100) wafer was cut to produce the side- and vertical-views of Ge micropatterns. Plan-view projection of the growth direction of the four sidewalls shows that those growth directions are parallel or perpendicular to each other, which implies that the growth directions possibly belong to the  $\langle 111 \rangle$  or  $\langle 101 \rangle$  family of cubic phase Ge. In this illustration, Arrow 2 stands for the growth direction of the sidewall because it is perpendicular to the wall. Arrow 1 is the projection of Arrow 2 on the Ge (100) substrate. It is easy to prove that the value of  $\theta$  is equal to  $90^\circ$  minus slope angle  $\gamma$ , because Arrow 1 and Arrow 2 are perpendicular to the two sides of the slope triangle of the micropattern. Since the value of  $\gamma$  is measurable via SEM imaging, the value of  $\theta$  can thus be determined. The calculated  $\theta$  value is  $\sim 34^\circ$  in this case, which will be used later to determine the growth direction of the sidewalls. It is noteworthy that the four  $\langle 111 \rangle$  orientations are perpendicular or parallel to each other, which is similar to those of the

sidewalls of Ge micropatterns. Furthermore, the  $\langle 111 \rangle$  growth directions have a  $\theta$  value of  $35.3^\circ$ , whereas  $\theta$  value for  $\langle 101 \rangle$  growth directions is  $54.7^\circ$ . Since our calculated  $\theta$  value is around  $34^\circ$ , the growth directions of the sidewalls of Ge micropatterns should belong to the  $\langle 111 \rangle$  family.

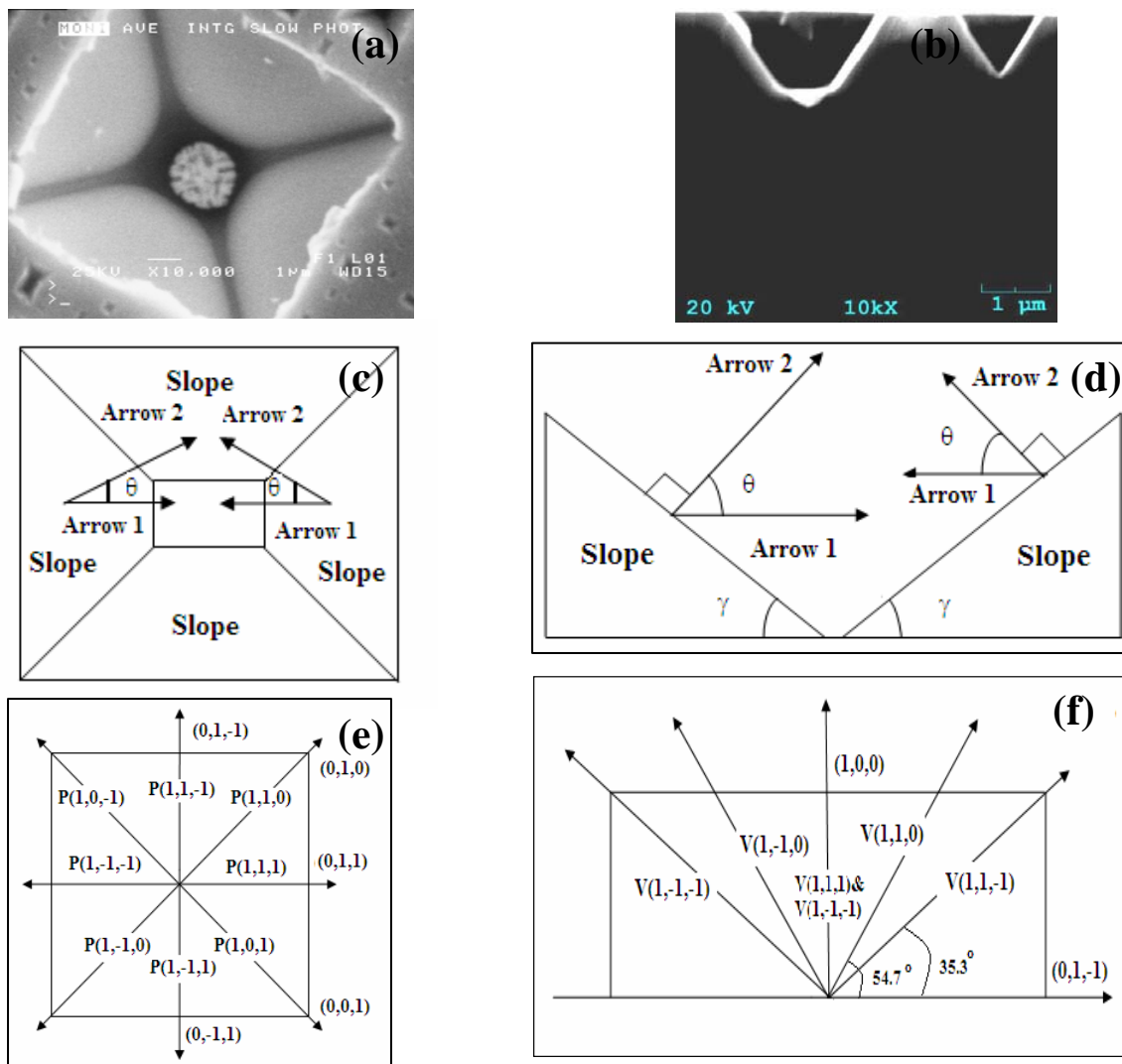


**Figure 124.** SEM images of (a) plane-view and (b) vertical-view of Ge micropatterns. (c) and (d) are simulated projections of plane-view and vertical-view of Ge micropatterns, respectively. (e) and (f) are schematic projections of both  $\langle 111 \rangle$  and  $\langle 101 \rangle$  families of diamond cubic phase Ge viewed along (100) substrate normal and the direction perpendicular to the substrate normal, respectively. (Note: Arrow 2 is perpendicular to the surface of sidewall, and Arrow 1 is the projection of Arrow 2 on the Ge (100) wafer. The  $\theta$  values for  $\langle 111 \rangle$  and  $\langle 101 \rangle$  families are  $35.3^\circ$  and  $54.7^\circ$ , respectively.)

## 7.2.5 Growth of CaCO<sub>3</sub> Nanowires Using Ge Micropatterns as Templates

### 7.2.5.1 Overview

It is known that calcium carbonate could be used as a promising biomaterial for bone replacement and regeneration since it can be easily resorbed by osteoclasts (bone-resorbing cells), which subsequently undergo apoptosis and are then replaced by osteoblasts (bone-producing cells) to generate native bone.<sup>221</sup> It has been reported that the microstructure of materials of this type will greatly affect their mechanical properties which are very important for its bioceramic applications.<sup>222,223</sup> Previously, calcium carbonate nanowires were prepared using polymer-controlled crystallization,<sup>224</sup> microemulsion-based synthesis,<sup>225</sup> polyelectrolyte-modified self-assembled monolayers,<sup>226</sup> and sonochemical methods.<sup>227</sup> Calcium carbonate has three polymorphs: calcite, aragonite, and vaterite. Calcite is the most thermodynamically stable phase at ambient temperature, aragonite is a high pressure polymorph, and vaterite is a metastable phase that tends to transform into calcite or aragonite.<sup>227</sup> To explore the possible patterning applications of Ge micropatterns in the field of biomineralization, we used them as templates to grow calcium carbonate nanowires via an electrochemical method using simulated body fluid (SBF) or aqueous CaCl<sub>2</sub>·2H<sub>2</sub>O & NaHCO<sub>3</sub> solution as electrolyte. CaCO<sub>3</sub> nanowires were produced on Ge micropatterns across the meniscus line. The effects of electrolyte, deposition time and substrate on the morphology of calcium carbonate were also systematically explored.

### 7.2.5.2 Characterization

A SEM image, XEDS spectrum and TEM image of  $\text{CaCO}_3$  nanowires produced on the patterned Ge surface in SBF solution are shown in Figure 125. The SEM image (Figure 125a) shows that the nanowires are  $\sim 150$  nm in diameter and  $\sim 5$   $\mu\text{m}$  long. It is notable that nanowires can only be found on the Ge micropatterns across the meniscus line as shown in Figure 125b. The corresponding XEDS spectrum (Figure 125c) indicates that the nanowires are mainly composed of calcium, as the  $\text{Ca-K}\alpha$  peak is located at 3.7 KeV. The  $\text{Ge-L}\alpha$  and  $\text{Au-M}\alpha$  peaks at 1.2 and 2.1 KeV, respectively, are from the substrate. The XEDS system attached to the JEOL JSM-6100 SEM at TCU cannot detect C and O signals due to the existence of a filtering Be window. The TEM image (Figure 125d) indicates that the  $\text{CaCO}_3$  nanorod is uniform in terms of width and possesses a diameter of  $\sim 80$  nm.

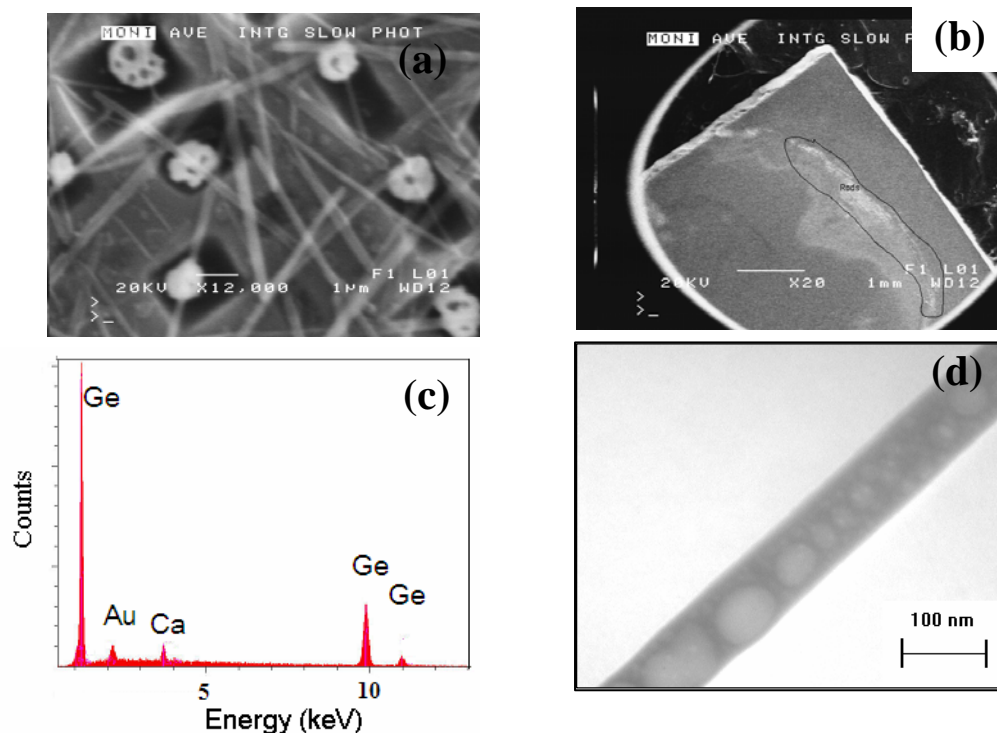


**Figure 125.** SEM images of (a)  $\text{CaCO}_3$  nanowires precipitated in SBF solution after a 10 minute deposition. (b)  $\text{CaCO}_3$  nanowires precipitated on the Ge micropatterns across the meniscus line. (c) XEDS spectrum collected from the area shown in (a). (d) A typical TEM image of  $\text{CaCO}_3$  nanorod with a diameter of  $\sim 80$  nm.

### 7.2.5.3 Effects of Electrolyte and Precipitation Position

To further prove that the nanowires are only composed of calcium carbonate and explore the effect of different electrolytes on the morphology of these nanowires, an aqueous  $\text{CaCl}_2 \cdot 2\text{H}_2\text{O}$  &  $\text{NaHCO}_3$  solution was used as electrolyte to fabricate  $\text{CaCO}_3$  nanowires, using again these Ge micropatterns as templates. SEM images and an XEDS spectrum of  $\text{CaCO}_3$  nanowires produced in an aqueous  $\text{CaCl}_2 \cdot 2\text{H}_2\text{O}$  &  $\text{NaHCO}_3$  solution are shown in Figure 126. The SEM image shows that the nanowires obtained in an aqueous  $\text{CaCl}_2 \cdot 2\text{H}_2\text{O}$  &

NaHCO<sub>3</sub> solution are much longer than those produced in SBF solution as shown in Figure 126a. Impurity ions in SBF solution such as Mg<sup>2+</sup>, known to terminate calcite crystal growth,<sup>228</sup> could possibly lead to the formation of shorter CaCO<sub>3</sub> nanowires obtained in this electrolyte. The typical length and diameter of the nanowires are ~20 μm, and 150 nm, respectively. XEDS spectra of the nanowires (Figure 126c) confirm that they have similar composition as that of the rods obtained from SBF solution. However, no nanowires-only cubes-can be obtained on the Ge micropatterns below the meniscus line (Figure 126b).

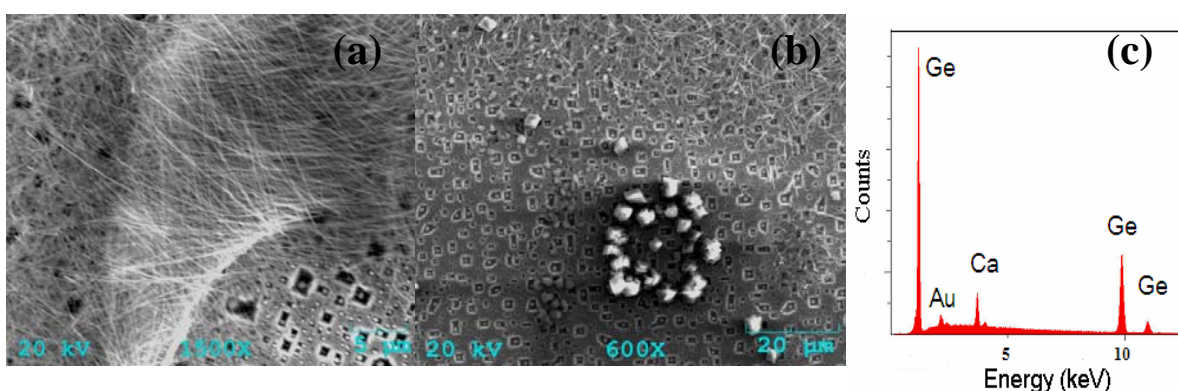


**Figure 126.** SEM images of (a) nanowires deposited on Ge micropatterns across the meniscus line and (b) microcubes deposited on the Ge micropatterns below the meniscus line. (c) XEDS spectrum collected from the area shown in (a). All nanowires are grown from an aqueous CaCl<sub>2</sub>·2H<sub>2</sub>O & NaHCO<sub>3</sub> solution.

#### 7.2.5.4 Effects of Substrates

Various substrates were used as cathodes to investigate the effects of substrates on the morphology of CaCO<sub>3</sub> grown via this process. Figure 127 shows the SEM images of calcium carbonate precipitated on different substrates, including a Ge wafer, a freestanding sputtered

Au film, and a Au-coated Si wafer. When a Ge (100) wafer or gold film was used as cathode, there are only cubes which precipitated, and no nanowires could be found either at the liquid-air interface or in the region below the interface. A Si (100) wafer coated with 15 nm Au was used as a cathode as well, on which only cubes are found to grow. It should be noted that more aggregates of cubes can be found at the meniscus than in the area below it, which is probably related to the relative higher concentration of  $\text{CO}_2$  at the interface. The width of the meniscus is about 0.5 mm.

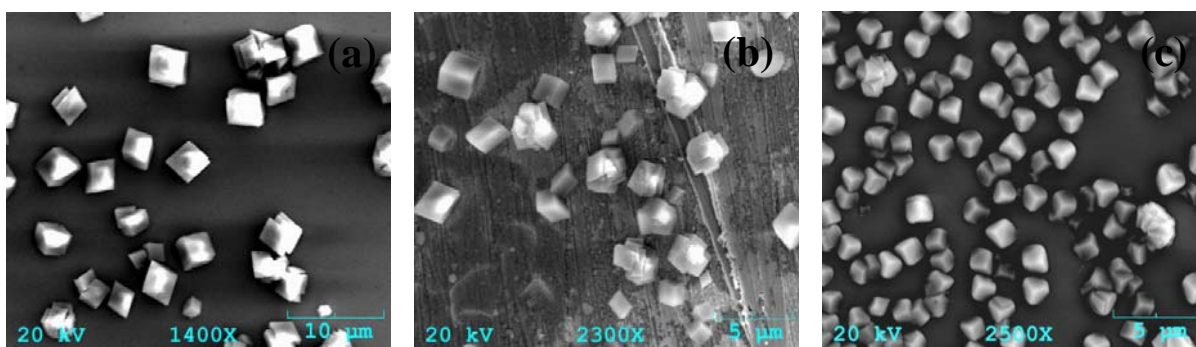


**Figure 127.** SEM images of  $\text{CaCO}_3$  cubes precipitated on (a) a Ge (100) n-type wafer, (b) a freestanding sputtered Au film, and (c) a 15 nm Au-coated p-type Si (100) wafer. Deposition time for all samples is 10 minutes, and an aqueous  $\text{CaCl}_2 \cdot 2\text{H}_2\text{O}$  &  $\text{NaHCO}_3$  solution was used as electrolyte.

#### 7.2.5.5 Micro-Raman Spectroscopy

Micro-Raman spectroscopy was chosen to further identify the composition and phase of these  $\text{CaCO}_3$  nanowires and microcubes. It has been reported that calcite is the most thermodynamically stable phase at ambient temperature among all three phases of calcium carbonate. Calcite has three characteristic Raman peaks at 1085, 712 and  $285 \text{ cm}^{-1}$ .<sup>229</sup> The

peak at  $1085\text{ cm}^{-1}$  is more than one order of magnitude stronger than other two peaks. Figure 128 presents the Raman spectra of  $\text{CaCO}_3$  nanowires and microcubes prepared on both Ge micropatterns and 15 nm Au-coated Si surfaces in an aqueous  $\text{CaCl}_2 \cdot 2\text{H}_2\text{O}$  &  $\text{NaHCO}_3$  solution. In the Raman spectrum of nanowires, the strongest peak is centered at  $\sim 310\text{ cm}^{-1}$ , which is consistent with the phonon scattering of the Ge substrate ( $298\text{ cm}^{-1}$ ).<sup>157</sup> The peak at  $1080\text{ cm}^{-1}$  is characteristic of the strongest Raman peak of calcite.<sup>229</sup> Other two characteristic peaks of calcite are too weak to be observed, presumably due to the relatively small amount of nanowires present. The intense and wide Ge Raman peak around  $310\text{ cm}^{-1}$  also affects the assignment of  $285\text{ cm}^{-1}$  peak from calcite. In contrast, the microcubes prepared on 15 nm Au-coated Si wafer have three much more distinct Raman peaks at  $1085$ ,  $710$ , and  $290\text{ cm}^{-1}$ , which definitely confirms that the microcubes are the calcite phase of calcium carbonate.<sup>229</sup> The Si-Si phonon scattering peak at  $523\text{ cm}^{-1}$  is from the Si substrate.<sup>158</sup> The  $710$  and  $290\text{ cm}^{-1}$  peaks are more distinguished relative to those of nanowires due to bigger size of the microcubes.

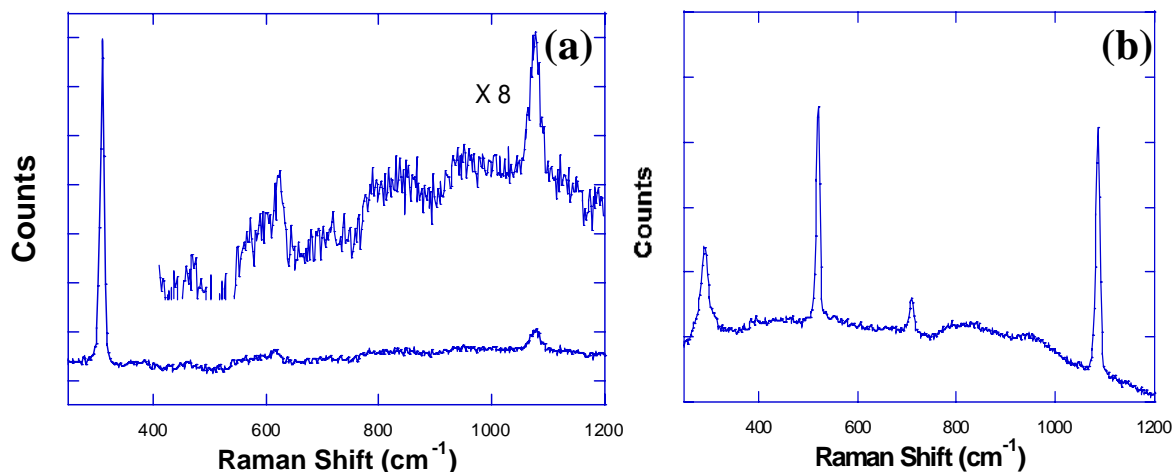


**Figure 128.** Raman spectra of (a)  $\text{CaCO}_3$  nanowires obtained using Ge micropatterns as substrate (inset is the  $\times 8$  magnified spectrum ranging from 400 to 1200  $\text{cm}^{-1}$ ). (b)  $\text{CaCO}_3$  microcubes prepared using a 15 nm Au-coated Si wafer as a substrate. Deposition time for all samples is 10 minutes, and aqueous solution of  $\text{NaHCO}_3$  and  $\text{CaCl}_2 \cdot 2\text{H}_2\text{O}$  was used as electrolyte.

#### 7.2.5.6 Mechanism Underlying the Formation of $\text{CaCO}_3$ Nanowires

Several mechanistic questions emerge as a consequence of the above measurements. First, why does  $\text{CaCO}_3$  precipitate on Ge micropatterns that were used as the cathode? The precipitation of calcium carbonate is induced by the increased local pH value resulting from the electrochemical reduction of the dissolved oxygen in the SBF and aqueous  $\text{CaCl}_2 \cdot 2\text{H}_2\text{O}$  &  $\text{NaHCO}_3$  solution, as given by equation (21). In basic conditions, the equilibrium of hydrogen carbonate ions is driven toward the formation of carbonate ions, which leads to the precipitation of calcium carbonate as shown in equation (22).<sup>229</sup>



Secondly, why does  $\text{CaCO}_3$  precipitate in the form of nanowires instead of microcubes on Ge micropatterns across the meniscus? Because different substrates have different electrode overpotentials for the oxygen reduction half reaction, the rates of local pH value changes associated with different substrates will be quite different. This will in turn greatly affect the nucleation and crystal growth process of calcium carbonate resulting in the formation of  $\text{CaCO}_3$  with various phases and morphologies.<sup>229</sup> Furthermore, the concentrations of  $\text{CO}_3^{2-}$  ions and  $\text{CO}_2$  can also influence the morphological evolution of calcium carbonate through changing its nucleation rates.<sup>227,229</sup> In our case, Ge micropatterns probably possess a suitable electrode overpotential for oxygen reduction reaction, which can help create a premium rate of local pH change for the one-dimensional (1-D)  $\text{CaCO}_3$  growth. Moreover, higher  $\text{CO}_2$  concentration at the liquid-air interface might be crucial to provide an appropriate nucleation rate for the growth of 1-D  $\text{CaCO}_3$  nanowires so that nanowires can only be obtained on Ge micropatterns across the meniscus. It should be noted that relatively large numbers of nanowires grow from one micropattern to another one as shown in Figure 129, which implies that 1-D  $\text{CaCO}_3$  growth might also be induced by the local concentration change of ions caused by the electrostatic potential difference present locally between two micropatterns. Due to the relatively high conductivities of the Au-rich islands, it is possible that the  $\text{Ca}^{2+}$  ions are locally confined in these Ge micropatterns, resulting in the initiation of 1-D  $\text{CaCO}_3$  nanorods.

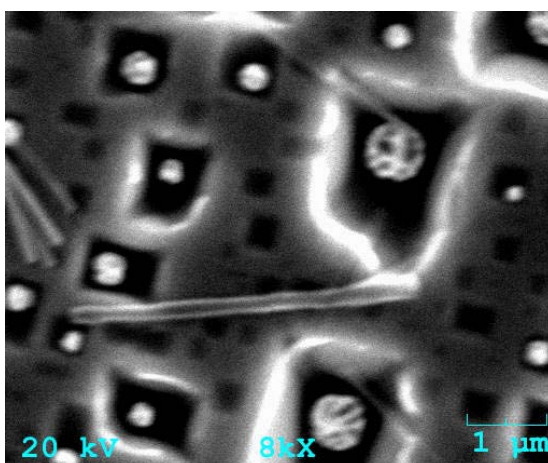


**Figure 129.** SEM of a typical  $\text{CaCO}_3$  nanorod growing from one micropattern to another.

## 7.2.6 Growth of Si Nanowires Using Ge Micropatterns as Templates

### 7.2.6.1 Overview

It is well known that Si nanowires (NWs) have broad applications in functional micro-electrical devices, micro-sensors, micro-biochips, etc.<sup>10,230</sup> As another demonstration of the utility of their templating character, these Ge micropatterns were employed as templates to grow patterned Si NWs through a well-known vapor-liquid-solid (VLS) mechanism. First, Ge micropatterns were obtained by annealing n-type Ge (100) wafers coated with thin Au films at 830 °C for 4 h. These micropatterns were then used as templates to grow patterned Si NWs of different densities.

### 7.2.6.2 Results and Discussion

SEM images and an XEDS spectrum of Si NWs grown on the Ge micropatterns are shown in Figure 130. It was found that the Si NWs grown on Ge micropatterns possess a

needle-like tapering structure as the result of simultaneous radial growth with axial elongation of silicon (Figure 130a).<sup>156</sup> Although most Si NWs can be grown within the sidewalls of Ge micropatterns (Figure 130b), nevertheless there are still some nanowires formed between these micropatterns due to the high mobility of AuGe alloys in flowing helium carrier gas at such a relatively high growth temperature (600 °C; recall that the eutectic temperature of AuGe alloy is only 361 °C). Higher magnification SEM images (Figures 19c and 19d) show that most of the Si NWs in valleys of the micropatterns are growing almost perpendicular to the sidewalls of the Ge micropatterns, which is consistent with the  $\langle 111 \rangle$  growth directions of these sidewalls. From these images, it is also evident that some Si NWs changed growth directions at the point where two wires met each other. Compositionally, the XEDS spectra (Figure 130e) confirm that the nanowires are composed of silicon, and the Ge peak is from the substrate.

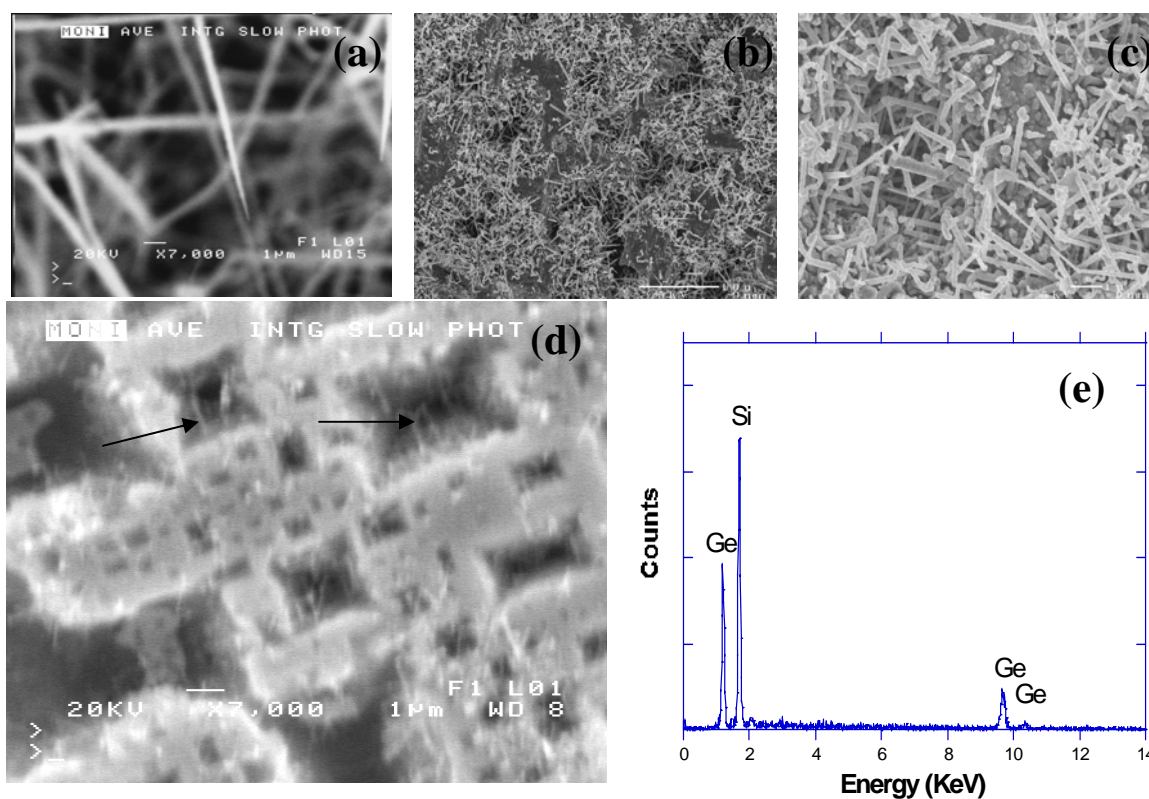


**Figure 130.** (a) SEM image of needle-like tapering Si NWs grown on a 20 nm Au-coated Ge wafer. (b) and (c) are low magnification and high magnification SEM images of Si NWs grown on an 8 nm Au-coated Ge wafer using a reaction time of 15 minutes, respectively. (d) A high magnification SEM image of Si NWs grown on an 8 nm Au-coated Ge wafer using a reaction time of 5 minutes. (e) A XEDS spectrum collected from the sample shown in (a). All wafers were annealed at 830 °C for 4 h to obtain micropatterned structures.

### 7.3 Summary

A facile self-assembly method was developed to prepare rectangular and square Ge micropatterns through a simple Au-assisted thermal annealing process. The presence of Au and a high temperature anneal are necessary to form such micropatterns. Thinner Au coatings and longer anneal times are crucial to forming more regular Ge micropatterns. The strain induced by the lattice misfit between Au and Ge and the following strain relaxation process presumably result in the formation of Ge micropatterns. The sidewalls of these Ge micropatterns possess  $\langle 111 \rangle$  orientations. To demonstrate proof-of-concept for their potential applications, Ge micropatterns were used as templates to prepare calcium carbonate nanowires via an electrochemical deposition method using SBF or aqueous solution of  $\text{NaHCO}_3$  &  $\text{CaCl}_2 \cdot 2\text{H}_2\text{O}$  as electrolytes. It was found that  $\text{CaCO}_3$  nanowires can be obtained on the Ge micropatterns across the meniscus line, and only  $\text{CaCO}_3$  microcubes were produced when a Au film, a Ge wafer and a Au-coated Si wafer were used as cathodes. It is believed that the relatively high  $\text{CO}_2$  concentration along the meniscus line and special electrode overpotential of Ge micropatterns for the oxygen reduction reaction initiate the 1-D  $\text{CaCO}_3$  growth. The electrostatic potential difference between two neighboring micropatterns and the geometry of spatial confinement might also directly influence the growth of  $\text{CaCO}_3$  nanowires. As another example of their application, Ge micropatterns were employed to fabricate Si NWs with tapering structures in these micropatterns. Such novel micropatterned structures may have other applications in the long term, such as bio-sensors, micro-optics, etc.

*CHAPTER VIII.*

Concluding Remarks

This dissertation has focused on the fabrication and optical properties of Er-doped Group IV semiconducting nanowires and their corresponding oxides. Erbium is technologically important due to its emission at 1540 nm, a wavelength at which silica has the minimum absorption. In addition, 1-D nanomaterials can be employed as building blocks to generate various kinds of nanodevices. Hence, the general goal of this research is to fabricate 1-D photonic building blocks emitting at 1.54  $\mu\text{m}$  efficiently.

In Chapter 3 the fabrication, characterization and optical properties of Er-doped Ge nanowires is described. The starting materials, Ge NWs are fabricated via a simple and safe vapor transport method. The mixture of carbon and germanium powder is heated up to 1000  $^{\circ}\text{C}$  to provide enough Ge vapor for the growth of Ge NWs via a well-known VLS synthetic route. The average diameters of Ge NWs range from 45 to 123 nm, depending on the He carrier gas flow rates and reaction times. Generally speaking, a longer reaction time and a higher He carrier gas flow rate can lead to the formation of thicker NWs. HRTEM imaging confirms that these Ge NWs are single crystals with a preferred (111) orientation. As-formed Ge NWs are then deposited with  $\text{Er}^{3+}$  ions via the pyrolysis of erbium CVD precursor,  $\text{Er}(\text{tmhd})_3$  at 500 or 600  $^{\circ}\text{C}$  in a quartz reactor. XEDS analyses of individual Er-doped Ge NWs show that the NWs possess a core-shell structure in terms of erbium concentration (~5% Er in core and ~18% Er on shell). XPS data suggest that the surface of these doped NWs is oxidized. UV-vis absorption spectrum of Er-doped Ge NWs annealed in air at 600  $^{\circ}\text{C}$  shows that there is a broad peak ranging from 300 to 600 nm due presumably to the presence of  $\text{GeO}_x$  that possesses tunable band gaps ranging from 0.75-5 eV. As fabricated Er-doped NWs are non-emissive unless they have been annealed in air. PL excitation spectra indicate that erbium ions in the host materials are presumably excited via a  $\text{GeO}_x$ -mediated process.

In the following chapter the impact of erbium incorporation on the structure and photophysics of silicon-germanium nanowires is described. Three different alloyed architectures are obtained by altering the deposition sequence of Si and Er<sup>3+</sup> on a Ge NW core. XEDS linescans of ‘Sandwich’ NWs show that the erbium is concentrated in the Ge-rich core (~2%, Er), whereas there is no detectable Er in the Si-rich shell. ‘Er-surface enriched’ NWs has a higher erbium concentration on the shell (21%, Er). ‘co-deposited’ NWs have a Si & Er rich shell. HRTEM imaging and micro-Raman spectroscopy confirm the formation of SiGe alloys after annealing these NWs at 600 or 700 °C. EXAFS data suggest that Er has a coordination number of ~8 with oxygen atoms in Er-doped Ge NWs, ‘Sandwich’ NWs, and ‘co-deposited’ NWs, which is quite different from that of standard Er<sub>2</sub>O<sub>3</sub> (coordination number = 6). Furthermore, the Er-O bond lengths are more relaxed in these NWs relative to standard Er<sub>2</sub>O<sub>3</sub>. As-formed NWs do not emit luminescence until they have been annealed in N<sub>2</sub> or air. Among three types of Er-doped SiGe NWs, ‘co-deposited Si&Er’ Ge NWs emit the strongest Er-related luminescence. The relative timing of introducing a dopant or impurity center can also affect the Er-related PL mechanism. PL excitation spectra suggest that when Er is deposited between Si layer and Ge core NW, a weak Er-related emission is obtained via the direct excitation of Er<sup>3+</sup> ions; whereas a much stronger emission at 1540 nm is acquired via a carrier-mediated excitation when Si and Er are co-deposited on the Ge core NW.

In the next chapter emissive erbium-doped Group IV oxide nanofibers derived from an electrospinning process are investigated. Er<sub>2</sub>O<sub>3</sub>, Er-doped SiO<sub>2</sub>, SnO<sub>2</sub>, and GeO<sub>2</sub> nanofibers have been prepared via a sol-gel assisted electrospinning method. The arrayed Er-doped nanofibers are prepared across an insulating gap between two conductive electrodes.

These arrays are believed to be controlled by two types of electrostatic forces. SEM imaging confirms that Er-doped GeO<sub>2</sub> nanofiber can maintain its fiber morphology until it has been annealed at above 700 °C. Annealed at lower temperatures Er-doped GeO<sub>2</sub> nanofibers show dark or yellow colors due probably to the presence of GeO<sub>x</sub>. HRTEM imaging shows that Er-doped SnO<sub>2</sub> nanofibers are composed of tin dioxide nanocrystals, most of which possess a (110) orientation. Both XRD and TEM imaging confirm that the presence of impurities (Er<sup>3+</sup> ions) and lower annealing temperatures are beneficial to forming smaller SnO<sub>2</sub> nanocrystals. Among all four types of fibers, Er<sub>2</sub>O<sub>3</sub> fibers emit very weak luminescence, and the PL intensity of Er-doped GeO<sub>2</sub> fibers is almost 10 times stronger than that of Er-doped SiO<sub>2</sub> fibers. PL excitation spectra suggest that the luminescence of Er<sub>2</sub>O<sub>3</sub>, Er-doped SnO<sub>2</sub>, and Er-doped SiO<sub>2</sub> fibers arises from the direct excitation of erbium ions. In Er-doped GeO<sub>2</sub> nanofibers annealed at 500 and 700 °C, a carrier-mediated excitation process is underlying the reason for the erbium photoluminescence.

In Chapter 6 GeO<sub>x</sub> is introduced purposely into Er-doped SnO<sub>2</sub> nanofibers via a vapor transport method in order to further enhance their PL intensity at 1540 nm. TEM and SEM imaging show that the front part of the fiber sample is melted to form film-like platelets, whereas the back part of the sample is still composed of fibers with lots of nanoparticles on their surface. Micro-Raman spectroscopy confirms the formation of metallic tin in the front part of the sample. However, no detectable metallic Sn is formed on the back part of the sample due presumably to the lower reaction temperature. It was found that longer deposition time of Ge can lead to the formation of Ge nanorods on the surface of Er-doped SnO<sub>2</sub> nanofibers, which might be catalyzed by elemental Sn nanoparticles via a VLS mechanism. Compared with the starting materials, Er-doped SnO<sub>2</sub> nanofibers sensitized by GeO<sub>x</sub> can emit

almost 3 orders of magnitude stronger Er-related luminescence. PL excitation spectra further confirm that this great enhancement in PL intensity is due to the presence of sensitizer,  $\text{GeO}_x$ . The front part of the sample demonstrates a more serious room temperature quenching effect relative to the back part of the sample. This fact is attributed to their difference in composition, which consequently can affect the energy backtransfer and exciton detrapping rates.

This research has demonstrated the possibility to fabricate strongly emissive 1-D semiconducting Ge and SiGe NWs, as well as Group IV oxide nanofibers. All researching results point to the fact that  $\text{GeO}_x$  is an effective sensitizer for erbium ions, the presence of which is the underlying reason for the strong enhancement in Er-related luminescence. Ideally, these semiconducting NWs could be used as building blocks in the fabrication of nanoscale near-IR semiconductor lasers, waveguides, and amplifiers. These oxide nanofibers could be used as building blocks to integrate high density optical units on a single chip. In the long run, much effort is needed to further quantify the sensitizing process of  $\text{Er}^{3+}$  ions by  $\text{GeO}_x$ , such as the measurements of the Er exciton lifetimes in these NWs and nanofibers.

## APPENDIX

**Introduction:**

Bioactive materials have been under extensive investigations due to their potential applications in the field of bone growth and tissue regeneration.<sup>231</sup> For example, bioactive glasses implanted into human body or soaked in simulated body fluid (SBF) can result in the formation of bone-like hydroxyapatite (HA) on their surface.<sup>232,233</sup>

Recently, Zn-containing bioactive glass is reported to be able to induce the precipitation of hydroxyapatite ( $\text{Ca}_{10}(\text{PO}_4)_6(\text{OH})_2$ , abbreviated as CaP) in SBF solution.<sup>234</sup> This glass can also stimulate the proliferation of osteoblasts (bone-forming cells), provided that the concentration of  $\text{Zn}^{2+}$  ions is below certain level ( $\sim 10^{-6}$  mol/L).<sup>234</sup> ZnO nanorods and nanobelts have been reported to possess good mechanical properties.<sup>235,236</sup> Therefore, 1-D ZnO materials should be a good potential bioactive material for bone growth and regeneration.

**Experimental:**

*Fabrication of ZnO microrods and microbelts:* ZnO microrods and microbelts were grown via a vapor transport method.<sup>237-239</sup> The reactor design for fabricating ZnO microrods and microbelts is shown in the Figure 131. Typically, one alumina boat holding a mixture of 0.36 g ZnO and 0.054 g C is placed in a 2.0 cm inner diameter quartz tubing reactor. One end of the reactor is closed and the other is open to air via a hole of the size of a 21 gauge needle. Another alumina boat is positioned downstream in the reactor to collect ZnO microrods. The front part of the boat is located right at the edge of the oven. The reactor is heated up to 1100 °C using a 30 cm ceramic oven and kept for 30 minutes. The ZnO microbelts are formed on

the alumina boat, and microrods are produced on the inner wall of the reactor above the alumina boat.

*Growth of hydroxyapatite (CaP) on ZnO microrods & microbelts in simulated body fluid (SBF):* ZnO microrods & microbelts, ranging in mass from 0.8-1.6 mg, were loaded into a 2 ml plastic vial that was filled up to 1.5 ml using a solution of simulated body fluid (SBF). The preparation of these SBF solutions is the same as that described in Chapter 7. These rods and belts were immersed in SBF solution for time periods ranging from 1 to 5 weeks at 37 °C prior to the SEM and XEDS measurements. In the control experiments, 4.5 mg Zn metal (99.7%, Fisher Scientific Co.) or ZnO powder (100.0%, J. T. Baker Chem. Co.) were placed into 2 ml plastic vials that was filled up to 1.5 ml of SBF.

*Instrumentation:* Structural characterization was performed using a JEOL JSM-6100 SEM at Texas Christian University with an X-ray energy dispersive spectroscopy (XEDS) analyzing system attached.

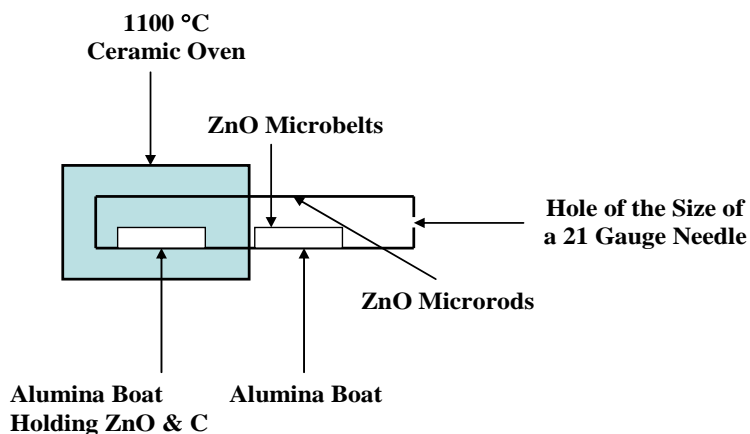


**Figure 131.** Reactor design for preparing ZnO microrods and microbelts.

## Results and Discussion:

Figure 132 shows the SEM images of as-prepared ZnO microrods and microbelts. Figure 132a shows the SEM image of ZnO microrods grown on the inner wall of the quartz tubing reactor. Typically, these ZnO microrods are of 1.5  $\mu\text{m}$  in width and tens of microns in length. It is interesting to find that some ZnO dendrites can also be produced on the inner wall of the reactor, as shown in Figure 132c. Recently, Yang et al. reported that these comb-like ZnO dendrites can be prepared via the thermal annealing of Zn metal in a 5-10% oxygen/argon mixture with a yield of  $\sim 90\%$ .<sup>240</sup> It is believed that the formation of these dendrites is caused by the rapid crystallization of ZnO at a large supersaturation.<sup>240</sup> ZnO microbelts can be produced on the alumina boat due presumably to the critical vapor flow rate of ZnO close to the surface of the boat (Figure 132b). These belts possess a tapering structure and are tens of microns long.

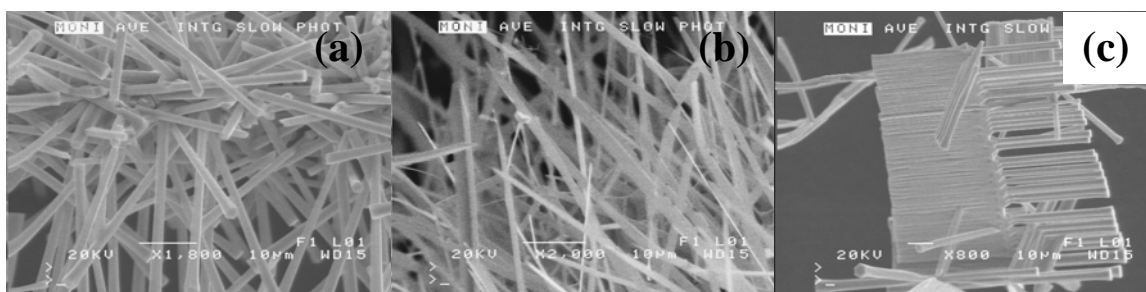


**Figure 132.** SEM images of as-prepared (a) ZnO microrods; (b) ZnO microbelts; (c) ZnO dendrites.

The as-formed ZnO microbelts and microrods were then immersed in a SBF solution for various times at 37 °C intending to grow CaP on these belts and rods, which could have potential applications in tissue engineering. It was found that CaP is not detected on these

rods and belts in the first 2 weeks of immersion in the SBF solution. However, a significant amount of CaP can be grown on these belts after a 3 week immersion in the SBF solution. Figure 133 shows the SEM images and XEDS spectra of the ZnO microbelts and microrods immersed in SBF solution for periods ranging from 3 to 5 weeks. It can be easily seen that a thicker layer of CaP can be grown on these rods and belts after a longer immersion in SBF based on the relatively higher intensity ratio of Ca to Zn in the XEDS spectra. The relative intensity ratios of Ca-K $_{\alpha}$  to Zn-K $_{\alpha}$  are 0.24, 0.36, and 0.59, for the samples immersed in SBF solutions for 3, 4, 5 weeks, respectively. XEDS spectra confirm the presence of zinc in these microrods, where the Zn-L $_{\alpha}$ , K $_{\alpha}$ , and K $_{\beta}$  peaks are located at 1.0, 8.5, and 9.4 KeV, respectively. Some chlorine is apparently trapped in the CaP crystals, which is reflected in the XEDS spectra. The Cl-K $_{\alpha}$ , Ca- K $_{\alpha}$ , and P-K $_{\alpha}$  peaks lie at 2.7, 3.7, 2.0 KeV, respectively.

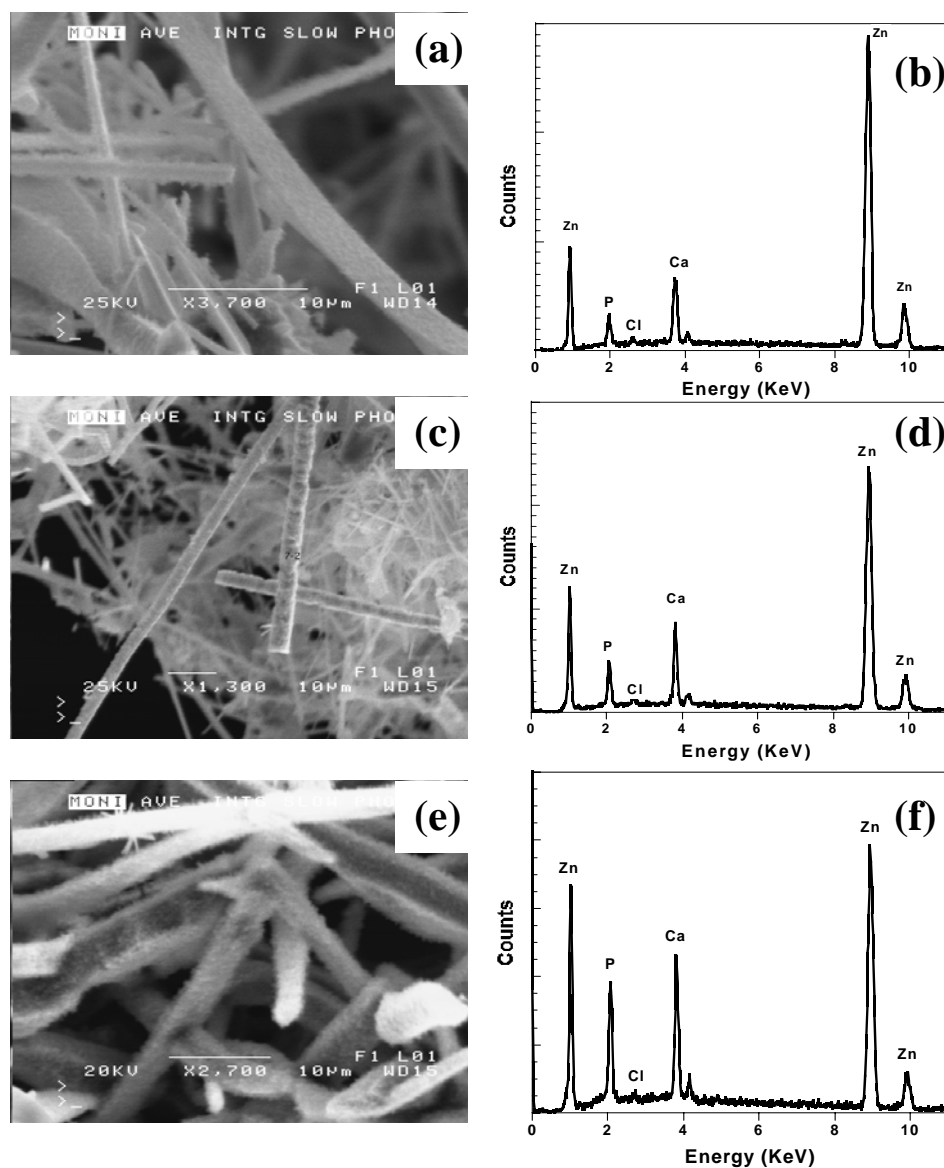


**Figure 133.** SEM images of ZnO microbelts and microrods immersed in SBF at 37 °C for (a) 3 weeks; (c) 4 weeks; (e) 5 weeks. XEDS spectra collected from ZnO rods and belts immersed in a SBF solution for (b) 3 weeks; (d) 4 weeks; (f) 5 weeks.

To further understand the mechanism underlying the growth of CaP on ZnO microrods and microbelts, two control experiments were performed: (1) Zn metal and (2)

ZnO powder were immersed in the SBF solution for the same amount of time in order to investigate the compositional dependence (Zn vs. ZnO) on CaP nucleation and growth. Figure 134 shows the SEM images and XEDS spectra of the Zn metal and ZnO powder samples that have been immersed in SBF solution for 3 weeks. It is found that CaP can be preferentially grown on Zn metal, and no detectable amount of CaP can be found on the surface of ZnO powder sample that was immersed in SBF solution for 3 weeks. It is also notable that CaP can be grown on the Zn metal even if the immersion time is as short as 1 week. Literature reported that  $Zn^{2+}$  can precipitate free  $Ca^{2+}$  and  $PO_4^{3-}$  ions in the form of  $CaZn_2(PO_4)_2 \cdot 2H_2O$ ,<sup>241</sup> which could serve as a nucleation site for the further growth of CaP. Furthermore, Zn deficiency is known to be associated with bone growth retardation.<sup>242</sup> Therefore, it can be inferred from the above results that the growth of CaP on ZnO microrods & microbelts is presumably due to the zinc-rich property of these one-dimensional structures. ZnO nanorods prepared using this carbothermal reduction method have been reported to possess a zinc-rich structure.<sup>239</sup>

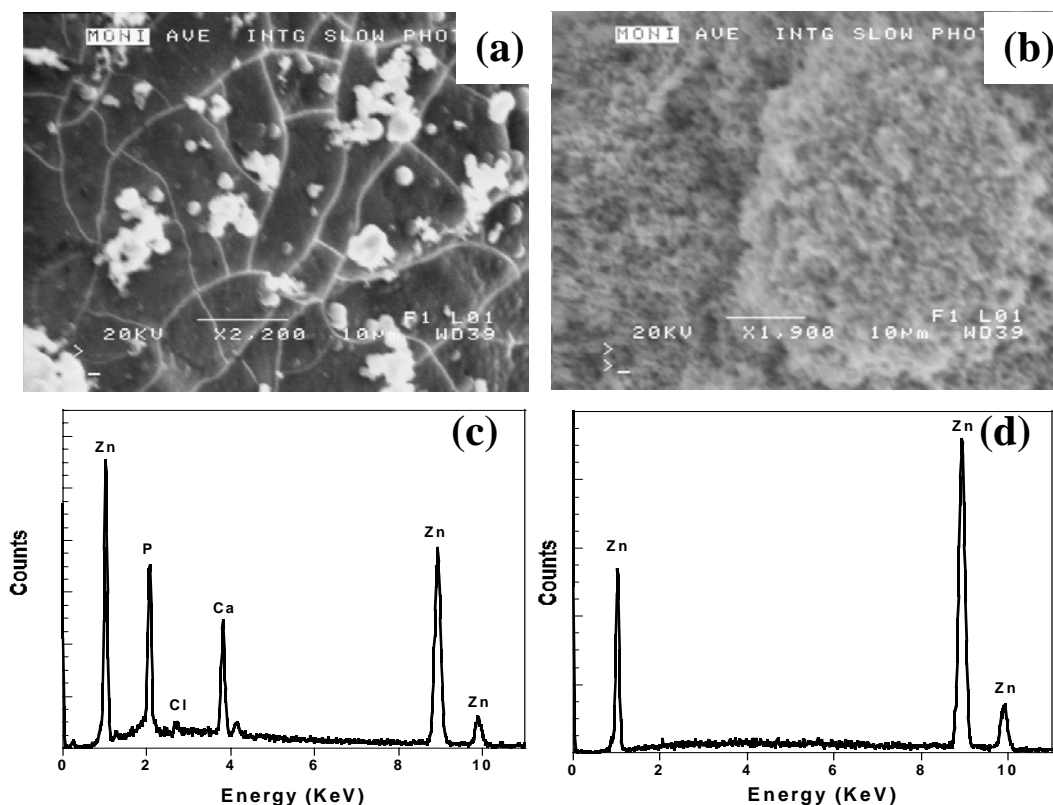


**Figure 134.** SEM images of (a) Zn metal and (b) ZnO powder that have been immersed in a SBF solution for 3 weeks. XEDS spectra (c) and (d) collected from the regions shown in (a) and (b), respectively.

### Summary:

A simple vapor transport method has been employed to fabricate ZnO microrods and microbelts. CaP can be grown on these rods and belts after a 3 week immersion in the SBF solution. A thicker layer of CaP has been grown on these rods and belts using a longer immersion time. In the control experiments, it was found that CaP can be preferentially grown on the Zn metals rather than on the ZnO powders. Therefore, it is inferred that the growth of CaP was presumably initiated by the zinc-rich property of these rods and belts

prepared using a carbothermal reduction method. This type of material might have potential application as scaffolds for facilitating bone growth.

## REFERENCES

1. Moore, G. *Electronics* **1965**, 38, No.8.
2. <http://sscs.org/History/MooresLaw>.
3. <http://www.techworld.com/opsys/news>.
4. Wallraff, G. M.; Hinsberg, W. D. *Chem. Rev.* **1999**, 99, 1801.
5. Momose, H. S.; Ono, M.; Yoshitomi, T.; Ohguro, T.; Nakamura, S.; Saito, M.; Iwai, H. *IEEE Trans. Electron Devices* **1996**, 43, 1233.
6. Huang, Y.; Lieber, C. M. *Pure Appl. Chem.* **2004**, 76, 2051.
7. Whitesides, G. M.; Love, J. C. *Sci. Am.* **2001**, 285, 38.
8. Shenhar, R.; Rotello, V. M. *Acc. Chem. Res.* **2003**, 36, 549.
9. <http://developer.intel.com/technology/itj/q31998/pdf/euv.pdf>.
10. Lieber, C. M. *MRS Bull.* **2003**, 28, 486.
11. Yoffe, A. D. *Adv. Phys.* **2001**, 50, 1.
12. Tricot, Y. M.; Fendler, J. H. *J. Am. Chem. Soc.* **1984**, 106, 2475.
13. Steigerwald, M. L.; Alivisatos, A. P.; Gibson, J. M.; Harris, T. D.; Kortan, R.; Muller, A. J.; Thayer, A. M.; Duncan, T. M.; Douglass, D. C.; Brus, L. E. *J. Am. Chem. Soc.* **1988**, 110, 3046.
14. Brennan, J. G.; Siegrist, T.; Carroll, P. J.; Stuczynski, S. M.; Brus, L. E.; Steigerwald, M. L. *J. Am. Chem. Soc.* **1989**, 111, 4141.
15. Murray, C. B.; Norris, D. J.; Bawendi, M. G. *J. Am. Chem. Soc.* **1993**, 115, 8706.
16. Peng, Z. A.; Peng, X. *J. Am. Chem. Soc.* **2001**, 123, 183.
17. Qu, L.; Peng, Z. A.; Peng, X. *Nano Lett.* **2001**, 1, 333.
18. Bruchez, M.; Moronne, M.; Gin, P.; Weiss, S.; Alivisatos, A. P. *Science* **1998**, 281, 2013.
19. Kim, S.; Lim, Y. T.; Soltesz, E. G.; De Grand, A. M.; Lee, J.; Nakayama, A.; Parker, J. A.; Mihaljevic, T.; Laurence, R. G.; Dor, D. M.; Cohn, L. H.; Bawendi, M. G.; Frangioni, J. V. *Nat. Biotechnol.* **2004**, 22, 93.
20. Wagner, R. S.; Ellis, W. C. *Appl. Phys. Lett.* **1964**, 4, 89.

21. Cui, Y.; Wei, Q. Q.; Park, H. K.; Lieber, C. M. *Science* **2001**, *293*, 1289.
22. Gudiksen, M. S.; Lauhon, L. J.; Wang, J.; Smith, D. C.; Lieber, C. M. *Nature* **2002**, *415*, 617.
23. Duan, X. F.; Huang, Y.; Agarwal, R.; Lieber, C. M. *Nature* **2003**, *421*, 241.
24. Wang, D. W.; Wang, Q.; Javey, A.; Tu, R.; Dai, H. J.; Kim, H.; McIntyre, P. C.; Krishnamohan, T.; Saraswat, K. C. *Appl. Phys. Lett.* **2003**, *83*, 2432.
25. Xiang, J.; Lu, W.; Hu, Y. J.; Wu, Y.; Yan, H.; Lieber, C. M. *Nature* **2006**, *441*, 489.
26. Martin, S. C.; Hitt, L. M.; Rosenberg, J. J. *IEEE Electron Dev. Lett.* **1989**, *10*, 325.
27. Huang, Y.; Duan, X. F.; Wei, Q. Q.; Lieber, C. M. *Science* **2001**, *291*, 630.
28. Whang, D.; Jin, S.; Wu, Y.; Lieber, C. M. *Nano Lett.* **2003**, *3*, 1255.
29. Yang, P. D. *Nature* **2003**, *425*, 243.
30. Melosh, N. A.; Boukai, A.; Diana, F.; Gerardot, B.; Badolato, A.; Petroff, P. M.; Heath, J. R. *Science* **2003**, *300*, 112.
31. Pavesi, L. *J. Phys. C* **2003**, *15*, R1169.
32. Sheu, B.; Ko, P. *IEEE Trans. Circuits Syst.* **1986**, *CAS-33*, 1030.
33. van den Hoven, G. N.; Koper, R. J. I. M.; Polman, A.; Dam, C. v.; Uffelen, J. W. M. v.; Smit, M. K. *Appl. Phys. Lett.* **1996**, *68*, 1886.
34. Kenyon, A. J. *Semicond. Sci. Technol.* **2005**, *20*, R65.
35. Nakamura, S. *Science* **1998**, *281*, 956.
36. Dehlinger, G.; Diehl, L.; Gennser, U.; Sigg, H.; Faist, J.; Ensslin, K.; Grutzmacher, D.; Muller, E. *Science* **2000**, *290*, 2277.
37. Myers, H. P. *Introductory Solid State Physics (Second Edition)*, **1997**, Talor & Francis, Philadelphia.
38. Tewksbury, S. K.; Hornak, L. A.; Nariman, H. E.; Langsjoen, S. M.; McGinnis, S. P. *Proceedings of Fifth Annual IEEE International Conference on Wafer Scale Integration*, **1993**, 358.
39. Hudait, M. K.; Lin, Y.; Wilt, D. M.; Speck, J. S.; Tivarus, C. A.; Heller, E. R.; Pelz, J. P.; Ringel, S. A. *Appl. Phys. Lett.* **2003**, *82*, 3212.
40. Eisenbeiser, K.; Emrick, R.; Droopad, R.; Yu, Z.; Finder, J.; Rockwell, S.; Holmes, J.; Overgaard, C.; Ooms, W. *IEEE Electron Dev. Lett.* **2002**, *23*, 300.

41. Yang, V. K.; Groenert, M.; Leitz, C. W.; Pitera, A. J.; Currie, M. T.; Fitzgerald, E. A. *J. Appl. Phys.* **2003**, *93*, 3859.
42. Chu, S. N. G.; Nakahara, S.; Pearton, S. J.; Boone, T.; Vernon, S. M. *J. Appl. Phys.* **1988**, *64*, 2981.
43. Georgakilas, A.; Panayotatos, P.; Stoemenos, J.; Mourrain, J. L.; Christou, A. *J. Appl. Phys.* **1992**, *71*, 2679.
44. Salanin, M. D. *Luminescence of Molecules and Crystals*, **1995**, Cambridge International Science, Cambridge.
45. Williams, F. E. *Annu. Rev. Phys. Chem.* **1952**, *3*, 339.
46. Iyer, S. S.; Xie, Y. H. *Science* **1993**, *260*, 40.
47. Ashcroft, N. W.; Mermin, N. D. *Solid State Physics*, **1976**, Holt, Rinehart and Winston, New York.
48. Salvador, G.; Dragica, V.; Alexander, A. D. *J. Comput. Electron.* **2002**, *1*, 179.
49. Cohen, M. L.; Bergstresser, T. K. *Phys. Rev.* **1966**, *141*, 789.
50. Oguz, S.; Paul, W.; Deutsch, T. F.; Tsauro, B. Y.; Murphy, D. V. *Appl. Phys. Lett.* **1983**, *43*, 848.
51. Gnutzmann, U.; Clausecker, K. *Appl. Phys. A* **1974**, *3*, 9.
52. Brus, L. *J. Phys. Chem.* **1994**, *98*, 3575.
53. Brus, L. *IEEE J. Quantum Electron.* **1986**, *22*, 1909.
54. Kleppner, D.; Jackiw, R. *Science* **2000**, *289*, 893.
55. Cullis, A. G.; Canham, L. T.; Calcott, P. D. *J. Appl. Phys.* **1997**, *82*, 909.
56. Uhlir, A. *Bell Syst. Tech. J.* **1956**, *35*, 333.
57. Canham, L. T. *Appl. Phys. Lett.* **1990**, *57*, 1046.
58. Lehmann, V.; Gosele, U. *Appl. Phys. Lett.* **1991**, *58*, 856.
59. Schoisswohl, M.; Cantin, J. L.; Chamarro, M.; Vonbardeleben, H. J.; Morgenstern, T.; Bugiel, E.; Kissinger, W.; Andreu, R. C. *Phys. Rev. B* **1995**, *52*, 11898.
60. Miyazaki, S.; Sakamoto, K.; Shiba, K.; Hirose, M. *Thin Solid Films* **1995**, *255*, 99.
61. Choi, H. C.; Buriak, J. M. *Chem. Commun.* **2000**, 1669.

62. Buriak, J. M. *Chem. Rev.* **2002**, *102*, 1271.
63. Wilcoxon, J. P.; Samara, G. A.; Provencio, P. N. *Phys. Rev. B* **1999**, *60*, 2704.
64. Heath, J. R. *Science* **1992**, *258*, 1131.
65. Wilcoxon, J. P. *U.S. Patent No. 5147841*, **1992**.
66. Wilcoxon, J. P.; Williamson, R. L.; Baughman, R. *J. Chem. Phys.* **1993**, *98*, 9933.
67. Bley, R. A.; Kauzlarich, S. M. *J. Am. Chem. Soc.* **1996**, *118*, 12461.
68. Baldwin, R. K.; Pettigrew, K. A.; Ratai, E.; Augustine, M. P.; Kauzlarich, S. M. *Chem. Commun.* **2002**, 1822.
69. Wilcoxon, J. P.; Provencio, P. P.; Samara, G. A. *Phys. Rev. B* **2001**, *64*, 035417.
70. Wilson, W. L.; Szajowski, P. F.; Brus, L. E. *Science* **1993**, *262*, 1242.
71. van den Hoven, G. N.; Snoeks, E.; Polman, A.; van Uffelen, J. W. M.; Oei, Y. S.; Smit, M. K. *Appl. Phys. Lett.* **1993**, *62*, 3065.
72. Snoeks, E.; van den Hoven, G. N.; Polman, A. *J. Appl. Phys.* **1993**, *73*, 8179.
73. Custer, J. S.; Polman, A.; van Pinxteren, H. M. *J. Appl. Phys.* **1994**, *75*, 2809.
74. Serna, R.; Shin, J. H.; Lohmeier, M.; Vlieg, E.; Polman, A.; Alkemade, P. F. A. *J. Appl. Phys.* **1996**, *79*, 2658.
75. Gusev, O. B.; Kuznetsov, A. N.; Terukov, E. I.; Bresler, M. S.; Kudoyarova, V. K.; Yassievich, I. N.; Zakharchenya, B. P.; Fuhs, W. *Appl. Phys. Lett.* **1997**, *70*, 240.
76. Piamonteze, C.; Iniguez, A. C.; Tessler, L. R.; Alves, M. C. M.; Tolentino, H. *Phys. Rev. Lett.* **1998**, *81*, 4652.
77. Voronkov, V. B.; Golubev, V. G.; Medvedev, A. V.; Pevtsov, A. B.; Feoktistov, N. A.; Gorshkov, N. I.; Suglobov, D. N. *Phys. Solid State* **1998**, *40*, 1301.
78. St John, J.; Coffey, J. L.; Chen, Y. D.; Pinizzotto, R. F. *J. Am. Chem. Soc.* **1999**, *121*, 1888.
79. Senter, R. A.; Chen, Y. D.; Coffey, J. L.; Tessler, L. R. *Nano Lett.* **2001**, *1*, 383.
80. Wang, Z. Y.; Coffey, J. L. *Nano Lett.* **2002**, *2*, 1303.
81. Craighead, H. G. *Science* **2000**, *290*, 1532.
82. Law, M.; Goldberger, J.; Yang, P. *Annu. Rev. Mater. Res.* **2004**, *34*, 83.

83. Duan, X.; Lieber, C. M. *Adv. Mater.* **2000**, *12*, 298.
84. Gates, B.; Yin, Y.; Xia, Y. *J. Am. Chem. Soc.* **2000**, *122*, 12582.
85. Gates, B.; Mayers, B.; Cattle, B.; Xia, Y. *Adv. Funct. Mater.* **2002**, *12*, 219.
86. Mayers, B.; Xia, Y. *J. Mater. Chem.* **2002**, *12*, 1875.
87. Mayers, B.; Gates, B.; Yin, Y.; Xia, Y. *Adv. Mater.* **2001**, *13*, 1380.
88. Stejny, J.; Trinder, R. W.; Dlugosz, J. *J. Mater. Sci.* **1981**, *16*, 3161.
89. Martin, C. R. *Science* **1994**, *266*, 1961.
90. He, R.; Law, M.; Fan, R.; Kim, F.; Yang, P. *Nano Lett.* **2002**, *2*, 1109.
91. Ajayan, P. M.; Stephan, O.; Redlich, P.; Colliex, C. *Nature* **1995**, *375*, 564.
92. Ringsdorf, H.; Schlarb, B.; Venzmer, J. *Angew. Chem., Int. Ed.* **1988**, *27*, 113.
93. Wu, Y.; Yang, P. *J. Am. Chem. Soc.* **2001**, *123*, 3165.
94. Lauhon, L.; Gudiksen, M.; Lieber, C. *Philos. Trans. Roy. Soc. A* **2004**, *362*, 1247.
95. Lauhon, L. J.; Gudiksen, M. S.; Wang, D.; Lieber, C. M. *Nature* **2002**, *420*, 57.
96. Barrelet, C. J.; Wu, Y.; Bell, D. C.; Lieber, C. M. *J. Am. Chem. Soc.* **2003**, *125*, 11498.
97. Wang, Z. L. *Mater. Today* **2004**, *7*, 26.
98. Wang, Y.; Schmidt, V.; Senz, S.; Gösele, U. *Nat. Nanotechnol.* **2006**, *1*, 186.
99. Li, D.; Xia, Y. *Adv. Mater.* **2004**, *16*, 1151.
100. Formhals, A. *US Patent, 1,975,504*, **1934**.
101. Reneker, D. H.; Yarin, A. L.; Fong, H.; Koombhongse, S. *J. Appl. Phys.* **2000**, *87*, 4531.
102. Li, D.; Xia, Y. *Adv. Mater.* **2004**, *16*, 361.
103. Pinto, N. J.; Johnson, J. A. T.; MacDiarmid, A. G.; Mueller, C. H.; Theofylaktos, N.; Robinson, D. C.; Miranda, F. A. *Appl. Phys. Lett.* **2003**, *83*, 4244.
104. Shin, Y. M.; Hohman, M. M.; Brenner, M. P.; Rutledge, G. C. *Polymer* **2001**, *42*, 9955.
105. Deitzel, J. M.; Kleinmeyer, K.; Harris, D.; Tan, N. C. B. *Polymer* **2001**, *42*, 261.
106. Li, D.; Xia, Y. *Nano Lett.* **2003**, *3*, 555.

107. Larsen, G.; Velarde-Ortiz, R.; Minchow, K.; Barrero, A.; Loscertales, I. G. *J. Am. Chem. Soc.* **2003**, *125*, 1154.
108. Viswanathamurthi, P.; Bhattarai, N.; Kim, H. Y.; Khil, M. S.; Lee, D. R.; Suh, E. K. *J. Chem. Phys.* **2004**, *121*, 441.
109. Li, D.; Wang, Y.; Xia, Y. *Nano Lett.* **2003**, *3*, 1167.
110. Theron, A.; Zussman, E.; Yarin, A. L. *Nanotechnology* **2001**, *12*, 384.
111. Polman, A. *Physica B* **2001**, *300*, 78.
112. Polman, A. *J. Appl. Phys.* **1997**, *82*, 1.
113. Polman, A.; Jacobson, D. C.; Eaglesham, D. J.; Kistler, R. C.; Poate, J. M. *J. Appl. Phys.* **1991**, *70*, 3778.
114. Polman, A.; van Veggel, F. *J. Opt. Soc. Am. B* **2004**, *21*, 871.
115. Kik, P. G.; Polman, A. *MRS Bull.* **1998**, *23*, 48.
116. van den Hoven, G. N.; Shin, J. H.; Polman, A.; Lombardo, S.; Campisano, S. U. *J. Appl. Phys.* **1995**, *78*, 2642.
117. Snoeks, E.; Kik, P. G.; Polman, A. *Opt. Mater.* **1996**, *5*, 159.
118. Slooff, L. H.; de Dood, M. J. A.; van Blaaderen, A.; Polman, A. *Appl. Phys. Lett.* **2000**, *76*, 3682.
119. Kik, P. G.; deDood, M. J. A.; Kikoin, K.; Polman, A. *Appl. Phys. Lett.* **1997**, *70*, 1721.
120. Strohhofer, C.; Polman, A. *J. Appl. Phys.* **2001**, *90*, 4314.
121. Strohhofer, C.; Polman, A. *Appl. Phys. Lett.* **2002**, *81*, 1414.
122. Fujii, M.; Yoshida, M.; Kanzawa, Y.; Hayashi, S.; Yamamoto, K. *Appl. Phys. Lett.* **1997**, *71*, 1198.
123. Kik, P. G.; Brongersma, M. L.; Polman, A. *Appl. Phys. Lett.* **2000**, *76*, 2325.
124. Slooff, L. H.; Polman, A.; Wolbers, M. P. O.; van Veggel, F.; Reinhoudt, D. N.; Hofstraat, J. W. *J. Appl. Phys.* **1998**, *83*, 497.
125. Oude Wolbers, M. P.; van Veggel, F. C. J. M.; Snellink-Ruel, B. H. M.; Hofstraat, J. W.; Geurts, F. A. J.; Reinhoudt, D. N. *J. Am. Chem. Soc.* **1997**, *119*, 138.
126. Wang, Z. *Synthesis and Characterization of Erbium-Surface Enriched Silicon Nanowires*, Master's Thesis, Texas Christian University, **2003**.

127. St. John, J. V. *Fabrication and Characterization of Rare Earth-Doped Silicon Nanocrystals and Rare Earth-Doped Silicon Dioxide Nanostructures*, Ph.D. Dissertation, Texas Christian University, **1998**.
128. Senter, R.A. *A Study of Structural and Electronic Effects in Erbium (III) Doped and Undoped Group 14 Nanostructures*, Ph.D. Dissertation, Texas Christian University, **2004**.
129. Hayashi, S.; Fujii, M.; Yamamoto, K. *Jpn. J. Appl. Phys.* **1989**, *28*, 1464.
130. Sato, S.; Nozaki, S.; Morisaki, H. *Appl. Phys. Lett.* **1995**, *66*, 3176.
131. Zhang, Y. F.; Tang, Y. H.; Wang, N.; Lee, C. S.; Bello, I.; Lee, S. T. *Phys. Rev. B* **2000**, *61*, 4518.
132. Zhao, H.; Wachter, S.; Kalt, H. *Phys. Rev. B* **2002**, *66*, 085337.
133. Chen, J. H.; Pang, D.; Cheong, H. M.; Wickboldt, P.; Paul, W. *Appl. Phys. Lett.* **1996**, *67*, 2182.
134. Jacquemin, J. L.; Bordure, G. *J. Phys. Chem. Solids.* **1975**, *36*, 1081.
135. Aita, C. R.; Marhic, M. E.; Sayers, C. N. *Diffus. Defect Data Pt. B* **1987**, *55*, 53.
136. Sato, S.; Nozaki, S.; Morisaki, H. *J. Appl. Phys.* **1997**, *81*, 1518.
137. Wu, J.; Panchaietch, P.; Wallace, R. M.; Coffey, J. L. *Adv. Mater.* **2004**, *16*, 1444.
138. Hanrath, T.; Korgel, B. A. *J. Am. Chem. Soc.* **2004**, *126*, 15466.
139. Yu, G.; Krishna, K. M.; Shao, C.; Umeno, M.; Soga, T.; Watanabe, J.; Jimbo, T. *J. Appl. Phys.* **1998**, *83*, 174.
140. Robillard, M.; Jessop, P. E.; Bruce, D. M.; Janz, S.; Williams, R. L.; Mailhot, S.; Lafontaine, H.; Kovacic, S. J.; Ojha, J. J. *J. Vac. Sci. Technol. B* **1998**, *16*, 1773.
141. Telford, M. *III-Vs Review* **2004**, *17*, 32.
142. Klocek, P. *Handbook of Infrared Optical Materials*, **1991**, Marcel Dekker, New York.
143. Ray, S. C.; Karanjai, M. K.; Dasgupta, D. *Surf. Coat. Technol.* **1998**, *102*, 73.
144. Morais, E. A.; Scalvi, L. V. A.; Ribeiro, S. J. L.; Geraldo, V. *Phys. Status Solidi A* **2005**, *202*, 301.
145. Pan, Z.; Morgan, S. H. *J. Lumin.* **1997**, *75*, 301.
146. Wang, J.; Lincoln, J. R.; Brocklesby, W. S.; Deol, R. S.; Mackechnie, C. J.; Pearson, A.; Tropper, A. C.; Hanna, D. C.; Payne, D. N. *J. Appl. Phys.* **1993**, *73*, 8066.

147. Lezal, D.; Pedlikova, J.; Kostka, P.; Bludska, J.; Poulain, M.; Zavadil, J. *J. Non-Cryst. Solids* **2001**, *284*, 288.
148. Terrasi, A.; Franzo, G.; Coffa, S.; Priolo, F.; Dacapito, F.; Mobilio, S. *Appl. Phys. Lett.* **1997**, *70*, 1712.
149. Munoz, M.; Argoul, P.; Farges, F. *Am. Mineral.* **2003**, *88*, 694.
150. Lytle, F. W.; Sayers, D. E.; Stern, E. A. *Phys. Rev. B* **1975**, *11*, 4825.
151. Heald, S. M. *X-ray Absorption: Principles, Applications, Techniques of EXAFS, SEXAFS, and XANES*, **1988**, John Wiley & Sons, New York.
152. Wu, Y.; Yang, P. *Appl. Phys. Lett.* **2000**, *77*, 43.
153. Wu, X. C.; Song, W. H.; Zhao, B.; Sun, Y. P.; Du, J. J. *Chem. Phys. Lett.* **2001**, *349*, 210.
154. Wang, D.; Chang, Y. L.; Wang, Q.; Cao, J.; Farmer, D. B.; Gordon, R. G.; Dai, H. J. *Am. Chem. Soc.* **2004**, *126*, 11602.
155. [http://www.cxro.lbl.gov/optical\\_constants/pert\\_form.html](http://www.cxro.lbl.gov/optical_constants/pert_form.html).
156. Yang, C.; Zhong, Z.; Lieber, C. M. *Science* **2005**, *310*, 1304.
157. Choi, W. K.; Ng, V.; Ng, S. P.; Thio, H. H.; Shen, Z. X.; Li, W. S. *J. Appl. Phys.* **1999**, *86*, 1398.
158. Piskanec, S.; Cantoro, M.; Ferrari, A. C.; Zapien, J. A.; Lifshitz, Y.; Lee, S. T.; Hofmann, S.; Robertson, J. *Phys. Rev. B* **2003**, *68*, 241312.
159. Biskupek, J.; Kaiser, U. *J. Electron Microsc.* **2004**, *53*, 601.
160. O'Connor, D. J.; Sexton, B. A.; Smart, R. St. C. *Surface Analysis Methods in Materials Science*, **1992**, Springer-Verlag, New York.
161. Van, T. T.; Chang, J. P. *Appl. Phys. Lett.* **2005**, *87*, 011907.
162. Bruno, M.; Palumbo, M.; Marini, A.; Del Sole, R.; Olevano, V.; Kholod, A. N.; Ossicini, S. *Phys. Rev. B* **2005**, *72*, 153310.
163. Zanatta, A. R.; Nunes, L. A. O.; Tessler, L. R. *Appl. Phys. Lett.* **1997**, *70*, 511.
164. Brusatin, G.; Guglielmi, M.; Martucci, A. *J. Am. Ceram. Soc.* **1997**, *80*, 3139.
165. Lezal, D.; Pedlikova, J. *Ceramics-Silikaty.* **1995**, *39*, 118.
166. Borak, A. *Science* **2005**, *308*, 638.

167. Lynch, S. A.; Bates, R.; Paul, D. J.; Norris, D. J.; Cullis, A. G.; Ikonik, Z.; Kelsall, R. W.; Harrison, P.; Arnone, D. D.; Pidgeon, C. R. *Appl. Phys. Lett.* **2002**, *81*, 1543.
168. Myronov, M.; Parry, C. P.; Mironov, O. A.; Parker, E. H. C. *Appl. Phys. Lett.* **2004**, *85*, 3145.
169. Lee, M. L.; Fitzgerald, E. A. *J. Appl. Phys.* **2005**, *97*, 011101 1.
170. Mitchell, M. J.; Ashburn, P.; Hemment, P. L. F. *J. Appl. Phys.* **2002**, *92*, 6924.
171. Snoeks, E.; Weber, T.; Cacciato, A.; Polman, A. *J. Appl. Phys.* **1995**, *78*, 4723.
172. Shin, H. K.; Lockwood, D. J.; Baribeau, J. M. *Solid State Commun.* **2000**, *114*, 505.
173. Brya, W. J. *Solid State Commun.* **1973**, *12*, 253.
174. Choi, W. K.; Teh, L. K.; Bera, L. K.; Chim, W. K.; Wee, A. T. S.; Jie, Y. X. *J. Appl. Phys.* **2002**, *91*, 444.
175. Priolo, F.; Franzo, G.; Coffa, S.; Polman, A.; Libertino, S.; Barklie, R.; Carey, D. J. *Appl. Phys.* **1995**, *78*, 3874.
176. Tessler, L. R.; Piamonteze, C.; Alves, M. C. M.; Tolentino, H. *J. Non-Cryst. Solids* **2000**, *266*, 598.
177. Billing, D. E.; Hathaway, B. J.; Nicholls, P. *J. Chem. Soc. A* **1970**, 1877.
178. Yamamoto, K.; Kojima, K.; Handa, K.; Wada, N.; Ozutsumi, K. *J. Ceram. Soc. Jpn.* **2004**, *112*, 245.
179. Yin, H.; Peterson, R. L.; Hobart, K. D.; Shieh, S. R.; Duffy, T. S.; Sturm, J. C. *Mat. Res. Soc. Symp. Proc.* **2003**, *765*, D4.7.1.
180. Krasil'nikova, L. V.; Stepihova, M. V.; Drozdov, Yu. N.; Drozdov, M. N.; Krasil'nik, Z. F.; Shengurov, V. G.; Chalkov, V. Yu.; Svetlov, S. P.; Gusev, O. B. *Phys. Solid State* **2005**, *47*, 93.
181. Teo, B. K.; Chen, W. W.; Sun, X. H.; Wang, S. D.; Lee, S. T. *J. Phys. Chem. B* **2005**, *109*, 21716.
182. Eaglesham, D. J.; Michel, J.; Fitzgerald, E. A.; Jacobson, D. C.; Poate, J. M.; Benton, J. L.; Polman, A.; Xie, Y. H.; Kimerling, L. C. *Appl. Phys. Lett.* **1991**, *58*, 2797.
183. Coffa, S.; Franzo, G.; Priolo, F.; Polman, A.; Serna, R. *Phys. Rev. B.* **1994**, *49*, 16313.
184. Selvarajan, A.; Srinivas, T. *IEEE J. Quantum Electron.* **2001**, *37*, 1117.
185. Kunitz, M. *J. Gen. Physiol.* **1926**, *9*, 715.

186. Haidekker, M. A.; Brady, T. P.; Lichlyter, D.; Theodorakis, E. A. *Bioorg. Chem.* **2005**, *33*, 415.
187. Hu, J. Q.; Li, Q.; Meng, X. M.; Lee, C. S.; Lee, S. T. *Adv. Mater.* **2002**, *14*, 1396.
188. Drucker, J. *Phys. Rev. B* **1993**, *48*, 18203.
189. Madon, M.; Gillet, Ph.; Julien, Ch.; Price, G. D. *Phys. Chem. Miner.* **1991**, *18*, 7.
190. Khanna, P. K.; Gokhale, R.; Subbarao, V. V. V. S. *J. Mater. Sci.* **2004**, *39*, 3773.
191. Kamitsos, E. I.; Yiannopoulos, Y. D.; Jain, H.; Huang, W. C. *Phys. Rev. B* **1996**, *54*, 9775.
192. Zacharias, M.; Bläsing, J. *Phys. Rev. B* **1995**, *52*, 14018.
193. Patterson, A. L. *Phys. Rev.* **1939**, *56*, 978.
194. Schurmann, U.; Hartung, W.; Takele, H.; Zaporojtchenko, V.; Faupel, F. *Nanotechnology* **2005**, *16*, 1078.
195. Karim, S.; Toimil-Molares, M. E.; Maurer, F.; Miehe, G.; Ensinger, W.; Liu, J.; Cornelius, T. W.; Neumann, R. *Appl. Phys. A* **2006**, *84*, 403.
196. Quochi, F.; Orru, R.; Cordella, F.; Mura, A.; Bongiovanni, G.; Artizzu, F.; Deplano, P.; Mercuri, M. L.; Pilia, L.; Serpe, A. *J. Appl. Phys.* **2006**, *99*, 053520.
197. Serna, R.; Snoeks, E.; van den Hoven, G. N.; Polman, A. *J. Appl. Phys.* **1994**, *75*, 2644.
198. Righini, G. C.; Pelli, S.; Ferrari, M.; Armellini, C.; Zampedri, L.; Tosello, C.; Ronchin, S.; Rolli, R.; Moser, E.; Montagna, M.; Chiasera, A.; Ribeiro, S. J. L. *Opt. Quant. Electron.* **2002**, *34*, 1151.
199. Snoeks, E.; van den Hoven, G. N.; Polman, A. *IEEE J. Quantum Electron.* **1996**, *32*, 1680.
200. Pacifici, D. *Erbium Doped Silicon Nanoclusters for Microphotonics*, Ph.D. Dissertation, University of Catania, **2003**.
201. Deng, X.; Yang, B. K.; Hackney, S. A.; Krishnamurthy, M.; Williams, D. R. M. *Phys. Rev. Lett.* **1998**, *80*, 1022.
202. Ovsyuk, N. N.; Gorokhov, E. B.; Grishchenko, V. V.; Shebanin, A. P. *JETP Lett.* **1988**, *47*, 298.
203. Menéndez, J.; Cardona, M. *Phys. Rev. B* **1984**, *29*, 2051.
204. Dieguez, A.; Romano-Rodriguez, A.; Vila, A.; Morante, J. R. *J. Appl. Phys.* **2001**, *90*, 1550.

205. Kravets, V. G.; Kolmykova, V. Y. *Opt. Spectrosc.* **2005**, *99*, 68.
206. Franzo, G.; Vinciguerra, V.; Priolo, F. *Appl. Phys. A* **1999**, *69*, 3.
207. Suh, K.; Shin, J. H.; Park, O.-H.; Bae, B.-S.; Lee, J.-C.; Choi, H.-J. *Appl. Phys. Lett.* **2005**, *86*, 053101.
208. Priolo, F.; Franzo, G.; Iacona, F.; Pacifici, D.; Vinciguerra, V. *Mat. Sci. Eng. B* **2001**, *81*, 9.
209. Krithivasan, R.; Yuan, L.; Cressler, J. D.; Jae-Sung, R.; Khater, M. H.; Ahlgren, D.; Freeman, G. *IEEE Electron Dev. Lett.* **2006**, *27*, 567.
210. Miguez, H.; Meseguer, F.; Lopez, C.; Holgado, M.; Andreasen, G.; Mifsud, A.; Fornes, V. *Langmuir* **2000**, *16*, 4405.
211. Tierney, M. J.; Kim, H. O. L. *Anal. Chem.* **1993**, *65*, 3435.
212. Cayre, O. J.; Paunov, V. N. *J. Mater. Chem.* **2004**, *14*, 3300.
213. Nuesch, F.; Li, Y.; Rothberg, L. J. *Appl. Phys. Lett.* **1999**, *75*, 1799.
214. Parekh, V.; Chunsheng, E.; Smith, D.; Ruiz, A.; Wolfe, J. C.; Ruchhoeft, P.; Svedberg, E.; Khizroev, S.; Litvinov, D. *Nanotechnology* **2006**, *17*, 2079.
215. Madou, M. J. *Anal. Bioanal. Chem.* **2004**, *378*, 11.
216. Uchida, M.; Kim, H.; Kokubo, T.; Miyaji, F.; Nakamura, T. *J. Am. Ceram. Soc.* **2001**, *84*, 2041.
217. Gray, J. L.; Hull, R.; Lam, C. H.; Sutter, P.; Means, J.; Floro, J. A. *Phys. Rev. B* **2005**, *72*, 155323.
218. Sun, H. P.; Chen, Y. B.; Pan, X. Q.; Chi, D. Z.; Nath, R.; Foo, Y. L. *Appl. Phys. Lett.* **2005**, *86*, 071904.
219. Fang, C.; Foll, H.; Carstensen, J. *J. Electroanal. Chem.* **2006**, *589*, 259.
220. Adhikari, H.; Marshall, A. F.; Chidsey, C. E. D.; McIntyre, P. C. *Nano Lett.* **2006**, *6*, 318.
221. Popescu, D. C.; van Leeuwen, E. N. M.; Rossi, N. A. A.; Holder, S. J.; Jansen, J. A.; Sommerdijk, N. *Angew. Chem., Int. Ed.* **2006**, *45*, 1762.
222. Addadi, L.; Raz, S.; Weiner, S. *Adv. Mater.* **2003**, *15*, 959.
223. Wang, Z. L. *Microsc. Microanal.* **2004**, *10*, 158.
224. Yu, Q.; Ou, H. D.; Song, R. Q.; Xu, A. W. *J. Cryst. Growth* **2006**, *286*, 178.

225. Viravaidya, C.; Li, M.; Mann, S. *Chem. Commun.* **2004**, *19*, 2182.
226. Balz, M.; Therese, H. A.; Li, J. X.; Gutmann, J. S.; Kappl, M.; Nasdala, L.; Hofmeister, W.; Butt, H. J.; Tremel, W. *Adv. Funct. Mater.* **2005**, *15*, 683.
227. Zhou, G. T.; Yu, J. C.; Wang, X. C.; Zhang, L. Z. *New. J. Chem.* **2004**, *28*, 1027.
228. Davis, K. J.; Dove, P. M.; De Yoreo, J. J. *Science* **2000**, *290*, 1134.
229. Gabrielli, C.; Jaouhari, R.; Joiret, S.; Maurin, G.; Rousseau, P. *J. Electrochem. Soc.* **2003**, *150*, C478.
230. Patolsky, F.; Timko, B. P.; Yu, G.; Fang, Y.; Greytak, A. B.; Zheng, G.; Lieber, C. M. *Science* **2006**, *313*, 1100.
231. Hench, L. L. *J. Biomed. Mater. Res.* **1998**, *41*, 511.
232. Hench, L. L.; Splinter, R. J.; Allen, W. C.; Greenlee, T. K. *J. Biomed. Mater. Res. Symp.* **1971**, *2*, 117.
233. Kokubo, T.; Kim, H.M.; Kawashita, M. *Biomaterials* **2003**, *24*, 2161.
234. Du, R. L.; Chang, J.; Ni, S. Y.; Zhai, W. Y.; Wang, J. Y. *J. Biomater. Appl.* **2006**, *20*, 341.
235. Wang, X.; Song, J.; Wang, Z. L. *J. Mater. Chem.* **2007**, *17*, 711.
236. Haque, M. A.; Desai, A. V. *Proc. SPIE* **2007**, *6464*, 64640B.
237. Yang, P. D.; Yan, H. Q.; Mao, S.; Russo, R.; Johnson, J.; Saykally, R.; Morris, N.; Pham, J.; He, R. R.; Choi, H. J. *Adv. Funct. Mater.* **2002**, *12*, 323.
238. Huang, M. H.; Mao, S.; Feick, H.; Yan, H.; Wu, Y.; Kind, H.; Weber, E.; Russo, R.; Yang, P. *Science* **2001**, *292*, 1897.
239. Yao, B. D.; Chan, Y. F.; Wang, N. *Appl. Phys. Lett.* **2002**, *81*, 757.
240. Yan, H. Q.; He, R. R.; Johnson, J.; Law, M.; Saykally, R. J.; Yang, P. D. *J. Am. Chem. Soc.* **2003**, *125*, 4728.
241. Gigliola, L.; Ledi, M.; Monica, S. *J. Mater. Sci.: Mater. Med.* **2002**, *13*, 91.
242. Rossi, L.; Migliaccio, S.; Corsi, A.; Marzia, M.; Bianco, P.; Teti, A.; Gambelli, L.; Cianfarani, S.; Paoletti, F.; Branca, F. *J. Nutr.* **2001**, *131*, 1142.

## VITA

Ji Wu was born in Chaohu, Anhui, China on September 3, 1972. He is the fourth child of Chunfu Wu and Guilin Zhang. In 1994, he received an associate degree of chemical engineering from Hefei United University, Hefei, Anhui, China. He then went to receive a Master of Science degree from the Department of Chemistry of Anhui University, Hefei, Anhui, China, in 2000. After receiving his Master of Science degree, he did two years nanotechnology research in the Department of Chemistry at the University of Science and Technology of China, Hefei, Anhui, China. In August 2002, he enrolled in Texas Christian University to pursue his doctorate in inorganic/materials under the direction of Prof. Jeffery L. Coffey.

He is married to Xueqian You of Suzhou, China. They have one child.

## ABSTRACT

# FABRICATION AND OPTICAL PROPERTIES OF ERBIUM-DOPED GROUP IV NANOWIRES AND THEIR CORRESPONDING OXIDES

by

Ji Wu, Ph. D., 2007  
Department of Chemistry  
Texas Christian University

Dissertation Advisor: Jeffery L. Coffey, Professor of Chemistry  
and Chair of the Department

As photolithography-based top-down methods are approaching their fundamental limits, new conceptual methods are emerging as possible alternatives to replace them. Alternatives based on bottom-up approach rely on the assembly of basic building blocks such as nanowires. One-dimensional Group IV semiconductors (Ge, SiGe) are very important electronic materials. However, they cannot be used in optoelectronics due to their intrinsic indirect band gap properties. One of the most effective approaches to make them luminescent is the introduction of impurities such as  $\text{Er}^{3+}$  ions.  $\text{Er}^{3+}$  is of technologically important because its emission lies at the transmission window of silica. Another focus of our research is to fabricate one-dimensional Er-doped Group IV *oxide* amplifiers. Ideally, these NWs could be used as building blocks in the field of near-IR nanophotonics.

The basic building block Ge NWs were first fabricated via a vapor-liquid-solid synthetic route. Next, these Ge NWs were doped with  $\text{Er}^{3+}$  ions. These NWs were characterized using electron microscopy and spectroscopy, showing that these nanowires

possess a core-shell structure. Activation and possible underlying mechanism for the Er-related emission have also been explored.

Since Ge NWs are readily oxidized, Si was introduced to form stable SiGe alloys in order to circumvent this problem. Three different alloyed architectures were prepared. A combination of electron microscopes in concert with both elemental and Raman microanalyses were used to investigate the composition and structure of these Er-doped SiGe NWs. The Er coordination environment and Er-related luminescence properties have also been investigated.

Er-doped group IV oxide nanofibers were fabricated via an electrospinning approach. These nanofibers were then characterized using X-ray diffraction, electron microscopy, and spectroscopy to investigate their structures and compositions. The Er<sup>3+</sup> ions in Er-doped GeO<sub>2</sub> nanofibers were found to be excited through a GeO<sub>x</sub>-mediated process.

Lastly, the Er sensitizer, GeO<sub>x</sub> was introduced deliberately into Er-doped SnO<sub>2</sub> nanofibers. These composite nanofiber structures were characterized using electron microscopy and spectroscopy, showing that SnO<sub>2</sub> can be reduced by Ge to form Sn metal. A longer Ge deposition time leads to the formation of Ge nanorods. The Er-related luminescence from these sensitized nanofibers has been enhanced by almost 2 orders of magnitude.